UNIFIER19
COMMUNITY FRIENDLY MINILINER

# D1.2.: The design framework for an NZE 19-seater

March 2020

PIPISTREL VERTICAL SOLUTIONS

POLITECNICO MILANO 1863

TU Delft
Delft University of Technology

This project has received funding from the Clean Sky 2 Joint Undertaking (JU) under grant agreement No 864901. The JU receives support from the European Union's Horizon 2020 research and innovation programme and the Clean Sky 2 JU members other than the Union

Clean Sky 2

# Document Control Sheet

| | |
|---|---|
| Project Number | 864901 |
| Project Acronym | UNIFIER19 |
| Project Full Title | Communty Friendly Miniliner 2019 |
| Project URL | https://www.unifier19.eu/ |
| Work Package | WP1 |
| Document URL | https://pipistrel.sharepoint.com/sites/UNIFIER19 |
| Issue Date | 31.3.2020 |
| Author(s) | Lorenzo Trainelli, Politecnico di Milano<br>Carlo E. D Riboldi, Politecnico di Milano<br>Alberto Rolando, Politecnico di Milano<br>Francesco Salucci, Politecnico di Milano<br>Fabrizio Oliviero, Technical University Delft<br>Jernej Pirnar, Pipistrel Vertical Solutions<br>Thomas Koopman, Pipistrel Vertical Solutions<br>Andres Žnidar, Pipistrel Vertical Solutions |
| Nature | Document |
| Dissemination Level | Open to the general public |

# Executive summary

The present document constitutes deliverable D1.1 "The design framework for an NZE 19-seater – Complete Report" resulting from the activities carried out in the WP1 "Design framework" of the UNIFIER19 - Community Friendly Miniliner project, funded by the Clean Sky JTI under GA no. 864901.

The document sets the design framework for the UNIFIER19 design activities by

- detailing a review and state of the art discussion of pure-electric and hybrid-electric technologies for aeronautical powertrains, airframe and propulsion aircraft architecture options, existing commuters and proposed concepts applicable to the scope of UNIFIER19;
- discussing the results of original market studies for miniliner service applications;
- discussing noise and chemical emission models and tools;
- discussing aircraft cost and infrastructural cost models and tools; and
- introducing a strategy for collaborative data management and exchange in the project.

A brochure, dedicated to the general public, is annexed, to provide information on the project, its approach and its goals.

# Table of contents

# List of Figures

# List of Tables

# 1 Introduction

## *1.1 Pure-electric and hybrid-electric technology review*

### 1.1.1 Powertrain architectures

Various options for electric aircraft powertrain architectures can be found in scientific literature, mirroring and/or inspiring real aircraft prototypes and concepts under developments. Two representative schematics of these topologies are displayed in Figure 1.1 and Figure 1.2.

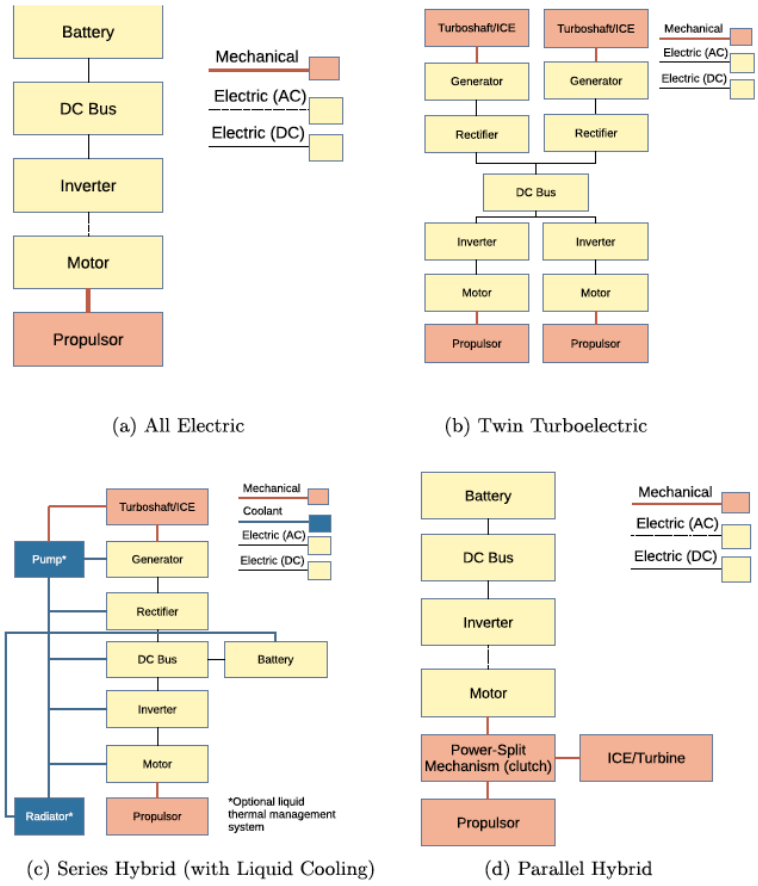


Figure 1.1: Notional electric propulsion architecture [1].

These architectures can be grouped in 4 categories:

1. Pure Electric (PE) or all electric, full electric, fully electric, universally electric, electric propulsion: no thermal engine is included. Battery is the only source of energy and electric power, which is converted into mechanical power by an electric motor. The electric motor is then connected to the propeller or fan to produce thrust.

2. Series or serial hybrid electric: electric motors are fed by batteries and/or electric energy coming from a Power Generation System (PGS). This power can be generated by a Thermal Engine (TE) or Fuel Cells (FCs). A variation of this architecture is the turboelectric one, where there is no battery present.
3. Parallel hybrid electric: both electric motors and thermal engines are mechanically connected to propellers/fans.
4. Conventional: the conventional powertrain.

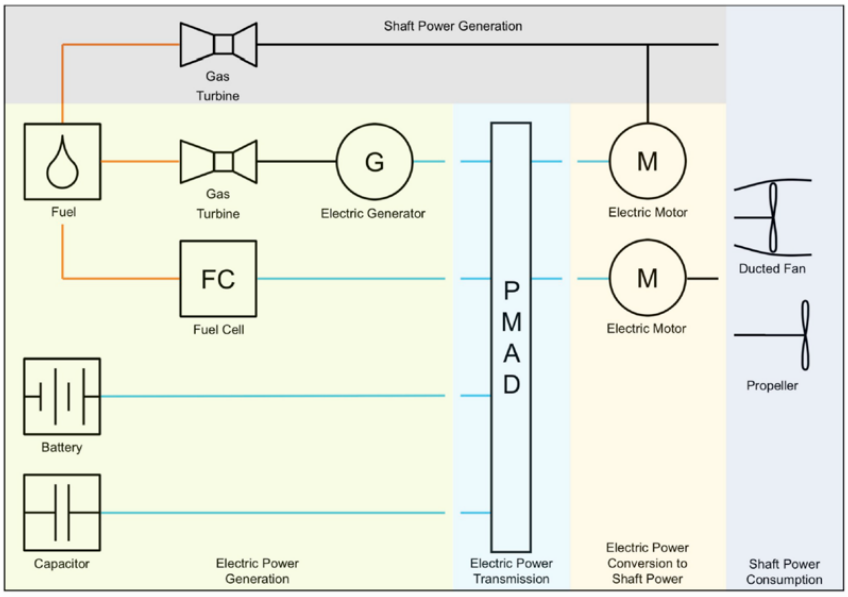


Figure 1.2: Electric aircraft propulsion system topologies [2].

These four configurations can be differentiated using quantitative indicators called *degrees of hybridization* or *hybridization factors*, trying to establish a connection among the various architectures. These were introduced in [3] and recalled by [1]:

$$H_P = \frac{P_m}{P_{tot}} \tag{1.1}$$

$$H_E = \frac{E_b}{E_{tot}} \tag{1.2}$$

where $P_m$ and $E_b$ are usually intended as the power and energy of the *non-polluting* source of energy, usually battery of hydrogen.

There is no clear understanding on which of these configurations can be the most sustainable for the environment. Very little studies have been done in this regard [4], [5], and cradle-to-grave environmental assessments concluded that there is a great difficulty to make an accurate prediction due to the dependence on many uncertain parameters, such as the energy sources employed to recharge the batteries, usage of

rare materials within the batteries etc. However, for what concerns the aviation field, two main programmes are in place to drastically reduce the sector's environmental impact: NASA N+3 goals and ACARE Flightpath 2050. The main objectives of these two programmes are summarized in Table 1.1.

Table 1.1: ACARE Flightpath 2050 and NASA N+3 goals for emission reduction [2].

| Emission | Flightpath 2050[a] | N+3[b] |
|---|---|---|
| Noise | −65%[c] | −71 dB[d] |
| LTO $NO_x$ | 0[e] | −75%[f] |
| $NO_x$ | −90% | – |
| $CO_2$ | −75% | – |
| Fuel Burn | – | −70%[g] |

[a] 2050 implementation, relative to state of the art aircraft in 2000.
[b] 2035 implementation.
[c] Perceived noise of flying aircraft.
[d] Relative to FAA Stage 4 noise regulation.
[e] Emission-free taxiing.
[f] Relative to CAEP 6.
[g] Relative to state of the art aircraft in 2008.

It has been widely demonstrated that incremental advancements in aircraft technologies, such as aerodynamics, structures/materials, and operations are insufficient to achieve these targets with the current conventional propulsion architectures [6]–[9]. Therefore, a switch towards less polluting architectures is necessary. We can see that NASA N+3 goals and ACARE pay a lot of attention to harmful gaseous emissions ($CO_2$ and $NO_X$) and noise. It's been demonstrated from several sources [2], [10] that the best way to cut gaseous emissions is trough electrification. So, a PE configuration is the winner among the new propulsion architectures. However, it is common knowledge that current batteries are too heavy for aeronautics. Hence, the hydrogen option has recently come up as one of the most promising alternative or addition to a PE powertrain. $H_2$ can be employed both as fuel for TEs and as a fuel for electrochemical reactions in FCs. Hydrogen combustion in TEs however achieves very low burning efficiencies (25%). On the other hand, using hydrogen with FCs brings higher efficiencies (50-60%) and only produces water vapour. This water vapour, being entirely free of soot particles cuts on the formation of contrails [11] which appear to be a significant portion of aviation-attributable climate warning.

Therefore, two configurations have been selected among the aforementioned ones:

1. Pure electric – PE
2. Hydrogen FC Serial Hybrid Electric – FCHE

These two architectures can be called *zero emission architectures* as they produce no harmful gaseous emissions.

As depicted inFigure 1.3, there is a shortlist of fundamental subsystems which compose these PE and FCHE powertrains:

- Energy Storage
  - Fuel tank
  - Batteries
  - Supercapacitors
- electric Power Generation System (ePGS)
  - Batteries
  - Supercapacitors
  - Fuel Cell System
- Power Management Control and Delivery (PMCD)
- Electric Drive –
  - Electric motors
  - Electric motor controller
- Thrust Generation System – (TGS)
  - Propellers
  - Ducted fans

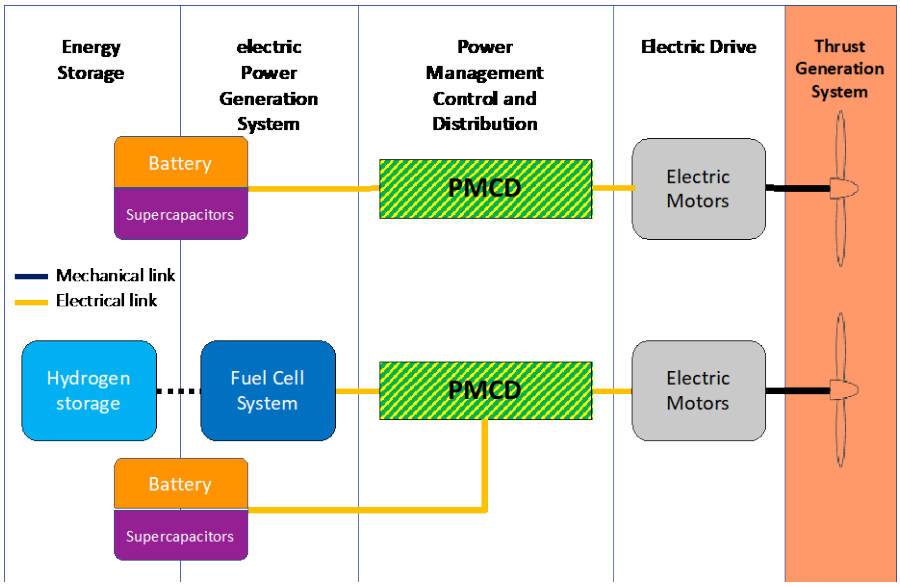


Figure 1.3: Schematics of zero-emission powertrains (top: pure electric, bottom: FC serial hybrid-electric).

In the following, a detailed description of the state of the art of most powertrain components is provided. Namely: battery, supercapacitors, hydrogen storage, fuel cell system and electric drive (electric motor + electric motor controller). PMCD, a complex part, made up by multiple elements (regulators, buck-boost converters, power electronic devices, high power and low power bus, fault current limiters, etc.) necessary for the good operation of the powertrain electrical system.

### 1.1.2 Subsystem technology

#### *1.1.2.1 Battery*

A crucial part of a PE or HE aircraft is battery. Batteries represent the source of all or part of the propulsive power. Sometimes, they can be also part of the aircraft structure itself [12]–[14]. Battery research and development has surged, mainly due to the spread of electric vehicles [15]–[17]. The most common battery types on the market and/or in development today are:

- Lithium-ion Batteries (LIBs)
- Lithium Sulfur Batteries (LSBs)
- Lithium-Air Batteries (LABs)

Batteries are usually compared and contrasted considering several parameters. Some of the most important are:

1. Specific energy: energy stored per mass unit [Wh/kg] or [J/kg], usually expressed in the charged state.
2. Specific power: available power output per mass unit. [W/kg]. Sometimes can be expressed in terms of C-Rate or rated power.
3. Energy density: the amount of energy stored per volume unit. [Wh/l] or [J/kg].
4. Cycle life: no. of full charge – discharge cycles that a battery can withstand before losing 20% of its original capacity.

Other parameters are operating temperature range, maximum and optimal charging rate, calendar life, safety and cost.

It is interesting to notice that battery technology developments are not following trends like Moore's law [18] (Moore's law defines that, the capacity of the computers doubles every 18 months): from 1950 to 1990 the specific energy of batteries has increased by 3 Wh/kg per year. Since then the growing rate was about 5-8 %/year [19].

##### *1.1.2.1.1 Li-ion*

The state of the art of modern electrochemistry for electric mobility applications is represented by Li-ion batteries [20]–[22]. LIBs are near an optimal performance and might reach their full potential on a shorter term than other battery types still in early development [23]. Many different kinds of LIBs exist (Table 1.2).

Table 1.2: Common cathode options for Li-ion batteries. Taken from [2]

| Li-ion Type | Chemical Description | Specific Capacity [Ah/kg] | | Voltage [V] | | Electric Vehicle Applications |
|---|---|---|---|---|---|---|
| | | Typical | Theoretical | Avg. | Mid. | |
| LCO | Lithium cobalt oxide, $LiCoO_2$ | 150 | 274 | 3.8 | 3.9 | Original B787 battery |
| LMO | Lithium manganese oxide, $LiMn_2O_4$ | 120 | 148 | 4.1 | 4.0 | 2011/2013 Nissan Leaf, 2012 Mitsubishi i-MiEV, 2013 Ford Focus EV |
| NCA | Lithium nickel cobalt aluminum oxide, $LiNi_{0.8}Co_{0.15}Al_{0.05}O_2$ | 190 | 278 | 3.7 | 3.7 | 2014 Tesla Model S, 2015 Mercedes-Benz B-Class ED, 2016 Tesla Model X |
| NMC | Lithium nickel manganese cobalt oxide, $LiNi_xMn_yCo_{1-x-y}O_2$ | 170 | 278 (NCM 333) | 3.7 | 3.8 | 2014 BMW i3, 2015 Chevrolet Spark EV, 2017 Nissan Leaf, Tesla Model 3 |
| LFP | Lithium iron phosphate, $LiFePO_4$ | 160 | 170 | 3.4 | 3.4 | 2011 Chevrolet Spark EV, eBuses |

Currently, commercially available batteries with the highest specific energy use NCA or NMC, such as the Panasonic NCR18650A or 2170 cells in current Tesla battery packs [24]. One of the biggest drawbacks of some LIBs is the intensive use of cobalt and nickel, which are at a premium and usually come from countries with disputable mining ethics [25].

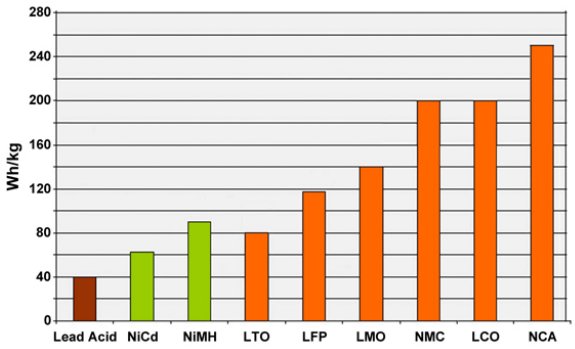


Figure 1.4: Typical specific energy of lead-, nickel- and lithium-based batteries [26].

Commercially widespread LIBs, show a specific energy of ca. 250 Wh/kg (at the cell level, see Figure 1.4). LIB energy density of 300 Wh/kg is considered attainable by the end of 2020, 400 Wh/kg by 2025 and 500 Wh/kg by 2030 according to [19]. However, due to physical and chemical limitations, LIBs will soon reach their ceiling in specific energy values. Considering a packing efficiency between 65-80 % [2], a specific energy density of 350 Wh/kg is the expected full potential for this type of batteries at the battery level [4], which is still two orders of magnitude lower than kerosene or jet fuel.


Figure 1.5: LIB price survey. From [27]

For what concerns battery life (usually intended as the no. of cycles before battery gets to 80% of its rated capacity), values ranging between 1,500 – 2,500 cycles are common [24], but recent tests showed that LIBs can get up to 5,000 cycles, claiming life ranges for cars in the order of millions [28].

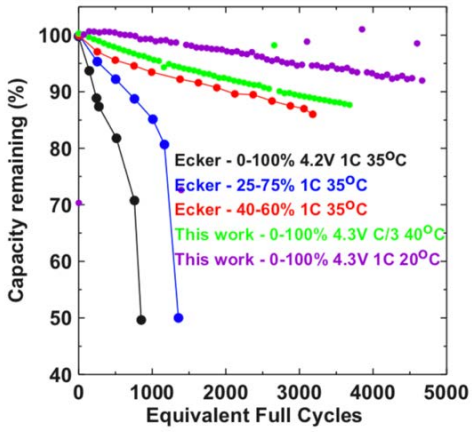


Figure 1.6: Cycling data for LIBs. From [28]

### *1.1.2.1.2 Lithium-Sulfur batteries*

Lithium-Sulfur Batteries (LSBs) feature lithium at the anode in coupling with sulfur cathode to generate high energy density. LSBs are the most promising low-cost, high-capacity energy storage device available due to their high charge-storage capacity, and the wide availability of low cost sulfur (Table 1.3). Sulfur is naturally abundant and therefore cheap, but the use of lithium-metal anode may soon be a problem due to the limited availability of lithium sources. An extensive review tailored for aeronautical applications of this technology can be found in [2], [4], [29]–[31]. The theoretical specific energy of LSBs is 2,567 Wh/kg but they have a low open circuit voltage of 2.1 V, compared to 4.2 of Li-ion. LSBs have also lower power rate when compared to LIBs [2].

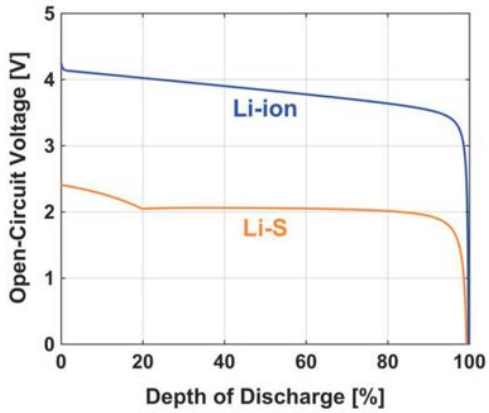


Figure 1.7: LIB and LSB discharge model [2].

Table 1.3: Theoretical parameters for potential aviation batteries [2].

| Battery Type | Discharge Reaction | Nominal Cell Voltage [V] | Cathode Specific Capacity [Ah/kg][a] | Specific Energy [Wh/kg][b] | Energy Density [Wh/L][c] |
|---|---|---|---|---|---|
| Li-ion[e] | $Li_{1-x}C_6 + Li_xMO_2 \leftrightarrow C_6 + LiMO_2$ | 3.4–4.1 | 148–278 | 396–607 | ~1000 |
| Li-metal | $Li_{1-x} + Li_xMO_2 \leftrightarrow LiMO_2$ | 3.4–4.1 | 148–278 | 578–1054 | > 1000 |
| Li-S | $2\,Li + S \leftrightarrow Li_2S$ | 2.2 | 1167 | 2567 | 2189 |
| Li-air | $2\,Li + O_2 \leftrightarrow Li_2O_2$ | 3.0 | 1168 | 3505 | 3492 |
| Li-Se | $2\,Li + Se \leftrightarrow Li_2Se$ | 2.0 | 577 | 1155 | 1824 |
| Al-air | $4\,Al + 6\,H_2O + 3\,O_2 \leftrightarrow 4\,Al(OH)_3$ | 2.71 | 1031 | 2793 | 3147 |
| Zn-air | $2\,Zn + O_2 \leftrightarrow 2\,ZnO$ | 1.65 | 659 | 1087 | 3736 |

[a] Discharged state (calculated).
[b] All active materials, including oxygen (calculated). Without oxygen, values for metal-air batteries are Li-air: 11584 Wh/kg, Al-air: 8075 Wh/kg, Zn-air: 1353 Wh/kg.
[c] Charged anode and discharged cathode (calculated).
[d] References for nominal cell voltage.
[e] Graphite anode.

A number of companies have the manufacturing capability to produce large capacity LSB cells featuring more than 300 Wh/kg in specific energy. Examples could be the American SionPower (500 W h/kg [32]), OxisEnergy [33] and works on developing batteries with 1,000 Wh/kg from Innolith [34] that is predicted to be available for industrial use between 2025 and 2030. The Global Lithium-Sulfur Battery Market [35] says that the global LSB market could grow of 71% during the period 2018-2022.

High performance cannot be maintained over long periods of time as the cycle lives and stability of current LSB cells are not competitive with the current-day lithium-ion technology (500 – 1,000 cycles vs 2,500 cycles, respectively). LSBs also have a lower energy density than lithium-ion batteries due to the use of sulfur cathode (700Wh/l vs 450 Wh/l), which naturally has a low density compared to LIB materials. Chung and Manthiram [29] points out that LSB cells may be most appropriate for applications where minimizing the mass is more important than the volume, so for powering electric heavy-duty vehicles, aerial vehicles, high altitude aeronautical vehicles, and energy-storage plants.

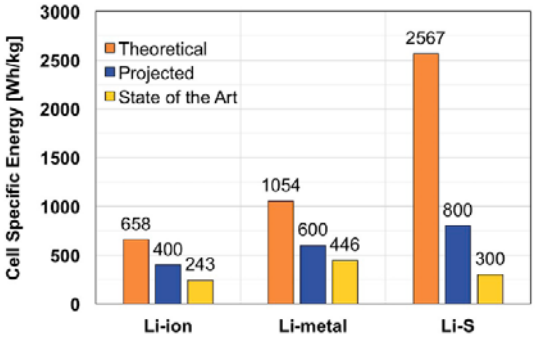


Figure 1.8: Specific energies of lithium-based batteries [2].

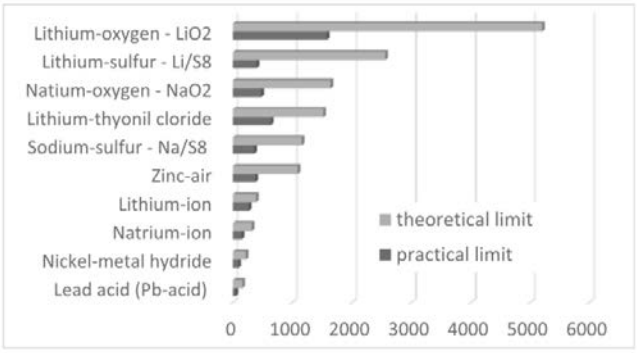


Figure 1.9: Practical and theoretical limits of specific energy of different battery technologies [19].

### *1.1.2.1.3 Lithium Air*

Lithium-Air Batteries (LABs) fall into the wider class of Metal-Air Batteries (MABs). Several MABs using alkali metals (Li, Na, and K), alkaline earth metal (Mg), and first-row transition metals (Fe, Zn) or Al as the anode have been investigated and their theoretical specific energies are presented in Figure 1.10.

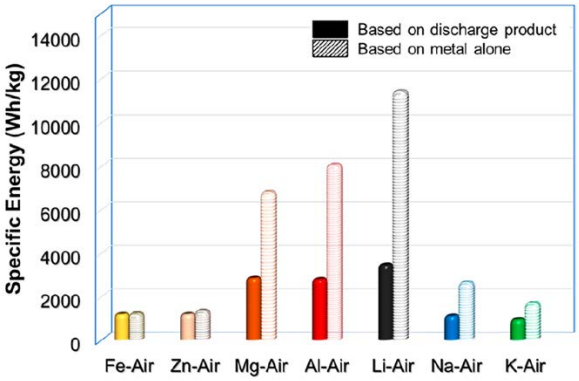


Figure 1.10: Theoretical specific energy of metal - air batteries [20].

LAB is composed of metallic lithium as the anode, and O2 as the cathode. The theoretical specific energy is around 115,000 Wh/kg or 3,500 Wh/kg depending on the inclusion of the oxygen in the calculation. LABs could deliver the required step-change in the battery market. Initial LAB systems required an air feed system with a compressor, as well as air filters and dehumidifiers to get rid of moisture on the oxygen side. [36]. Additionally, capacity fading was present, strongly dependent on the purity of oxygen. However, LAB has been transformed over the last six years with the introduction of redox mediators and Li anode protections. Now, significant quantities of $H_2O$ can be tolerated, alleviating the need for heavy, complex and bulky air handling. Considering these recent advances, [20] predicts the specific energy and

the energy density of a full air battery, including the balance of plant, to be 610 Wh/kg and 680 Wh/L respectively, without specifying a precise time frame. Other authors speculated differently as in Table 1.4.

Table 1.4: Specific energy of future battery systems of LSBs and LABs. From [4]

| Authors | Li–S [W.h/kg] | Li-air [W.h/kg] | Year |
|---|---|---|---|
| Hepperle (Hepperle, 2012) | 500–1250 | 800–1750 | 2025 |
| Zamboni (Zamboni, 2018) | 600–700 | 800–1500 | 2035 |
| Kuhn et al. (Kuhn et al., 2012) | – | 1000–1500 | 2035 |
| Stückl et al. (Stückl et al., 2012) | 600 | 720–2000 | 2035 |
| Johnson (Johnson, 2010) | – | 2000 | 2035 |
| Rajashekara (Rajashekara, 2013) | – | 2000–3500 | 2035 |
| Ritzert et al. (Ritzert et al., 2013) | 500–650 | 600–750 | 2028 |
| Ritzert et al. (Ritzert et al., 2013) | 800–950 | 1200–1400 | 2043 |

The LAB depicted in Figure 1.11, by Samsung [37] proved a performance of 1,214 Wh/kg and 896 Wh/l at the cell level.

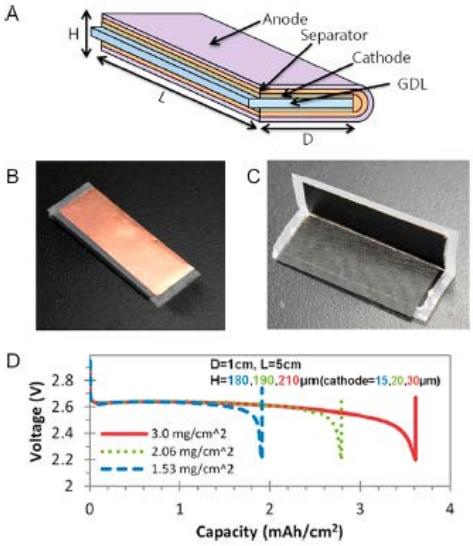


Figure 1.11: (A) Schematic, (B,C) images, and (D) discharge curves of a single folded cell [37].

### *1.1.2.1.4 Metal-S, Metal-ion and Metal-air*

Based on the development and progress achieved with LSBs, and due to the rising price and scarcity of lithium on the planet, researchers have explored a broad range of Metal-Sulfur Batteries (MSBs), Metal-Air Batteries (MABs) and Me-ion Batteries (MIBs). In general, Metal-X Batteries (MXBs). Metallic anodes examples are sodium, potassium, magnesium. MXBs have all high theoretical capacity and low material cost.

However, MXBs also face similar challenges as LSBs and LABs in regard to, stability, number of cycles and corrosion of the metallic anodes. MXBs are actively being researched in [20], [29], [30], [36]–[39].

#### *1.1.2.2 Supercapacitors*

Supercapacitors are electronic devices which derive from conventional capacitors. They are called supercapacitors for being able to store a certain amount of electric energy. A supercapacitor consists of two electrodes with a solid or liquid electrolyte in the middle. The thickness of the electric double layer is around 1 nm. Usual materials employed for the manufacturing of the electrodes are nano-structured carbon applied on aluminium foil as a current collector. Analogously to battery cells, supercapacitor cases are usually cylindrical or prismatic (pouch) [40].

Lots of attention is being payed to supercapacitors as they are very efficient, can be rapidly charged and discharged at extremely high power. Moreover, they feature a high cycle life, and are considered safe. As for batteries, the main performance parameters for supercapacitors is represented by

- Specific energy [Wh/kg]
- Energy density [Wh/l]

Supercapacitors have higher specific energy than conventional capacitors, but less than batteries (e.g. 10 Wh/kg, compared to 200-250 Wh/kg for LIBs).

On the other hand, they can deliver power much faster. For instance, current specific power values are 5 to 10 times bigger than the batteries (10 kW/kg vs 1-2 kW/kg). This enables rapid charge and discharge, which is ideal if a sudden burst of power is required. The calendar life of supercapacitors can be >15 years, compared to approximately five years for batteries.

Research is currently under way worldwide to improve the specific energy of supercapacitors without losing their high specific power [41]–[43].

Yunasko [44], an energy storage company based in Ukraine, has reported working towards marketing a 30-40 Wh/kg hybrid battery-supercapacitor while retaining the power density at 3-5 kW/kg with an efficiency of 80%.

Research at universities aims to increase the specific energy of supercapacitors on a laboratory scale too. Reported numbers for specific energy range from 50 to 150 Wh/kg. Such result is based on studies on a laboratory scale and must be proven on a manufacturing scale. Graphene and carbon nanotubes seems to be the root of these improvements [38]. A recent supercapacitor breakthrough was reported by start-up company Superdielectrics, Ltd. [45], which has developed a novel polymeric material. The new polymer has largely higher capacitance than usual supercapacitor materials and could potentially actualize energy densities of up to 180 Wh/kg. Rolls-Royce is working together with Superdielectrics on these topics [46].

A supercapacitor with high specific power and reasonable specific energy (50 – 100 Wh/kg), could be employed during power intense flight phases helping possibly smaller battery/FC.

#### *1.1.2.3 Fuel cells*

Fuel cells are similar to conventional batteries, but the reactants are stored outside the cell. Fuel cell operation is based on a redox reaction that takes place in two separate, but electrically connected, anode and cathode. As usual, oxidation happens in the anode and reduction in the cathode. When operating with pure hydrogen, $H_2$ molecules are oxidized and lose 2 electrons which feed the electric load. At the same time, Hydrogen ions (H+) travel through the electrolyte, closing the circuit. $O_2$ is reduced producing, in this case, just water. FC can be fed also with compounds containing hydrogen, such as methanol or ethanol. In this case emissions are not just water, but also carbon compounds (i.e. CO and $CO_2$) [47]. We remark that FCs are not energy storage devices, but electric power generation devices. Two types of FCs are mostly used: the Solid Oxide Fuel Cell (SOFC) and the Proton Exchange Membrane Fuel Cell (PEMFC) [48]–[50]. The former uses solid ceramic oxide as electrolyte and works at high temperatures (800-1000° C). SOFCs are usually used for stationary applications, due to their heavy weight, slow start up time (in the order of hours) and fragile nature of the ceramic materials. PEMFCs have proven to be the most successful commercially, especially for mobility applications [51]–[53]. The PEMFC runs at relatively low temperatures (70-80°C). The performance of the PEMFC is highly sensitive to impurities, such as carbon monoxide and sulfur, which are produced during the reforming of hydrocarbon-based fuel to hydrogen. Therefore, pure hydrogen is the preferred fuel choice for the PEMFC [38].

Single FCs are connected in series in order to reach the desired voltage value, creating a subsystem called stack. Different stacks can be connected in parallel and the resulting current is the sum of each stack current. A complete FC system include one or multiple stacks, as well as balance of plant equipment, such as heat exchangers, pressure regulators, water management systems and air compressors to eventually pressurize oxygen.

Details and curiosities about FCs can be found in the textbooks [47], [54]. Within these textbooks, it is outlined that performance of a FC system can be evaluated trough some key figures of merits:

- Specific power (kW/kg)
- Cost per power unit ($/kW)
- Lifetime: usually given as the loss of the cell voltage per 1000 h, as electrodes and the electrolyte gradually deteriorate. The FC life is over when it can no longer deliver the rated power
- Efficiency: electrical energy delivered by the system compared with the energy supplied as fuel.

PEMFC efficiency ranges between 50 and 60 %. For what concerns specific power, DOE Technical Targets for Fuel Cell Systems and Stacks for Transportation Applications [55] says that the specific power of current state of the art FC system (including balance of plant: compressor, stack modules, cooling system) ranges between 0.6 – 1 kW/kg. Developmental PEMFC systems have specific power the order of 1.6 kW/kg at the system level. However, increasing the power density of the PEMFC is not the current focus of development efforts for automobile and ground power

applications. Instead, the emphasis today is on reducing costs, decreasing platinum loading, and increasing life [38], [56]. Kadyk et al. estimate that specific power could be improved up to 8 kW/kg only optimizing current FCs for aviation applications [52].

Current costs at system level are around 45 US$/kW. However, this figure is expected to drop as production of PEMFCs for middle to heavy ground transport application will scale up.

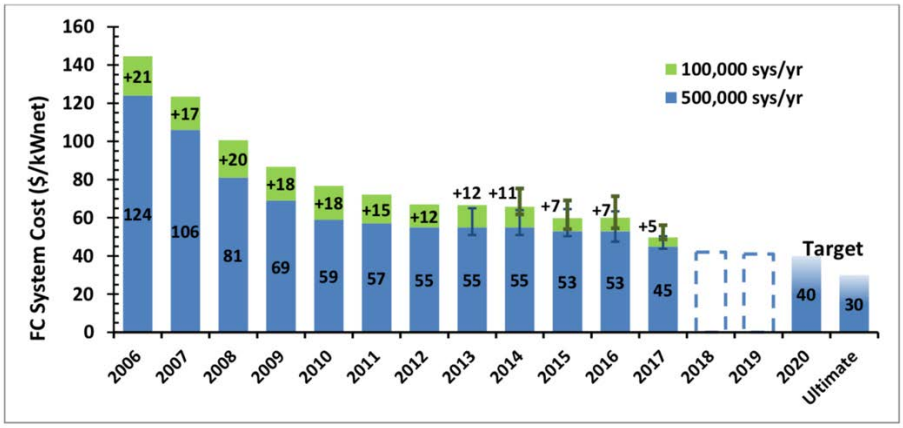


Figure 1.12: Modelled cost of an 80-kW PEM fuel cell system based on projection to high volume manufacturing (100,000 and 500,000 units/year). Taken from [57]

### *1.1.2.4 Hydrogen storage*

Hydrogen is present on Earth only in the form of compounds with other elements. Once separated from these compounds, it naturally rises and dissipates. Hydrogen is indeed a very light element and its state is gaseous at ambient temperature, which implies some difficulties in storing it efficiently. The storage of hydrogen is the most difficult challenge associated with the hydrogen economy [58], [59].

According to [48], the main quantities to assess the goodness of a storage device are:

- Gravimetric density: usually the ratio between the fuel mass and the total storage + fuel mass [% wt].
- Volumetric density: same as gravimetric density, but for volumes [% wt].
- Operating temperatures
- Operating pressure
- Cost

$H_2$ storage methods can be divided in physical and chemical methods as illustrated in Figure 1.13.

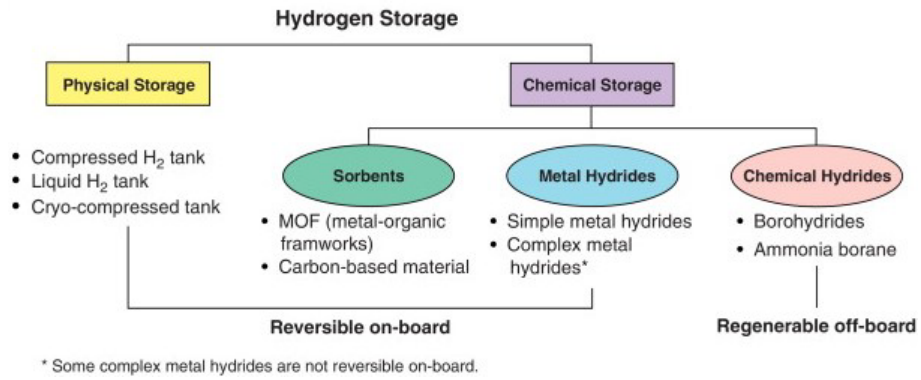


Figure 1.13 Hydrogen storage methods [60].

A comparative summary of the main performance indicators is in Table 1.5.

Table 1.5: Overview of hydrogen storage methods [61].

| Method | Gravimetric Energy Density (wt %) | Volumetric Energy Density (MJ/L) | Temperature (K) | Pressure (barg) | Remarks |
|---|---|---|---|---|---|
| Compressed | 5.7 | 4.9 | 293 | 700 | Current industry standard |
| Liquid | 7.5 | 6.4 | 20 | 0 | Boil-off constitues major disadvantage |
| Cold/cryo compressed | 5.4 | 4.0 | 40–80 | 300 | Boil-off constitues major disadvantage |
| MOF | 4.5 | 7.2 | 78 | 20–100 | Attractive densities only at very low temperatures. |
| Carbon nanostructures | 2.0 | 5.0 | 298 | 100 | Volumetric density based on powder density of 2.1 g/mL and 2.0 wt % storage capacity. |
| Metal hydrides | 7.6 | 13.2 | 260–425 | 20 | Requires thermal management system. |
| Metal borohydrides | 14.9–18.5 | 9.8–17.6 | 130 | 105 | Low temperature, high pressure thermal management required |
| Kubas-type | 10.5 | 23.6 | 293 | 120 | |
| LOHC | 8.5 | 7 | 293 | 0 | Highly endo/exothermal requires processing plant and catalyst. Not suitable for mobility |
| Chemical | 15.5 | 11.5 | 298 | 10 | Requires SOFC fuel cell. |

As testified by the rise in the number of technical reports and normative guidelines, $H_2$ usage on airplane is moving from successful isolated experiments on small airplanes, to bigger applications. [62], [63].

Types of H2 storage system exist which involve chemical absorption of hydrogen in other materials (see [61], [64]). Although many of them might seem appealing, they are at a very early development stage and not suited for application with PEMFC. Therefore, only physical storage systems are illustrated hereafter.

### *1.1.2.4.1 Compressed $H_2$*

Compressed $H_2$ (CH2) tanks are the current industry standard for mobility applications. Several engineering and normative standards are already in place, to detail the production and testing of this type of storage (Figure 1.14). An extensive review of these Regulations, Codes and Standards is reported in [65].

| Code | Applicable object | Water capacity | Content |
|---|---|---|---|
| UN GTR 13 | Hydrogen-fueled vehicles of Category 1-1 and 1–2, with a gross vehicle mass of 4536 kg or less | Up to 330 L | Compressed or liquefied hydrogen |
| EC REGULATION 406 | Hydrogen-powered vehicles, hydrogen-related components and systems | Not specified | Compressed or liquefied hydrogen |
| SAE J2579 | Hydrogen fuel storage and handling systems | Not specified | Compressed or liquefied hydrogen |
| ISO 19881<br>ANSI HGV 2 | Type I, Type II, Type III and Type IV tanks | Up to 1000 L | Compressed hydrogen |
| GB/T 35544 | Fully-wrapped carbon fiber reinforced tanks with an aluminum liner | Up to 450 L | Compressed hydrogen |

Figure 1.14: Regulations, codes and standards for on-board gaseous hydrogen storage [65].

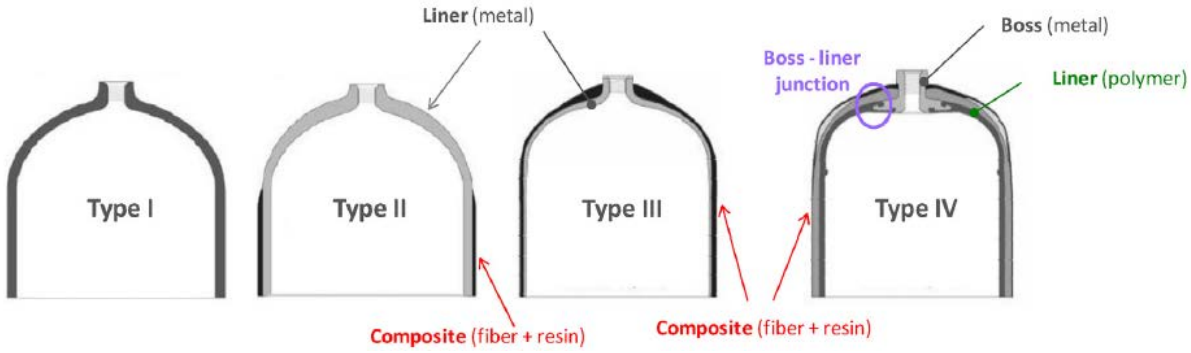


Figure 1.15: Hydrogen pressure vessel types [66].

Table 1.6: Hydrogen pressure vessel type details [61].

| Type | Materials | Typical Pressure (bar) | Cost ($/kg) | Gravimetric Density (wt %) |
|---|---|---|---|---|
| I | All-metal construction | 300 | 83 | 1.7 |
| II | Mostly metal, composite overwrap in the hoop direction | 200 | 86 | 2.1 |
| III | Metal liner, full composite overwrap | 700 | 700 [65] | 4.2 [66] |
| IV | All-composite construction | 700 | 633 [65] | 5.7 (Toyota Mirai) |

CH2 pressure for mobility applications typically ranges between 200 and 700 bar. The trend in transport field is to use a pressure storage value of 700 bar [64]. There are four main types of hydrogen pressure vessels (see Figure 1.15).

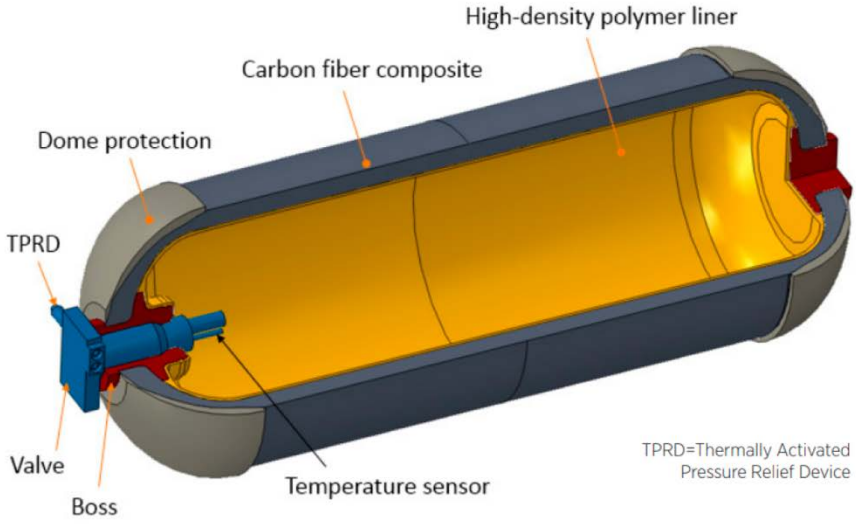


Figure 1.16: Type IV gaseous hydrogen pressure vessel [61].

Most of FC-driven cars use CH2 carbon-fibre Type IV tanks (Figure 1.16) that are pressurized at a global standard of 70MPa. Some public transport applications use 350 bar composite tanks since gravimetric density is less important in larger vehicles. Composite fibres are usually assembled using filament winding. However, a public's concern exists because of such high pressure (70MPa). Moreover, the hydrogen compression can use up to 20% of the energy content. Future outlook of compressed hydrogen storage in terms of gravimetric density is still unclear. More attention is being payed to safety, cost reduction and operation optimization. Refuelling compressed gaseous hydrogen tanks takes no more than 5 min, which is comparable to gasoline [59], [64], [67]–[70].

#### *1.1.2.4.2 Liquid $H_2$*

$H_2$ liquefies at -253°C, therefore, a Liquid $H_2$ (LH2) tank must be designed to minimize heat transfer through its walls. However, zero heat transfer is not possible, so, in order to avoid pressure increase inside the tank, a relief valve is added, usually called boil off valve. This valve lets expanded $H_2$ escape. The best shape for a LH2 tank is the one that maximises volume to surface area ratio, a sphere. This shape minimizes the heat transfer, main responsible for the boil off effect. Of course, this shape is not particularly suitable for aeronautical application. LH2 storage has been extensively used for industrial and space applications and has improved significantly in the last years, achieving the best gravimetric density (15%) among other hydrogen storage systems [59], [62], [71], [72]. The cost of hydrogen liquefaction is significant, both in terms of energy and equipment, resulting in a 40 % energy loss. However, LH2 storage is strongly temperature-dependent and implies the addition of a heat management system which adds cost, complexity, and mass. Liquid hydrogen tanks do not have to

withstand high pressure, but they must be heavily insulated, which results in reservoirs with thick walls. The costs associated with hydrogen liquefaction reach approximately 1.00 $/kg because the plants are "capital and footprint intensive" [61]. Examples of LH2 tanks on aircraft are well described in [73]. Among them, LH2 integral tanks fitted in the semi-monocoque fuselage structure. A picture of the peculiar cabin layout featuring these tanks is in Figure 1.17.

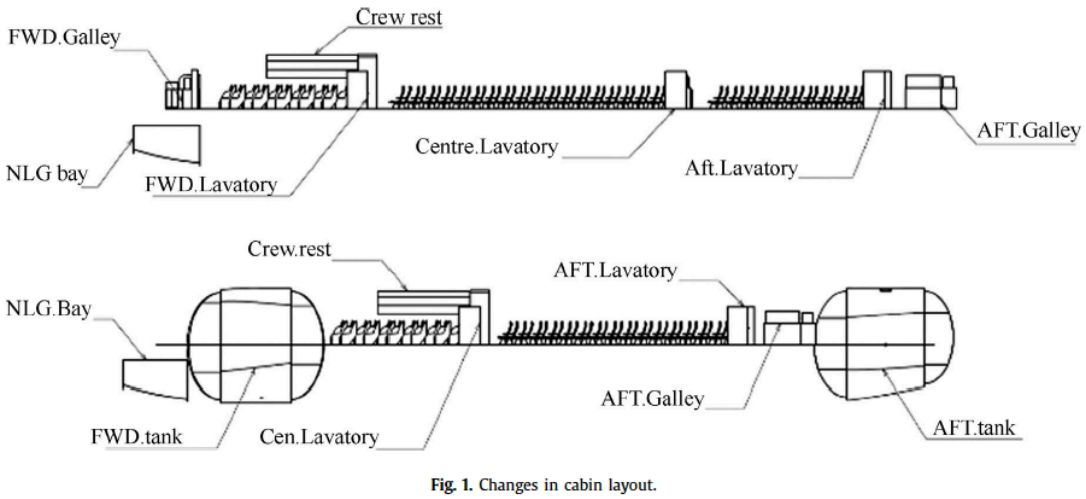


Fig. 1. Changes in cabin layout.

Figure 1.17: Changes in cabin layout due to integration of LH2 tanks [73].

### *1.1.2.4.3 Cryo-compressed $H_2$*

Since LH2 storage requires a certain level of complexity and a careful heat management system to handle very small temperature, it might be impractical for small-scale use in mobility. A possible workaround is to store hydrogen in liquid form but under pressure. This process is commonly called cryo-compression. Smaller internal pressure than CH2 allows for less high strength material, less expensive composites and more cheap metals. The boil off problem is extremely limited, with a record of 0% losses within a week of time [48].

References [74], [75]. report that CCH2 turned out to be the most attractive hydrogen storage method for what concerns overall energy efficiency and global well to wheel cost, even though this system had the highest energy use, hydrogen cost and GHG emissions. GreenHouse Gas (GHG) emissions were particularly high, mainly due to the significant amount of energy to convert the gaseous hydrogen into a liquid state. This drawback affects also LH2 storage. However, GHG emissions are largely dictated by the method used to produce the hydrogen. Currently, limited development has been made for onboard liquid hydrogen fuel tanks for automotive use [48], [76].

### *1.1.2.5 Electric drive system*

Regardless of the picked powertrain architecture, another key component is represented by electric motors and their controllers. There are several types of Electric Motors (EMs). A good summary of the most used in aeronautical applications is shown in Table 1.7.

Table 1.7: Summary of electric machine types [1].

| Machine Type | Stator | Rotor | Controller | Features |
|---|---|---|---|---|
| Squirrel-cage induction machine (SCIM) [27,130] | 3-phase AC | Short-circuit coils (induced current electromagnet) | None | Self-starting, simple |
| Wound-rotor induction machine (WRIM) [131] | 3-phase AC | Winding connected to external load | Simple | Speed control, requires slip-ring |
| AC synchronous machine [27,130] | 3-phase AC | Permanent magnet (PM), reluctance, or windings | Simple | Efficient, not self-starting |
| Doubly-fed induction machine (DFIM) [131] | 3-phase AC | Separate, 3-phase AC coils | Simple | Speed control, generally requires slip-rings |
| Brushless DC motor [19,46,108,132,133] | Multiple DC coils | Permanent magnet | Complex | Less suitable for generation |
| Switched-reluctance machine (SRM) [17,134] | Multiple DC coils | Soft magnetic material (reluctance) | Complex | Good high-speed and high-heat performance |

Usually EMs are coupled with a controller or converter. For instance, brushless DC motors need an inverter to provide electricity to the windings with the correct phase [77]. Aeronautical propulsive applications of (EMs) are found in several works on general aviation and ultralight aircraft. Main motor manufacturers are Siemens, Compact Dynamics, EMRAX, YUNEEC International. [78]–[81].

EMs are usually much simpler and durable than thermal engines, allowing for scalability, working well for both small and big applications. Aircraft EMs must be designed with particular focus on safety and redundancy. Apart from this, two main quantities are usually named when comparing different EMs:

- Specific power [kW/kg]
- Efficiency

NASA [82] claims that EMs with specific power of 13.2 kW/kg and efficiency greater than 96% and power converters with 19 kW/kg and efficiency greater than 98% will be attainable by 2030. These results are reported in Table 1.8 and Table 1.9.

Table 1.8: NASA-sponsored Megawatt-scale electric machine developments [82].

| | Continuous power rating, MW | Specific power goal, kW/kg | Efficiency goal, % | Motor type | Speed | Nominal dimensions |
|---|---|---|---|---|---|---|
| University of Illinois | 1 | 13 | >96 | Permanent magnet | 18,000 | Cylinder 0.45 m by 0.12 m |
| Ohio State University | 2.7 | 13 | >96 | Induction | 2,500 | Ring 1.0 m by 0.12 m |
| NASA Glenn Research Center | 1.4 | 16 | >98 | Wound field | 6,800 | Cylinder 0.40 m by 0.12 m |

Table 1.9: NASA-sponsored Megawatt-scale converter developments [82].

| | Continuous power rating, MW | Specific power goal, kW/kg | Efficiency goal, % | Topology | Switch material | Cooling |
|---|---|---|---|---|---|---|
| General Electric | 1 | 19 | 99 | 3 level | SiC/Si | Liquid |
| University of Illinois | 0.2 | 19 | 99 | 7 level | GaN | Liquid |
| Boeing | 1 | 26 | 99.3 | | Si | Cryogenic |

Several research programmes have addressed both cryogenic and ambient temperature conducting electric technologies for EMs [83]. A superconducting system has the largest capacity in the Mega-Watt (MW) class spectrum to achieve superior performance and lower heat waste. A superconducting system features peculiar zero-resistance conductors, but this property vanishes at ambient temperature. Therefore, liquid nitrogen is usually employed to control the temperature. It is immediate to reckon the possibility of using LH2 instead. In fact, $H_2$ must be heated up before entering the FCs and the EMs must be cooled down. This would be a win-win solution. However, the same NASA in [84] envisages that cryogenic systems would not be ready for the operation on an aircraft in the mid-term due to the lower development of cryogenic superconductors. Furthermore, the National Academies of Sciences , Engineering and Medicine is even more cautions, hypothesizing a shy value of 9 kW/kg for the specific power of MW order EMs in the next 20 years [8]. Schnell et al. [85] lay in the middle, considering specific power in the range of 13-16 kW/kg. or the electrical machine and 10-19 kW/kg for the power converters for a turbo electric 150-seat aircraft.

Table 1.10: Performance parameters for electric motors and other electric components assumed in [85]. Pess. = pessimistic, Opt. = optimistic assumptions.

| Component | | Efficiency | Specific Power | |
|---|---|---|---|---|
| | | [%] | [kW/kg] *[A/(kg/m)] | |
| | | | *Pess.* | *Opt.* |
| Motor | 1 | 96.0 | 13 | 16 |
| Inverter | 1 | 99.0 | 10 | 19 |
| Circ. Protection | 4 | 99.5 | 200 | 200 |
| Cable | 2 | 99.6 | 170* | 170* |
| Rectifier | 2 | 99.0 | 10 | 19 |
| Generator | 2 | 96.0 | 13 | 16 |
| Thermal System | | | 0.68 | 1.6 |

## *1.2 Airframe and propulsion configurations*

With the scope to explore the design space as much as possible, an initial identification of all the possible technologic solutions for both the aerodynamic and the propulsion systems is carried out. In this contest possible interaction effect are also considered.

The scope of the reported task is to gather these configurations in a unique design option tree; consequently, through a qualitative trade off analysis, an initial set of the most promising configuration will be further analysed in the concurrent conceptual design stage.

The aforementioned configuration are reported in the block diagram of Figure 1.18. The top part of the diagram with blue block represents an overall System Breakdown Structure (SBS) [86] where the aircraft is decomposed in system and sub-systems that are arranged in a hierarchical manner. The systems of interest for the UNIFIER-19 project are therefore decomposed in multiple levels so that, for each sub-(sub-)system, adequate design options can be identified: those last ones are indicated in the same figure with the green boxes.

As an example, the "wing" is the system of the aircraft deputed in fulfilling the function "generate aerodynamic forces": for this system, 4 possible different configurations can be identified: Conventional wing, Box-Wing, Truss-Braced and "Flying V".

The identification of the possible design options according to a "system" classification is not the only possible one: in fact, according to System Engineering approaches, also a "Functional Breakdown Structure" can be determined. The intrinsic advantage of the adopted SBS is that the same classification and the same structure can be also used for the data management and the adoption of a unified data format compatible for instance with an Object Oriented Programming as it is explained in Section 4 of the present document.

It has to be mentioned that not all the solutions available in literature will be actually considered and reported in the design option tree: only the design option for which a correspondent analysis models exists (and is available) are reported so that a preliminary sizing is actually guaranteed with an adequate level of reliability.

In the following sub-paragraphs, the possible design options are briefly discussed: at the same time without the intention to write a compendium of the current state of the art of various aerospace engineering disciplines, a literature of possible sizing models is also reported that represents a useful basis for the design activities foreseen in the UNIFIER-19 project.

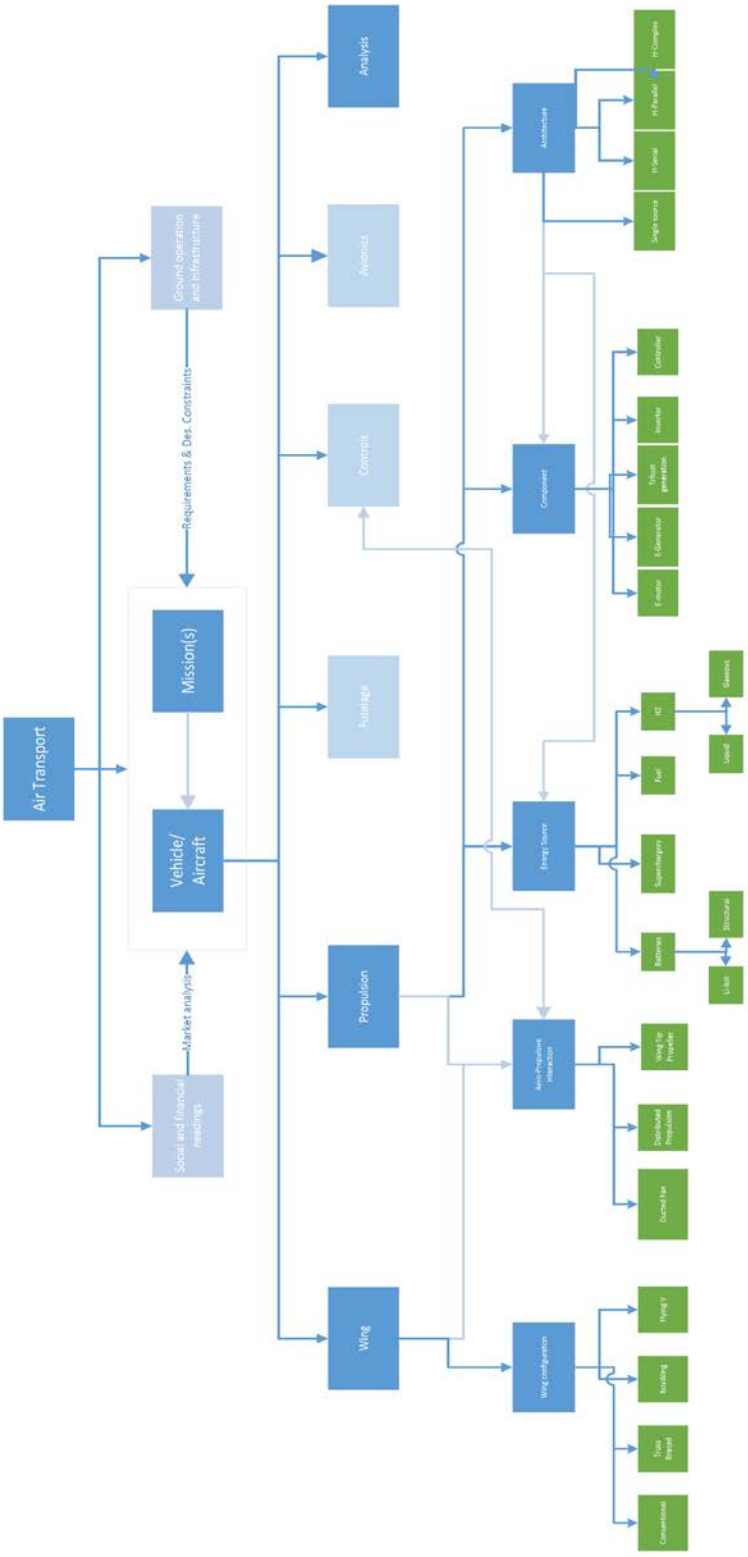


Figure 1.18: Aircraft architecture option tree diagram.

### 1.2.1 Wing (aerodynamics)

A good design of the wing system is intended to achieve high Lift-over-Drag ratio during cruise in order to reduce the energy consumption during the longest flight phase. Conventional tube and wing configuration has been widely adopted (and optimized) in the last 50 years and a wide literature and experience exist that allow to design an efficient wing in this sense for several categories of aircraft and/or flight conditions (e.g. [87]–[89]). Disruptive non-conventional wing configuration are today based on two different design philosophies: the first one is based in the reduction of the friction drag terms by the "removal" of all the non-lifting bodies so that the wetted area is minimized. Therefore, in both the "Blended Wing Body" (BWB) and "Flying-V" (FV) concepts the fuselage results integrated in the wing structure; preliminary design studies on both subsonic and transonic study cases [90], [91] showed a possible 10 to 20% increase in the aerodynamic efficiency. On the other side, the wing span of the aircraft must be increased to accommodate the payload within the wing volume. Other ongoing research activities are also exploring the flight mechanics characteristics of such this configuration in comparison with a conventional correspondent.

The second design philosophy is intended to minimize the induced drag component; in this contest the Box-wing configuration based on the "Best Wing System" by Prandtl is in principle able to guarantee up to a 15% reduction of total drag in cruise for a wide variety of aircraft study case together with some secondary flight mechanics and structural effects as reported in [92]. Another design solution, actually widely used in general aviation (especially ultralight categories) due to its structural simplicity and effectiveness consists in the presence of a truss (TBW) that allows for a higher wingspan. The resulted increase in Aspect Ratio has direct benefits in the induced drag component.

### 1.2.2 Propulsion – Energy sources

The selection of the energy source to be used to generate the requested power is critical when considering emissions (including noise) as well costs. Today a variety of possible sources exists to be used for air-transport application at least at a theoretical level.

In the UNIFIER-19 the following option will be considered for the qualitative trade off:

- Fossil Fuel: conventional AVGAS and Jet Fuel represent the unique real benchmark when different energy sources are analysed. Wide literature as well as existing engine data map can be used to determine the fuel flow and the emission in each flight conditions.
- Batteries: batteries are used as storage of electrical energy and in order to be applied (efficiently) for air transportation purposes, development and production effort is currently oriented in enhance their characteristics especially in terms of specific energy density, operating life and safety operations. Li-Ion technology allows today to realistically achieve energy densities compatible with commercial application in GA aircraft even though this aspect unfortunately represents a bottleneck for the complete affirmation as primary

energy source on bigger air transport categories. For design purposes, a wide literature has been produced in the last 5 years [93], [94] that can be applicable to the present project in order to size the batteries and to estimate their performance taking a series of primary and secondary effect (e.g. temperature [95]) into account. Even if they are at a very preliminary exploratory concept, Structural Batteries (SB) [14]might represent a good alternative to overcome the existing with penalties in terms of additional weight for full electric flight based on "conventional" batteries.

- Hydrogen: hydrogen is in principle a very appealing energy source because of its very high specific (gravimetric) energy density together with the low emissions production when used in a combustion engine. Even more importantly, the hydrogen is the primary fuel used in Fuel Cell (FC) technologies where electric energy is obtained by its electrochemical reaction with an oxiding agent (usually oxigen). This technology allows to achieve potentially a zero-emission propulsion system. Fuel cell technology has been widely used in the last decade in other transport system, mainly automotive and design studies and even technologic demonstrator have been built to prove the feasibility of the FC system into an air frame (e.g.[96]–[98]). Limitations of hydrogen application are represented by current forms of storage since either the liquid and gaseous state require high pressurized tank and low (sometimes) cryogenic temperatures [61].

As previously mentioned, only options that can be suitable and for which already preliminary sizing models are available, are considered despite other promising solutions (as, for instance, superchargers) with a very low TRL are mentioned in the literature.

### 1.2.3 Propulsion – Architectures and components

Several topological classifications exist to determine the layout of the propulsion system. In the contest of the UNIFIER-19 project, a preliminary distinction is carried out based on the number of used energy sources to that one can distinguish:

- Single Energy Source: all the conventional jet engines, turboprop, and IC based system used in automotive applications, belong to this category as well as full electric systems. In this case, energy is extracted from a single source and converted through intermediate step into mechanical power that can be linked to a thrust generation device (that can be a propeller or a jet turbine in case of an aircraft, a wheel shaft in case of an automotive application).
- Hybrid configuration: in this case, two or more energy source can be used alternatively or at the same time to produce useful work. Usually the utilization of a second source is intended to overcome limitations of a primary source in such a way the overall performance of the system (in terms of peak power or in terms of efficiency for instance) are somehow increased.

The utilization of different sources (at the same time) as well as the implication of a chemical reactions or a combustion or an electric phenomenon, open a huge variety

of propulsion architectures whose unfortunately it is not available at present a unified classification.

In the contests of the project, we refer to the well know distinction based on conventional, Hybrid Series, Hybrid Parallel, Hybrid Parallel/Series powertrain architecture as reported in Figure 1.19 and as also identified in previous projects [99].

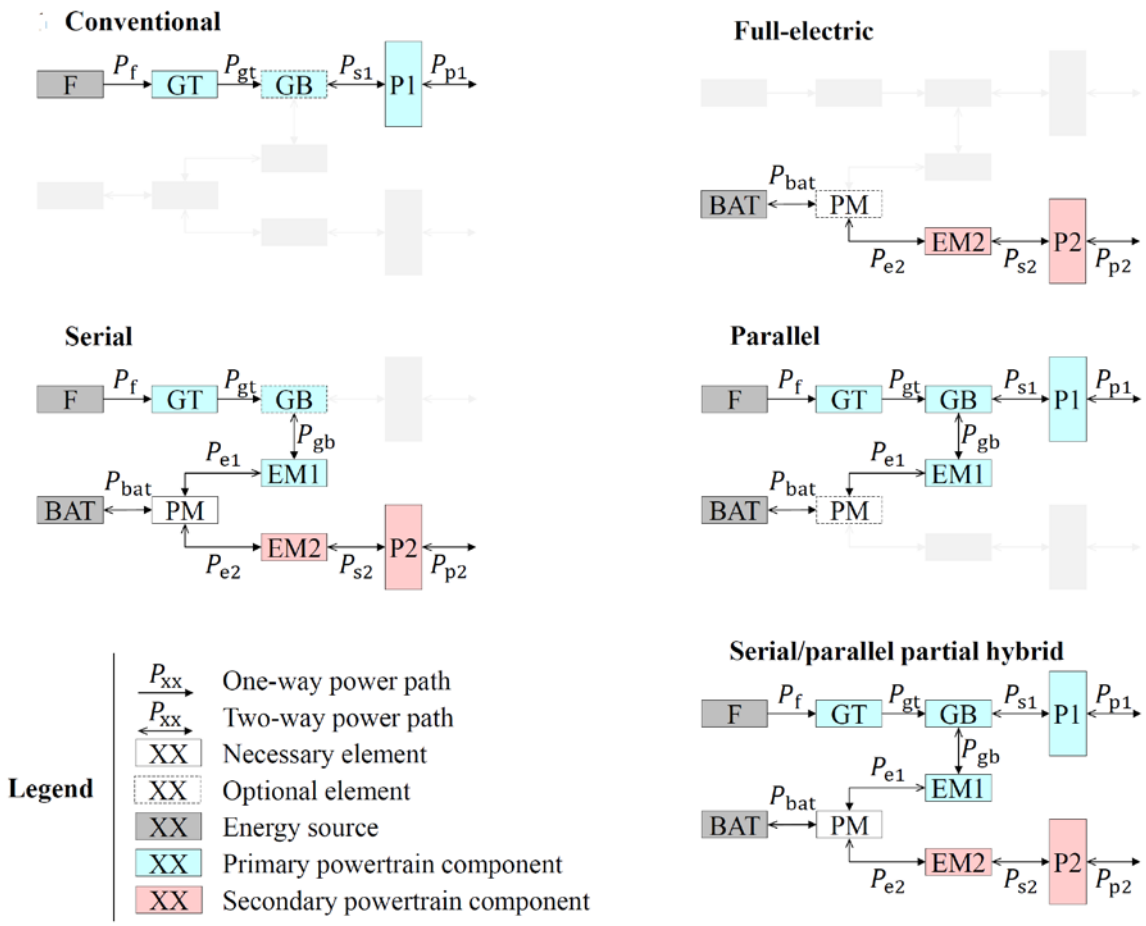


Figure 1.19: Identification of possible common architectures for conventional and electric-based propulsion [100].

It is noted that the schemes reported in Figure 1.19 cannot fully describe all the design option especially when multiple thrust devices (as for instance in the case of Distributed Propulsion, DP) are considered. Nevertheless, the identification of similar diagrams for the specific study cases will be essential to assess the overall performance of the powertrain and, in particular, to identify and size each component as the Electric Motor(s) EM, Power Management modules (PM), Gas Turbine (GT) or Internal Combustion Engine (ICE).

Excluding energy sources and thrust devices that are covered in separate paragraphs, the following common components will be considered in the project activities:

- Electric motors convert electrical energy into mechanical energy. There are several types of electric motors, including synchronous/asynchronous, single phase/multi-phase, alternate (AC)/direct (DC) current, etc. The main characteristics of interest for selecting a motor in a preliminary hybrid-electric powertrain design are the power-to-weight ratio and operating rotational speed. At the current technological level, a reasonable power-to-weight ratio value for an electric motor is between 6-8 kW/kg, which entails compacts and light components. In addition, the wide design space allows to design a motor that fits also the rotational speed of the coupled propeller. By constitution, an electric motor may act as an electric generator receiving mechanical power from outside. On aircraft, this makes energy recuperation easier in phases of the flight with low demanded propulsive power.
- Inverters: most electric motors for aviation work with alternate current (AC), and electric generators produce AC power. On the contrary, batteries or fuel cells invariably work with direct current (DC). Hence inverters – converting DC power to AC and vice versa – are needed to make power connection between the corresponding modules. The main characteristics to consider when sizing an inverter are its power-to-weight ratio, the switching frequency and the allowable maximum continuous power. With today's technology, a reasonable value of the power-to-weight ratio of an inverter is about 15 kW/kg. Inverters are very critical components in terms of temperature limitations. Currently inverters can operate only up to a temperature of 60-70°C. In order to avoid overheating, a suitable cooling system should be included in the design of the power system.
- Power Generation: those systems consist of a conversion for the energy storage into electrical power This module usually supplies a substantial share of the total power flowing in the powertrain. The constructive elements in this module may change depending on the form of energy storage. An internal combustion engine (ICE) or a turbine engine are used to treat hydrocarbon fuel, whereas a fuel cell system is needed to convert energy stored as Hydrogen. In an ICE-based hybrid-electric aircraft, the power generation module may consist of the ICE itself, connected in series to an electric generator. In a fuel-cell-based hybrid-electric aircraft a DC-DC converter may be needed to match the voltages of the battery and fuel-cell, since these elements might operate at largely different voltage levels. When included in the design, fuel cells with all subcomponents – like pumps, elements of the cooling systems, etc. – are part of the power generation module.
- Power Management: the versatility of a hybrid-electric powertrain allows to adapt the mode of operation to cope with different power requirements, typical to different phases of the flight, thus optimizing energy expenditure in many diverse scenarios. The power management module (PM) has the authority to assign the power flows from the energy storage(s)and power generation system(s). Based on sensor measurements of the other components, the PMCD will apply pre-defined logics to manage power flows. The PMCD is usually based on an electric hardware part, including electric and electronic subcomponents like power switches, relays, fuses, diodes, and all that is necessary to practically

manage power routing. There is also a controller, composed of an electronic hardware and a software part.

- Human-Machine Interface: this module is primarily needed to allow the pilot to monitor the state of the powertrain – measured through temperatures, energy levels and power flows. It may enable the pilot to operate on selectable energy management profile options, which affect the logics implemented in the PMCD, or to operate directly on key components of the hybrid-electric system, especially in case of malfunctions of the PMCD or of other modules.

### 1.2.4 Propulsion – Thrust devices (aero-propulsive interactions)

The introduction of alternative propulsion system based for instance either on FC or on full electric propulsion or even on a hybrid-electric combination, opens also new possibilities and solutions for a better and more efficient generation of adequate thrust level in all the flight conditions. As done in the previous cases, possible (non) conventional options are briefly discussed, in order to highlight the most interesting aspect of each technology:

- Distributed Propulsion: the term 'distributed propulsion' is not uniquely defined and has been used in countless different applications. In general, it refers to three or more propellers placed along the wing semi-span and/or in other different placements of the later. The general goal of these concepts is to improve the aero-propulsive performance of the vehicle by achieving beneficial interaction of the propulsion units and the rest of the airframe. Distributed propulsion systems promise improvements in aero-propulsive efficiency through, for example, reduced wing area or increased effective bypass ratio. This recent growth in distributed-propulsion concepts can be attributed to the development of hybrid-electric powertrains for which compact and light EMs can be placed over the wings. Research design studies [100] shows possible methodologies to take these interaction effects into account, with notable consequences on both the installed Power-to-Weight ratio and the Wing Loading values even though those studies are highly dependent on the exact location of the propulsors with respect the lifting surfaces.
- Wing Tip Propellers: The physical phenomenon which this technology is based on is relatively simple; in fact, it consists in two propellers placed at the tips of the wing, counter-rotating with respect to tip vortices with the consequences that the induced drag is reduced. From design perspective this solution entails a higher apparent wing's Aspect Ratio with improved flight performance in most mission conditions. Fundamental research [101] based also on experimental campaigns [102], shows a potential benefits in drag reduction up to 20% (for high lift coefficient) as reported also in Figure 1.20. In the past, the installation of this technology was not compatible with the relatively heavy weight of ICEs to be installed at the wing tip with unsolvable aero-elastic problems. With the advent of light EMs this option appears now feasible and potentially advantageous provided that One Engine Inoperative condition can be fulfilled according to the regulation requirements.

- Ducted Fans: A ducted fan consists of a propeller contoured by a cylindrical shroud. This last system has the dual effects to improve the aerodynamic at the propeller blades tip and, when properly designed) to generate aerodynamic forces because of the differences in the flows inside and outside the duct. As a consequence, ducted fans show significant improvements in terms of both static thrust and propeller efficiency at the design point. In some design study cases [103] those devices are placed in the tail part of the aircraft, as shown in Figure 1.21 in such a way the system beneficially interacts with the stability and controllability characteristics of the aircraft. Again, when driven by conventional propulsion, these solutions lead to notable weight penalties. Nevertheless, these problems can potentially be overcome if electric drive are considered.

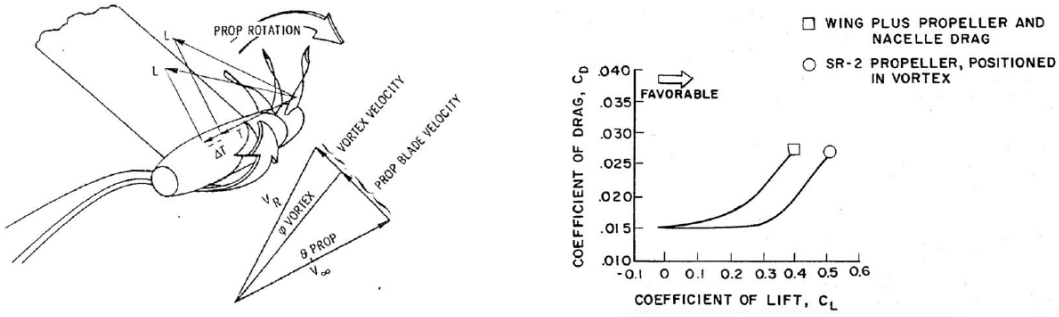


Figure 1.20: Analysis of wing tip propellers [101].

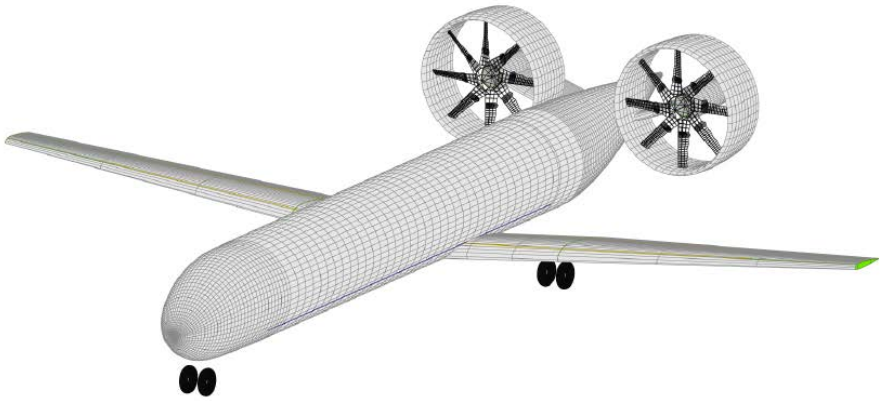

Figure 1.21: Conceptual design study of a regional aircraft featuring propulsive ducted empennage [103].

## *1.3 Benchmark Aircraft Models and Concepts*

This section presents contemporary aircraft in the commuter category and proposed concepts with a possible relationship with the UNIFIER19 miniliner concept.

### 1.3.1 Existing Commuter Aircraft and CS-23

Commuter aircraft serve a distinct niche in the air travel industry. These airliners are flown on the short and thin haul routes in order to feed the airline hubs enabling the hub-and-spoke network paradigm [104]. There is a vast diversity in the design and passenger carrying capacity of these airplanes. The maximum capacity is usually limited to 100 seats. Recent ongoing developments, in the commercial aviation sector, are paving the way for the adaption this network scheme, on a smaller and more prolific scale with new propulsion system [105].

The candidate aircraft for this innovative scheme will have 9 to 19 seats and are classified in the light transport category. These aircraft have traditionally been used in the roles of commuter, executive transport and private charter with conventional engines. Under the European Aviation Safety Agency (EASA), light transport aircraft are certified with the Certification Specification code CS-23. Table 1.11 lists the prominent examples of this category in service around the globe. A short description of noteworthy aircraft from the list is presented in the following paragraphs.

Table 1.11: List of notable light commuter aircraft

| No. | Aircraft | Seats | MTOM [kg] | Range [km] | Cruise Speed [km/h] |
|---|---|---|---|---|---|
| 1 | Pilatus PC-12NG | 9 | 4,740 | 3,417 | 528 |
| 2 | Cessna Conquest II | 9 | 4,468 | 4,064 | 480 |
| 3 | PAC P-750 XSTOL | 9 | 3,402 | 2,183 | 259 |
| 4 | Beechcraft 350ER | 11 | 7,484 | 4,986 | 561 |
| 5 | Mitsubishi MU-2L | 12 | 5,273 | 2,334 | 483 |
| 6 | Cessna 208 Caravan | 13 | 3,629 | 1,982 | 344 |
| 7 | Beechcraft Model 99A | 15 | 4,727 | 1,686 | 380 |
| 8 | GAF Nomad N24A | 16 | 4,264 | 1,352 | 311 |
| 9 | Harbin Y-12 F | 17 | 8,400 | 1,333 | 390 |
| 10 | Embraer EMB 110 | 18 | 5,900 | 1,964 | 341 |
| 11 | BAe Jetstream 31 | 19 | 6,950 | 1,260 | 264 |
| 12 | Beechcraft 1900D | 19 | 7,764 | 1,279 | 518 |
| 13 | Dornier Do 228NG | 19 | 6,575 | 2,363 | 413 |
| 14 | Fairchild Metroliner III | 19 | 7,257 | 2,131 | 318 |
| 15 | Let L-410 Turbolet NG | 19 | 7,000 | 2,570 | 417 |

#### *1.3.1.1 Pilatus PC-12*

The Pilatus PC-12 is a single engine turboprop aircraft with variants ranging from multipurpose cargo to executive transport and regional airliner. The popularity of PC-12 is attributed to its versatility, range and affordability of operations [106]. In addition to its excellent short-field performance and easy handling characteristics, PC-12 has comparatively slow take-off and landing speeds [107].

PC-12NG has a pressurized cabin and a seating capacity for 9 passengers arranged on either side of the aisle. It has a low mounted wing with an aspect ratio of 10.3 resulting in a wing loading of 184 kg/m$^2$. The maximum take-off mass is 4,740 kg and empty weight fraction is 61%. The aircraft stalls at 124 km/h and cruises at 528 km/h. The powerplant on the aircraft is a Pratt & Whitney Canada PT6A-67P turboprop engine with shaft power of 890 kW and it burns 250 l/h of fuel.

#### *1.3.1.2 Beechcraft 1900*

The Beechcraft 1900 is a twin-engine turboprop aircraft designed to operate in all weather conditions. There are many variants of this aircraft but 1900D is among the most popular versions mainly because of a spacious cabin which allows passengers to walk upright while embarking. It features a low wing design with an engine attached on each wing. The PT6A-67D turboprops, produce a shaft power 955 kW each. The aircraft requires a length of 1,160 meters in order to avoid 50-foot obstacle at take-off and can climb at a rate of 13.3 m/s. The landing distance is 850 m.

#### *1.3.1.3 Dornier Do 228NG*

The Dornier Do 228NG is a twin-engine turboprop aircraft with short takeoff and landing (STOL) capabilities. Although it is a multirole platform, but airlines prefer it due to its short field performance which is a desired feature to access remote airfields and short mountainous airstrips. It is a high wing design with an engine slung under each wing offering another advantage of ground clearance for cargo and passenger loading. The aircraft stall speed is 137 km/h and it requires a ground run of 792 m while the landing distance is 451 m.

#### *1.3.1.4 Certification Specification number 23 (CS-23)*

The airworthiness code CS-23 is applicable to Normal, Utility, Aerobatic, and Commuter Category of Airplanes. Although CS-23 came into force on 14$^{th}$ November 2003, but there are many later revisions and amendments, which subsequently became part of it. These amendments are incorporated to accommodate the technological and regulatory changes. There are two broad categories in this certification. First category includes airplanes with seating configuration of 9 or fewer excluding pilots. The maximum certificated take-off weight limit for this type is 5670 kg or less. Second category is twin-engine, propeller driven airplanes in the commuter class that have a seating configuration of 19 or fewer excluding pilot seats. The maximum certificated take-off weight for this category is 8618 kg or less [108].

Light transport category of aircraft shows a promising potential as the future of aviation moves towards pre-electric and hybrid-electric propulsion systems. Earlier

electric flight demonstrators were mostly powered gliders with one or two seats. As the battery technology has improved since, the first niche for the rapid commercialization of EHPS is aimed at this class of aircraft. But currently with CS-23 amendment 4, no plane with EHPS can be certified [109].

In conjunction with the previous practices, EASA has issued several Special Conditions (SCs) to address the introduction of EHPS to the general aviation and light commuter aircraft. These special conditions augment CSs to provide certification requirements. There are two notable documents in this regard as listed below:

- Special Condition: Electric / Hybrid Propulsion System [110]
- Special Condition: Electric Propulsion Units for CS-22 Sailplanes and Powered Sailplanes, CS-LSA Light Sport Aeroplanes, CS-VLA Very Light Aeroplanes and CS-23 Normal, Utility, Aerobatic and Commuter Aeroplanes [111].

Moreover, these SCs are independent of propulsion system design/architecture and provide only the objective based certification requirements. System specific details are covered in the Acceptable Means of Compliance (AMC) depending on the type of Electric / Hybrid Propulsion System (EHPS).

Table 1.12 lists terminologies and definitions adopted from reference [110].

**Table 1.12: EHPS.15 Terminology [110]**

| | |
|---|---|
| EHPS | Electric / Hybrid Propulsion System.<br>An Electric / Hybrid Propulsion System may include, but is not limited to, electric motors, inverters, turbine engines, piston engines, generators, electrical wiring interconnection systems, electrical power generation, energy storage systems, integrated fans, cooling systems and power management system. An EHPS is intended to produce lift, thrust or power for flight. |
| Sub-system of EHPS | A sub-system of the EHPS may include examples such as a turbine engine, a piston engine, an electric engine, a generator, an electrical power distribution system, a EHPS control system or, an energy storage system |
| EHPS Control System | A system or device that controls, limits, monitors or protects the operation of the EHPS or a sub-system of the EHPS excluding any battery or energy storage device management system |

Table 1.13: List of proposed pure-electric and hybrid-electric commuter aircraft.

| No. | Aircraft | Seats | MTOM [kg] | Range [km] | Cruise Speed [km/h] |
|---|---|---|---|---|---|
| 1 | Zunum Aero ZA10 | 12 | 5216 | 1,100 | 550 |
| 2 | Eviation Alice | 9 | 6,350 | 1,046 | 444 |
| 3 | Ampaire TailWind-E | 9 | - | 600 | - |
| 4 | Samad e-Starling | 7 | - | 645 | 483 |
| 5 | Carter Air Taxi | 6 | 2,495 | 181 | 282 |
| 6 | NASA UAM | 6 | - | 139 | 181 |
| 7 | Karem Butterfly | 5 | - | 135 | - |
| 8 | Lilium Jet | 5 | | 300 | 300 |
| 9 | AirisOne | 5 | - | 322 | 282 |

### 1.3.2 Proposed concepts

Many companies and research groups, around the world, are pursuing the idea f electric aviation. The multitude of efforts in this regard have resulted in numerous concepts, studies, designs and prototypes. This section explores some of the most prominent works to date considering the prospects of microfeeder and intercity networks.

Table 1.13 lists the proposed electric and hybrid commuter aircraft while the following paragraphs mention the noteworthy concepts from the list.

#### *1.3.2.1 Zunum Aero ZA10*

Zunum Aero has presented a family of hybrid electric aircraft concepts for the regional air travel market. The model ZA10 is being designed to carry a maximum of 12 passengers with two other configurations accommodating 9 and 6 passengers. It is a series hybrid electric plane of a conventional airframe design with two electric ducted fans attached on either side of the rear fuselage. A gas turbine engine is placed in the centerline of rear fuselage. Short trips will be powered by batteries alone while the engine will be used on long range flights acting as a generator for the two ducted fans.

#### *1.3.2.2 Eviation Alice*

Eviation Aircraft of Israel has developed this all electric aircraft with composite airframe. It is currently under development and expected to take first flight in 2020. It is designed to capture two distinct markets with aircraft powered by two types of battery chemistries. The first version is aimed at air taxi operation with a lithium-ion battery and the second version is targeting the long-range executive transport with aluminum-air batteries. Initially the aircraft will be certified with no-pressurized cabin although it is capable of pressurized operations.

Alice features a low wing deign with three motors in the pusher configuration. The synergetic placement of motors is expected to result aerodynamic efficiency. Two motors are mounted on wingtips on either sides and one motor in the aft fuselage. With a promise of affordable, sustainable aviation the direct operating cost is a fraction of turboprop aircraft operations with similar performance characteristics.

#### *1.3.2.3 Ampaire TailWind*

Tailwind is under conceptual studies and development by the United States based startup Ampair. Meanwhile the company has modified a Cessna O-2 Skymaster airframe to host electric hybrid propulsion to test and develop technologies for their future aircraft Tailwind. It is a 9-seat electric regional aircraft with a unique design. The aircraft features a ducted propulsor in the tail section to increase aerodynamic efficiency through Boundary Layer Ingestion (BLI). This configuration results in the reduction of power requirement and noise [112], [113].

## 1.4 References


[1] B. J. Brelje and J. R. R. A. Martins, "Electric, hybrid, and turboelectric fixed-wing aircraft: A review of concepts, models, and design approaches," *Progress in Aerospace Sciences*, vol. 104, pp. 1–19, Jan. 2019, doi: 10.1016/j.paerosci.2018.06.004.

[2] A. R. Gnadt, R. L. Speth, J. S. Sabnis, and S. R. H. Barrett, "Technical and environmental assessment of all-electric 180-passenger commercial aircraft," *Progress in Aerospace Sciences*, vol. 105, pp. 1–30, Feb. 2019, doi: 10.1016/j.paerosci.2018.11.002.

[3] C. Pornet and A. T. Isikveren, "Conceptual design of hybrid-electric transport aircraft," *Progress in Aerospace Sciences*, vol. 79, pp. 114–135, Nov. 2015, doi: 10.1016/j.paerosci.2015.09.002.

[4] J. Ribeiro *et al.*, "Environmental assessment of hybrid-electric propulsion in conceptual aircraft design," *Journal of Cleaner Production*, vol. 247, p. 119477, Feb. 2020, doi: 10.1016/j.jclepro.2019.119477.

[5] B. Cox, W. Jemiolo, and C. Mutel, "Life cycle assessment of air transportation and the Swiss commercial air transport fleet," *Transportation Research Part D: Transport and Environment*, vol. 58, pp. 1–13, Jan. 2018, doi: 10.1016/j.trd.2017.10.017.

[6] A. W. Schäfer, A. D. Evans, T. G. Reynolds, and L. Dray, "Costs of mitigating CO 2 emissions from passenger aircraft," *Nature Climate Change*, vol. 6, no. 4, pp. 412–417, Apr. 2016, doi: 10.1038/nclimate2865.

[7] "Global Market Forecast 2019-2038," *Airbus*. https://www.airbus.com/aircraft/market/global-market-forecast.html (accessed Apr. 01, 2020).

[8] N. A. of S. Medicine Engineering, and, D. on E. and P. Sciences, A. and S. E. Board, and C. on P. and E. S. to R. C. A. C. Emissions, *Commercial Aircraft Propulsion and Energy Systems Research: Reducing Global Carbon Emissions*. National Academies Press, 2016.

[9] "Boeing: Commercial Market Outlook." https://www.boeing.com/commercial/market/commercial-market-outlook/ (accessed Apr. 01, 2020).

[10] C. Grobler *et al.*, "Marginal climate and air quality costs of aviation emissions," *Environ. Res. Lett.*, vol. 14, no. 11, p. 114031, Nov. 2019, doi: 10.1088/1748-9326/ab4942.

[11] C. S. Dorbian, P. J. Wolfe, and I. A. Waitz, "Estimating the climate and air quality benefits of aviation fuel and emissions reductions," *Atmospheric Environment*, vol. 45, no. 16, pp. 2750–2759, May 2011, doi: 10.1016/j.atmosenv.2011.02.025.

[12] C. E. D. Riboldi, L. Trainelli, and F. Biondani, "A Sizing Procedure for Structural Batteries in Hybrid-Electric Aircraft," presented at the Advanced Aircraft Efficiency in a Global Air Transport System Conference (AEGATS 2018), 2018, pp. 1–8, Accessed: Apr. 01, 2020. [Online]. Available: https://re.public.polimi.it/handle/11311/1069132#.XoTU4pMzZQM.

[13] A. Bernasconi *et al.*, "Aircraft with electric batteries, in particular a hybrid aircraft," US20190263498A1, Aug. 29, 2019.

[14] C. E. D. Riboldi, L. Trainelli, and F. Biondani, "Structural Batteries in Aviation: A Preliminary Sizing Methodology"," *Journal of Aerospace Engineering*, 2020.

[15] A. N. Varyukhin, V. S. Zakharchenko, A. V. Vlasov, M. V. Gordin, and M. A. Ovdienko, "Roadmap for the Technological Development of Hybrid Electric and Full-Electric Propulsion Systems of Aircrafts," in *2019 International Conference on Electrotechnical*

*Complexes and Systems (ICOECS)*, Ufa, Russia, Oct. 2019, pp. 1–7, doi: 10.1109/ICOECS46375.2019.8949910.

[16] X. Lü, P. Wang, L. Meng, and C. Chen, "Energy optimization of logistics transport vehicle driven by fuel cell hybrid power system," *Energy Conversion and Management*, vol. 199, p. 111887, Nov. 2019, doi: 10.1016/j.enconman.2019.111887.

[17] C. Depcik *et al.*, "Electrifying Long-Haul Freight—Part II: Assessment of the Battery Capacity," *SAE Int. J. Commer. Veh.*, vol. 12, no. 2, pp. 02-12-02–0007, Jan. 2019, doi: 10.4271/02-12-02-0007.

[18] F. Schlachter, "No Moore's Law for batteries," *PNAS*, vol. 110, no. 14, pp. 5273–5273, Apr. 2013, doi: 10.1073/pnas.1302988110.

[19] J. Rohacs and D. Rohacs, "Energy coefficients for comparison of aircraft supported by different propulsion systems," *Energy*, vol. 191, p. 116391, Jan. 2020, doi: 10.1016/j.energy.2019.116391.

[20] W.-J. Kwak *et al.*, "Lithium–Oxygen Batteries and Related Systems: Potential, Status, and Future," *Chem. Rev.*, p. acs.chemrev.9b00609, Mar. 2020, doi: 10.1021/acs.chemrev.9b00609.

[21] N. Nitta, F. Wu, J. T. Lee, and G. Yushin, "Li-ion battery materials: present and future," *Materials Today*, vol. 18, no. 5, pp. 252–264, Jun. 2015, doi: 10.1016/j.mattod.2014.10.040.

[22] G. E. Blomgren, "The Development and Future of Lithium Ion Batteries," *J. Electrochem. Soc.*, vol. 164, no. 1, p. A5019, Dec. 2016, doi: 10.1149/2.0251701jes.

[23] B. Khandelwal, A. Karakurt, P. R. Sekaran, V. Sethi, and R. Singh, "Hydrogen powered aircraft : The future of air transport," *Progress in Aerospace Sciences*, vol. 60, pp. 45–59, Jul. 2013, doi: 10.1016/j.paerosci.2012.12.002.

[24] G. Zubi, R. Dufo-López, M. Carvalho, and G. Pasaoglu, "The lithium-ion battery: State of the art and future perspectives," *Renewable and Sustainable Energy Reviews*, vol. 89, pp. 292–308, Jun. 2018, doi: 10.1016/j.rser.2018.03.002.

[25] J. F. Peters, M. Baumann, B. Zimmermann, J. Braun, and M. Weil, "The environmental impact of Li-Ion batteries and the role of key parameters – A review," *Renewable and Sustainable Energy Reviews*, vol. 67, pp. 491–506, Jan. 2017, doi: 10.1016/j.rser.2016.08.039.

[26] "Types of Lithium-ion Batteries – Battery University." https://batteryuniversity.com/learn/article/types_of_lithium_ion (accessed Apr. 02, 2020).

[27] "A Behind the Scenes Take on Lithium-ion Battery Prices," *BloombergNEF*, Mar. 05, 2019. https://about.bnef.com/blog/behind-scenes-take-lithium-ion-battery-prices/ (accessed Apr. 01, 2020).

[28] J. E. Harlow *et al.*, "A Wide Range of Testing Results on an Excellent Lithium-Ion Cell Chemistry to be used as Benchmarks for New Battery Technologies," *J. Electrochem. Soc.*, vol. 166, no. 13, p. A3031, Sep. 2019, doi: 10.1149/2.0981913jes.

[29] S. Chung and A. Manthiram, "Current Status and Future Prospects of Metal–Sulfur Batteries," *Adv. Mater.*, vol. 31, no. 27, p. 1901125, Jul. 2019, doi: 10.1002/adma.201901125.

[30] L. Huang *et al.*, "Electrode Design for Lithium–Sulfur Batteries: Problems and Solutions," *Adv. Funct. Mater.*, p. 1910375, Mar. 2020, doi: 10.1002/adfm.201910375.

[31] S. Urbonaite, T. Poux, and P. Novák, "Progress Towards Commercially Viable Li–S Battery Cells," *Advanced Energy Materials*, vol. 5, no. 16, p. 1500118, 2015, doi: 10.1002/aenm.201500118.

[32] “Licerion® high energy density, lithium-metal rechargeable battery.” https://sionpower.com/ (accessed Apr. 01, 2020).

[33] D. Lerwill, “OXIS Energy is close to achieving 500Wh/kg and is targeting 600Wh/kg with Solid State Lithium Sulfur technology,” *Oxis Energy*, Jan. 22, 2020. https://oxisenergy.com/https-oxisenergy-com-wp-content-uploads-2020-01-500-and-600-whkg-pressor-pdf/ (accessed Apr. 01, 2020).

[34] “Home,” *Innolith Science and Technology GmbH*. https://innolith.com/ (accessed Apr. 01, 2020).

[35] R. and M. ltd, “Global Lithium-Sulfur Battery Market 2018-2022 - Research and Markets.” https://www.researchandmarkets.com/reports/4535214/global-lithium-sulfur-battery-market-2018-2022 (accessed Apr. 01, 2020).

[36] K. G. Gallagher *et al.*, “Quantifying the promise of lithium–air batteries for electric vehicles,” *Energy Environ. Sci.*, vol. 7, no. 5, pp. 1555–1563, Apr. 2014, doi: 10.1039/C3EE43870H.

[37] H. C. Lee *et al.*, “High-Energy-Density Li-O2 Battery at Cell Scale with Folded Cell Structure,” *Joule*, vol. 3, no. 2, pp. 542–556, Feb. 2019, doi: 10.1016/j.joule.2018.11.016.

[38] A. Misra, “Energy Storage for Electrified Aircraft: The Need for Better Batteries, Fuel Cells, and Supercapacitors,” *IEEE Electrific. Mag.*, vol. 6, no. 3, pp. 54–61, Sep. 2018, doi: 10.1109/MELE.2018.2849922.

[39] X. Pu *et al.*, “Recent Progress in Rechargeable Sodium-Ion Batteries: toward High-Power Applications,” *Small*, vol. 15, no. 32, p. 1805427, 2019, doi: 10.1002/smll.201805427.

[40] B. B. Beenarani and C. P. Sugumaran, “Postulates of Supercapacitor and Performance Assessment Parameters: A Technical Overview,” *Materials Today: Proceedings*, vol. 21, pp. 1911–1918, Jan. 2020, doi: 10.1016/j.matpr.2020.01.275.

[41] P.-P. Sun *et al.*, “Cu powder decorated 3D Mn-MOF with excellent electrochemical properties for supercapacitors,” *Inorganica Chimica Acta*, p. 119629, 2020.

[42] Z. Sha, “A bendable solid-state supercapacitor based on alkaline polyvinyl alcohol.”

[43] B. Fan *et al.*, “High-performance potassium ion capacitors enabled by hierarchical porous, large interlayer spacing, active site rich-nitrogen, sulfur Co-doped carbon,” *Carbon*, 2020.

[44] “Li-ion Capacitors - Yunasko is the developer and licensor of high power ultracapacitors.” https://yunasko.com/en/products/lithium-ion-capacitors (accessed Apr. 01, 2020).

[45] “Superdielectrics | Home.” https://www.superdielectrics.com/ (accessed Apr. 01, 2020).

[46] “Rolls-Royce and Superdielectrics explore supercapacitor technology.” https://www.sae.org/news/2018/05/rolls-royce-and-superdielectrics-explore-supercapacitor-technology (accessed Apr. 01, 2020).

[47] R. P. O’Hayre, S.-W. Cha, W. G. Colella, and F. B. Prinz, *Fuel cell fundamentals*, Third edition. Hoboken, New Jersey: John Wiley & Sons Inc, 2016.

[48] S. E. Hosseini and B. Butler, “An overview of development and challenges in hydrogen powered vehicles,” *International Journal of Green Energy*, vol. 17, no. 1, pp. 13–37, Jan. 2020, doi: 10.1080/15435075.2019.1685999.

[49] J. A. Stockford, C. Lawson, and Z. Liu, “Benefit and performance impact analysis of using hydrogen fuel cell powered e-taxi system on A320 class airliner,” *Aeronaut. j.*, vol. 123, no. 1261, pp. 378–397, Mar. 2019, doi: 10.1017/aer.2018.156.

[50] J. Wang, H. Wang, and Y. Fan, “Techno-Economic Challenges of Fuel Cell Commercialization,” *Engineering*, vol. 4, no. 3, pp. 352–360, Jun. 2018, doi: 10.1016/j.eng.2018.05.007.

[51] J. Büsselmann *et al.*, “Analysis of HT-PEM MEAs’ Long-Term Stabilities,” *Energies*, vol. 13, no. 3, p. 567, Jan. 2020, doi: 10.3390/en13030567.

[52] T. Kadyk, C. Winnefeld, R. Hanke-Rauschenbach, and U. Krewer, “Analysis and Design of Fuel Cell Systems for Aviation,” *Energies*, vol. 11, no. 2, p. 375, Feb. 2018, doi: 10.3390/en11020375.

[53] I. Staffell *et al.*, “The role of hydrogen and fuel cells in the global energy system,” *Energy Environ. Sci.*, vol. 12, no. 2, pp. 463–491, Feb. 2019, doi: 10.1039/C8EE01157E.

[54] A. Dicks and D. A. J. Rand, *Fuel cell systems explained*, Third edition. Hoboken, NJ, USA: Wiley, 2018.

[55] “DOE Technical Targets for Fuel Cell Systems and Stacks for Transportation Applications,” *Energy.gov*. https://www.energy.gov/eere/fuelcells/doe-technical-targets-fuel-cell-systems-and-stacks-transportation-applications (accessed Apr. 01, 2020).

[56] T. Kadyk, R. Schenkendorf, S. Hawner, B. Yildiz, and U. Römer, “Design of Fuel Cell Systems for Aviation: Representative Mission Profiles and Sensitivity Analyses,” *Front. Energy Res.*, vol. 7, p. 35, Apr. 2019, doi: 10.3389/fenrg.2019.00035.

[57] “Fuel Cell System Cost - 2017,” DOE Hydrogen and Fuel Cells Program Record, Sep. 2017.

[58] J. Andersson and S. Grönkvist, “Large-scale storage of hydrogen,” *International Journal of Hydrogen Energy*, vol. 44, no. 23, pp. 11901–11919, May 2019, doi: 10.1016/j.ijhydene.2019.03.063.

[59] M. Hirscher *et al.*, “Materials for hydrogen-based energy storage – past, recent progress and future outlook,” *Journal of Alloys and Compounds*, vol. 827, p. 153548, Jun. 2020, doi: 10.1016/j.jallcom.2019.153548.

[60] Y. Zhang, Z. Jia, Z. Yuan, T. Yang, Y. Qi, and D. Zhao, “Development and Application of Hydrogen Storage,” *Journal of Iron and Steel Research, International*, vol. 22, no. 9, pp. 757–770, Sep. 2015, doi: 10.1016/S1006-706X(15)30069-8.

[61] E. Rivard, M. Trudeau, and K. Zaghib, “Hydrogen Storage for Mobility: A Review,” *Materials*, vol. 12, no. 12, p. 1973, Jun. 2019, doi: 10.3390/ma12121973.

[62] SAE EUROCAE Fuel Cell Task Group, “EUROCAE/SAE WG80/AE-7AFC Hydrogen Fuel Cells Aircraft Fuel Cell Safety Guidelines,” SAE International. doi: 10.4271/AIR6464.

[63] SAE EUROCAE Fuel Cell Task Group, “Considerations for Hydrogen Fuel Cells in Airborne Applications,” SAE International. doi: 10.4271/AIR7765.

[64] H. Barthelemy, M. Weber, and F. Barbier, “Hydrogen storage: Recent improvements and industrial perspectives,” *International Journal of Hydrogen Energy*, vol. 42, no. 11, pp. 7254–7262, Mar. 2017, doi: 10.1016/j.ijhydene.2016.03.178.

[65] D. Wang *et al.*, “Development of regulations, codes and standards on composite tanks for on-board gaseous hydrogen storage,” *International Journal of Hydrogen Energy*, vol. 44, no. 40, pp. 22643–22653, Aug. 2019, doi: 10.1016/j.ijhydene.2019.04.133.

[66] B. Iso, “BSI Standards Publication,” p. 64.

[67] M. Zhang, H. Lv, H. Kang, W. Zhou, and C. Zhang, “A literature review of failure prediction and analysis methods for composite high-pressure hydrogen storage tanks,” *International Journal of Hydrogen Energy*, vol. 44, no. 47, pp. 25777–25799, Oct. 2019, doi: 10.1016/j.ijhydene.2019.08.001.

[68] E. Yamada and T. Mashiba, “Development of Technical Regulations for Fuel Cell Motorcycles in Japan—Hydrogen Safety,” *WEVJ*, vol. 10, no. 3, p. 48, Jul. 2019, doi: 10.3390/wevj10030048.

[69] D. Halm, F. Fouillen, E. Lainé, M. Gueguen, D. Bertheau, and T. van Eekelen, “Composite pressure vessels for hydrogen storage in fire conditions: Fire tests and burst simulation,” *International Journal of Hydrogen Energy*, vol. 42, no. 31, pp. 20056–20070, Aug. 2017, doi: 10.1016/j.ijhydene.2017.06.088.

[70] B. D. James, C. Houchins, J. M. Huya-Kouadio, and D. A. DeSantis, “Final Report: Hydrogen Storage System Cost Analysis,” DOE-SA--0005253, 1343975, Sep. 2016. doi: 10.2172/1343975.

[71] R. Moradi and K. M. Groth, “Hydrogen storage and delivery: Review of the state of the art technologies and risk and reliability analysis,” *International Journal of Hydrogen Energy*, vol. 44, no. 23, pp. 12254–12269, May 2019, doi: 10.1016/j.ijhydene.2019.03.041.

[72] M. Genovese, D. Blekhman, M. Dray, and P. Fragiacomo, “Hydrogen losses in fueling station operation,” *Journal of Cleaner Production*, vol. 248, p. 119266, Mar. 2020, doi: 10.1016/j.jclepro.2019.119266.

[73] A. Gomez and H. Smith, “Liquid hydrogen fuel tanks for commercial aviation: Structural sizing and stress analysis,” *Aerospace Science and Technology*, vol. 95, p. 105438, Dec. 2019, doi: 10.1016/j.ast.2019.105438.

[74] S. M. Aceves *et al.*, “High-density automotive hydrogen storage with cryogenic capable pressure vessels,” *International Journal of Hydrogen Energy*, vol. 35, no. 3, pp. 1219–1226, Feb. 2010, doi: 10.1016/j.ijhydene.2009.11.069.

[75] J. Moreno-Blanco, G. Petitpas, F. Espinosa-Loza, F. Elizalde-Blancas, J. Martinez-Frias, and S. M. Aceves, “The storage performance of automotive cryo-compressed hydrogen vessels,” *International Journal of Hydrogen Energy*, vol. 44, no. 31, pp. 16841–16851, Jun. 2019, doi: 10.1016/j.ijhydene.2019.04.189.

[76] B. L. Salvi and K. A. Subramanian, “Sustainable development of road transportation sector using hydrogen energy system,” *Renewable and Sustainable Energy Reviews*, vol. 51, pp. 1132–1155, Nov. 2015, doi: 10.1016/j.rser.2015.07.030.

[77] Electric Motors and Drives. Elsevier, 2013.

[78] “Compact Dynamics | Unternehmen.” https://www.compact-dynamics.de/unternehmen/ (accessed Apr. 01, 2020).

[79] Siemens AG, “Electric propulsion components with high power densities for aviation,” 2015.

[80] “EMRAX | Axial flux e-motors | lightweight | powerful,” *EMRAX*. https://emrax.com/ (accessed Apr. 01, 2020).

[81] “Quadcopters & Aerial Drones,” *YUNEEC*. https://www.yuneec.com/en_US/home.html (accessed Apr. 01, 2020).

[82] R. H. B. Jansen, “Overview of NASA Electrified Aircraft Propulsion Research for Large Subsonic Transports,” presented at the AIAA Propulsion and Energy 2017 Forum, Atlanta, GA, United States, Jul. 2017, Accessed: Apr. 01, 2020. [Online]. Available: https://ntrs.nasa.gov/search.jsp?R=20170006235.

[83] T. Shinzato, S. Arakawa, H. Oyama, H. Saka, and T. Hayasaki, “Development of High-Temperature Superconducting Motor for Automobiles,” p. 4.

[84] T. P. Dever *et al.*, “Assessment of Technologies for Noncryogenic Hybrid Electric Propulsion,” p. 54, 2015.

[85] R. Schnell *et al.*, "Assessment of a Turbo-Electric Aircraft Configuration with Aft-Propulsion Using Boundary Layer Ingestion," *Aerospace*, vol. 6, no. 12, p. 134, Dec. 2019, doi: 10.3390/aerospace6120134.

[86] Mavris D. N. and Pinon O. J, A Systems Engineering Approach to Aircraft Design Encyclopedia of Aerospace Engineering. ed: John Wiley & Sons, 2012.

[87] J. Roskam, *Airplane Design*, vol. Vols. VIII. 1989.

[88] D. P. Raymer, *Aircraft Design: A Conceptual Approach*, 2nd ed. Washington, D.C., USA: AIAA, Inc, 1992.

[89] S. Gudmundsson, *General Aviation Aircraft Design: Applied Methods and Procedures*, 1st ed. USA: Butterworth-Heinemann, 2013.

[90] R. H. Liebeck, "Design of the Blended Wing Body Subsonic Transport," *Journal of Aircraft*, vol. 41, no. 1, 2004.

[91] F. Faggiano and Al, "Aerodynamic Design of a Flying V Aircraft," in *17th AIAA Aviation Technology, Integration, and Operations Conference: 5-9*, Denver, Colorado, 2017.

[92] R. Cavallaro and L. De Masi, "Challenges, Ideas, and Innovations of Joined-Wing Configurations: A Concept from the Past, an Opportunity for the Future," *Progress in Aerospace Sciences*, vol. 87, 2016.

[93] O. Tremblay, L. A. Dessaint, and A. I. Dekkiche, "A Generic Battery Model for the Dynamic Simulation of Hybrid Electric Vehicles," in *Proceedings of Vehicle Power and Propulsion Conference*, 2007.

[94] Q. Yu, R. Xiong, and L. Wang, "A Comparative Study on Open Circuit Voltage Models for Lithium-ion Batteries," *Chin. J. Mech. Eng*, vol. 31, p. 65, 2018, doi: 10.1186/s10033-018-0268-8.

[95] Y. K. Tan, J. C. Mao, and K. Tseng, "Modelling of battery temperature effect on electrical characteristics of Li-ion battery in hybrid electric vehicle," in *Proceedings of the International Conference on Power Electronics and Drive Systems*, 2011.

[96] G. Romeo, I. Moraglio, and C. Novarese, "ENFICA-FC: Preliminary Survey and Design of 2-Seat Aircraft Powered by Fuel Cells Electric Propulsion," in *Proceedings of 7th AIAA Aviation Technology, Integration and Operation Conference 18-20*, 2007.

[97] J. Kallo, "DLR leads HY4 project for four-seater fuel cell aircraft," *Fuel Cells Bulletin*, no. 11, p. 13, 2015.

[98] C. E. D. Riboldi, L. Trainelli, and F. E. A. Salucci, "Sizing and Performance of Hydrogen-Driven Airplanes," in *Proceedings of 2019 AIDAA conference*, Rome, 2019.

[99] VV.AA., MAHEPA D1.1: Concept of Modular Architecture for Hybrid Electric Propulsion of Aircraft. Public deliverable of the H2020 project MAHEPA. 2017.

[100] R. Vries, M. T. Brown, and R. Vos, "A preliminary sizing method for hybrid-electric aircraft including aero-propulsive interaction effects," in *2018 Aviation Technology, Integration, and Operations Conference [AIAA 2018-4228*, 2018.

[101] J. C. Patterson, G. Bartlett, and J., "Evaluation of installed performance of a wing-tip-mounted pusher turboprop on a semispan wing." 1987.

[102] T. Sinnige, N. Arnhem, T. C. A. Stokkermans, and Al, "Wingtip-Mounted Propellers: Aerodynamic Analysis of Interaction Effects and Comparison with Conventional Layout," *Journal of Aircraft*, vol. 56, no. 1, pp. 295–312, 2019.

[103] N. H. M. Dungen, "Synthesis of an Aircraft Featuring a Ducted-Fan Propulsive Empennage," TU Delft Master Thesis, Aerospace Engineering Faculty, 2017.

[104] J. K. Brueckner, “Network Structure and Airline Scheduling,” *J Industrial Economics*, vol. 52, no. 2, pp. 291–312, Jun. 2004, doi: 10.1111/j.0022-1821.2004.00227.x.

[105] L. Trainelli, M. Bruglieri, C. E. D. Riboldi, F. Salucci, and D. Gabrielli, “OPTIMAL DEFINITION OF A SHORT-HAUL AIR TRANSPORTATION NETWORK FOR DOOR-TO-DOOR MOBILITY,” p. 8.

[106] M. Sirak, “US Air Force targets light transport aircraft needs,” *Jane’s Defence Weekly*, no. DEC., pp. 159–160, 2005.

[107] F. George, “Finnoff PC-12 Upgrade | Aviation Week Network.” https://aviationweek.com/business-aviation/finnoff-pc-12-upgrade (accessed Mar. 29, 2020).

[108] “CS-23 / Initial issue |,” *EASA*. https://www.easa.europa.eu/document-library/certification-specifications/cs-23-initial-issue (accessed Mar. 29, 2020).

[109] M. Kreimeier and E. Stumpf, “Benefit evaluation of hybrid electric propulsion concepts for CS-23 aircraft,” *CEAS Aeronaut J*, vol. 8, no. 4, pp. 691–704, Dec. 2017, doi: 10.1007/s13272-017-0269-9.

[110] “Proposed Special Condition: Electric / Hybrid Propulsion System |,” *EASA*. https://www.easa.europa.eu/document-library/product-certification-consultations/proposed-special-condition-electric-hybrid (accessed Mar. 26, 2020).

[111] “Proposed Electric Propulsion Units for CS-22 Sailplanes and Powered Sailplanes, CS-LSA Light Sport Aeroplanes, CS-VLA Very Light Aeroplanes and CS-23 Normal, Utility, Aerobatic and Commuter Aeroplanes up to Level 1 |,” *EASA*. https://www.easa.europa.eu/document-library/product-certification-consultations/proposed-electric-propulsion-units-cs-22 (accessed Mar. 29, 2020).

[112] K. A. Brown, J. Fleming, M. Langford, W. Ng, K. Schwartz, and C. Combs, “Development of a ducted propulsor for BLI electric regional aircraft-part I: Aerodynamic design and analysis,” presented at the AIAA Propulsion and Energy Forum and Exposition, 2019, 2019, doi: 10.2514/6.2019-3853.

[113] K. Schwartz, R. Burdisso, B. Witcher, K. A. Brown, J. L. Fleming, and C. Combs, “Development of a Ducted Propulsor for BLI Electric Regional Aircraft - Part II: Aeroacoustic Analysis,” in *AIAA Propulsion and Energy 2019 Forum*, Indianapolis, IN, Aug. 2019, doi: 10.2514/6.2019-3854.

# 2 Market studies

UNIFIER19 investigates the concept of a new miniliner aircraft for passenger transportation on short and very-short haul routes, to be used in two flavours: the microfeeder and the intercity services.

The microfeeder service is intended as a hub-to-spoke air transportation service, used to feed major airports from smaller cities and open country territories.

The intercity service is intended as a point-to-point air transportation service, used to connect smaller cities and open country territories.

Both are conceived as key components in the future development of a more connected European transportation network through enhanced, environmentally-sustainable regional air travel.

The new community-friendly short-haul airliner may drastically enhance connectivity in territories with inefficient ground transportation services to major airports or between towns, enabling Europe's Flightpath 2050 vision, which envisages that virtually all EU citizens shall reach any continental destination in less than four hours, door to door, by the year 2050.

As these concepts apply to a market that is not at all developed in Europe yet, marked studies concern the analysis of the current status of land-based transportation network performance, the prediction of the potential passenger demand for short-haul air travel services, and the optimal sizing of air transportation networks that fulfil such predicted services.

## *2.1 General*

A key-element in understanding the applicability and profitability of novel near-zero emission aircraft is the quantitative analysis of the air transport network they can support [1]. Thanks to the stark reduction in noise and chemical emissions, especially during terminal maneuvers [2], airliners endowed with this new type of propulsion system may operate from secondary airports and smaller airfields often built very close to towns or in densely populated city areas, which are nowadays constrained by traffic limitations to reduce social cost and public annoyance.

The upgrade of these overlooked assets to the role of nodes in a new air transportation infrastructure would be possible especially when coupled with the microfeeder/intercity miniliner concept [3]. The microfeeder idea would be for passengers living in larger urban areas or at a distance from major cities and traveling to distant destinations currently reachable from larger hub airports, to start their journey from a local airport, making use of a connection operated by means of a smaller aircraft. This should replace the trip from home to the hub airport, today usually covered by car, train or bus. In the intercity case, similar arguments apply with respect to commuting journeys between smaller cities and open country locations.

As said, the low-emission propulsive technology would play an enabling role for the spreading of this concept. Yet the need to provide airports with adequate battery storage and recharging and/or hydrogen (or other types of fuel) storage and refueling

facilities, as implied by the adoption of such type of propulsion, has to be coped with through the development of existing airports and airfields. Studies devoted to battery-recharging airport facilities have been initiated within the MAHEPA project (WP10) and published in [4]-[7].

On secondary airports, this produces a delicate trade-off scenario, where profitability from air traffic revenues should be sufficiently high to justify the procurement cost of an upgrade of the local airport facility, needed to operate with the new aircraft.

In this sense, predicting the potential traffic demand in terms of seats traveling from a secondary airport or airfield to a hub airport is of paramount importance to forecast the potential profitability of a given microfeeder/intercity route.

A relevant aspect in the network sizing problem is the effect of aircraft passenger capacity. Clearly, the larger (i.e. higher-capacity) the aircraft, the heavier the batteries and/or the larger the tanks and the longer the duration of the battery-recharging/tank-refueling process. The latter has an impact on time efficiency of the miniliner service. In other words, a less frequent service with a larger aircraft may be apparently more efficient from the airline standpoint, but would have a detrimental effect on the flexibility of the transport system from the passenger's perspective – if sufficiently frequent connections to the hub are not offered, the whole miniliner system may easily turn time-inefficient for passengers.

Furthermore, the risk of flying with a reduced passenger load factor most of the time, more typical to a larger aircraft designed to cope with peak demand encountered only rarely in a day schedule, makes the definition of aircraft capacity a sensible parameter also from the standpoint of miniliner operators (airlines).

Other relevant aspects in the network sizing problem, also with a considerable impact on aircraft design, are connected to the fundamental performance of maximum range, cruising speed, and take-off and landing distances. Therefore, the following market studies include the effects of different values for such performance items in the assessment of the potential traffic demand.

## *2.2 Analysis of ground transportation*

An analysis of the European ground transportation data was carried out in the MAHEPA project (WP10) and was here revised and completed. The goals are the identification of possible transport mode competitors for the miniliner service and the evaluation of the "transport efficiency" on a local territorial basis, in order to provide information for the areas where a miniliner service can be more competitive and time-efficient.

To do so, EUROSTAT data were analyzed leading to the mapping of Europe with respect to the density of the ground-transportation infrastructures.

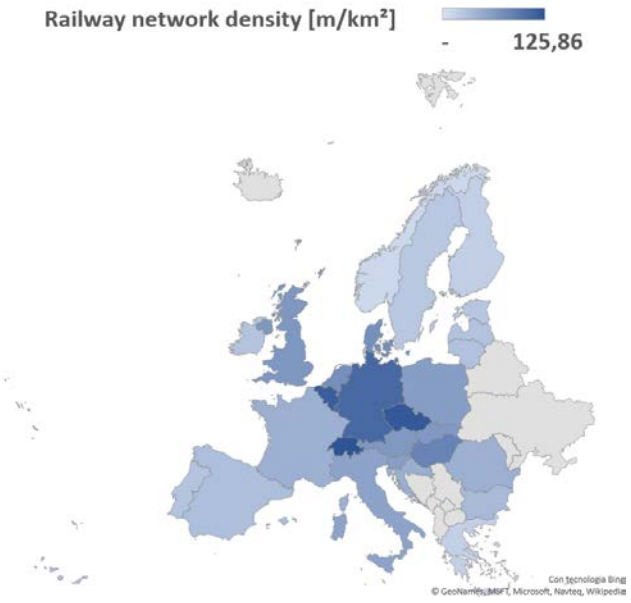


Figure 2.1: Density of the railway network in European countries.

Figure 2.1 shows the distribution of a railway network efficiency index across European countries. This index is computed as the total length of railways in m divided by the country area in km. As reported, the maximum values are reached in Belgium, Switzerland, and Czech Republic, while minimum values are found especially in Northernmost, Easternmost, and Westernmost countries.

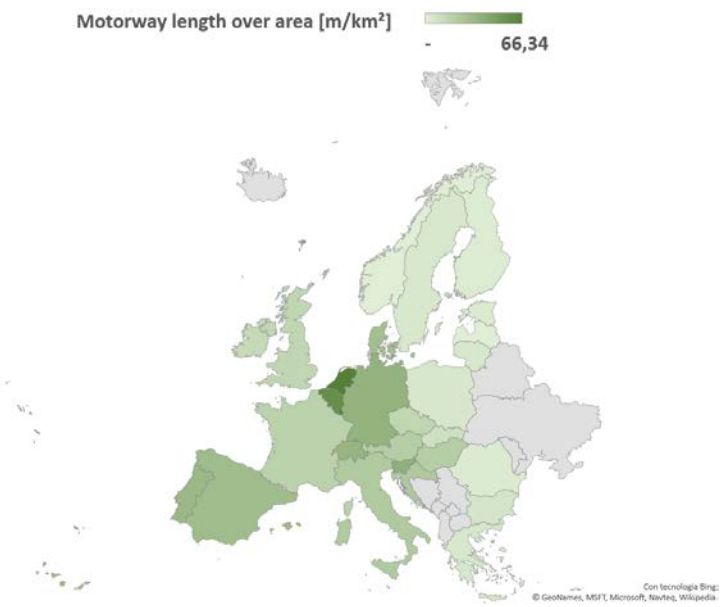


Figure 2.2: Density of the motorway network in European countries.

Figure 2.2 shows the distribution of a motorway network efficiency index across European countries. This index is computed as the total length of motorways in m divided by the country area in km. As reported, the maximum values are reached in Netherlands and Belgium, while minimum values are found especially in Easternmost countries, from North to South.

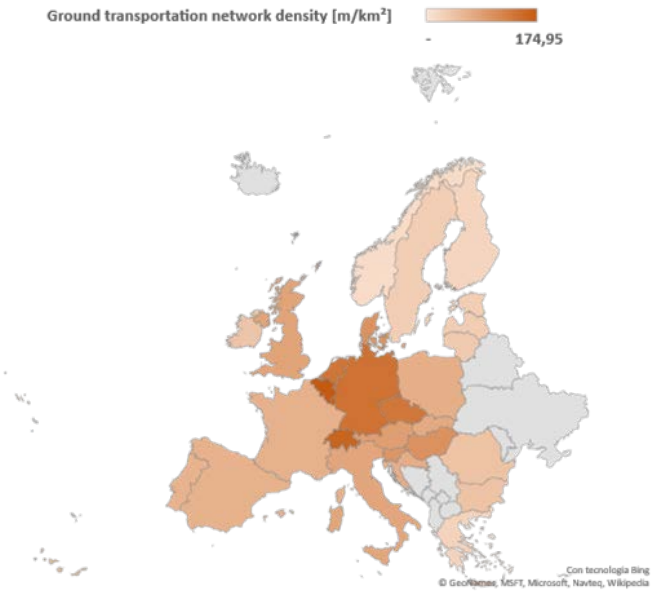


Figure 2.3: Ground transportation efficiency in European countries.

In order to derive a single index, the two quantities above have been combined, yielding the "ground transportation efficiency". Figure 2.3 shows the distribution of such index across European countries. This index is computed as the total length of motorways plus railways in m divided by the country area in km. As reported, the maximum values are reached in Central Europe, with a peak in Belgium, while minimum values are found especially in North-easternmost and South-easternmost countries.

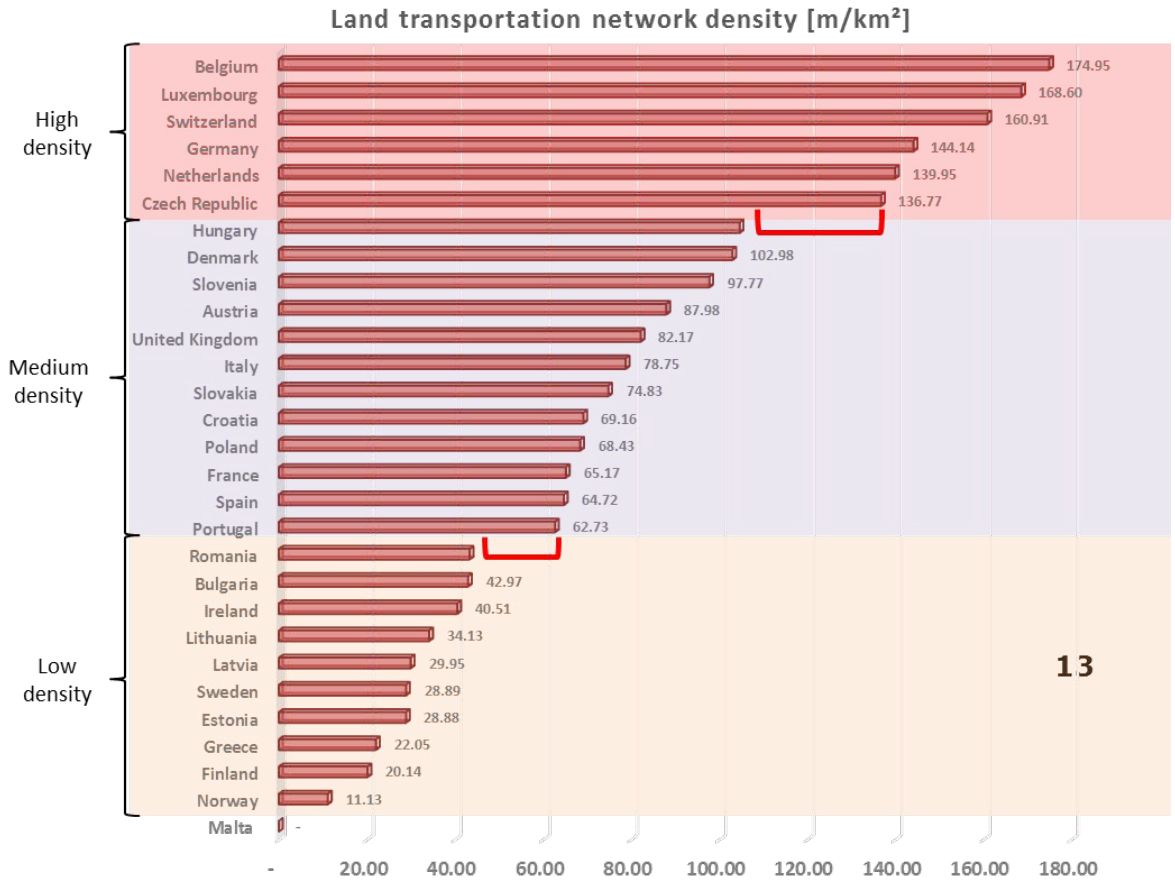


Figure 2.4: Classification of European countries according to ground transportation efficiency.

This analysis leads to a classification of European countries, seen in Figure 2.4: Classification of European countries according to ground transportation efficiency.. As apparent, the wide differences in the ground transportation efficiency index values found across Europe yield the possibility of a clustering in three subsets. In fact, discrete jumps (marked in red in the figure) are found between the values for Romania and Portugal, and for Hungary and Czech Republic. This inspires the definition of three subsets with high, medium, and low ground transportation efficiency.

Given the impracticality of an analysis of the potential demand for a miniliner service extended to the whole of Europe, this study is considered preliminary to the analysis of selected cases that may be seen as representative of the different conditions encountered in the three country subsets.

## *2.3 Potential demand estimation methodology*

### 2.3.1 Potential aerodrome network

The starting point for the estimation of the potential demand for a miniliner service is the definition of the existing and potential airport infrastructures in a geographical area of interest.

Typically, three types of aerodromes can be defined, based on regulations:

1. Major airports, which are most typically adopted as hubs, support a volume above 10,000,000 passengers per year.
2. Secondary airports, which are below this volume threshold.
3. Airfields, by far the majority of aerodrome infrastructures in any European country, which are currently distinguished by their inability to support scheduled transport services – a definition likely to change in case they are going to be included in a novel miniliner transport network. Aircraft operating on airfields are subject to weight and capacity restrictions (5,700 kg MTOW and nine seats maximum). Runway specifications and the quality of emergency services also have an impact on the chance of an airfield to carry out public services altogether.

The existing (i.e. already in use for public service) and potential infrastructures have been identified through an analysis of the European data available, including the EU-defined Trans-European Transport Network (TEN-T).

The TEN-T network is shown in Figure 2.5, where the airports forming the “core network” (i.e. the hubs) are shown as white aircraft silhouettes in black circles, while those included in the “comprehensive network” (i.e. secondary airports) are shown as clack aircraft silhouettes. This framework has been completed with the vast number and distribution of airfields over the European continent.

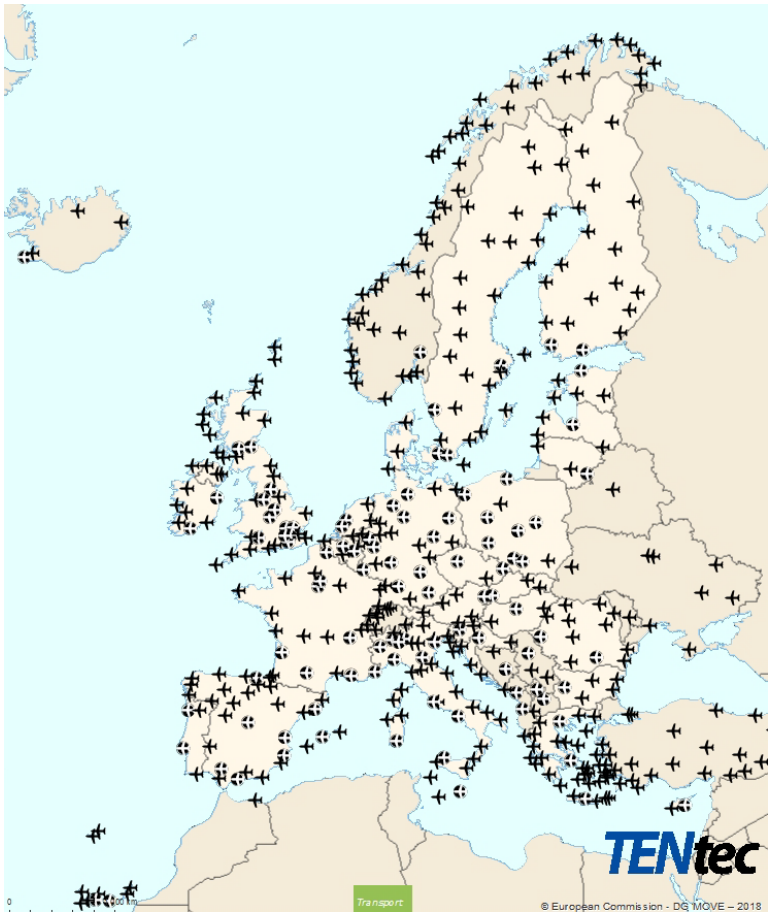


Figure 2.5: TEN-T airport network.

### 2.3.2 Identification of potential routes

Once the aerodrome infrastructure is known, a vast number of routes may be traced connecting all locations. Those based on the TEN-T network only (excluding airfields) in the sole microfeeder framework (i.e. hub-to-spoke) amount to 124,256 point-to-point connections. It is clearly crucial to be able to downselect possibly interesting routes from these large sets in an appropriate way.

In the present, preliminary phase of the market studies, a selection is enforced according to time-saving criterion: the air route which guarantees a minimum time advantage with respect to the alternatives provided by the ground transportation network are considered, while the others are discarded. Of course, in a subsequent phase of the UNIFIER19 project, when other important parameters will be adequately estimated, further functions of merit in addition to travel time may be included, such as ticket cost and passenger comfort.

The data used for the travel time estimations have been retrieved from publicly available databases, such as those offered by various internet mapping and navigation services. Air route distances have been calculated by referring to orthodromic

distances while ground travel distance and times have been gathered through HERE Maps APIs.

In order to preliminarily assess the potential demand for each connection between a hub and a secondary airport/airfield or between secondary airports/airfields, the number of passengers that may find this type of connection more convenient than others can be computed by comparing the time needed to reach the destination from a municipal area using the current land-based links and that corresponding to the use of a miniliner service from a location close to the origin to a location close to or at the destination.

For a microfeeder service, the travel time is retrieved as the sum of the time needed to reach a secondary airport/airfield from the considered municipal area using land-based means and the travel time of an airline flight to the hub. For an intercity service, the time needed to reach the destination from the arrival secondary airport/airfield must be added as well. In both cases, the travel time for the miniliner flight must combine the block flight time (depending on the actual length of the route considered) and the other elements that contribute to the total travel duration.

#### *2.3.2.1 Microfeeder service travel time*

In quantitative terms, for each municipality on a territory of interest, time $t^{T-H}$ to reach the hub airport using normal means of transportation is obtained by interrogating a public database. Similarly, time $t^{T-S}$ for reaching a secondary airport/airfield from the municipal area of origin is computed in the same manner. Time $t^{T-S}$ is then added to the time needed for the miniliner to reach the hub airport from the secondary base, $t^{mf}$.

The latter is clearly a function of the flight performance characteristics of an assumed aircraft, and is obtained from a set of components:

$$t^{mf} = t^{c-in} + t^{ta} + t^{to-lnd} + t^{t-in} + t^{t-out} + t^{c}, \tag{2.1}$$

where the variables on the right-hand side are (from left to right): the time durations for check-in $t^{c-in}$, aircraft turnaround $t^{ta}$, take-off and landing $t^{to-lnd}$, taxi-in $t^{t-in}$, taxi-out $t^{t-out}$, and block cruise $t^{c}$ (including climb, cruise, and descent flight phases). It is remarked that only the last term actually depends on the trip distance, while the other terms are constant.

#### *2.3.2.2 Identification of microfeeder route catchment areas*

Given the previous travel time definitions, the catchment area for a route traced between a secondary airport and a hub is defined based on the positive evaluation of the following time constraints:

$$t^{mf} + t^{T-S} \leq \frac{t^{T-H}}{k}, \tag{2.2}$$

$$\left| t^{T-H} - (t^{mf} + t^{T-S}) \right| \geq t_{ref}. \tag{2.3}$$

Eq. (2.2) represents an imposed, significative time advantage of the novel miniliner-based transport solution with respect to the usual, purely ground-based one, where $k$ is a parameter that can be defined by the analyst at will.

Eq. (2.1) further stresses this advantage, imposing a minimum difference of a duration $t_{ref}$. This can be explained for instance by considering a possibly higher fare of the miniliner solution with respect to a purely ground-based one. Adding a more significant time difference between the two services in favour of the miniliner may balance out a possible slight economical shortcoming of this solution.

An example of a catchment area defined according to the proposed method is shown in Figure 2.6 for the case with $k = 2$ and $t_{ref} = 1\ \text{hour}$.

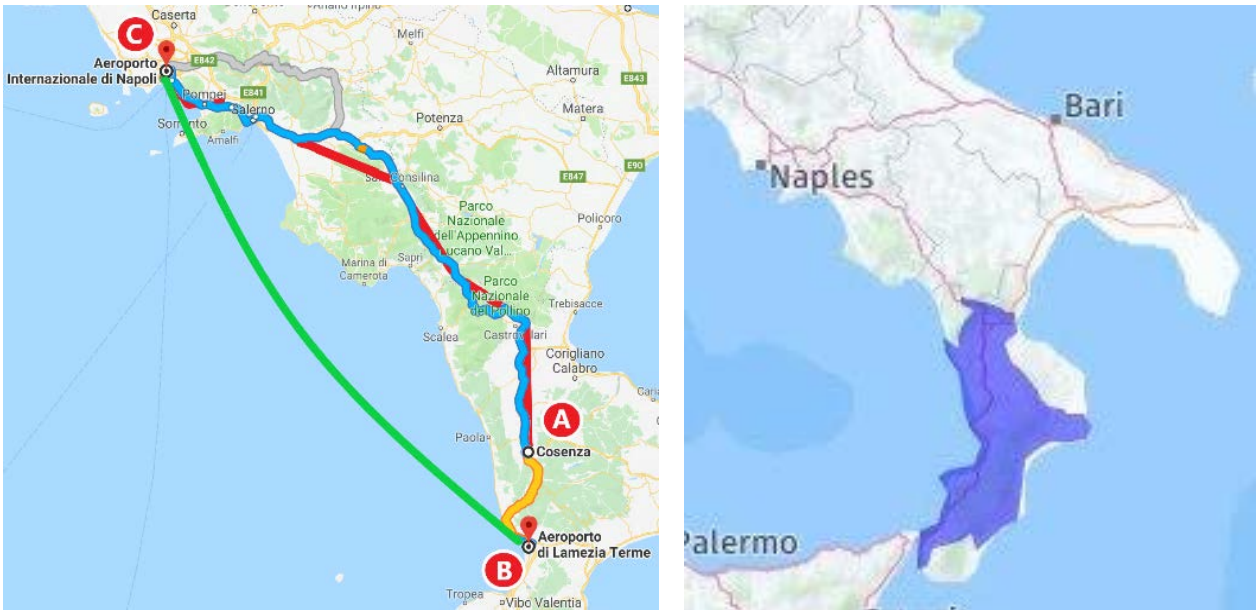


Figure 2.6: Catchment area example for the route between Lamezia Terme and Naples, in Italy.

The considered travel alternatives can be seen on the left part of Figure 2.6: location A is a municipality (Cosenza) close to the secondary airport in Lamezia Terme (IATA: SUF, ICAO: LICA) denoted with B, while C is the destination Naples International Airport (IATA: NAP, ICAO: LIRN). The blue path represents the travel between A and C by car, yielding a travel time $t_1^{T-H}$. The red path represents the travel between A and C by train, yielding a travel time $t_2^{T-H}$. The yellow path represents the travel between A and B by car, yielding a travel time $t^{T-S}$. Finally, the green path represents the travel between B and C by the miniliner flight, yielding a block cruise time $t^c$, which contributes to the total microfeeding travel time $t^{mf}$.

The catchment area for the route from B to C is depicted in the right part of Figure 2.6, which shows the territory of all origins for which it is more convenient to use the miniliner from Lamezia Terme to reach Naples International Airport than land-transportation means.

#### *2.3.2.3 Origin and infrastructure pre-selection*

It should be noted that the comparison between the two mentioned travel solutions to reach a hub airport, even though not involving any optimization, is a computationally intensive problem by itself. For this reason, and for easing the optimization problem to follow by reducing the number of candidate secondary bases (and consequently of the connection routes between secondary bases and hubs), it is recommendable to pre-process the database as follows.

A first simplification is represented by neglecting the municipal areas with a population not reaching a given threshold. Especially in regions where towns are geographically scattered, the demand not computed (lost) due to smaller towns far from secondary airports should not be significant.

A second simplification is obtained by clustering secondary airports/airfields together. This can be carried out based on a criterion of geographical proximity, and besides easing the optimization phase, it avoids the unrealistic scenario where two secondary bases very close to each other are both included in the network, feeding the same hub from origins that are just too close to one another (parallel routes).

### 2.3.3 Microfeeder potential demand estimation algorithm

#### *2.3.3.1 Route function*

The application of Eqs. (2.2) and (2.3) to all considered municipal areas, airport clusters and hubs allows defining a number of connections between hubs and secondary clusters, representing a potential traffic demand. This can be expressed in terms of the total number of passengers $P_i$ with an advantage in reaching the $i$-th hub via the miniliner service.

However, this datum, based only on demography, may be too little sensitive to the potential interest to travel of the local population. A second factor is thus considered besides demography (population distribution), namely the local distribution of the national gross domestic product (GDP). Therefore, considering the pair represented by the $i$-th hub and the $j$-th secondary cluster, the corresponding route is associated to a demographic level $D_{ij}$, bound to the population size, and to an economic index $GDP_{ij}$, representing the will/need to travel of the population associated to the route.

Based on these parameters, it is possible to define the route value function $F_s(i,j)$ as

$$F_s(i,j) = \alpha \frac{D_{ij} - \min_{j\in H} D_{ij}}{\max_{j\in H} D_{ij} - \min_{j\in H} D_{ij}} + (1-\alpha)\frac{GDP_{ij} - \min_{j\in H} GDP_{ij}}{\max_{j\in H} GDP_{ij} - \min_{j\in H} GDP_{ij}} \tag{2.4}$$

where $H$ represents the group of all hubs, and $\alpha$ is a tuning parameter defining the relative relevance of the economical or travel need aspect, with respect to a purely demographic datum.

#### *2.3.3.1.1 Hub feeding demand*

The analysis of the traffic potential of the connection routes must match with the actual feeding needs of the hubs. This can be quantified through the variables $P_i^{arr}$ and $P_i^{dep}$, retrieved from publicly available databases and representing the number of passengers arriving and departing hourly from the $i$-th hub, respectively.

In order to obtain a match between the actual airport needs and the potential traffic quota pertaining to each route connecting the $i$-th hub with secondary clusters, the following algorithm has been proposed.

The values $P_i^{arr}$ and $P_i^{dep}$ are normalized by the population corresponding of the area connected with the considered hub, $N$, generating the following indices:

$$O_i = \frac{P_i^{arr}}{N} \tag{2.5}$$

$$D_i = \frac{P_i^{dep}}{N} \tag{2.6}$$

where the values of $O_i$ and $D_i$ represent the hourly number of passengers generated and attracted by the $i$-th hub, respectively.

Next, the route value functions for all hub-secondary airport/cluster pairs are normalized with respect the sum over the number of secondary airports/clusters, yielding

$$\varphi(i,j) = \frac{F_s(i,j)}{\sum_{j \in S} F_s\,(i,j)} \tag{2.7}$$

where $S$ represents the group of secondary airports/clusters.

Finally, the hourly rate of generated (input) traffic on the routes from all hubs to a secondary airport/cluster is defined as

$$o_j = \sum_{i \in H} \varphi(j,i)\; D_i \tag{2.8}$$

whereas the hourly traffic rate input on the route from the $j$-th secondary airport/cluster to the hubs is defined as

$$d_j = \sum_{i \in H} \varphi(i,j)\; O_i \tag{2.9}$$

For clarity, the potential hourly demand of the route from the $i$-th hub to the $j$-th secondary airport/cluster appears in Eq. (2.8) as $G_{ji} = \varphi(j,i)\, D_i$, whereas the dual value is $g_{ij} = \varphi(i,j)\, O_i$, appearing in Eq. (2.9).

Both $g_{ij}$ and $G_{ji}$ are potential traffic demand parameters. Based on airport records, these are usually a function of the time in the day, as airport passenger flow in hubs typically features traffic peaks.

## *2.4 Potential demand estimation studies*

The methodology described above has been applied to the study of a number of cases, in order to verify its capabilities to provide useful data for market studies. In particular, three cases are presented in the following, all related to a possible microfeeder service for a single-hub operated by a 19-passenger aircraft.

The three cases have been chosen as representative examples of the different situations encountered across the European countries when looking at their ground transportation efficiency. Therefore, one case per each of the subsets identified in Section 0 was considered:

1. High ground transportation efficiency: Brussels (Belgium).
2. Medium ground transportation efficiency: Venice (Italy).
3. Low ground transportation efficiency: Riga (Latvia).

### 2.4.1 General setup

In order to derive useful information on the effect of some of the miniliner design top-level requirements (TLAR) on the demand-capturing capability of a microfeeder service, parametric studies have been performed, considering a range in the design values of the following performance parameters:

a. Trip distance: considered values for range are from 100 to 300 km with 50 km step increments (5 cases).
b. Cruising speed: considered values for cruising speed are 200±50 KTAS (3 cases).
c. Take-off and landing distances: considered values are 800±200 m (3 cases).

It is remarked that the trip distance is not to be intended as the design range of the miniliner, which is roughly estimated no less than 500 km for the time being, allowing the possible execution of multiple trips without refueling.

Cruising altitude is typically 4,000 ft. This is possibly reduced in case the trip is so short that the climb phase ends before reaching cruise altitude.

Other mission profile parameters include optimal climb at a rate of climb of 500 ft/min and descent at cruising airspeed at a rate of descent of 250 ft/min.

The size threshold for towns to be considered in the analysis is 20,000 inhabitants.

The total time corresponding to the difference $(t^{mf} - t^{c})$, i.e. the constant part of the total travel time including check-in, release, and ground procedures, is set at 40 min.

Finally, the parameters defining the time advantage in the constraint equations (2.2)(2.3) and (2.3) are set as $k = 3$ and $t_{ref} = 30\ \mathrm{min}$.

### 2.4.2 Case 1: Brussels (EBBR)

In this case, the hub for the microfeeder service has been chosen as Brussels Zaventem Airport (IATA: BRU, ICAO: EBBR), which lies in the European country, Belgium, with the highest ground efficiency index, and therefore, the highest possible competition with a miniliner service.

In this case, given the geographical position of the hub, the neighboring countries of Netherlands, Luxembourg, Germany (all in the high ground transportation efficiency subset), and France (a medium ground transportation efficiency country) have been included in the analysis.

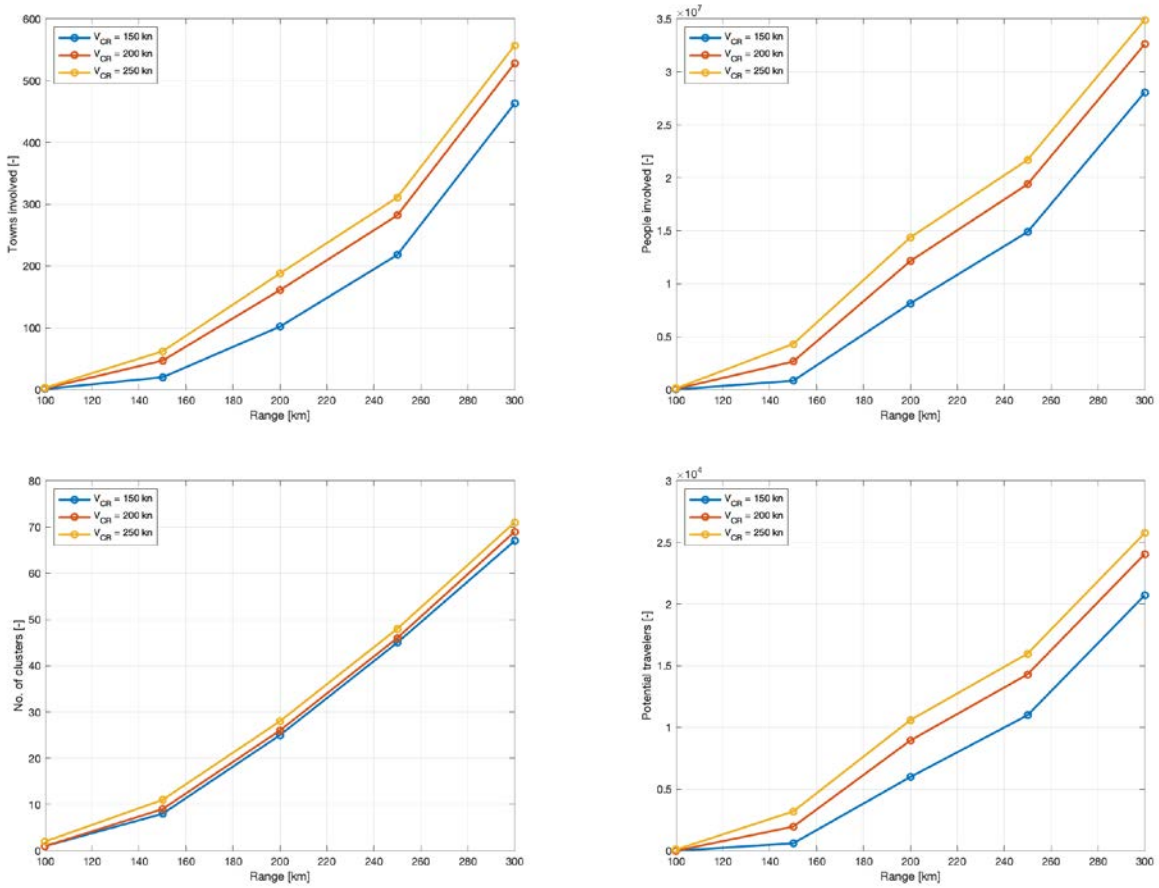


**Figure 2.7: Potential demand estimation results for a microfeeder service to EBBR in the case of 600 m long runways for secondary airports (top left: towns involved, top right: number of citizens in such towns, bottom left: number of secondary airports involved, bottom right: potential passenger demand).**

The graphs in Figure 2.7 refer to the case of selecting a maximum take-off and landing distance of 600 m (a markedly STOL case). The graphs show the behavior of the number of towns involved, the number of citizens in such towns, the number of secondary airports in the network, and the potential demand associated to the routes

of such network. All quantities are displayed as functions of the range and parameterized with cruising speed.

It is apparent that the potential demand that may be captured has a higher-than-linear rise with the increase of maximum trip distance, while the increase is significant, but less marked, in dependence of cruising speed. Also, as a result of the high efficiency of ground transportation in the regions surrounding the hub under scrutiny, the lower values for the trip distance provide very poor results (null for 100 km), since the miniliner service cannot compete with alternative land-based travel means. It is also noted that the number of secondary airports involved is not very sensitive to cruising speed.

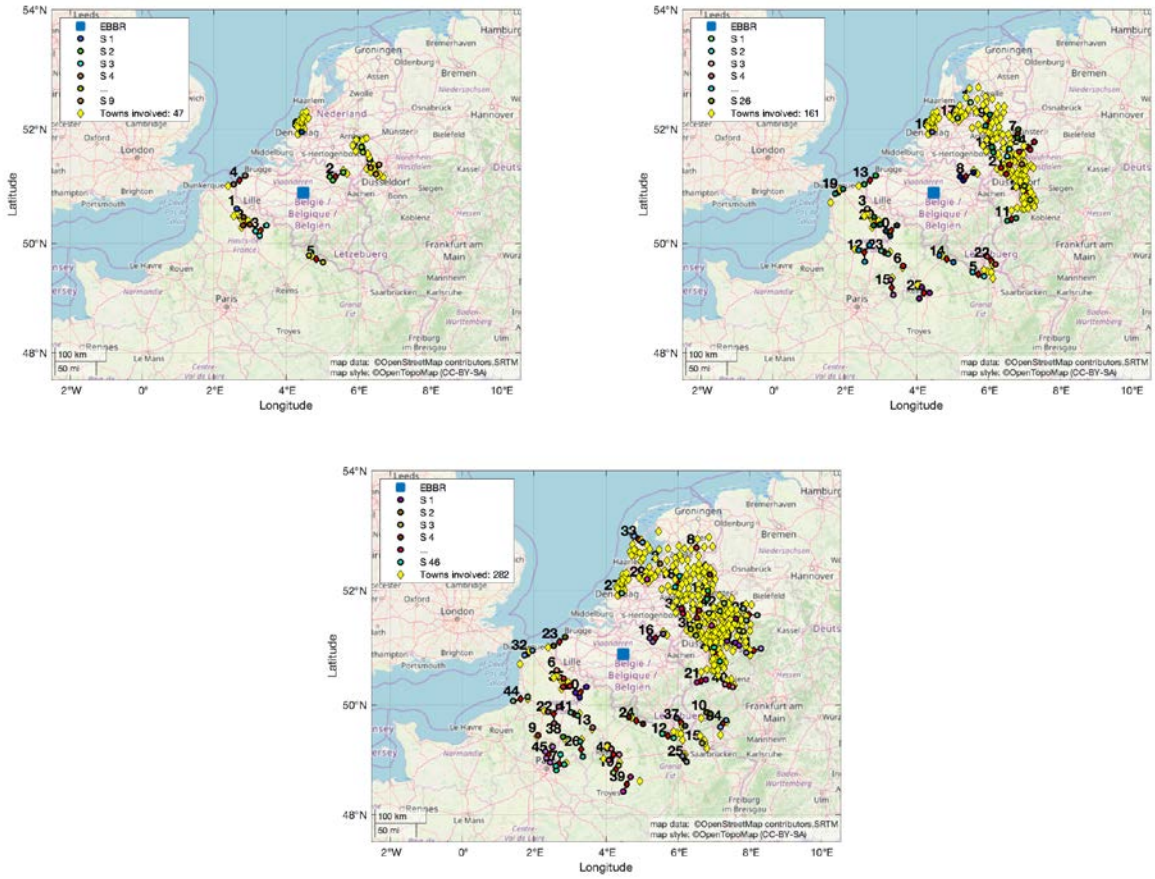


**Figure 2.8: Distribution of towns and secondary airports involved in a microfeeder service to EBBR in the case of 600 m long runways for secondary airports and a cruising speed of 200 KEAS (top left: maximum trip distance of 150 km, top right: maximum trip distance of 200 km, bottom: maximum trip distance of 250 km).**

For the same case of picking secondary airports with 600 m long runways or more, Figure 2.8 shows the changes in the number and location of the towns and secondary airports involved when increasing the maximum trip distance from 150 to 200 and to

250 km. It is apparent that more and more towns in neighboring countries get involved in the service.

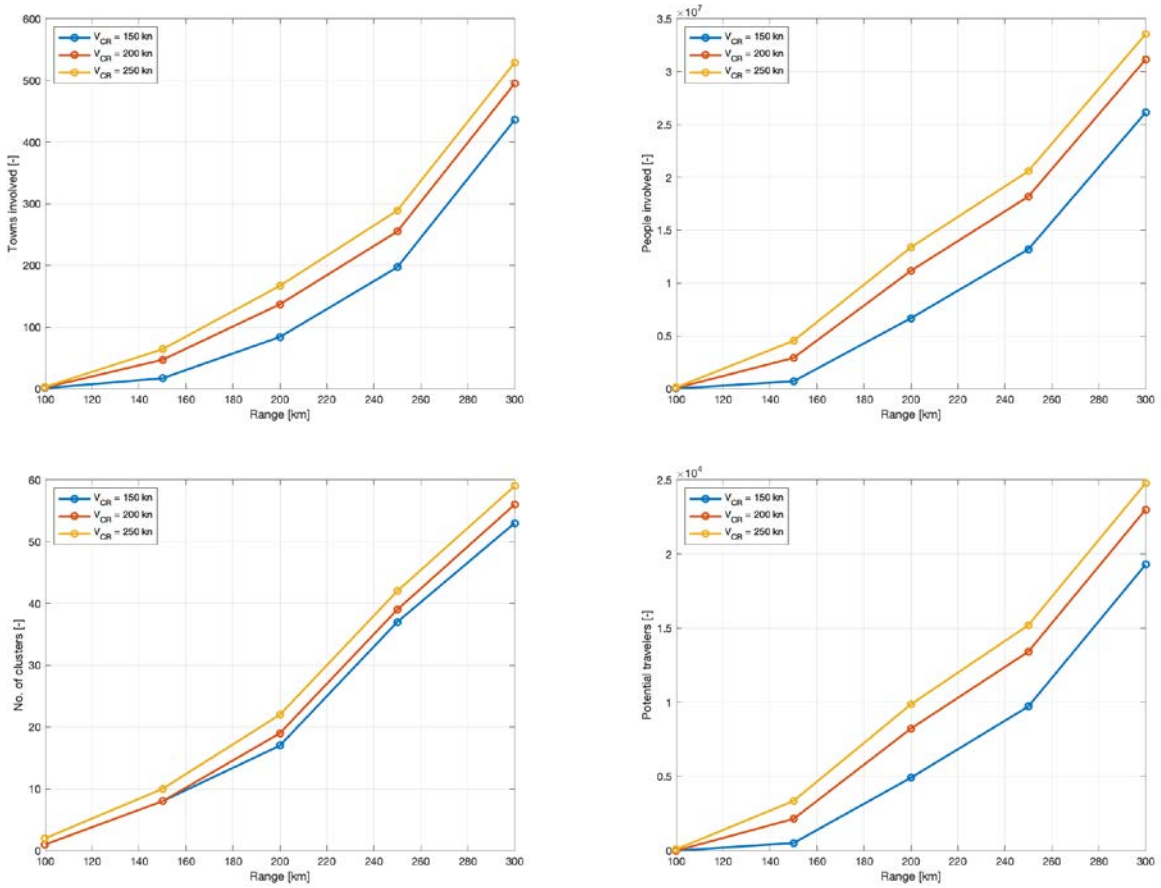


**Figure 2.9: Potential demand estimation results for a microfeeder service to EBBR in the case of 800 m long runways for secondary airports (top left: towns involved, top right: number of citizens in such towns, bottom left: number of secondary airports involved, bottom right: potential passenger demand).**

The graphs in Figure 2.9 refer to the case of selecting a maximum take-off and landing distance of 800 m (a less-marked STOL case). The graphs are analogous to those seen in Figure 2.7. Similar trends are observed, with a higher-than-linear rise of the potential demand with the increase of maximum trip distance.

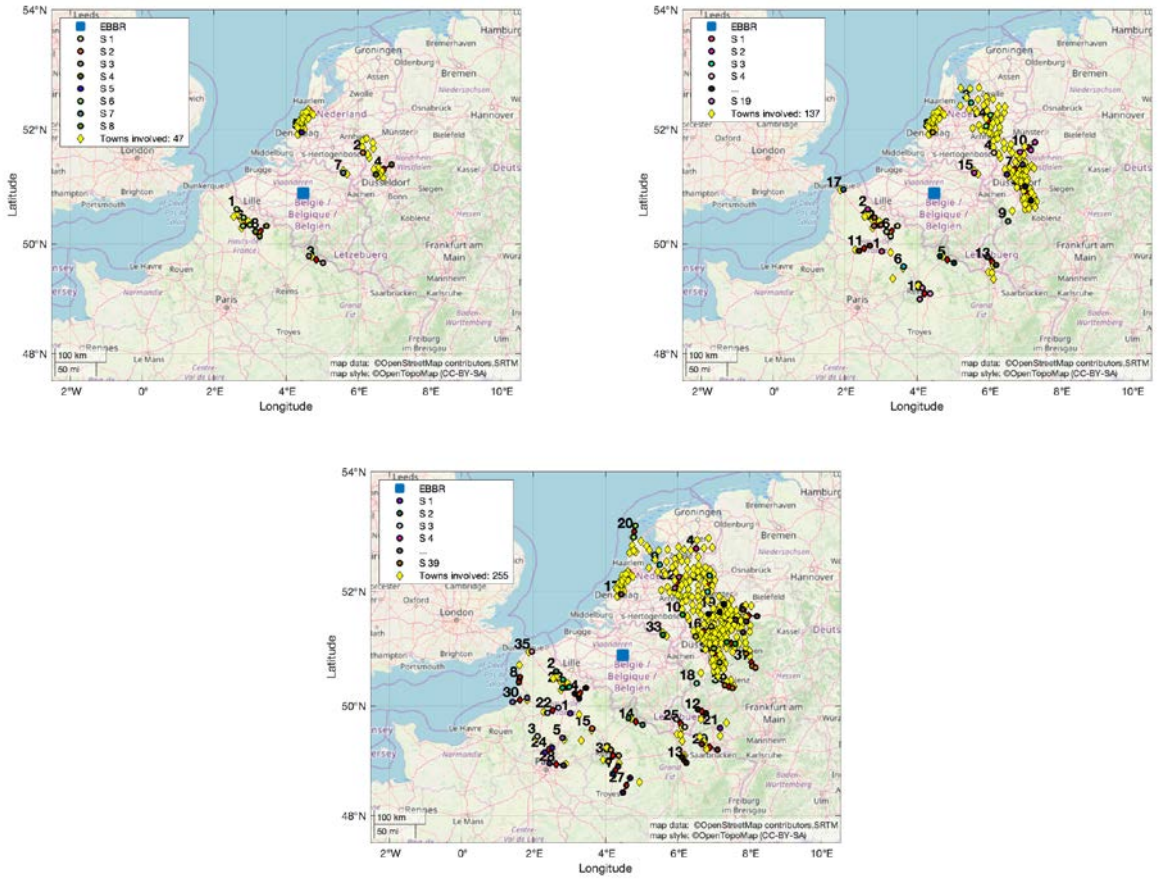


Figure 2.10: Distribution of towns and secondary airports involved in a microfeeder service to EBBR in the case of 800 m long runways for secondary airports and a cruising speed of 200 KEAS (top left: maximum trip distance of 150 km, top right: maximum trip distance of 200 km, bottom: maximum trip distance of 250 km).

For the same case of picking secondary airports with 800 m long runways or more, Figure 2.10 shows the changes in the number and location of the towns and secondary airports involved when increasing the maximum trip distance from 150 to 200 and to 250 km. Again, it is apparent that more and more towns in neighboring countries get involved in the service, although with respect to the previous case there is a slight reduction in the number of these elements as well as in the potential demand, due to the fact that some secondary airports included before have been left out as a result of the lower takeoff and landing performance.

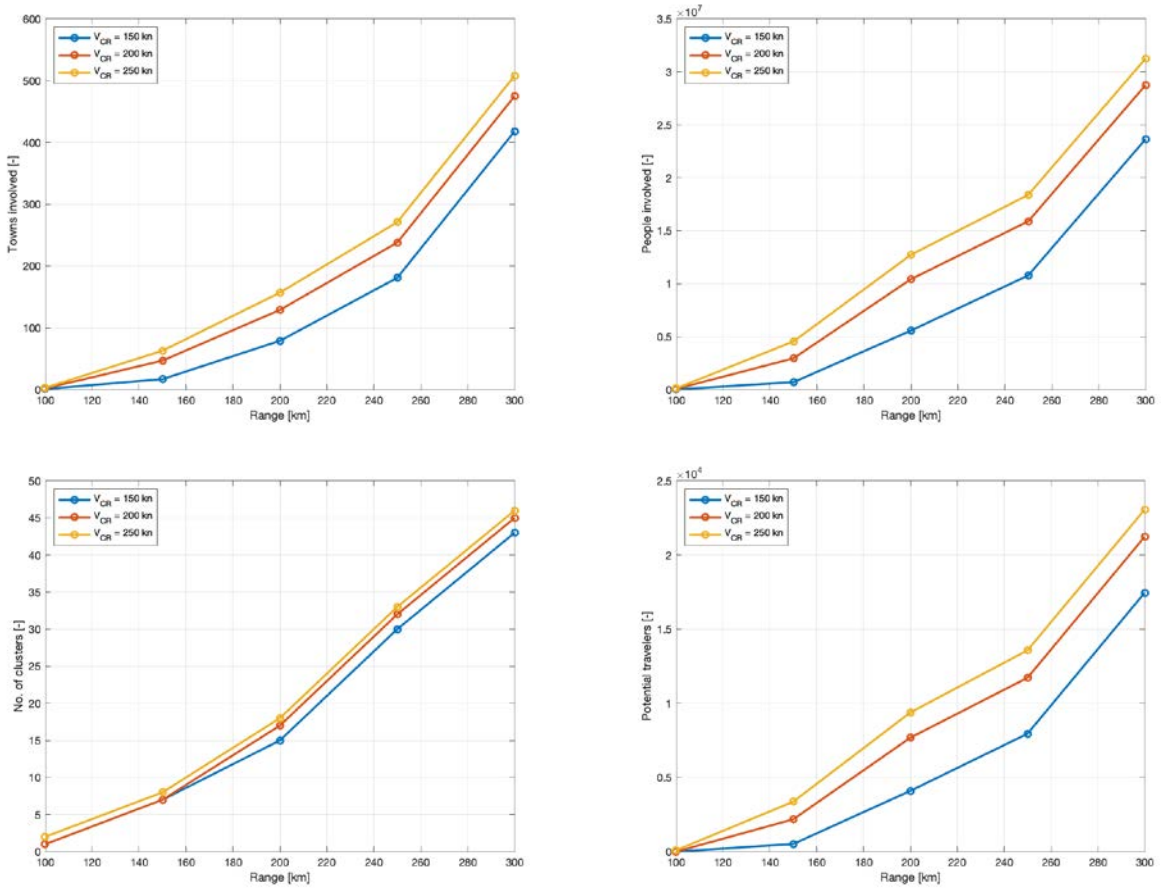


**Figure 2.11: Potential demand estimation results for a microfeeder service to EBBR in the case of 1,000 m long runways for secondary airports (top left: towns involved, top right: number of citizens in such towns, bottom left: number of secondary airports involved, bottom right: potential passenger demand).**

The graphs in Figure 2.11 refer to the case of selecting a maximum take-off and landing distance of 1,000 m. The graphs are analogous to those seen in the previous figures, with more or less similar trends. However, the reduction in the potential demand is pretty marked, potentially rising to about 11.5%, as the relatively poor takeoff and landing performance now entails the inclusion of a maximum of 48 secondary airports (against a maximum of 71 in the 600 m case).

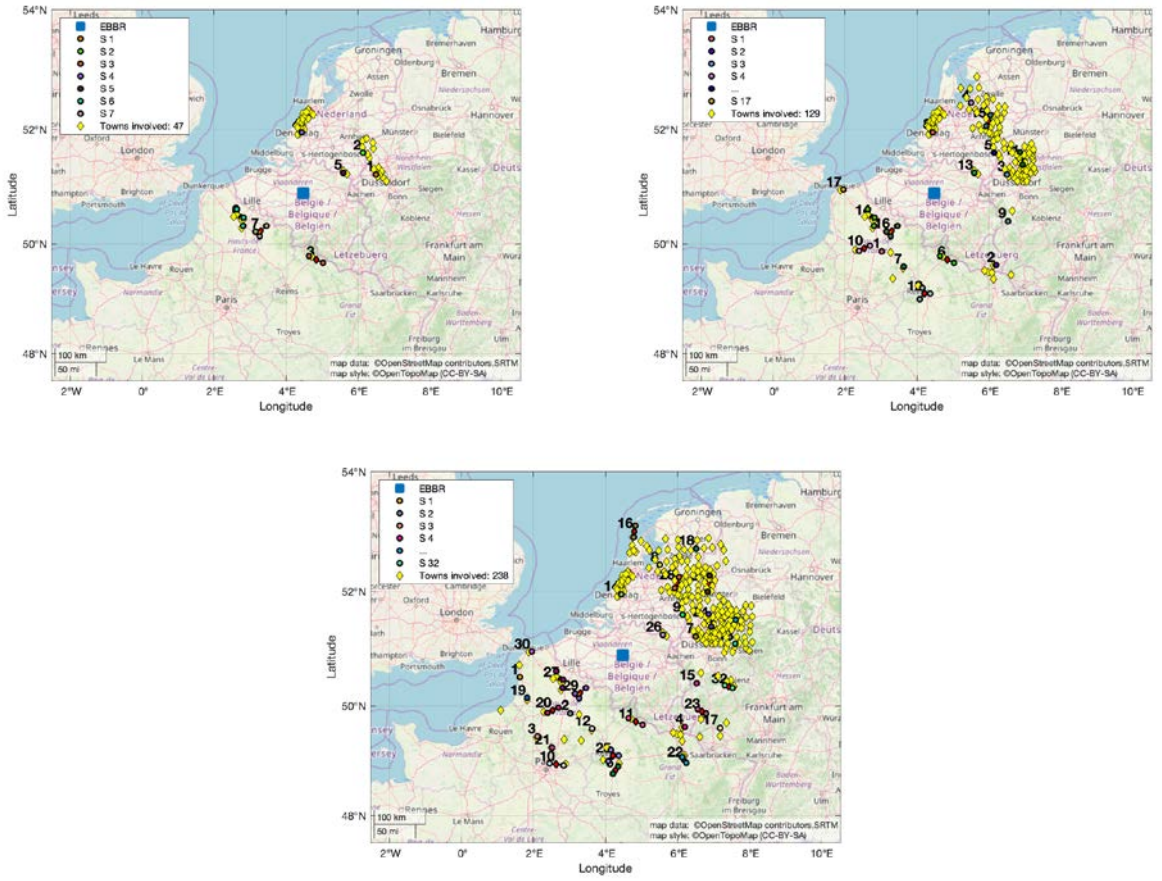


**Figure 2.12: Distribution of towns and secondary airports involved in a microfeeder service to EBBR in the case of 1,000 m long runways for secondary airports and a cruising speed of 200 KEAS (top left: maximum trip distance of 150 km, top right: maximum trip distance of 200 km, bottom: maximum trip distance of 250 km).**

For the same case of picking secondary airports with 1,000 m long runways or more, Figure 2.12 shows the changes in the number and location of the towns and secondary airports involved when increasing the maximum trip distance from 150 to 200 and to 250 km. The marked reduction in the number of secondary airports due to runway length requirements is apparent.

### 2.4.3 Case 2: Venice (LIPZ)

In this case, the hub for the microfeeder service has been chosen as Venice Marco Polo Airport (IATA: VCE, ICAO: LIPZ), which lies in a European country, Italy, with a medium ground efficiency index.

In this case, given the geographical position of the hub, the neighboring countries of Slovenia, Croatia, Austria (all in the medium ground transportation efficiency subset), and even Germany (a high ground transportation efficiency country) have been included in the analysis.

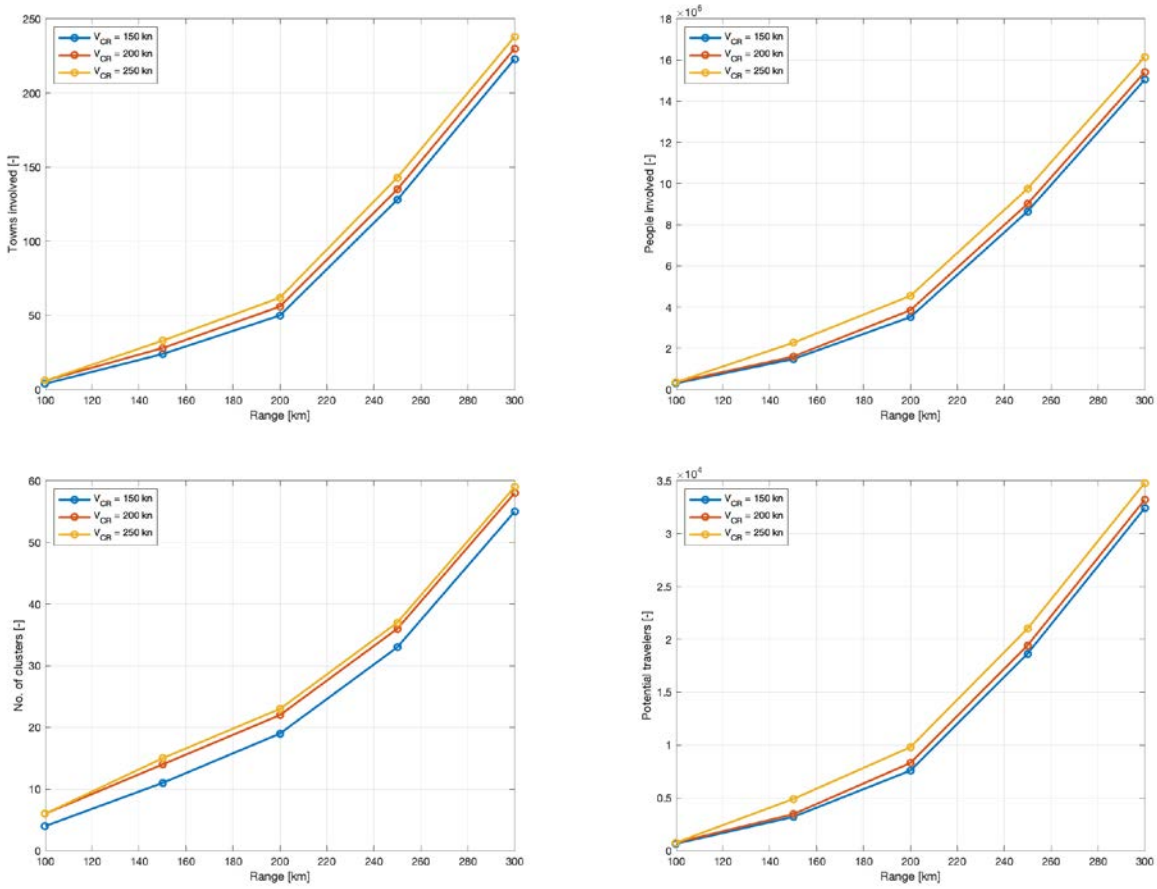


**Figure 2.13: Potential demand estimation results for a microfeeder service to LIPZ in the case of 600 m long runways for secondary airports (top left: towns involved, top right: number of citizens in such towns, bottom left: number of secondary airports involved, bottom right: potential passenger demand).**

The graphs in Figure 2.13 refer to the case of selecting a maximum take-off and landing distance of 600 m. The graphs are analogous to those seen in the EBBR case.

Also in this case, the potential demand that may be captured has a higher-than-linear rise with the increase of maximum trip distance, while the increase is now more marked in dependence of cruising speed. Also, even in the presence of a medium efficiency of ground transportation in the regions surrounding the hub under scrutiny,

the lower values for the trip distance provide very poor results (almost null for 100 km). With respect to EBBR, the present LIPZ case shows the possibility to capture a significantly higher potential demand (up to 35,000 potential passengers against 26,000) with more or less the same amount of secondary airports activated (59 instead of 61).

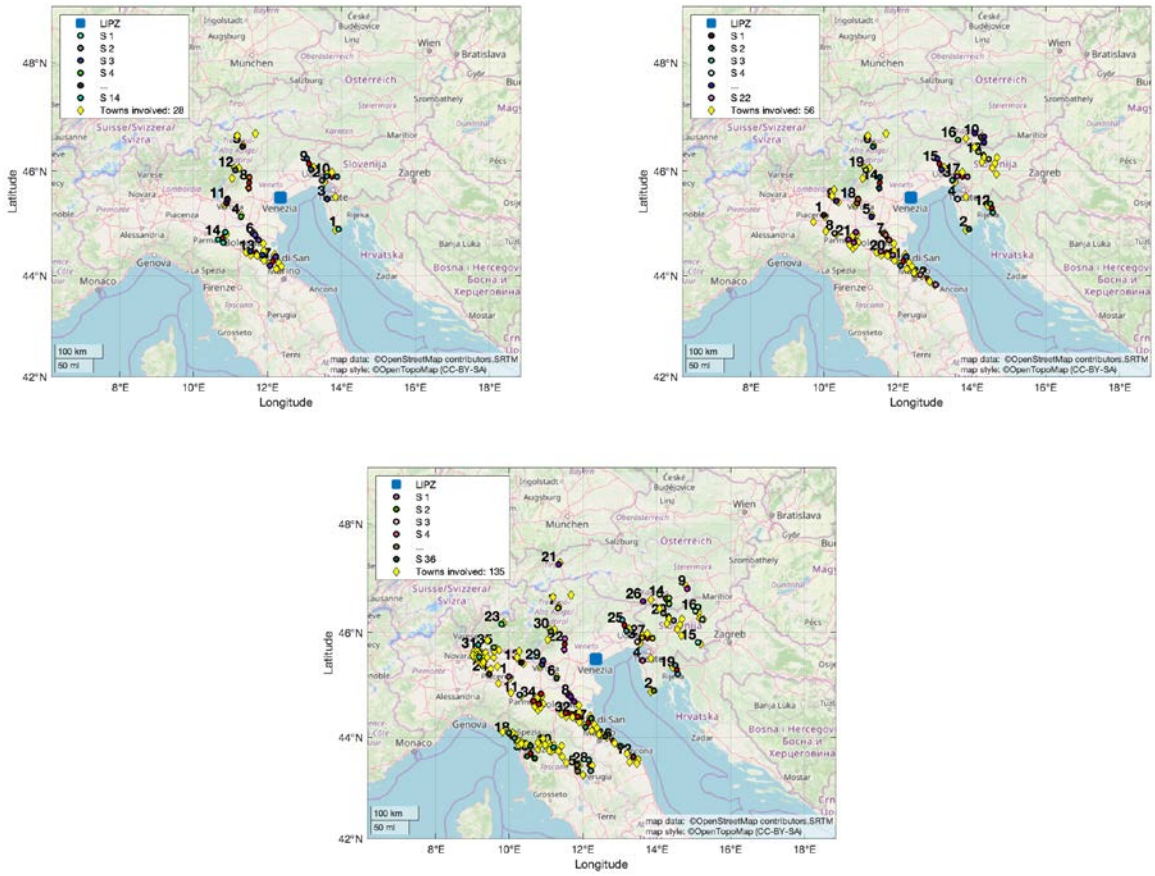


**Figure 2.14: Distribution of towns and secondary airports involved in a microfeeder service to LIPZ in the case of 600 m long runways for secondary airports and a cruising speed of 200 KEAS (top left: maximum trip distance of 150 km, top right: maximum trip distance of 200 km, bottom: maximum trip distance of 250 km).**

For the same case of picking secondary airports with 600 m long runways or more, Figure 2.14 shows the changes in the number and location of the towns and secondary airports involved when increasing the maximum trip distance from 150 to 200 and to 250 km. Again, it is apparent that more and more towns in neighboring countries get involved in the service.

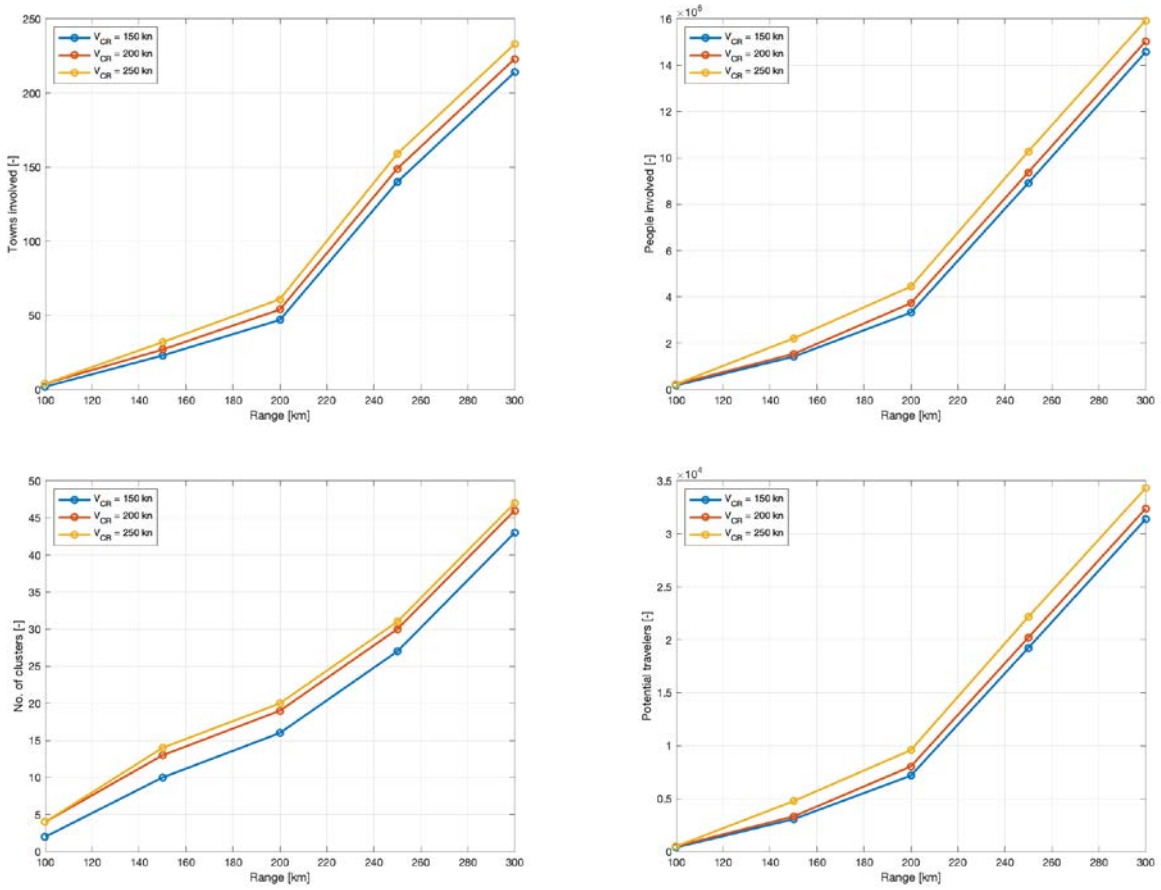


Figure 2.15: Potential demand estimation results for a microfeeder service to LIPZ in the case of 800 m long runways for secondary airports (top left: towns involved, top right: number of citizens in such towns, bottom left: number of secondary airports involved, bottom right: potential passenger demand).

The graphs in Figure 2.15 refer to the case of selecting a maximum take-off and landing distance of 800 m. The graphs show similar trends, but with a higher-than-linear rise flattening towards a linear one for higher trip distances. The resulting values for the potential demand do not show significant changes with respect to the 600 m long runway case. The benefits of an increased cruising speed are also visible.

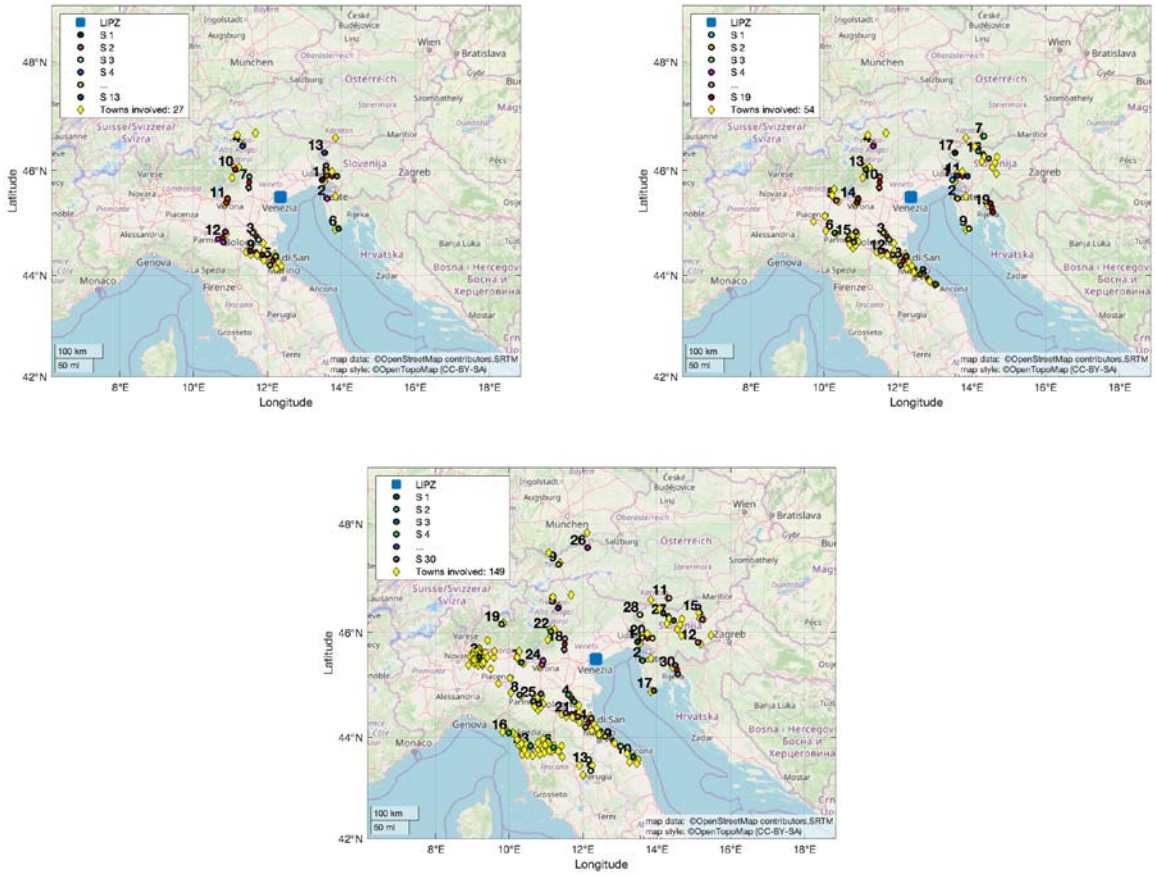


Figure 2.16: Distribution of towns and secondary airports involved in a microfeeder service to LIPZ in the case of 800 m long runways for secondary airports and a cruising speed of 200 KEAS (top left: maximum trip distance of 150 km, top right: maximum trip distance of 200 km, bottom: maximum trip distance of 250 km).

For the same case of picking secondary airports with 800 m long runways or more, Figure 2.16 shows the changes in the number and location of the towns and secondary airports involved when increasing the maximum trip distance from 150 to 200 and to 250 km. Again, it is apparent that more and more towns in neighboring countries get involved in the service. Only the case for the higher cruising speed shows a significant reduction in activated secondary airports with respect to the 600 m long runway case.

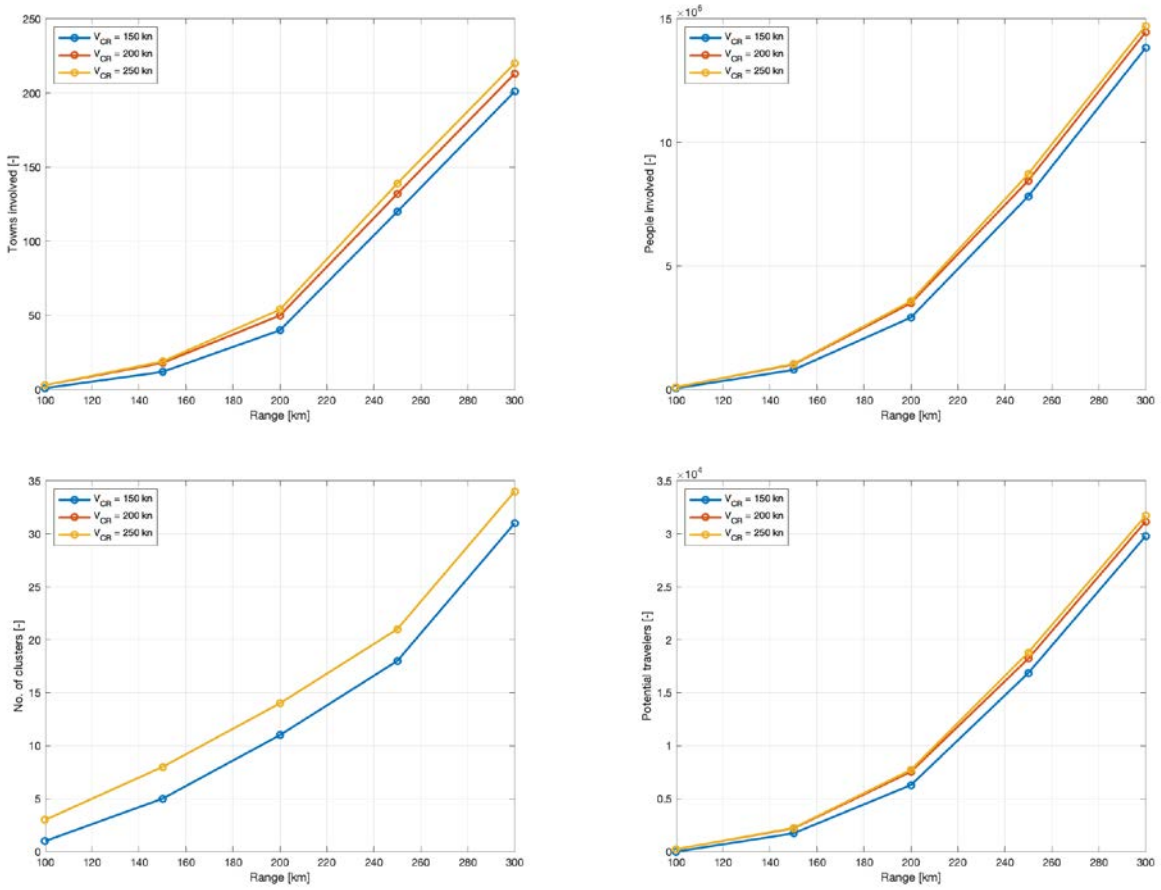


Figure 2.17: Potential demand estimation results for a microfeeder service to LIPZ in the case of 1,000 m long runways for secondary airports (top left: towns involved, top right: number of citizens in such towns, bottom left: number of secondary airports involved, bottom right: potential passenger demand).

The graphs in Figure 2.17 refer to the case of selecting a maximum take-off and landing distance of 1,000 m. The graphs are analogous to those seen in the previous figures, with more or less similar trends, but now the benefits of increasing the cruising airspeed from 200 to 250 KTAS appear very scarce, as the number of airports activated in the two cases is exactly the same. Compared to the EBBR case, the reduction in the potential demand with the rising in runway length appears of the same order, reaching a maximum of 8.5%, with a corresponding reduction of the maximum number of activated secondary airports from 59 to 34, corresponding to 600 and 1,000 m runway length, respectively.

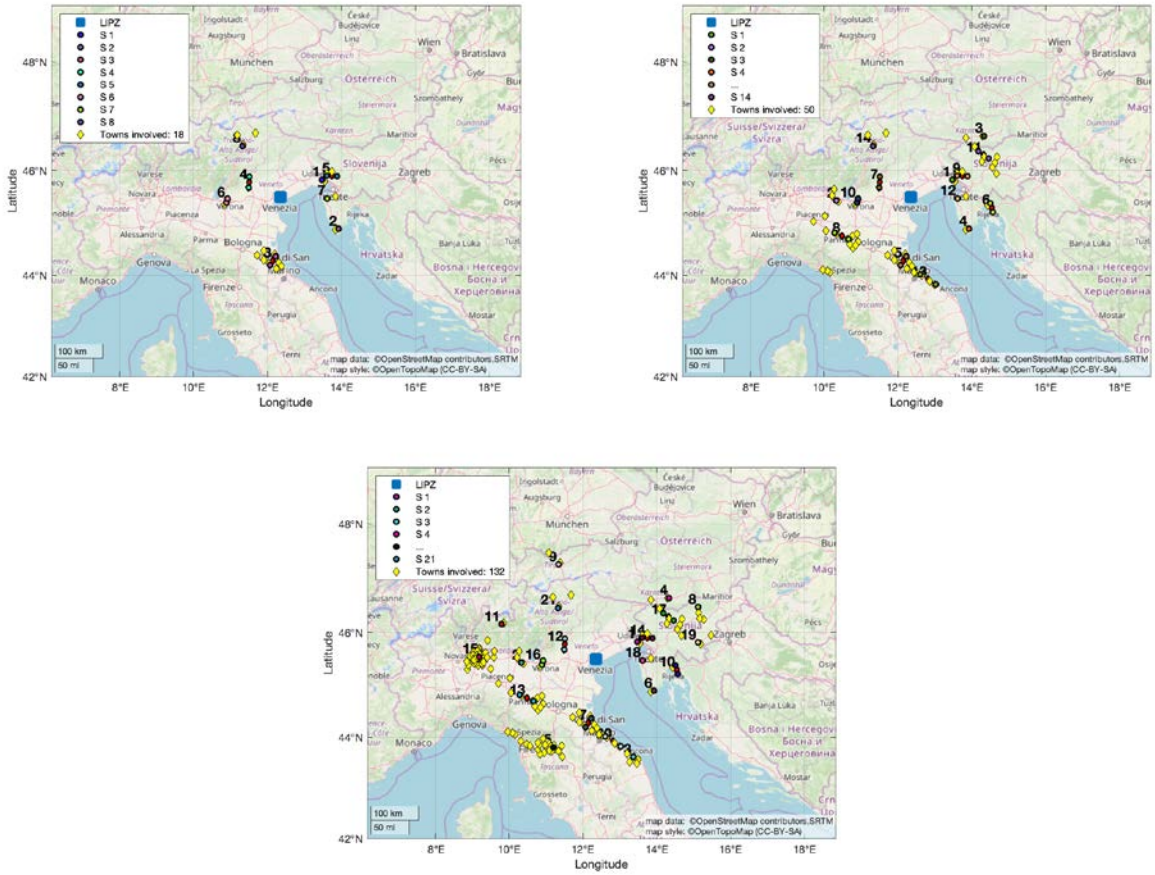


Figure 2.18: Distribution of towns and secondary airports involved in a microfeeder service to LIPZ in the case of 1,000 m long runways for secondary airports and a cruising speed of 200 KEAS (top left: maximum trip distance of 150 km, top right: maximum trip distance of 200 km, bottom: maximum trip distance of 250 km).

For the same case of picking secondary airports with 1,000 m long runways or more, Figure 2.18 shows the changes in the number and location of the towns and secondary airports involved when increasing the maximum trip distance from 150 to 200 and to 250 km. The marked reduction in the number of secondary airports due to runway length requirements is apparent.

### 2.4.4 Case 3: Riga (EVRA)

In this case, the hub for the microfeeder service has been chosen as Riga International Airport (IATA: RIX, ICAO: EVRA), which lies in a European country, Latvia, with a very low ground efficiency index, and therefore, a high possible interest a miniliner service.

In this case, given the geographical position of the hub, the neighboring countries of Estonia and Lithuania (both in the low ground transportation efficiency subset have been included in the analysis.

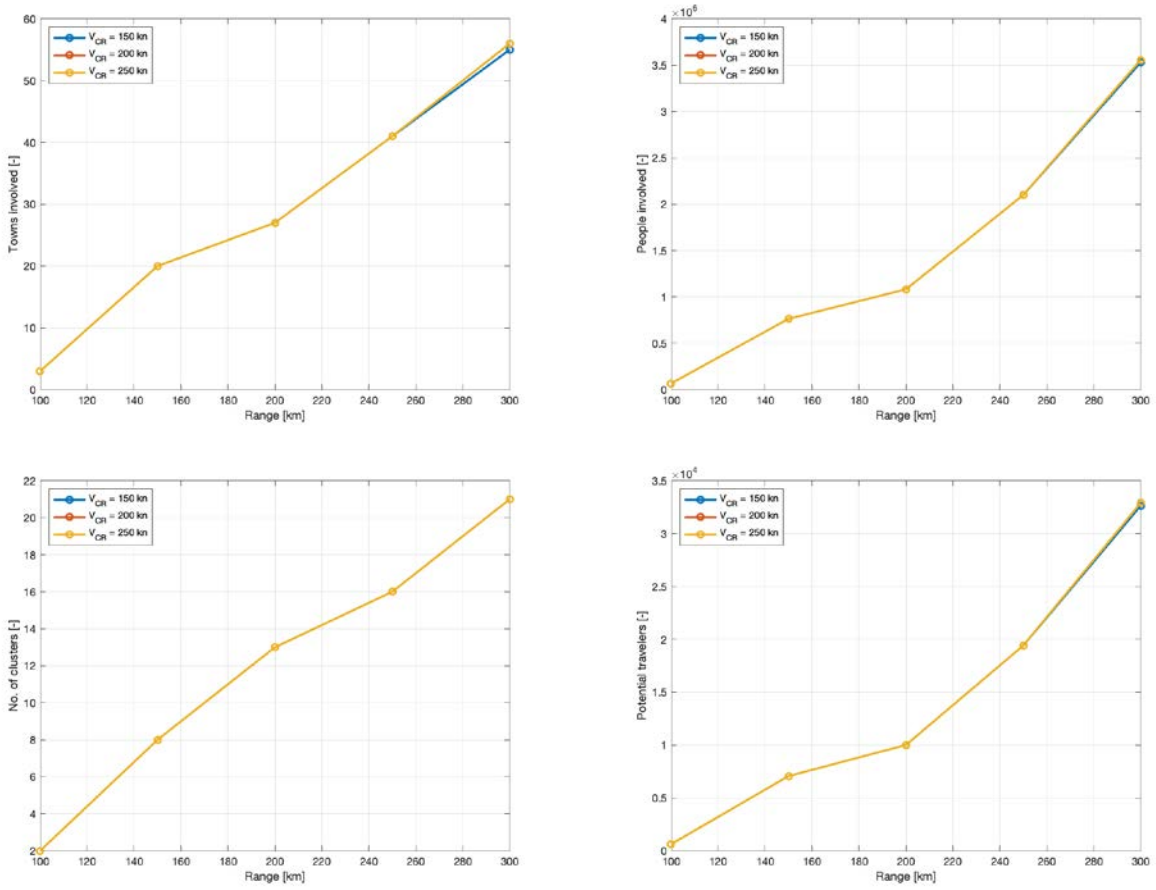


**Figure 2.19: Potential demand estimation results for a microfeeder service to EVRA in the case of 600 m long runways for secondary airports (top left: towns involved, top right: number of citizens in such towns, bottom left: number of secondary airports involved, bottom right: potential passenger demand).**

The graphs in Figure 2.19 refer to the case of selecting a maximum take-off and landing distance of 600 m. The graphs are analogous to those seen in the EBBR and LIPZ cases.

Two differences are observed with respect to the cases previously examined. First, the rise in the potential demand that may be captured, as well as the other quantities of interest, looks roughly linear rise with the increase of maximum trip distance. Second, all results look completely insensitive to the value of cruising speed. This is clearly

related to the low efficiency of ground transportation in the regions surrounding the hub under scrutiny, together with the relative sparsity of towns reaching the threshold size. The values or the potential demand are comparably higher with respect to the EBBR and LIPZ cases at medium values of the trip distance, and approximately the same at the higher distance, with much less secondary airports activated.

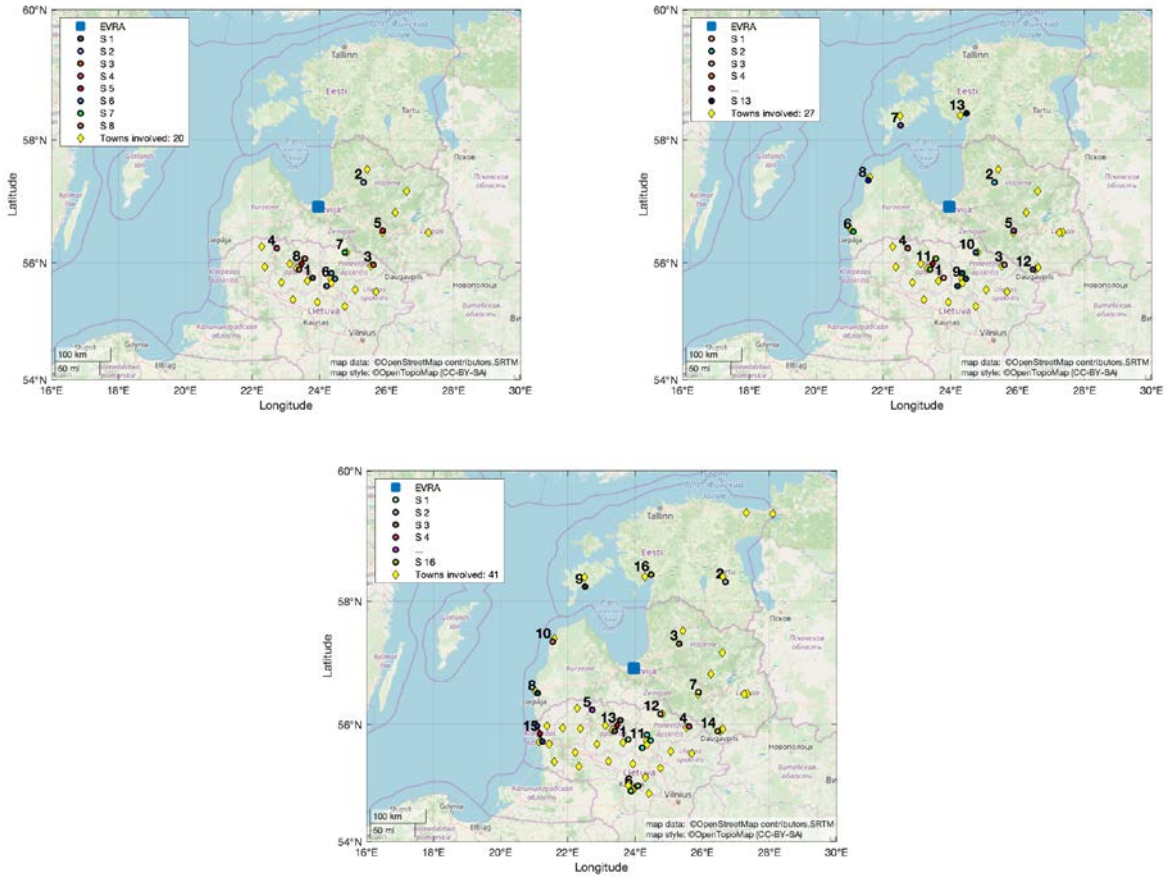


**Figure 2.20: Distribution of towns and secondary airports involved in a microfeeder service to EVRA in the case of 600 m long runways for secondary airports and a cruising speed of 200 KEAS (top left: maximum trip distance of 150 km, top right: maximum trip distance of 200 km, bottom: maximum trip distance of 250 km).**

For the same case of picking secondary airports with 600 m long runways or more, Figure 2.20 shows the changes in the number and location of the towns and secondary airports involved when increasing the maximum trip distance from 150 to 200 and to 250 km. Again, it is apparent that more and more towns in neighboring countries get involved in the service.

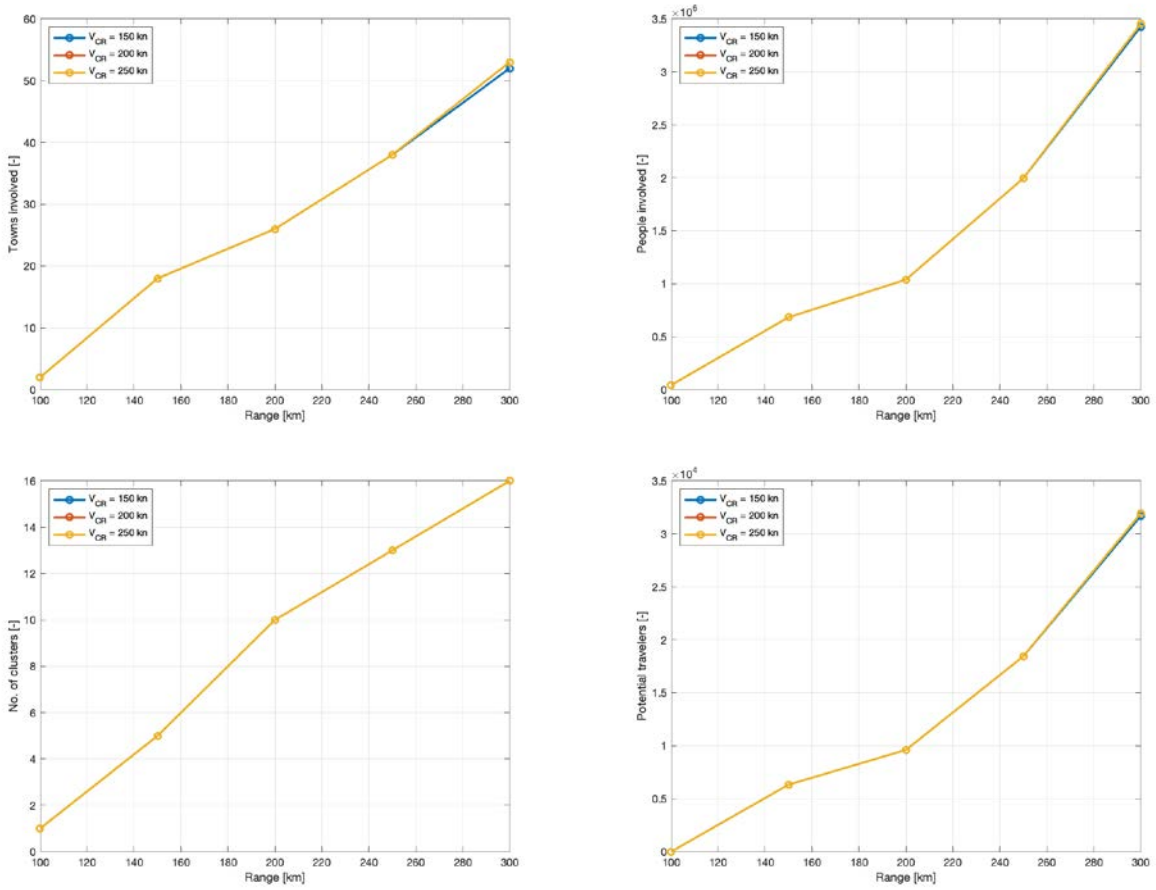


Figure 2.21: Potential demand estimation results for a microfeeder service to EVRA in the case of 800 m long runways for secondary airports (top left: towns involved, top right: number of citizens in such towns, bottom left: number of secondary airports involved, bottom right: potential passenger demand).

The graphs in Figure 2.21 refer to the case of selecting a maximum take-off and landing distance of 800 m. The graphs confirm the previous trends, with a slight reduction in the potential demand.

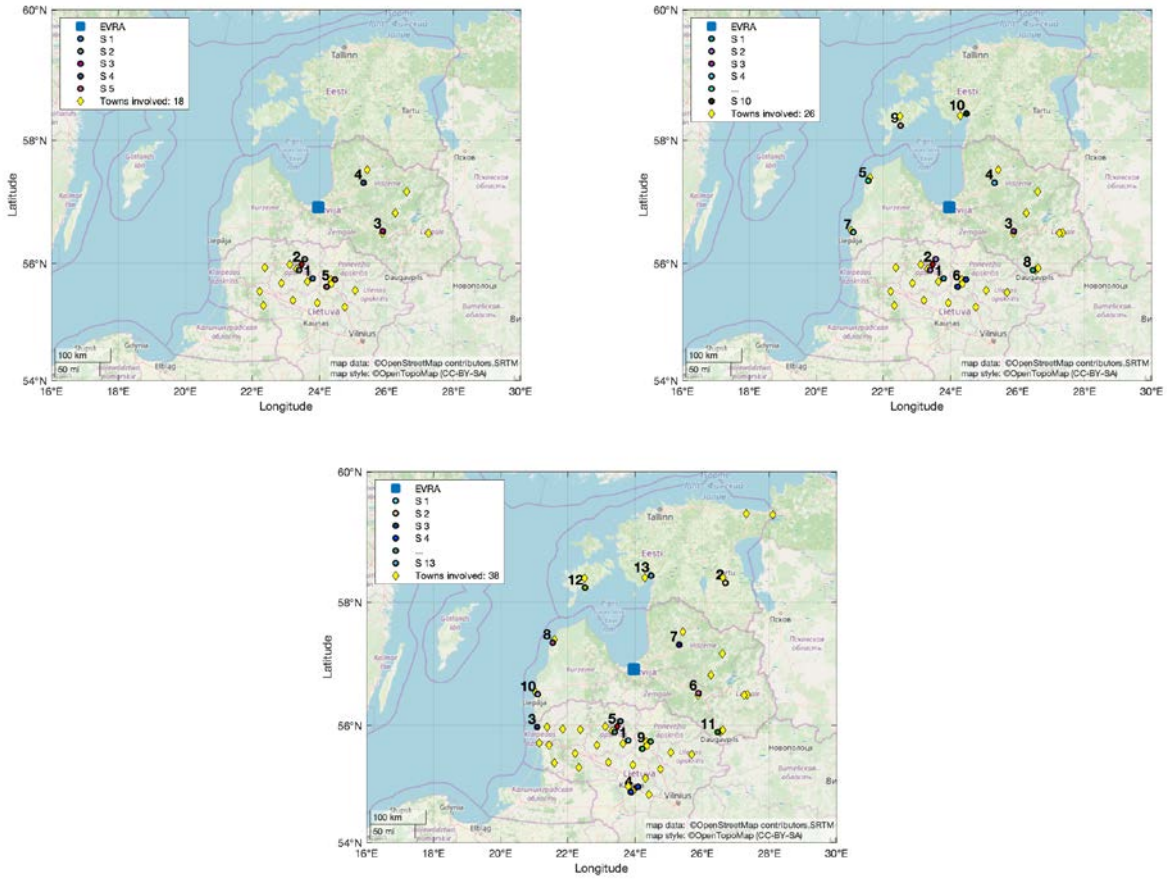


Figure 2.22: Distribution of towns and secondary airports involved in a microfeeder service to EVRA in the case of 800 m long runways for secondary airports and a cruising speed of 200 KEAS (top left: maximum trip distance of 150 km, top right: maximum trip distance of 200 km, bottom: maximum trip distance of 250 km).

For the same case of picking secondary airports with 800 m long runways or more, Figure 2.22 shows the changes in the number and location of the towns and secondary airports involved when increasing the maximum trip distance from 150 to 200 and to 250 km.

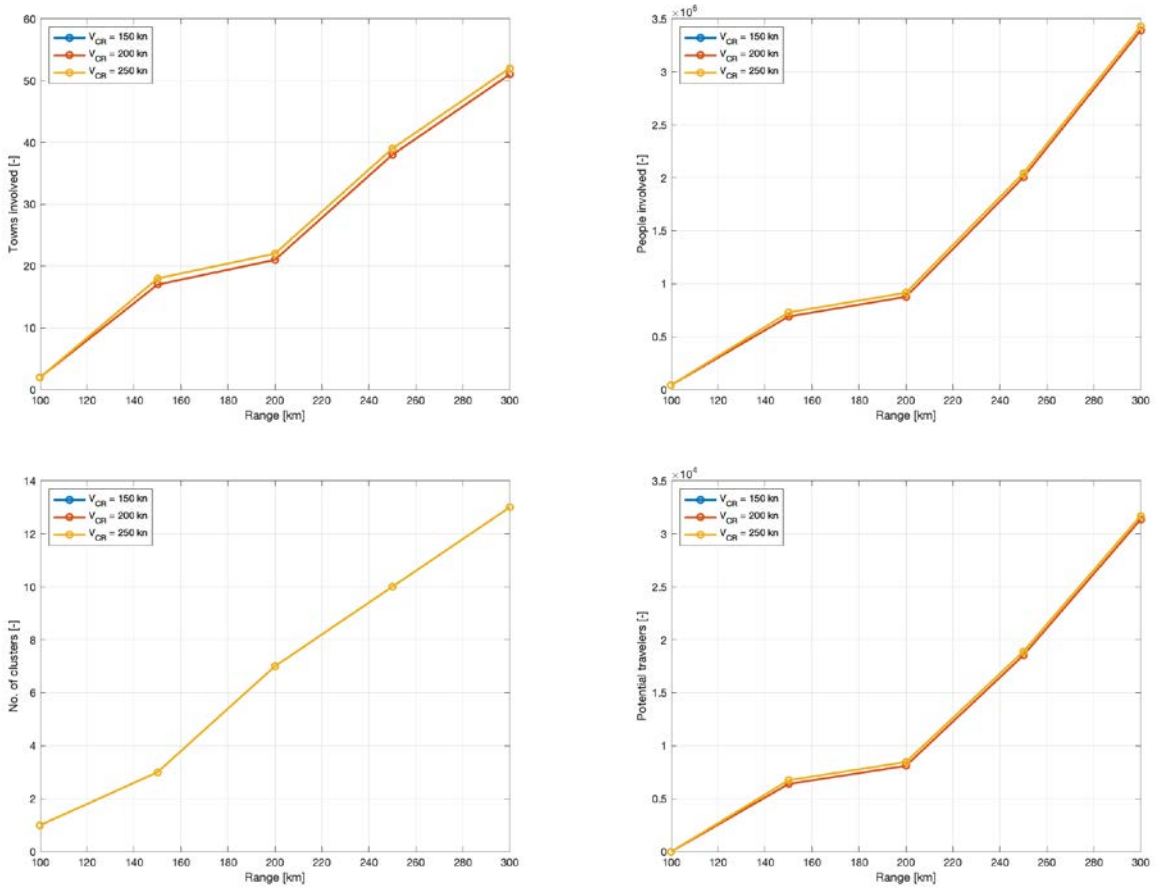


**Figure 2.23: Potential demand estimation results for a microfeeder service to EVRA in the case of 1,000 m long runways for secondary airports (top left: towns involved, top right: number of citizens in such towns, bottom left: number of secondary airports involved, bottom right: potential passenger demand).**

The graphs in Figure 2.23 refer to the case of selecting a maximum take-off and landing distance of 1,000 m. The graphs are analogous to those seen in the previous figures, with more or less similar trends, but a slight beneficial effect of increasing the cruising airspeed from 200 to 250 KTAS appears, while the number of airports activated in the two cases is exactly the same. Compared to the EBBR and LIPZ cases, the reduction in the potential demand with the rising in runway length seems much less important, reaching a maximum of approximately 3%, with a corresponding reduction of the maximum number of activated secondary airports from 21 to 13, corresponding to 600 and 1,000 m runway length, respectively.

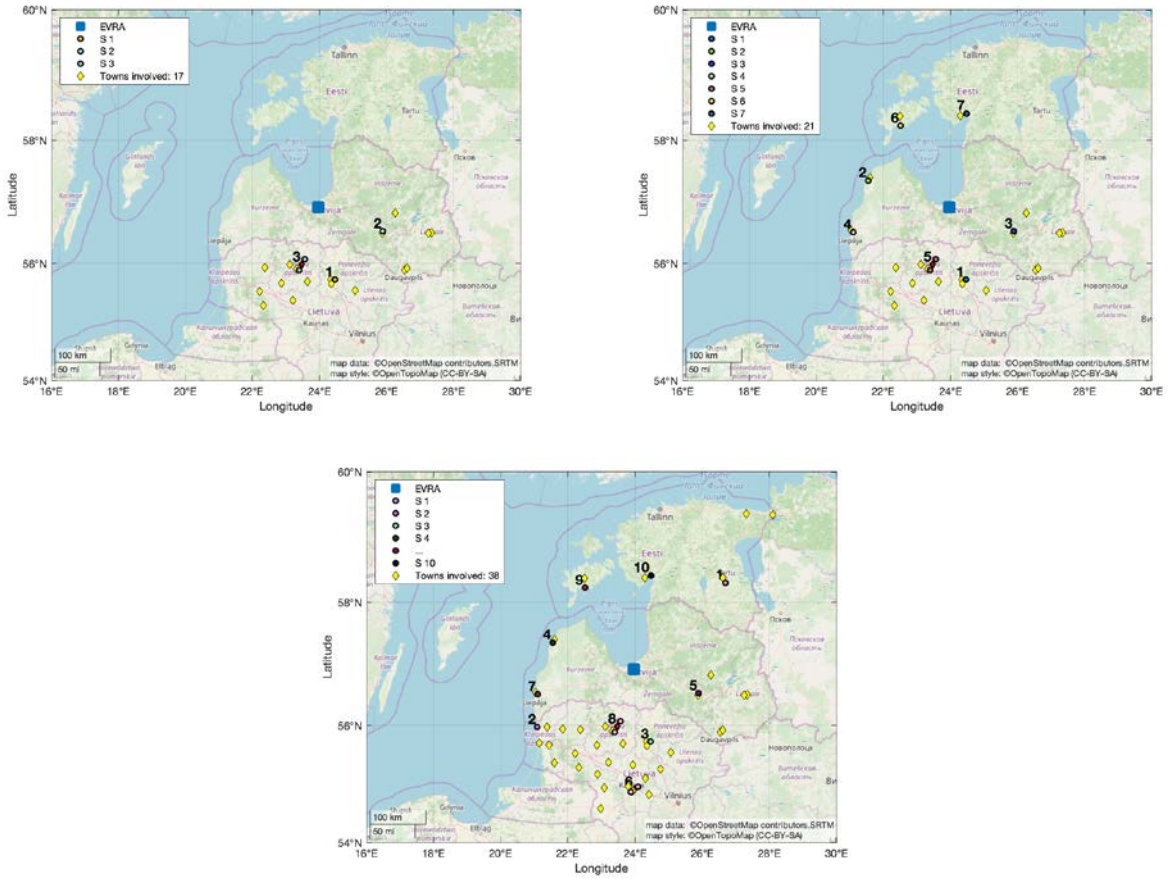


Figure 2.24: Distribution of towns and secondary airports involved in a microfeeder service to EVRA in the case of 1,000 m long runways for secondary airports and a cruising speed of 200 KEAS (top left: maximum trip distance of 150 km, top right: maximum trip distance of 200 km, bottom: maximum trip distance of 250 km).

For the same case of picking secondary airports with 1,000 m long runways or more, Figure 2.24 shows the changes in the number and location of the towns and secondary airports involved when increasing the maximum trip distance from 150 to 200 and to 250 km. The relatively limited reduction in the number of secondary airports due to runway length requirements is apparent.

## 2.5 References


[1] R. Ibrahim, “Market and cost analysis for hybrid-electric aircraft,” Politecnico di Milano, Milan, Italy, 2018.

[2] C. E. D. Riboldi, L. Mariani, L. Trainelli, A. Rolando and F. Salucci, “Assessing the effect of hybrid-electric power-trains on acoustic and chemical pollution,” in Aerospace Europe Conference (AEC2020), Bordeaux, France, 2020.

[3] A. Rolando, F. Salucci, L. Trainelli, C. E. D. Riboldi and Y. M. Khan, “On the Design of an Electric-Powered Micro-Feeder Aircraft,” in Aerospace Europe Conference 2020 (AEC2020), Bordeaux, France, 2020.

[4] Trainelli L., Riboldi C. E. D., Rolando A., Salucci F., "Evaluating the Impact of Fleet Switching to Hybrid-Electric Aircraft on Airport Infrastructures", More Electric Aircraft Conference (MEA 2019), Toulouse, France, February 6-7, 2019.

[5] Salucci F., Trainelli L., Faranda R., Longo M., "An Optimization Model for Airport Infrastructures in Support to Electric Aircraft", 13th IEEE Power & Energy Society PowerTech Conference, Milano, Italy, June 23-27, 2019. doi:10.1109/PTC.2019.8810713

[6] Riboldi C. E. D., Bigoni F, Salucci F., Rolando A., Trainelli L., "Switching to Electric Propulsion: Aero Club Fleet and Infrastructure Sizing", XXV Congresso Nazionale AIDAA, Roma, Italy, September 9-12, 2019.

[7] F. Salucci, C. E. D. Riboldi, L. Trainelli and A. Rolando, “Optimal Sizing and Operations of a Battery Recharging Infrastructure for a Regional Airport,” in Aerospace Europe Conference (AEC 2020), Bordeaux, France, 2020.

# 3 Emission and cost analysis

In the quest for the reduction of chemical and noise pollution, novel hybrid-electric powertrains promise to provide a substantial, twofold contribution. Firstly, they allow reducing the working time of the conventional, fuel-burning component of the propulsive system, by running part of the mission profile in pure-electric mode. Secondarily, they allow reducing the power of the fuel-burning component, which does not need to support the total power requirement for the flight.

Despite these evident advantages, a methodology to quantify the emissions of this novel type of powertrain has not been identified yet – a fundamental step towards the assessment of the potential contribution of hybrid-electric aviation to a greener aviation global scenario.

## *3.1 Acoustic emissions*

### 3.1.1 Introduction

Noise is usually defined as “unwanted sound” (ECAC, 2016). Every aircraft operation is associated to a noise emission, which produces annoyance and, on the long run, may also produce health issues among people working at the airports or just living nearby. According to Filippone (Filippone, 2014), “aircraft noise is a high-profile issue that commands the attention of experts in the aviation industry, airframe and engine manufacturers, airline operators, the general public, health and occupational services.” New types of transports in aviation are likely to appear in the form of microfeeders and miniliners, often operating from smaller airfields located in densely populated areas. Therefore, the abatement of aircraft noise is especially important for the success of these novel concepts.

Aircraft manufacturers are among the subjects primarily involved in the quest for the decrease of emissions, that must adhere to the regulations (or recommendations) currently published by competent Authorities.

The International Civil Aviation Organization, ICAO Annex 16, Volume 1 (International Civil Aircraft Organization, 2014), gives a noise certification basis for various aircraft classes. In the UNIFIER19 project, take-off mass will most likely not exceed 8,618 kg. For the corresponding weight an propulsion category of interest, namely propeller-driven aircraft not exceeding 8,618 kg, the constraints listed in Chapter 10 (International Civil Aircraft Organization, 2014) should be complied with. Based on that, the noise evaluation measure shall be the maximum A-weighted noise level. The measurement shall be taken in aircraft-sensor mutual positions, as well as in prescribed conditions, specified by certification standards.

In turn, civil aviation Authorities and planners are responsible for minimizing the community impact of aircraft-borne noise. To track and report noise impact (in terms of surface interested and intensity) these bodies adopt noise exposure contour maps (Synodinos, Self, & Torija, 2018). An example of a noise exposure contour map is shown in Figure 3.1. In general, aircraft noise perceived on the ground depends on the flight path, operational configuration (e.g. aircraft weight, engine and flap settings, speed

and rate of climb or descent), environment (temperature, presence of precipitations), and local topology. The noise exposure contour maps in Europe are produced according to the standard ECAC (European Civil Aviation Conference) method, described in Doc. 29 – Report on Standard Method of Computing Noise Contours around Civil Airport (ECAC, 2016). The method can be used to predict the noise quota pertaining to a certain movement, defined as "The noise from aircraft in flight while departing from and arriving at an aerodrome. That includes the noise of the take-off ground roll and use of reverse thrust after landing. It excludes the noise of taxiing and from all other aircraft and non-aircraft sources within the aerodrome boundaries - which together are referred to as ground-noise." The most important inputs to the method (besides the aircraft flight path) are the noise-power-distance (NPD) curves. NPD curves are obtained experimentally (e.g. during certification flight testing) and provide the relationship between the sound level of a given aircraft at a reference flight speed and atmospheric condition, and the slant distance from the flight path, for a certain aircraft configuration and a number of engine power settings (Synodinos, Self, & Torija, 2018). The noise metrics data is given for 10 standard slant distances and is different for aircraft take-off or landing. The Aircraft Noise and Performance (ANP) Database (EUROCONTROL, The Aircraft Noise and Performance (ANP) database: an international data resource for noise modellers, 2006) is an online data resource accompanying the ECAC Doc. 29 and ICAO Doc. 9911 guidance documents on airport noise contour modelling. Although the database provides the NPD curves for most existing aircrafts, there is clearly no available data on electric/hybrid-electric aircrafts, due to the relative immaturity of these technologies and the near-complete lack of flying production examples to date. To construct NPD curves for a vehicle that does not yet exists (or there is no experimental data), an alternative approach has to be considered (Synodinos, Self, & Torija, 2018; Riboldi, Mariani, Trainelli, Rolando, & Salucci, 2020)


Figure 3.1 Example of noise exposure contour map (Gasco, Asensio, & de Arcas, 2017).

Usually, noise sources are considered and modelled separately, e.g. propeller noise, airframe noise, electric motor noise, ICE noise, gearbox noise. However, simply adding the outcome of these predictions to one another may provide very poor results, due to the incorrect treatment of mutual interference and shadowing effects, bearing a total noise emission at an aircraft level which is invariably different from the sum of its components, when their respective contributions are computed one by one.

With this deliverable, generation of noise exposure contour maps following ECAC Doc. 29 is presented. We introduce CHANCES (Riboldi, Mariani, Trainelli, Rolando, & Salucci, 2020), a framework developed at POLIMI for the prediction of electric/hybrid-electric aircrafts noise and chemical footprint. The tool models different noise sources of the aircraft. Furthermore, as propeller is one of the primary sources of noise, a new model for propeller noise is also synthesized, and implemented as a module in CHANCES (applying XROTOR modelling of exemplary propeller) for use in the UNIFIER19 project.

### 3.1.2 Review of existing models and methodologies

Due to the relative novelty of hybrid-electric technology, prediction models for acoustic and chemical pollution effects are not directly available for such propulsion systems, whereas of course this topic has been thoroughly explored for conventionally-propelled aircraft.

Concerning prevision models for acoustics, two major classes exist, namely semi-empirical models based on data-driven corrections of simple theoretical models, and detailed theoretical models starting from physical principles. The former are generally easier to use than the latter, but their applicability is limited to specific scenarios.

Comprehensive models in the first category, capable of predicting the noise emitted by an aircraft considered as a whole emitter (instead of an assembly of different noise sources), include the best-practice procedures for noise prediction by ECAC (ECAC, 2016), which refer to the ANP database by EUROCONTROL (EUROCONTROL, The Aircraft Noise and Performance (ANP) database: an international data resource for noise modellers, 2006). Similar procedures are the base of suites like ANCON (Ollerhead, Rhodes, Viinikainen, Monkman, & Woodley, 1999), FLULA (Pietrzko & Bütikofer, 13-15 November 2002), SIMUL (Isermann, Matschat, & Müller, 21-23 July 1986) and AzB (Deutsche Umweltbundesamt, 2007). Comprehensive theoretical methods, partly based on empirical models to ease the computation of sound propagation, are implemented in ANOPP2 (Lopes & Burkley, 5-8 June 2011) and PANAM (Bertsch, Dobrzynski, & Guerin, 2010).

Due to their numerically more demanding features, theoretical models typically treat noise from a sub-system perspective, separately predicting the impact of the major sources on-board an aircraft.

Models for propeller noise are well-documented (Farassat & Succi, 1980) (Chase, 1972), and some include the airframe interference effect (Hanson, 1984). Indeed, semi-empirical models for this component have been studied too, as in (SAE Aerospace, Prediction procedure for near-field and far-field propeller noise - AIR 1407, 1977). For

the airframe, sub-components like the wing, flaps/slats and landing gear have been treated separately, with fully theoretical (Howe, 1978) (Guo, Flap side edge noise modeling and prediction, 2013) (Guo, A statistical model for landing gear noise prediction, 2005) and semi-empirical models as well (Fink, 1979). Well documented are also the models for the engine, either jet or piston-powered (Tada, 1999) (Moshkov, 2018). The latter category, more studied for application in the automotive field, is of greater interest in this work, centred on light GA aircraft.

Typically not considered for application to the aeronautical field, but of major interest for hybrid-electric aircraft, electric motor (Miller, Wood, Hoover, Thompson, & Patterson, 1984) (Bruce, Moritz, & Bommer, 2007) and gearbox (Lim & Singh, 1991) noise have been studied for some industrial applications.

A few suites capable of simultaneously predicting noise and chemical effects are available for conventionally-powered aircraft (EUROCONTROL, IMPACT: EUROCONTROL's ingegrated aircraft noise and fuel burn & emission modelling platform, 2016) (United States Department of Transportation, 2017).

Being based on data for conventionally-powered engines, all cited comprehensive models are not applicable to hybrid-electric (or fully-electric) aircraft. In order to overcome this limitation, starting from acoustic pollution a new model is envisaged, where the sound pertaining to all components on board a hybrid-electric GA aircraft are combined together to bear the total noise footprint on ground. The combination is obtained through an accurate blending, where the contribution of the sources is tuned so as to capture the overall noise emission in reference validation cases. The procedure will be then demonstrated on some theoretical testbeds, as well as in the case of the Pipistrel Panthera Hybrid (Pipistrel Vertical Solutions d.o.o., 2012), an existing GA hybrid-electric aircraft, derived from an original conventional version. The circuit around Milan-Bresso (ICAO: LIMB) GA airport is considered for a practical assessment.

### 3.1.3 Reference methodology

Procedures by ECAC (ECAC, 2016) provide the means to setup and validate a comprehensive noise prediction method, for application to conventionally powered aircraft and compliant with accuracy standard. Such a method has been prepared as a term of comparison for novel procedures constituting the core of the present research.

The ECAC model is based on the concept of a standardized discretization of terminal manoeuvres in proximity to the ground. The resolution of the discretization is bound to both geometrical quantities and flight mechanics parameters. Segmentation of the trajectory is such that the turn angle corresponding to each segment does not exceed 10 deg, speed excursion does not exceed 10m/s and no alteration in the power setting (throttle) is imposed by the pilot along the considered segment. Nodal values of thrust, true airspeed (hence power) and bank angle are defined for each segment along the trajectory.

The Aircraft Noise and Performance (ANP) database by ECAC provides the values of the maximum sound pressure level (SPL) and sound exposure level (SEL), depending

on power and on the slant distance between the noise source and a receiver on ground, for several aircraft and corresponding engine options. Once the trajectory has been assigned and properly discretized based on aircraft characteristics, it is possible to compute the baseline contribution to the SEL $L_{E,j}$ in a location on the ground, as well as the overall maximum SPL perceived $L_{m,j}$, due to each $j$-th segment. Ruling out all dependencies which do not apply to propeller-driven aircraft, the baseline values taken from the database $L_m(P,d)$ and $L_E(P,d)$, where $P$ is power and $d$ the slant distance between the source and receiver, can be corrected for three effects. These are:

- the lateral attenuation effect, through an assigned function $\Lambda(\beta,l)$ of the elevation angle $\beta$ of the line connecting the source and receiver, and of the lateral displacement $l$ of the receiver from the trace on ground of the same line
- the speed correction ($\Delta_V$), function of the ratio between the actual nodal airspeed and the reference value of 160 kn
- a correction $\Delta_F$ modelling the finite length of each segment, which applies to the SEL from the database, obtained from ideal infinite length segments

This yields the final equations for the ECAC prediction model in Eq. (3.1)

$$L_{m,j} = L_m(P,d) + \Lambda(\beta,l) \qquad (3.1)$$
$$L_{E,j} = L_E(P,d) + \Delta_F + \Delta_V + \Lambda(\beta,l)$$

Figure 3.2 shows the three-dimensional trajectories for a departure and arrival manoeuvre for a Cessna C172R Skyhawk operating from the standard RWY18 right-hand circuit of Milan-Bresso, a GA airport north of Milan, totally surrounded by a densely populated area. The Aero Club Milano Flying School (Aero Club Milano, 2019) operates a large number of instructional and pleasure flights from here, making this a test case of special interest for the present study.

An original implementation of the ECAC model has been validated based on a prescribed standard procedure. This assumes a nominal circuit, discretization and data for three test aircraft. The level of accuracy of the method in its original implementation allows to consider its prediction as ground truth in the following steps.

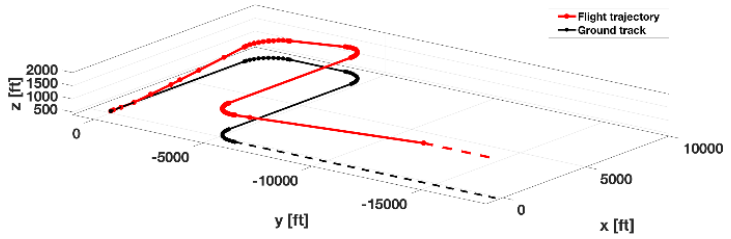


(a)

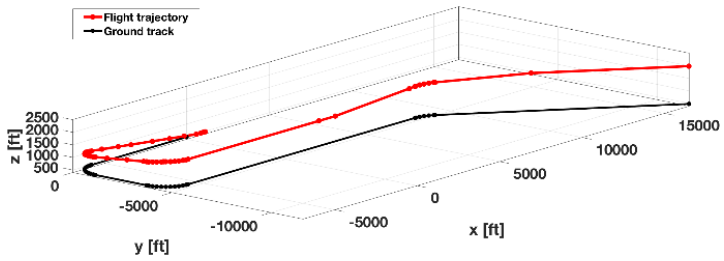


(b)

Figure 3.2 Three- dimensional trajectories for departure (a) and arrival (b), Milan-Bresso RWY18 right-hand standard circuit. Discretization based on ECAC prescription for noise emission analysis.

### 3.1.4 Models for noise sources on-board

The first step towards a novel noise prediction method applicable to aircraft featuring a hybrid-electric powertrain is that of selecting suitable models for each sub-source.

Concerning propeller noise, the model proposed in SAE AIR1407 (SAE Aerospace, Prediction procedure for near-field and far-field propeller noise - AIR 1407, 1977) has been adopted. This takes as input some geometrical parameters (propeller diameter, number of blades and number of propellers), quantities describing the equilibrium condition (propeller rotational speed, power input and flight speed) and environmental conditions (air temperature). Based on this data, the model produces the A-weighted SPL accounting for atmospheric absorption as a function of the slant distance between noise source and sensor, and of the elevation of the line connecting the two.

Airframe noise can be treated with the sub-models presented by Fink (Fink, 1979). All models take as input geometric quantities and the relative position (distance and direction with respect to the ground) between the aircraft and receiver. The output quantity obtained depends on the airframe component. In particular, the models for all sub-components return a frequency spectrum of the SPL evaluated at each one-third of octave band. Models for the empennages, flaps, slats and landing gear do not account for atmospheric absorption, which is responsible for a pure energy loss. The wing contribution instead correctly accounts for this effect. The atmospheric absorption effect can be retrieved via the SAE AIR1845 model (SAE Aerospace, Procedure for the calculation of airplane noise in the vicinity of airports - AIR 1845, 1986) as in Eq.(3.2),

$$L_{p,n_\alpha} = L_{p,n} - \alpha_n d \tag{3.2}$$

where $L_{p,n_\alpha}$ is the absorption-reduced spectrum of the SPL, obtained from the unattenuated $L_{p,n}$ value through a correction bound to the slant distance $d$ and an atmospheric absorption coefficient $\alpha_n$.

The model for engine noise is taken from Dobrzynski formulation (Bertsch, Dobrzynski, & Guerin, 2010), and provides the A-weighted SPL from the actual and

maximum rotational speed of the engine, maximum engine power and the slant distance between source and sensor on ground.

Models for the gearbox and electric motor are taken from the work by Bruce (Bruce, Moritz, & Bommer, 2007), not originally studied for aviation. For electric motors, the sound power level $L_w$ can be obtained as a function of the size, rotational speed and power output. This quantity can be translated into SPL $L_p$ based on the propagation law in Eq.(3.3),

$$L_P = L_w + 10\log_{10}\left(\frac{Q}{4\pi r^2}\right), \tag{3.3}$$

where $Q$ is a shape parameter defined as the ratio between a sphere with radius $r$, equal to the slant distance between the source and receiver, and the actual area of the surface over which propagation is taking place at a given time. For the gearbox, the sound power level can be assigned as a function of the rotational speed of the shaft, the power transferred by the gearbox, and the area of a conformal surface at 1 m from the gearbox, computed through an assigned model. The value of the instantaneous SPL can be propagated recurring to Eq.(3.3).

All three models for the engine, gearbox and electric motor do not account for atmospheric absorption and produce a value of SPL not depending on frequency – i.e. a frequency integral of the spectrum. In order to correctly include the atmospheric attenuation effect, the loss on the SPL $\Delta L_P(d)$ function of the slant distance can be estimated starting from the ANP database. The latter provides the value of $L_{p,n_\alpha}(\bar{d})$ for $\bar{d} = 1{,}000$ ft and attenuated according to SAE AIR1845. The provided values are only functions of the aircraft size, not of the engine model. With Eq.(3.2), it is possible to estimate $L_{p,n}(\bar{d})$. The propagation model in Eq.(3.4) can be adopted to obtain

$$L_{p,n}(d) = L_{p,n}(\bar{d}) - 20\log_{10}\left(\frac{d}{\bar{d}}\right), \tag{3.4}$$

and from $L_{p,n}(d)$ the value accounting for absorption can be obtained again through Eq.(3.2). In order to finally estimate the loss, it is possible to integrate the spectra and subtracting, as per Eq.(3.5),

$$\Delta L_p(d) = 10\log_{10}\left(\sum_n 10^{\frac{L_{p,n_\alpha}(d)+A_n}{10}}\right) - 10\log_{10}\left(\sum_n 10^{\frac{L_{p,n}(d)+A_n}{10}}\right). \tag{3.5}$$

The quantity estimated in Eq.(3.5) can be applied to the noise contributions of the engine, electric motor and gearbox, making them compatible with those from the propeller and airframe.

### 3.1.5 Propeller noise – An alternative model

A proposed alternative method for modelling the noise emitted by the propeller, which may be prospectively adopted for implementation in CHANCES, makes use of in-house assets of PVS. This will be introduced in the next sub-paragraphs.

#### *3.1.5.1 Propeller noise theory*

The propeller noise theory presented in this section is summarized from (H. Hubbard, 1991), if not stated otherwise. By definition, a propeller is an open rotor featuring either an adjustable or fixed pitch. The blade design allows for converting rotary motion from the engine into translational thrust. Generally speaking, the acoustic signature of the propeller is the result of the following sub-sources (their relative importance depends on propeller design and operating conditions):

- thickness noise,
- steady-loading noise,
- unsteady-loading noise,
- quadrupole (high-speed-impulsive noise source) noise,
- broadband noise.

Thickness noise stems from the volume displacement of the propeller blades. Its maximum magnitude is to be found in the propeller plane. Thickness noise is a function of the blade volume where frequency depends on the blade cross-section shape and rotational speed (it increases with increasing blade-tip Mach number). A smaller blade volume (thinner airfoils) and a more significant planform sweep help in reducing this kind of noise.

Steady- and unsteady-loading noise are a consequence of the steady and circumferentially nonuniform blade loading, respectively. Steady-loading noise stems from the forces that blades exert on the surrounding fluid (Villafana, 2016) and is important at low to moderate speeds. An example of the unsteady-loading noise is blade vortex interaction (BVI) noise. It is especially important for counter-rotating propellers where the blades of the second propeller hit tip vortex created by the first propeller. Thickness and loading noise are known together as rotational noise (S. Brentner & Farrasat, 2003).

When the advancing tip speed of the propeller is so high that the flow becomes transonic, the quadrupole noise (modelled through nonlinear terms in complete first-principle models, hence the name) increases significantly.

Broadband noise results mainly from turbulence, in turn associated to a specific, broad-band distribution of energy on a dense scale of characteristic sizes of turbulent vortex structures.

We should be aware that for an operational propeller the total noise depends also on various distortions of the flow field, e.g., due to aircraft angle-of-attack or wakes generated upstream, possibly due also to atmospheric perturbation (both cause unsteady loading).

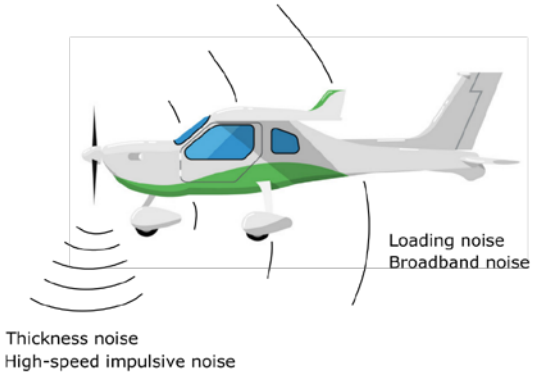


Figure 3.3 Directivity of thickness, loading and broadband noise.

The spectrum of propeller noise features multiple components. We have a primary tonal (or harmonic) component featuring peaks at discrete frequencies, generated by the regular rotation of the blades and some ensuing periodic effects. Thus, the time trace we can measure is periodic, where first harmonic is fundamental an associated to the highest energy peak, and higher harmonics are integer multiples of the fundamental frequency.

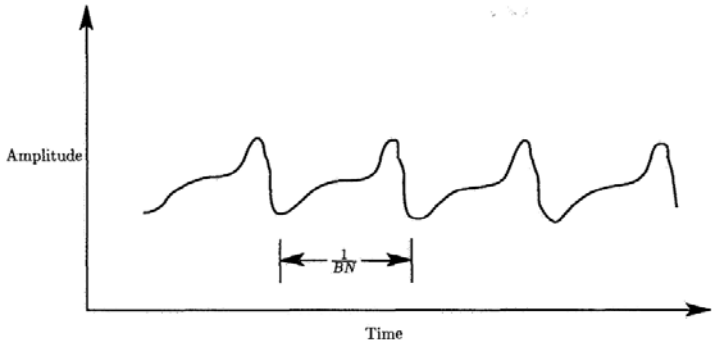


Figure 3.4 Trace of the tonal component of the propeller noise (H. Hubbard, 1991).

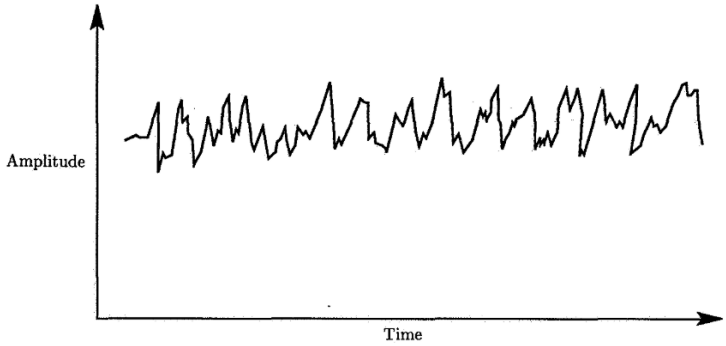


Figure 3.5 Trace of the propeller broad-band noise (H. Hubbard, 1991).

On the other hand, the broadband noise results from the turbulent flow conditions at the leading edge (interaction of inflow turbulence with leading edge of the blade), at the trailing edge, and at the tip of each blade. The broadband noise is random in nature and contains many nonharmonic frequencies. In general, its frequency range is between 1 kHz and 5 kHz, and for this frequency band the human ear is very sensitive (Villafana, 2016). We also distinguish a narrow-band random noise. This kind of noise is almost periodic, but the energy is not concentrated at isolated frequencies.

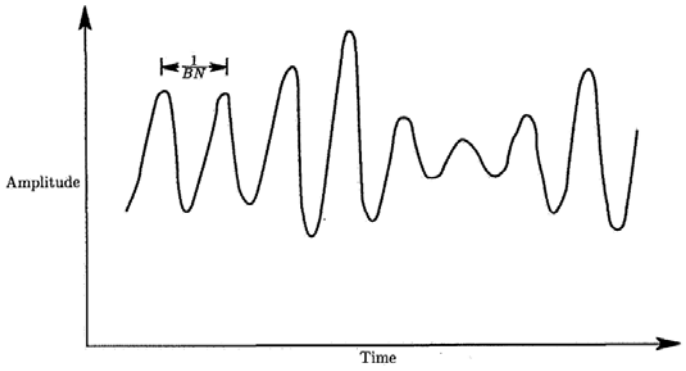


Figure 3.6 Trace of the propeller narrow-band noise (H. Hubbard, 1991).

### *3.1.5.2 XROTOR modelling of propeller noise*

From the XROTOR (Drela & Youngren) description: "XROTOR is an interactive program for the design and analysis of ducted and free-tip propellers and windmills. It consists of a collection of menu-driven routines which perform various useful functions such as:

- design of minimum induced loss rotor (propeller or windmill),
- prompted input of an arbitrary rotor geometry,
- interactive modification of a rotor geometry,
- twist optimization of an arbitrary rotor for minimum induced loss,
- analysis of a rotor with a wealth of choices of operating parameters,
- incoming slipstream effects (from an upstream propeller, viscous wake, ...),
- multi-point parameter display,
- structural analysis and corrections for twist under load,
- acoustic analysis with dB noise footprint predictions,
- interpolation of geometry to radii of interest,
- plotting of geometry, aerodynamic parameters, and performance maps."

Especially important from the perspective of acoustic emissions estimation is the XROTOR capability to conduct propeller acoustic analysis, including noise footprint predictions. XROTOR calculation method originates from the works (P. Succi, Design of Quiet Efficient Propellers, SAE Paper 790584, 1979; P. Succi, Munro, & Zimmer, Experimental Verification of Propeller Noise Prediction, 1982) and is based on the retarded-time concept. Result of the calculation is an instantaneous acoustic pressure

as seen by the observer or sensor located at a given point (*x, y, z*) in space over the one-blade-passing period. Using XROTOR, propeller thickness noise, steady-loading noise, and their sum, can be predicted. The method requirement is that the blade speed along the observer's line of sight be subsonic.

The observer's perception of loudness highly depends on sound frequency (Ginsberg, 2018). Although XROTOR can provide sound pressure level (SPL) predictions (i.e. a common measure of the loudness of an acoustic signal), it lacks the ability to compute the A-weighted SPL, which accounts for the human perception of loudness. The A-weighting function is shown in Figure 3.7. Therefore, the XROTOR output we are interested in is only the acoustic pressure trace over one blade-passing period. The signal analysis is done afterwards using separate routines developed in Python (see Section 3.1.5.4). To confirm the XROTOR noise prediction accuracy (and broadband noise modelling presented later), the results will be validated by simulations in CHARM (CHARM), a computer software for modelling the complete aerodynamics and dynamics of rotorcraft in general flight conditions.

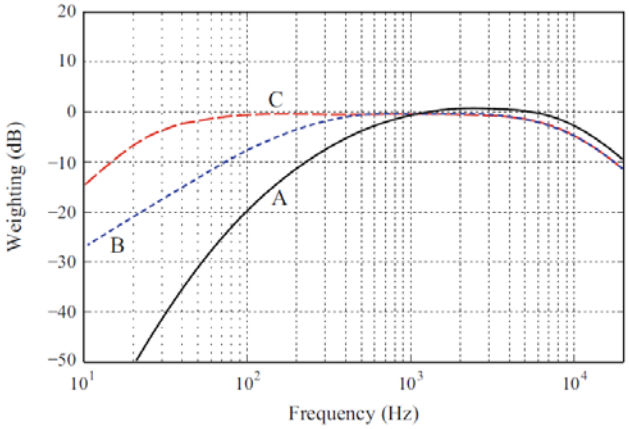


Figure 3.7 A-, B-, and C-weighting. Adopted from (Ginsberg, 2018).

### *3.1.5.3 Example propeller*

Geometries of the reference propeller and propeller blade developed in XROTOR are shown in Figure 3.8. Propeller and hub diameters are 2.2 meters and 0.54 meters respectively. The example propeller features 6 blades. Blade planform area is 0.19228 $m^2$. Blade airfoil cross-sectional area effect (thickness noise) on the acoustic pressure is set via specifying the ratio $A/c^2$. Each blade is defined using 6 airfoils. The airfoil characteristics are as specified in Table 3.1.

Table 3.1 Airfoil characteristics in example propeller.

| N | $r/R$ | Zero-lift AOA (°) | $dCl/d\alpha\ (1/°)$ | $Cl_{max}$ | $A/c^2\ (/)$ |
|---|---|---|---|---|---|
| 1 | 0.29 | -4 | 7 | 1.15 | 0.17374 |
| 2 | 0.43 | -2.7 | 7.5 | 1.2 | 0.11594 |
| 3 | 0.59 | -2.3 | 6.9 | 1.10 | 0.08836 |
| 4 | 0.74 | -2.1 | 7 | 1.0 | 0.07807 |
| 5 | 0.90 | -2 | 6.6 | 1.0 | 0.07006 |
| 6 | 1 | -1.2 | 7.5 | 0.85 | 0.07989 |

In Table 3.1, $R$ represents the blade radius, $r$ the radial coordinate, AOA (or $\alpha$) the angle-of-attack, $Cl$ the lift coefficient, $A$ the cross-sectional area of the airfoil, and $c$ the chord.

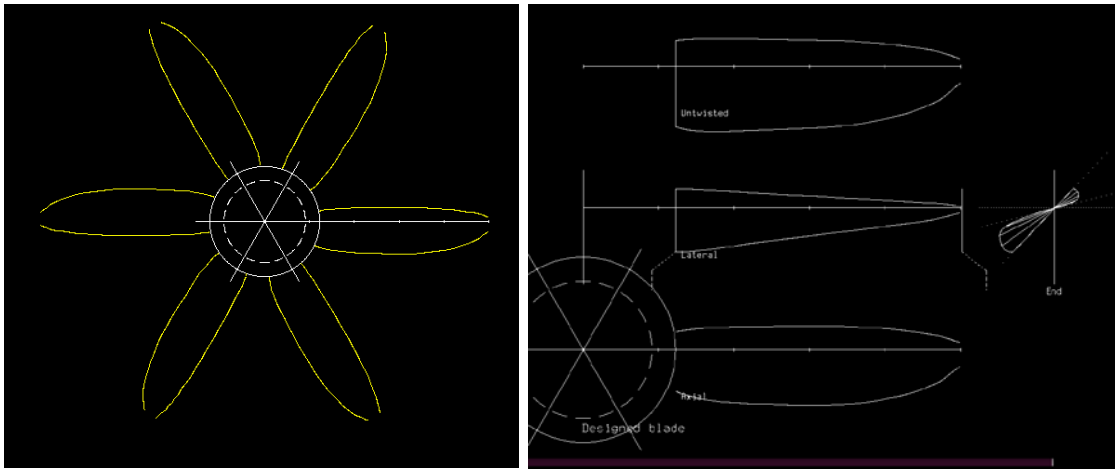


Figure 3.8 Reference propeller geometry.

### *3.1.5.4 Propeller noise ground footprint calculation procedure*

In order to estimate the noise footprint on ground due to the propeller, firstly an acoustic pressure due to thickness and loading noise for a given observer/sensor location is calculated by XROTOR.

Each calculation point is defined by the following variables:

- x coordinate of the ground sensor,
- y coordinate of the ground sensor,
- flight altitude,
- climb angle,
- propeller power,
- propeller rpm,
- aircraft speed.

Figure 3.9 represents thickness and loading noise acoustic pressure *p(t)* at ground location x = -100 m, y = 200 m, at a flight altitude of 200 m, and climb angle of 10°. Propeller power is 1 MW, rotational speed is 2,250 rpm, and aircraft speed is 30 m/s.

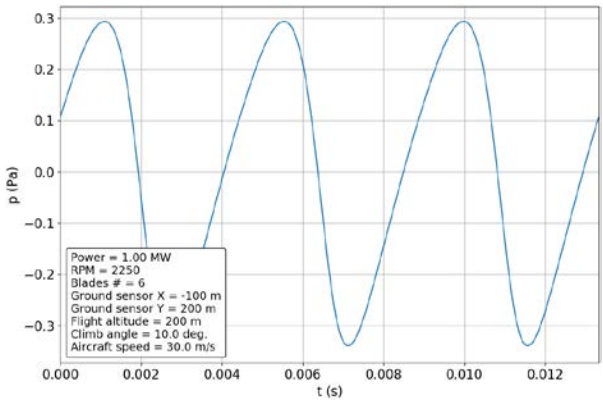


Figure 3.9 Example of thickness and loading noise acoustic pressure calculated by XROTOR.

In the next step, the signal is Fourier-decomposed (applying Python routines) to find harmonic frequencies. For the acoustic pressure trace shown in Figure 3.9, the harmonic frequencies versus acoustic pressure amplitudes are given by Figure 3.10. Sound pressure level (unit dB, denoted as $L_{p,n}$) for every harmonic frequency is calculated as in Eq.(3.6),

$$\mathrm{L_{p,n}} = 10log_{10}\left(\sum_{n=1}^{N}\frac{|P_n|^2}{2p_{ref}^2}\right), \tag{3.6}$$

where $P_n$ represents signal amplitude of *n*-th harmonics, and $p_{ref}$ is a reference pressure value of 20 μPa. Total sound pressure level for a signal (summation of incoherent sources) is obtained as in Eq.(3.7),

$$\mathrm{L_{p,\Sigma}} = 10log_{10}\left(\sum_{i=1}^{n}10^{\frac{L_{p,n}}{10}}\right). \tag{3.7}$$

A-weighted sound pressure level for every harmonic frequency is calculated as follows,

$$\mathrm{L_{p,A,n}} = \mathrm{L_{p,n}} + \Delta(\mathrm{f}), \tag{3.8}$$

where $\Delta(f)$ represents gain (in dB) applied for a given frequency, $f$. The analytic expression of the A-weighting function is

$$\mathrm{R_A(f)} = \frac{12194^2 \cdot f^4}{(f^2 + 20.6^2)\sqrt{(f^2 + 107.7^2)(f^2 + 737.9^2)}(f^2 + 12194^2)}, \tag{3.9}$$

so that

$$\Delta(\mathrm{f}) = 20\log_{10}\big(\mathrm{R_A(f)}\big) - 20\log_{10}\big(\mathrm{R_A}(1000)\big). \tag{3.10}$$

The total A-weighted sound pressure level ($L_{p,A}$) is then calculated following Eq.(3.37). For example, for the pressure trace from Figure 3.9, the (A-weighted) rotational noise sound pressure level is 80.7 dB, and 71.7 dB(A).

Considering multiple ground points/sensors shown in Figure 3.11, the propeller ground noise (thickness and loading) footprint contour map is produced. For example, the plots on Figure 3.12 show contours (without and with A-weighting of sound pressure level respectively to the left and right) for an aircraft flight altitude of 200 m and climb angle of 10°. Propeller power is 1 MW, rotational speed is 2,250 rpm, and aircraft speed is 30 m/s.

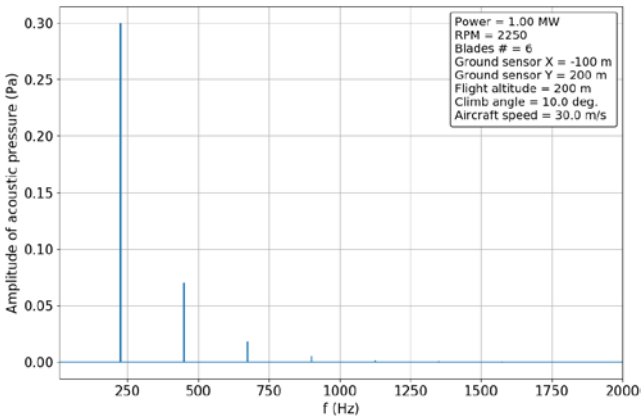


Figure 3.10 Thickness and loading noise acoustic pressure in frequency domain.

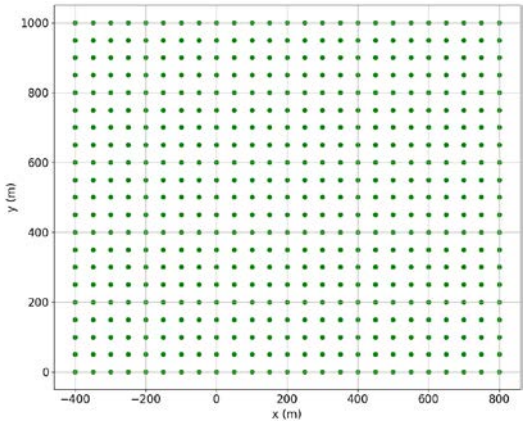


Figure 3.11 Location of ground sensors.

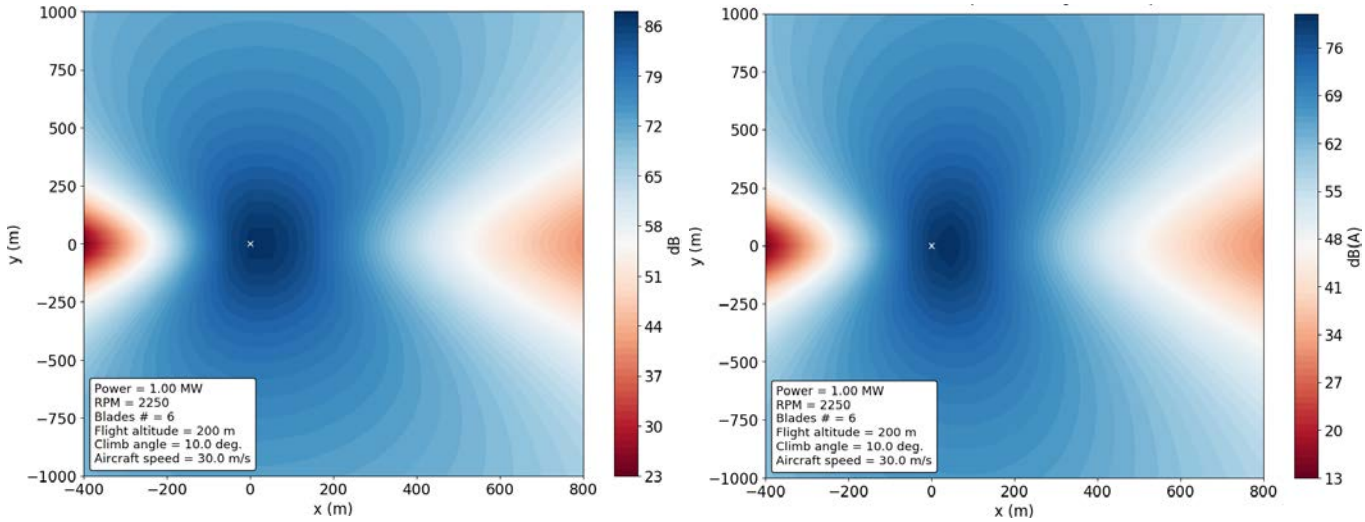


Figure 3.12 Sound pressure level ground noise (thickness and loading) footprint contour map. (a) no weighting, (b) A-weighted.

Next, broadband noise is estimated applying Pegg's broadband noise prediction method. The method is defined in (Pegg, 1979). The implementation of the method in PSU-WOPWOP (CHARM's submodule for noise prediction) is given in (Goldman, 2012). First, we calculate the peak broadband noise frequency,

$$f_p = -240 \log_{10} T + 2.448 V_T + 942, \quad (3.11)$$

where $T$ is propeller thrust, and $V_T$ represents blade rotational tip speed. The 1/3-octave band containing this frequency (each octave band is defined by centre frequency, and upper and lower limits), $f_{c,p}$, is identified.

Finally, peak 1/3-octave band acoustic pressure level is calculated,

$$L_{c,p,1/3}^{n} = 20 \cdot \log_{10}\left(\frac{V_T}{c_0}\right)^3 + 10 \cdot log_{10}\left[\frac{A_b}{r^2}(cos^2\,\theta_1 + 0.1)\right] + S_{1/3} + f(\overline{C_L}) + 130 \qquad (3.12)$$

where $c_0$ is the speed of sound, $A_b$ is the total blade (planform) area of the propeller, $r$ is distance from source to observer, and $\theta_1$ represents the angle between the negative thrust axis and the line from the hub to the observer. Finally, $\overline{C_L}$ is the average blade lift coefficient, written as

$$\overline{C_L} = \frac{6T}{\rho A_b V_T^2}, \qquad (3.13)$$

where ρ is air density.

$$f(\overline{C_L}) = \begin{cases} 10\log_{10}(\overline{C_L}\,/\,0.4) & \overline{C_L} \le 0.48 \\ 0.8 + 80\log_{10}(\overline{C_L}\,/\,0.48) & \overline{C_L} > 0.48 \end{cases} \qquad (3.14)$$

Pegg's model assumes frequencies ranging between 50 Hz and 10 kHz. Out of this scope, the contributions of other 1/3-octave bands are determined as

$$f_c^n = f_{c,p} \cdot 2^n, \qquad (3.15)$$

where n is an integer. $S_{1/3}$ is determined from Figure 3.13.

The result of the prediction, in form of the spectral curve for different 1/3-octaves at ground location x = -100 m, y = 200 m, at the flight altitude of 200 m, and climb angle of 10°, is shown in Figure 3.14. Propeller power is 1 MW, thrust is 13300 N, and rotational speed is 2250 rpm. Blade rotational tip speed is approx. 260 m/s (0.763 Ma), and average blade lift coefficient is 0.58. For example, for the sound pressure level spectrum from Figure 3.14, the (A-weighted) broadband noise sound pressure level is 85.6 dB, and 84.2 dB(A).

Considering multiple ground points/sensors shown in Figure 3.11, the propeller ground noise (broadband) footprint contour map is generated. Plots on Figure 3.15 show contours (without and with A-weighting of sound pressure level respectively to the left and right) for an aircraft flight altitude of 200 m, and a climb angle of 10°.

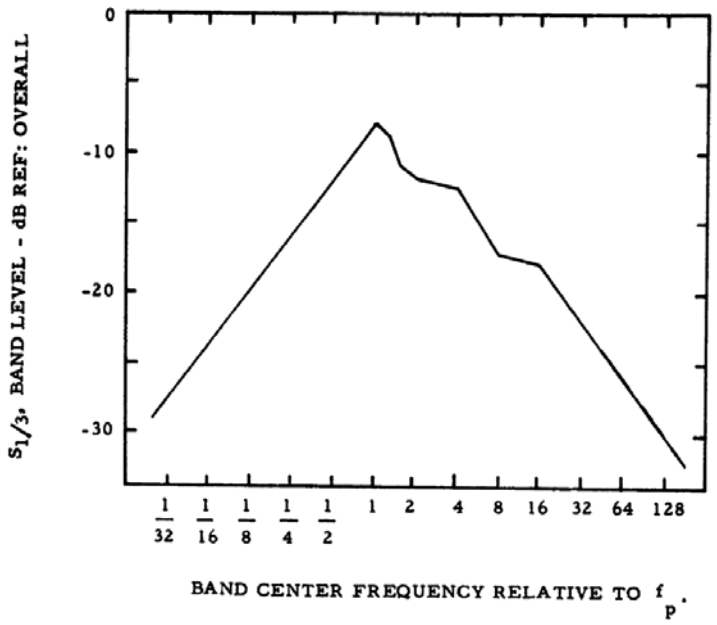


Figure 3.13 Normalized rotor broadband noise empirically determined spectrum shape (Pegg, 1979).

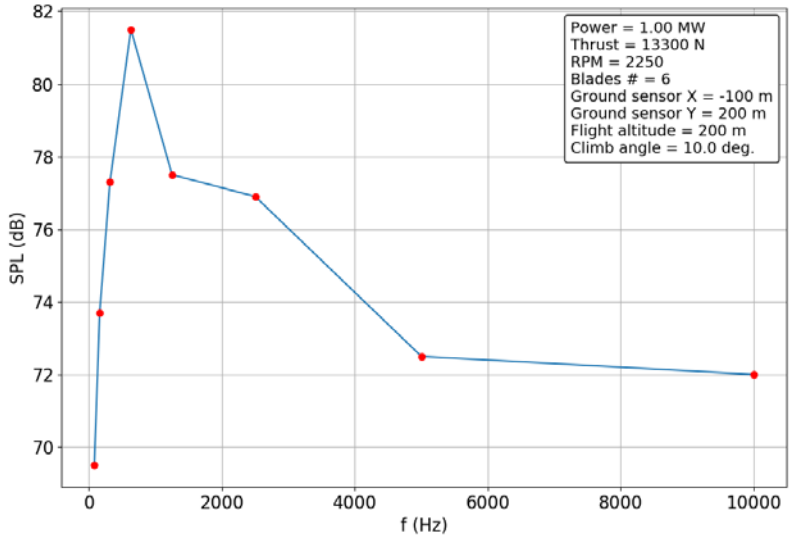


Figure 3.14 Example of propeller broadband noise spectrum calculated by Pegg's method.

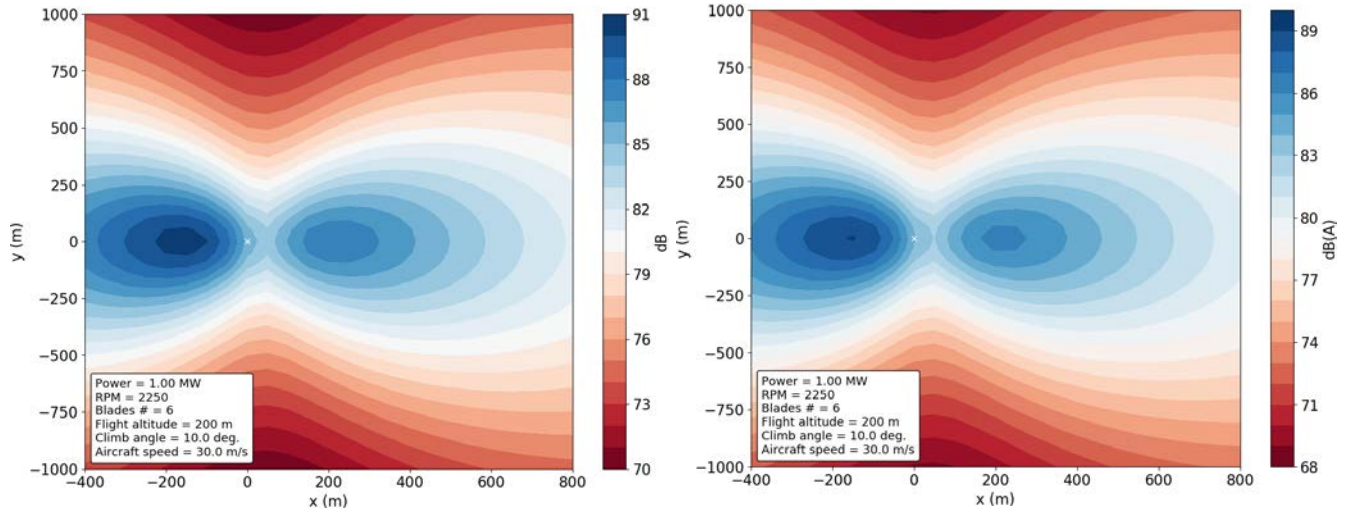


Figure 3.15 Sound pressure level ground noise (broadband) footprint contour map. (a) no weighting, (b) A-weighted.

### *3.1.5.5 Propeller total noise footprint on ground*

The total (A-weighted) sound pressure level ground noise contour map is shown in the plots of Figure 3.16. It is obtained by addition of rotational (thickness and loading) and broadband noise dB or dB(A) values (to the left and right of the figure respectively), computed based on Eq. (3.37).

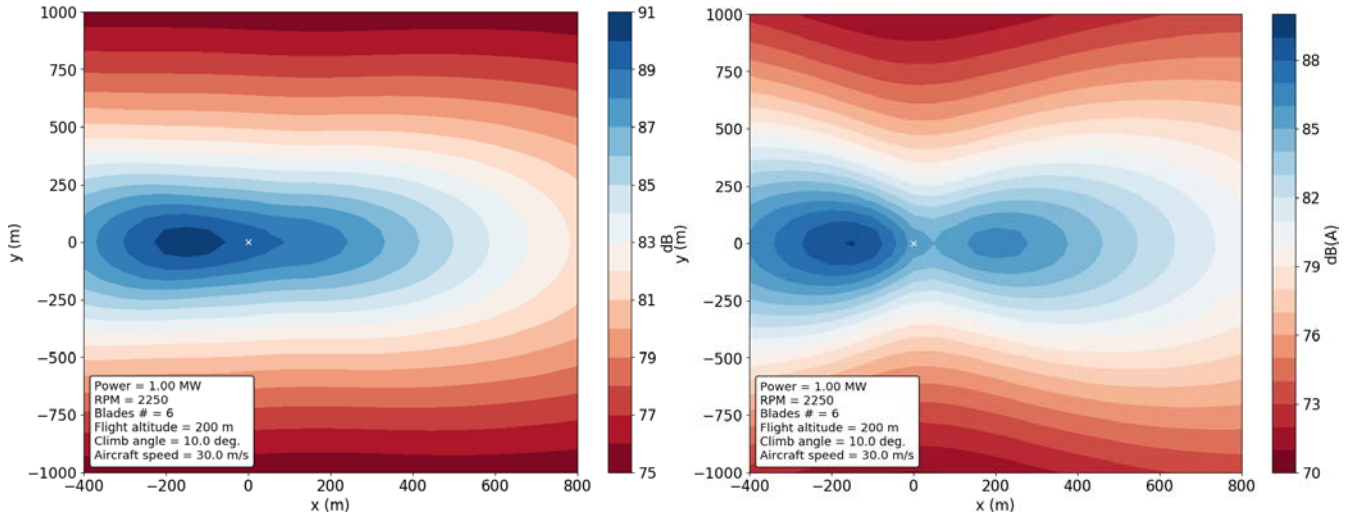


Figure 3.16 Total sound pressure level ground noise footprint contour map. (a) no weighting, (b) A-weighted.

### 3.1.6 The source-blending noise prediction method

A global value of the SEL $L_{E,A}\,(d)$ can be obtained based on an energetic sum of the contributions from all considered sources, measured through the corresponding SPL values. In order to account for the inaccuracy of the predictions for these sources, which would yield a highly inaccurate result if simply summed to one another, a blending method is proposed, where each contribution is weighted through a blending coefficient to be determined, so that the SPL pertaining to the whole aircraft is defined by Eq.(3.16),

$$L_{E,A}(d) = 10\log_{10}\left(\int_{t_1}^{t_2} 10^{x_1\frac{L^a_{p,A}(d,t)}{10}} + 10^{x_2\frac{L^p_{p,A}(d,t)}{10}} + 10^{x_3\frac{L^e_{p,A}(d,t)}{10}} + 10^{x_4\frac{L^m_{p,A}(d,t)}{10}} + 10^{x_5\frac{L^g_{p,A}(d,t)}{10}}\,dt\right) \qquad (3.16)$$

Here the SPL values pertaining to the airframe $L^a_{p,A}(d,t)$, propeller $L^p_{p,A}(d,t)$, engine $L^e_{p,A}(d,t)$, electric motor $L^m_{p,A}(d,t)$ and gearbox $L^g_{p,A}(d,t)$ are energetically summed, after weighting through the blending coefficients $x_i, i = 1, \dots 5$. It is noteworthy that the SPL are specified as functions of the time instant $t$, and the SEL is obtained through integration over a time frame.

The way proposed to design the blending coefficients is based on tuning the SEL obtained through Eq.6 in such a way to match the data of the ANP database. More in depth, as mentioned the database provides value of the SEL for a number of aircraft in several weight categories. These values are obtained through overflight testing, for ten slant distances between 500 ft and 25,000 ft, a speed of 160 kn, and for at least four power settings, two corresponding to arrival configurations (relatively lower power, flaps and landing gear as required, etc.), and two to departure configurations (higher power setting, etc.). The SEL values in the database are obtained considering a time frame during the flight when the SPL of the whole aircraft is not more than 10 dB below the maximum recorded during the test.

**Table 3.2 Aircraft in the ANP database considered for the design of the blending coefficients in the source-blending method.**

| Aircraft model | Engines (number) | MTOW [lb] |
|---|---|---|
| Piper PA-28-161 Warrior | 1 | 2,325 |
| Cessna C172R Skyhawk | 1 | 2,450 |
| Cessna C182H Skylane | 1 | 2,800 |
| Cessna C206H Stationair | 1 | 3,600 |
| Cessna T206H Stationair | 1 | 3,600 |
| Piper PA-30 Twin Comanche | 2 | 3,600 |
| Beechcraft B58P Baron | 2 | 6,100 |
| Piper PA-31-350 Navajo Chieftain | 2 | 7,000 |

For a set of eight aircraft in the database capable of operating from Milan-Bresso and reported in Table 3.2, the ten available values of the SEL have been extracted from the ANP database. These have been considered as reference values $\overline{L_{E,A_j}}$, based on the presumed accuracy of the method (already commented above).

The models for the considered noise sources are applied to the same conditions adopted for obtaining the values in the ANP database. The following further hypotheses have been considered to make for a fair comparison:

- take-off and landing flap setting have been retrieved from flight manuals and adopted for database entries corresponding to take-off at maximum power and landing at minimum power respectively
- when retractable, landing gear has been considered down for the same database entries just mentioned
- the database by Yakovitch (Yakovitch, et al., 2016) and sheet data for the engines of the considered aircraft have been used to translate the boundary conditions of the entries in the ANP database into input power and rotational speed needed for the noise of the propeller model, and maximum power, current and maximum speed required by the engine model.

It is noteworthy that no electrical motor nor gearbox is present in the considered aircraft, hence the corresponding coefficients $x_4$ and $x_5$ are not considered for now (this will be discussed later). Nonetheless, the theoretical procedure presented next is general, and considers all possible coefficients.

Once the values for the SEL $L_{E,A}(d)$ has been computed from the corresponding sources as per Eq.6, the blending coefficients can be computed in an optimal fashion by minimizing the cost function in Eq.(3.17)

$$J = \frac{\sum_{j=1}^{10}\left(\overline{L_{E,A_j}} - L_{E,A_j}\right)^2}{10} + \sum_{k=1}^{5}(x_k - 1)^2. \tag{3.17}$$

Here if the SEL obtained from the prediction models for all sources and combined (Eq.(3.16)) for each considered overflight were the same as the corresponding record in the ANP database, the first term on the RHS of Eq.(3.17) would be null. Furthermore, the elastic term reported as a second term on the RHS would be null if the blending coefficients were equal to 1, i.e. again in an ideal condition, where consequently the value of $J$ would be null. In non-ideal conditions, where the combination of all sources would not match the expected value of SEL from the database, the value of $J > 0$. Nonetheless, the blending coefficients should not shift too far from the ideal value of one, thanks to the elastic term. This is on account of the fact that the models for the sub-components provide realistic results, even though not matching the expected total without a proper blending.

The coefficients designed considering together the aircraft in Tab.1, and all database entries for each of them, are validated computing the SEL through Eq.(3.16), and comparing the results with the output of the ANP database. As an example, a comparison of the two methods is presented in Figure 3.17 for the Cessna T206H Stationair. The SEL as a function of the distance with respect to the receiver, i.e. the

altitude of the overflight in this case, is presented for four configurations, two for departure and two for arrival.

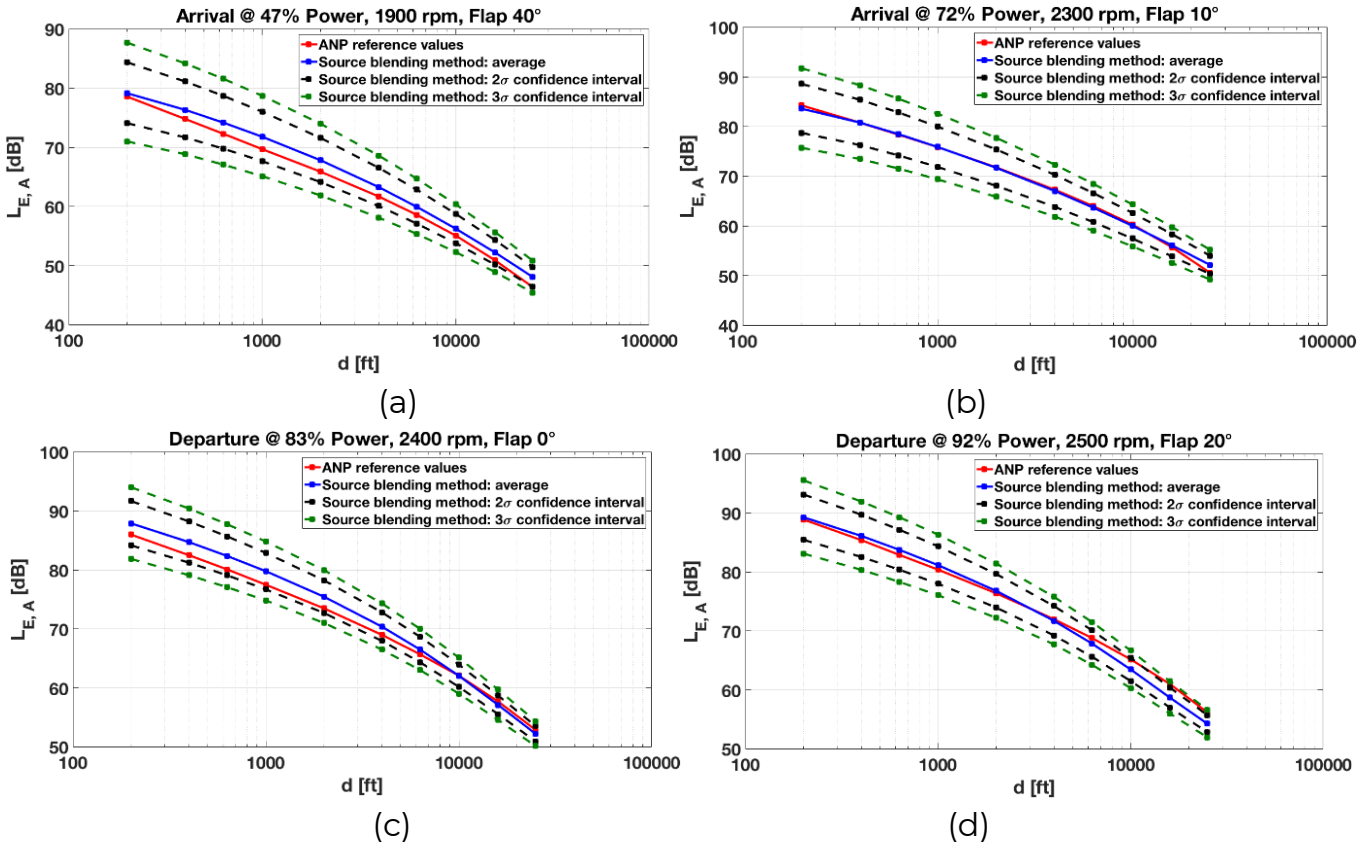


Figure 3.17 Comparison of SEL data from ANP database and predictions from the source-blending method, with coefficients designed on the aircraft in Tab.1. Results for a Cessna T206H Stationair. (a,b) Arrival procedures. (c,d) Departure procedures.

Comparing the red (ANP) and blue (source-blending) lines, the similarity between the output of the two methods is remarkable. The dashed lines on the plot are obtained considering a confidence interval over the values of the blending coefficients. The dispersion is rather high, due to the fact that the data from the database are rather scattered, with an ensuing scatter effect when applying the blending coefficients uncertainty limits to the case of a singly aircraft.

Application of the source-blending case to hybrid-electric aircraft will be shown for the case of the Pipistrel Panthera Hybrid, a novel series-hybrid version with similarities to its conventionally powered version. Considering the series-hybrid configuration, the propeller and electric motor work in a strictly coupled fashion, and the same applies to the internal combustion engine and gearbox. For this reason it makes sense to compare the noise level pertaining to these two couples of sources.

Concerning the propeller and electric motor, five values of power and propeller rotational speed have been selected in the case of the Pipistrel Panthera,

corresponding to fractions between 20% and 100% every 20% of the nominal value. A linear relationship between power and rotational speed for the propeller is implicitly assumed. The corresponding noise emissions are computed through the respective models, and the results are presented in Table 3.3. The more intense contribution from the propeller is clearly evident, and allows to exclude electric motor from the noise sources.

Table 3.3 Predicted sound power comparison between propeller and electric motor for a Pipistrel Panthera.

| Motor power/speed setting | Propeller [dB] | Electric motor [dB] | Difference [dB] |
|---|---|---|---|
| 200 kW, 2,400 rpm | 130.6 | 102.7 | 27.9 |
| 160 kW, 1,920 rpm | 123.5 | 100.3 | 23.2 |
| 120 kW, 1,440 rpm | 115.7 | 97.1 | 18.6 |
| 80 kW, 960 rpm | 106.9 | 92.7 | 14.2 |
| 40 kW, 480 rpm | 96.1 | 85.2 | 10.9 |

Table 3.4 Predicted sound power comparison between engine and gearbox for a Pipistrel Panthera.

| Engine power/speed setting | Engine [dB] | Gearbox [dB] | Difference [dB] |
|---|---|---|---|
| 115 hp, 5,800 rpm | 123.0 | 113.3 | 9.7 |
| 92 hp, 5,800 rpm | 123.0 | 112.9 | 10.1 |
| 69 hp, 5,220 rpm | 121.2 | 112.3 | 8.9 |
| 46 hp, 3,828 rpm | 115.8 | 111.2 | 4.6 |
| 23 hp, 3,828 rpm | 115.8 | 110.0 | 5.8 |

A similar comparison is carried out considering the internal combustion engine and gearbox. Here the database by Yakovitch (Yakovitch, et al., 2016) has been adopted to convert the rotational speed into power. The results of the comparison are presented in Table 3.4. It can be noticed that the noise pertaining to the engine changes with the rotational speed, and not with power, according to the corresponding model. From Table 3.4 the prevailing contribution of the engine is clearly apparent. This in turn allows to rule out the contribution of the gearbox.

### 3.1.7 Example analysis on acoustic prediction with CHANCES

The methodologies presented in 3.1.4 and 3.1.6 have been assembled in a comprehensive computational tool called CHANCES, an acronym for *Component-Based, Hybrid-electric Aircraft Noise and Chemical Emission Simulation*. The

application of this tool to noise prediction examples will be presented in the next paragraphs.

#### *3.1.7.1 Noise prediction – Effect of power generation system use*

The method described above has been deployed to compute the noise of hybrid-electric aircraft. As stated above, the test-case of Milan-Bresso aerodrome has been selected, as this is a noise-critical airport surrounded by densely populated areas. The fleet of Aero Club Milano operates from here with aircraft in the category considered for the design of the blending coefficients.

Results are presented for the case of a Cessna T206H Stationair and for a twin-engined Piper PA-31-350 Navajo Chieftain. In order to simulate hybrid-electric aircraft corresponding to these two models, it has been hypothesized to be able to fly the circuit with or without their actual internal combustion engines running. As no original aircraft specification has been altered, it has been implicitly hypothesized that having the hybrid-electric powertrain (including the batteries) on board would not alter the weight and performance of these aircraft.

In order to assess the effect of the activation of the power generation system over a circuit, seven cases have been considered, reported in Table 3.5. The extreme cases correspond to a conventional, fuel-burning circuit (1) and to a completely electric strategy (7).

Table 3.5 Power generation system activation options.

| ID | Circuit legs w. piston engine running |
|---|---|
| 1 | All |
| 2 | Departure, Crosswind |
| 3 | Departure, Crosswind, Downwind |
| 4 | Downwind |
| 5 | Downwind, Base, Final |
| 6 | Base, Final |
| 7 | None |

Noise has been predicted in terms of SEL on two different grids of sensors. The first is more refined and covers the ground trace of RWY18 right-hand circuit of Milan-Bresso with 76 sensors (see Figure 3.18).

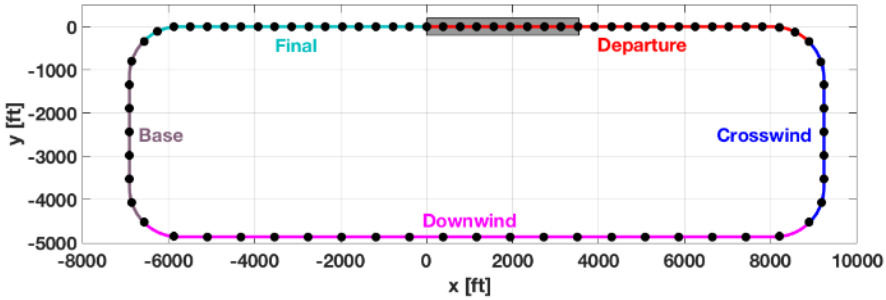


Figure 3.18 Ground trace geometry discretization for the RWY18 right-hand circuit of Milan-Bresso.

In order to provide a comprehensive measurement, the SEL values corresponding to all sensor in a leg along the ground trace are energetically summed together (see Figure 3.18). A comparison of the effect of the different strategies in Table 3.5 is shown in Table 3.6 and Table 3.7 respectively for the Cessna T206H and for the Piper PA-31-350.

It can be noticed that the departure, crosswind and final legs are associated to a generally higher SEL. The result for the first two can be expected, whereas the higher noise in final is due to the spill-over on the corresponding sensors from the departure phase. Downwind and base are associated to generally lower noise, due to lower power regimes and greater distance from the ground. In terms of aircraft, noise for the Piper is generally higher, thanks to the greater size, weight and multiple-engines configuration. Considering activation strategies, of course number strategies 1 and 7 correspond to the highest and lowest SEL respectively. Intermediate strategies tend to polarize around two extreme solutions. Considering cases 4 to 7, where at most only legs corresponding to low power settings are flown with the power generation system running, these produce lower noise values over all circuit than the cases 1 to 3, where the engine is running in circuit phases closer to the ground and at higher power settings.

Table 3.6 Global SEL for the Cessna T206H Stationair. Results for activation strategies in Table 3.5.

| ID | Departure [dB] | Crosswind [dB] | Downwind [dB] | Base [dB] | Final [dB] | All [dB] |
|---|---|---|---|---|---|---|
| 1 | 93.18 | 83.22 | 78.82 | 76.22 | 88.92 | 88.15 |
| 2 | 93.15 | 83.02 | 76.44 | 74.39 | 88.68 | 87.99 |
| 3 | 93.16 | 83.22 | 78.79 | 74.82 | 88.69 | 88.08 |
| 4 | 90.22 | 80.45 | 78.48 | 74.79 | 86.21 | 85.43 |
| 5 | 90.26 | 80.45 | 78.52 | 76.20 | 86.62 | 85.55 |
| 6 | 90.26 | 80.06 | 75.97 | 75.89 | 86.61 | 85.38 |
| 7 | 90.22 | 80.06 | 75.91 | 74.36 | 86.20 | 85.25 |

Table 3.7 Global SEL for the Piper PA-31-350 Navajo Chieftain. Results for activation strategies in Table 3.5.

| ID | Departure [dB] | Crosswind [dB] | Downwind [dB] | Base [dB] | Final [dB] | All [dB] |
|---|---|---|---|---|---|---|
| 1 | 97.25 | 87.83 | 83.19 | 80.30 | 91.72 | 92.03 |
| 2 | 97.22 | 87.69 | 80.66 | 78.66 | 91.33 | 91.83 |
| 3 | 97.22 | 87.83 | 83.17 | 78.99 | 91.34 | 91.94 |
| 4 | 93.68 | 85.01 | 82.96 | 78.97 | 88.84 | 88.87 |
| 5 | 93.75 | 85.01 | 82.99 | 80.29 | 89.49 | 89.05 |
| 6 | 93.75 | 84.73 | 80.34 | 80.04 | 89.47 | 88.83 |
| 7 | 93.67 | 84.73 | 80.29 | 78.64 | 88.82 | 88.65 |

A second less refined grid has been adopted to study the map of the SEL in the vicinity of the airport. Here the sensor number has been increased to 496, covering an area 30,000 ft long (in the direction of the runway) and 15,000 ft wide.

Example results on this grid are shown pictorially in Fig.4 for both considered aircraft and for the two extreme activation strategies (1 and 7 inTable 3.5).

From Figure 3.19(a) and (b), corresponding to activation strategy 1, it is possible to notice a high intensity core close to the runway threshold and reaching to the final leg of the circuit. This further explains the relatively high noise associated to this phase, as seen through the analysis on the first grid of sensors. Figure 3.19 (c) and (d), referring to strategy 7, show the disappearance of the high intensity core, and show a generally lower value of SEL, as expected. The noise pertaining to the Piper aircraft is clearly higher than that for the smaller Cessna, as it can be seen comparing Figure 3.19 (a) to (b) and Figure 3.19 (c) to (d) respectively.

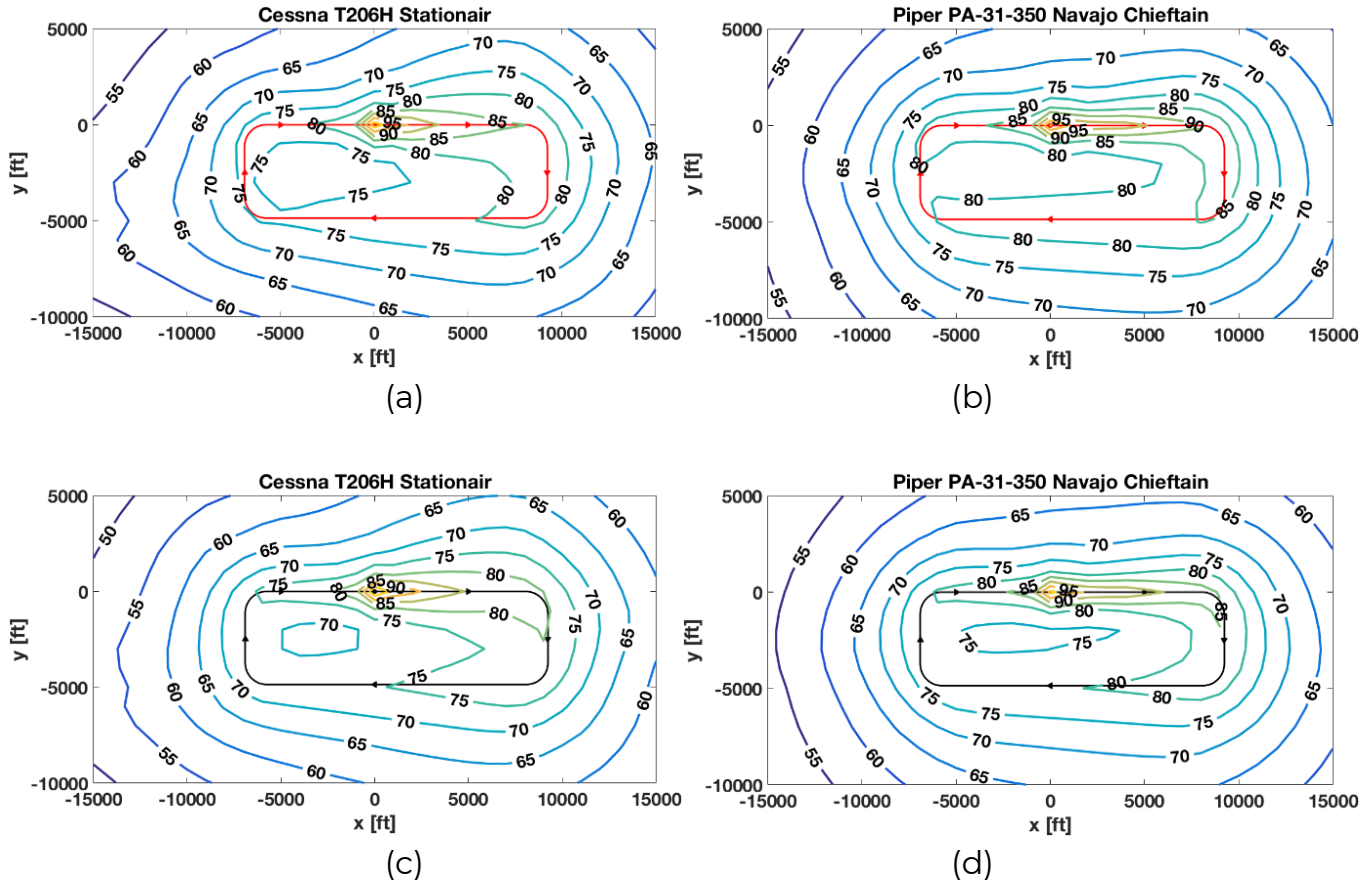


Figure 3.19 Contour plots of SEL over and extended sensor grid around Milan-Bresso aerodrome. (a,b) Case 1, (c,d) case 7 (seeTable 3.5). (a,c) Cessna T206H Stationair, (b,d) Piper PA-31-350 Navajo Chieftain. Values in dB.

### *3.1.7.2 Noise prediction – Comparison of different aircraft*

Based on the same circuit analysed in 3.1.7.1, a second assessment of noise is proposed, this time considering three existing aircraft, namely a Cessna C172R Skyhawk, a Pipistrel Panthera, and the hybrid-electric version of the latter, the Pipistrel Panthera Hybrid.

The trajectory computed for the C172R along the circuit, based on ANP databases performance data, has been adopted also for the two Panthera aircraft. While on one side slightly inaccurate with respect to reality, this choice carries the advantage of a fairer noise comparison, where distance from ground is not a possible cause for unfair advantages. The C172R and the conventionally-powered Panthera fly the circuit with the engines always operating, whereas the power generation system of the Panthera Hybrid is switched on only above the altitude prescribed by the manual, corresponding to the downwind altitude of 1,000 ft AGL.

The resulting maps, computed on the same grid as the case portrayed inFigure 3.19, are reported in Figure 3.20. As observed in 3.1.7.1, the most intense values of SEL have

been recorded on ground and along the short final, which correspond to higher power setting and lower slant distances between the aircraft and sensor.

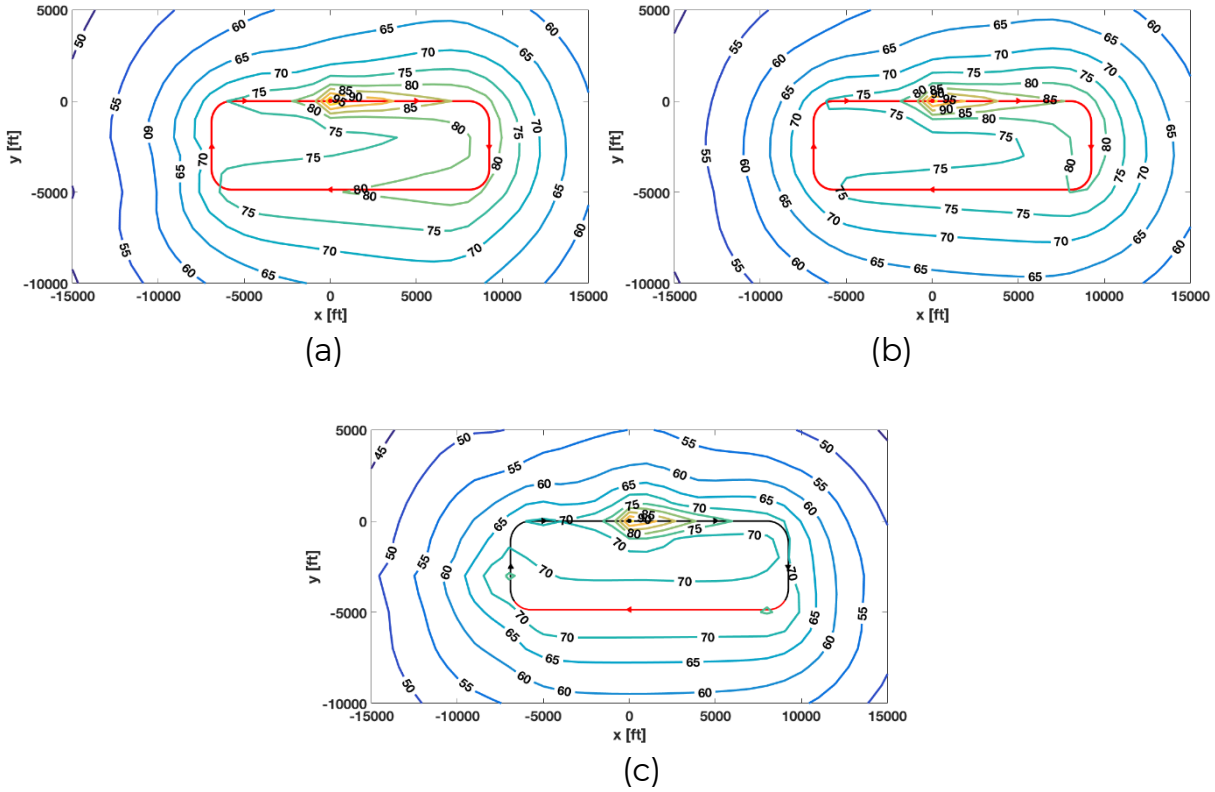


Figure 3.20 Contour plots of the SEL, same grid as Figure 3.19 (a) Cessna C172R, (b) Pipistrel Panthera, (c) Pipistrel Panthera Hybrid. Values in dB.

Looking at the two conventionally-powered aircraft in Figure 3.20 (a) and (b), the maps are generally similar, except for a somewhat higher intensity in the first part of the downwind for the C172R. On the other hand, the map for the Panthera Hybrid (Figure 3.20 (c)) features a markedly lower noise intensity, especially along the take-off run and crosswind. The SEL level is lower than for conventionally-powered aircraft also for the downwind leg, which is flown with the power generation system on, but a contour line parallel to the trajectory at 70 dB makes this map rather different from the other two.

### 3.1.8 Conclusions

A method blending the output of several sources on board the aircraft to obtain an overall figure comparable to that of comprehensive methods based on database (currently inapplicable to hybrid-electric aircraft) has been proposed. The coefficients are tuned in the case of conventionally-powered aircraft, and applied to hybrid-electric aircraft, making possible to quantitatively assess the advantages provided by an innovative power-train in terms of acoustic pollution around the reference case of an existing General Aviation airport.

## *3.2 Chemical emissions*

### 3.2.1 Introduction

In this section, how to assess chemical emissions in the scenarios of interest for the UNIFIER19 project will be discussed. First, the targets for this project will be recalled, followed by a short background on chemical emissions and pertinent measures. Then, an overview of the available methods to compute chemical emissions as a result of combustion are presented. Furthermore, the indications of current regulations will be touched upon. A comparison will be made between existing emission inventories, aircraft performance codes considered in those inventories, as well as the most important emission databases. Finally, a short description of the chemical module in CHANCES is presented, followed by some final considerations.

### 3.2.2 Target for the current project

The target at this stage of the project is that of defining a novel metric that takes into account the different and contrasting aspects of designing an aircraft for both environmental sustainability and marketability.

The emission parameters will be related in particular to $CO_2$ and $NO_x$ emissions, i.e. the most relevant side-products of combustion processes with a potential impact on climate-alteration and pollution respectively. A match will be tried with respect to the social reduction goals identified in T1.2.

In the initial agreement for UNIFIER19, it was stated that this project aims at a $CO_2$ and $NO_x$ emission reduction of 20%. After further analysis of the state of the art and of current designs under study, however, it has been agreed that the target improvement on emissions was not ambitious enough, and consequently it has been increased to above 40% with respect to a reference based on 2014 standard propulsion technology.

### 3.2.3 Background on emissions

To fully evaluate the emissions impact of aviation, ideally one has to take the whole lifecycle into account. Taking inspiration from the *Greenhouse gases, Regulated Emissions, and Energy use in Transportation* (GREET) model, sponsored by the Argonne National Laboratory, the fuel cycle "from well to wheel", as well as the vehicle cycle through material recovery and vehicle disposal, need to be considered.

Processes involved in the lifecycle of an (hybrid-electric) aircraft which produce chemical emissions include combustion, production of electricity, and production of batteries.

Considering combustion, aircraft emissions result from the oxidization of fuel by air. The reactants are:

- Fuel, $C_nH_m + S$
- Air, $N_2 + O_2$

Ideally, the combustion products should be:

- Carbon dioxide, $CO_2$
- Water (vapour), $H_2O$
- Sulphur dioxide, $SO_2$

However, due to incomplete sub-reactions and to the effect of the separation of products, primarily bound to high temperature of reaction, the products of real combustion include as well:

- Nitrogen oxides, $NO_x$
- Unburned hydrocarbons, UHC
- Carbon monoxide, $CO$
- Soot, $C_{soot}$
- Sulphur oxides, $SO_x$

The average aviation fuel is assumed to be kerosene, with a basic molecule $C_{12}H_{22.4}$. On average, civil aviation in 2002 has been responsible for the following emissions, according to (Eyers, et al., 2004), as shown in Table 3.8.

Table 3.8 Average emission of products of combustion for aviation in 2002.

| Species | Emission index [g/kg] | Emission rate [Mt/year] |
|---|---|---|
| $CO_2$ | 3,154 | 492 |
| $H_2O$ | 1,237 | 193 |
| $NO_X$ | 13.2 | 2.06 |
| $CO$ | 3.25 | 0.507 |
| UHC | 0.4 | 0.063 |
| Soot | 0.025 | 0.0039 |

Considering the species of interest reported in Table 3.8, where $CO_2$ and $H_2O$ emissions are basically function of fuel flow, dependencies are more articulated for other exhaust components. Since the combustion process is not ideal and often incomplete, unburned hydrocarbons (UHC) and carbon monoxide ($CO$) are being produced during real engine operation. They are mostly produced at low power settings, when fuel/air mixing processes are less efficient. On the contrary, nitric oxides ($NO_x$) are mainly produced at high power levels, when high temperatures ( $T > 1{,}300°C$ ) are encountered. In the latter case, the formation rate is primarily a function of temperature and of the residence time of nitrogen at that temperature.

The three most relevant figures related to emissions of any species are the total amount of thrust (T in N) or power (P in W), the fuel flow ($\dot{m}_{fuel}$ in kg/s) and the emission index ($EI_k$ in $g_{species}/kg_{fuel}$).

Now the emission $m_k$, pertaining to a given chemical component $k$ and to a flight movement can be defined as:

$$m_k = \int_0^t EI_k \cdot \frac{dm_{fuel}}{dt} dt \approx \sum \dot{m}_{fuel} \cdot EI_k \cdot \Delta t \tag{3.18}$$

### 3.2.4 Overview of calculation methods for combustion

The method that can be used to compute chemical emissions depends on the considered combustion product. The first distinction that can be made is whether or not emissions are proportional to fuel burn. For emissions that are not directly proportional to fuel burn, methods with different levels of fidelity are available. The species that are directly proportional to fuel burn are carbon dioxide ($CO_2$), water vapour ($H_2O$) and sulphur oxides ($SO_x$).

#### *3.2.4.1 Proportional to fuel burn*

Considering the average aviation fuel, the emission indices for carbon dioxide ($CO$) and water vapour ($H_2O$) are 3,154 and 1,237 g/kg respectively. The emission indices are based on the assumption of an ideal and complete combustion. As the combustion is typically not ideal (i.e. 100% complete), an attempt to correct the emission index of carbon dioxide can be made using the following equation, relating the emission indices of $CO_2$ and $CO$,

$$EI_{CO_2} = EI_{CO_2}^{ideal} - \frac{44}{28} EI_{CO}. \tag{3.19}$$

#### *3.2.4.2 Engine cycle modelling*

Thermodynamic cycle analysis is often considered a reliable technique for the analysis and design of gas turbine engines. The object of cycle analysis is to obtain estimates of the performance parameters (thrust, power and specific fuel consumption) in terms of design parameters, either more free to set (such as the compressor pressure ratio etc.) or more heavily constrained by technological limitations (such as maximum allowable turbine temperature), and of flight conditions.

When designing a new engine, a cycle analysis is commonly the first step in the process. However, seen from the standpoint of chemical emission assessment, it brings in as a side-product a significantly more detailed and complete description than lower-fidelity methods. As argued in (Hendricks & Gray, 2019), the design of an electric propulsion system concept can greatly benefit from a tightly coupled cycle analysis tool, as a result of the strong interactions between the power-train electrical and thermal management systems.

In the work (Hendricks & Gray, 2019), the Authors compare their open source cycle tool "pyCycle" with the legacy code NPSS by NASA. The reference engine they compared is the NASA advanced technology high-bypass geared turbofan engine cycle, referred to as the "N+3" engine. They model its cycle with a multi-design-point process that simultaneously considers performance at four different flight conditions. Examples of components that can be modelled include inlets, compressor stages, combustion

chambers, turbine stages, nozzles, gearboxes, etc. The maximum relative error between this open-source cycle tool and NPSS for any thermodynamic property was found to be approximately 0.03%, which can be considered an excellent agreement. Both codes can be henceforth considered as reliable tools for cycle characterization, and in turn as source of data for predicting chemical emissions.

#### *3.2.4.3 The P3T3 method*

Possibly the most widespread method for computing aircraft engine emissions of $NO_x$, $HC$, and $CO$ is the so-called *P3T3* method. It requires a detailed knowledge of some parameters along the path followed by the gas mixture moving in the engine. The name of the method comes from a basic relationship assumed between the total pressure and temperature at the inlet of the combustion chamber ($P_3$ and $T_3$) and the fuel flow $\dot{m}_f$. In addition, knowledge of ambient atmospheric humidity is required for calculating $NO_x$ emissions.

Over the course of time, semi-empirical correlations of emissions with $P_3$ and $T_3$ have been developed. These correlations are generally applied as follows. First, the aircraft mission profile is assigned. Then, an airplane performance prediction code is executed to run the mission, producing as output engine thrust and fuel flow at discrete points along the mission profile. These points are used as an input for the engine performance model, that will output the respective $P_3$ and $T_3$ for each point. For each point, the corresponding $T_3$ for that flight condition is used to enter a lookup table provided for each emission index at sea level (for instance, $EI_{NO_x}^{SL}$) and reference sea level compressor exit pressure ($P_3^{SL}$). The lookup is based on the sea level static, standard day emissions correlation developed from emission certification testing.

The so-obtained reference emission indices are then corrected to flight conditions.

In (DuBois & Paynter, 2006), the following relations have been suggested for the estimation of $EI_{NO_x}^{alt}$ at an altitude:

$$EI_{NO_x}^{alt} = EI_{NO_x}^{SL} \cdot \left(\frac{P_3^{alt}}{P_3^{SL}}\right)^{y} \cdot e^{H} \cdot \left(\frac{FAR^{alt}}{FAR^{SL}}\right)^{z}. \tag{3.20}$$

The exponents of $x$ and $y$ are unique to an assigned engine, and are empirically derived by the manufacturers.

Following another approach, (Kyprianidis, Nalianda, & Dahlquist, 2015) presents the following relation for $NO_x$ in modern RQL combustors:

$$EI_{NO_x} = (a + b \cdot e^{c \cdot T_{31}}) \left(\frac{P_{31}}{P_{31}^{ref}}\right)^{d} e^{f(\Phi^{SL} - \Phi)} \left(\frac{\Delta T_c}{\Delta T_c^{ref}}\right)^{TF}, \tag{3.21}$$

where $a = 8.4$, b $= 0.0209$, $c = 0.0082$, $d = 0.4$, $f = 16$. Furthermore, $P_{31}^{ref} = 3{,}000$ kPa, $\Delta T_c^{ref} = 300$ K, and $\Phi^{SL} = 0.006344$ $\frac{kg_{H_2O}}{kg_{air}}$. Factor $TF$ can be considered as a technology factor, for adapting the proposed correlation to experimental data as technology improves.

In (Tacina & Wey, 2008) the following correlation has been found for Lean Direct Injection (LDI) combustors:

$$EI_{NO_x} = 1.359 e^{\frac{T_3}{194}} FAR^{1.69} P_3^{0.595} \left(\frac{\Delta P}{\Delta P_3}\right)^{-0.565}. \quad (3.22)$$

One of the major shortcomings of the *P3T3* method is that it requires some knowledge of the airplane – like thrust and some engine internal parameters, as well as some correlations – that are engine specific.

In an attempt to let public subjects perform calculations on aircraft emissions, a new model needed to be found that was solely based on publicly available data, in contrast to the proprietary data required for the *P3T3* methods. In this quest, it was found that fuel flow was the most easily measurable engine operation parameter yielding a correlation with chemical emissions. For this reason, a special effort was dedicated towards the synthesis of emission prediction methods based fuel flow as a measure.

#### *3.2.4.4 Fuel flow methods*

Again, the *P3T3* method determines the emission indices using the $T_3$ at altitude to look up an $EI^{SL}$ at sea level, and then applying a pressure correction.

The $EI^{SL}$ at sea level are typically available to operators only as functions of fuel flow and thrust. Engine power in flight can be measured too, similar to fuel flow. Therefore, if a connection can be envisaged to correlate $T_3$ and fuel flow, then a basis for a prediction method based on fuel flow could be synthesized. This correlation was investigated by (DuBois & Paynter, 2006). They propose also a correction based on ambient (or freestream) pressure.

Following this approach, they developed the *Boeing Fuel Flow Method 2* (BFFM2), which also takes into account the difference in airflow rates through the combustor between sea level and actual flight conditions at an altitude. The steps considered in the fuel flow method are described below.

The first step is to correct the tabulated data from engine certification for installation effects by use of the following equation:

$$\dot{m}_{fuel}^{SL} = r \cdot \dot{m}_{fuel}^{ICAO}. \quad (3.23)$$

where $r$ is a correction factor coming from Table 3.9.

**Table 3.9 Correction factor on nominal data for fuel flow, as a function of the operation regime, for Boeing Fuel Flow Method 2.**

| | Take-off | Climb | Approach | Taxi / Idle |
|---|---|---|---|---|
| Thrust setting [% $F_{00}$] | 100 | 85 | 30 | 7 |
| Correction factor $r$ | 1.01 | 1.013 | 1.02 | 1.1 |

The fuel consumption at a reference condition is computed combining the following expressions:

$$\dot{m}_{fuel}^{SL} = \dot{m}_{fuel}^{alt} \frac{\theta^{3.8}}{\delta_{amb}} e^{0.2M^2} \tag{3.24}$$

$$\delta_{amb} = \frac{P_{amb}}{101.3} \tag{3.25}$$

$$\theta_{amb} = \frac{T_{amb}}{288.15} \tag{3.26}$$

where $\dot{m}_{fuel}^{SL}$ is the actual fuel flow at reference conditions in kg/s, $\dot{m}_{fuel}^{alt}$ is the actual fuel flow at altitude in $kg/s$, $P_{amb}$ is the ambient pressure at altitude in kPa, $T_{amb}$ is the ambient temperature at altitude in K, and $M$ is the Mach number.

Based on $\delta_{amb}$ and $\theta_{amb}$ parameters, the following relations can be used to produce the emission indices:

$$EI_{HC}^{alt} = EI_{HC}^{SL} \left( \frac{\theta_{amb}^{3.3}}{\delta_{amb}^{1.02}} \right)^{x} \tag{3.27}$$

$$EI_{CO}^{alt} = EI_{CO}^{SL} \left( \frac{\theta_{amb}^{3.3}}{\delta_{amb}^{1.02}} \right)^{x} \tag{3.28}$$

$$EI_{NO_x}^{alt} = EI_{NO_x}^{SL} \left( \frac{\delta_{amb}^{1.02}}{\theta_{amb}^{3.3}} \right)^{y} e^{H} \tag{3.29}$$

with:

$$H = -19(\omega - 0.0063). \tag{3.30}$$

Here $EI_k$ is the emission index for species $k$ at flight condition in g/kg, $EI_k^{ref}$ is the emission index for species $k$ at reference condition in g/kg, $H$ is a humidity correction factor, and $\omega$ is specific humidity. The coefficients $x$ and $y$ are assumed to be 1 and 0.5, unless engine-specific values are known from the manufacturer.

From emission indices and fuel flows, it is possible to retrieve the relative flow of each emitted species.

#### *3.2.4.5 Omega correlation method*

With the *Omega correlation*, the German Aerospace Centre (DLR) uses an alternative method to estimate the emissions of $CO$ and $UHC$. The emissions of these species result from incomplete combustion and are mostly produced at lower power settings of the engines, where the efficiency of the combustion process is low. The combustion efficiency can be correlated with a parameter Ω, which is the reciprocal value of the simplified combustor loading parameter Θ. Omega is given by

$$\Omega = \frac{w_{air}}{V_C P_3^{1.8} e^{\frac{T_3}{300}}}. \tag{3.31}$$

The emission indices for the two mentioned species come in the following form

$$EI_{CO}, EI_{HC} = f(\Omega V_C) \cdot \left\{ \frac{T_3}{T_{3,ref}} \cdot \frac{P_{3,ref}}{P_3} \right\}^c. \tag{3.32}$$

Compared to a fuel flow correlation method, the *Omega correlation* method may describe the physical processes more accurately. The main drawback of such method however is the fact that detailed engine simulation is required in order to estimate combustor inlet properties.

### 3.2.5 Regulation

Aircraft engines have to comply with emission standards defined by the ICAO in Annex 16 Volume II to the Convention on International Civil Aviation. This regulation contains upper limits for $CO$, $UHC$, $NO_x$ and soot emissions during a standardized landing and take-off (LTO) cycle. As part of the certification process, emission data for new engines are provided by the engine manufacturer and collected in the publicly available aircraft *Engine Emissions DataBank* (EEDB). The standards apply for engines with a take-off thrust of more than 26.7 kN at ISA sea level static conditions.

The ICAO standards where instrumental in controlling local air quality in the vicinity of big airports, according to (Schaefer, 2006). Therefore, the aircraft movements of interest where taken below a 3,000 ft altitude (see Figure 3.21).

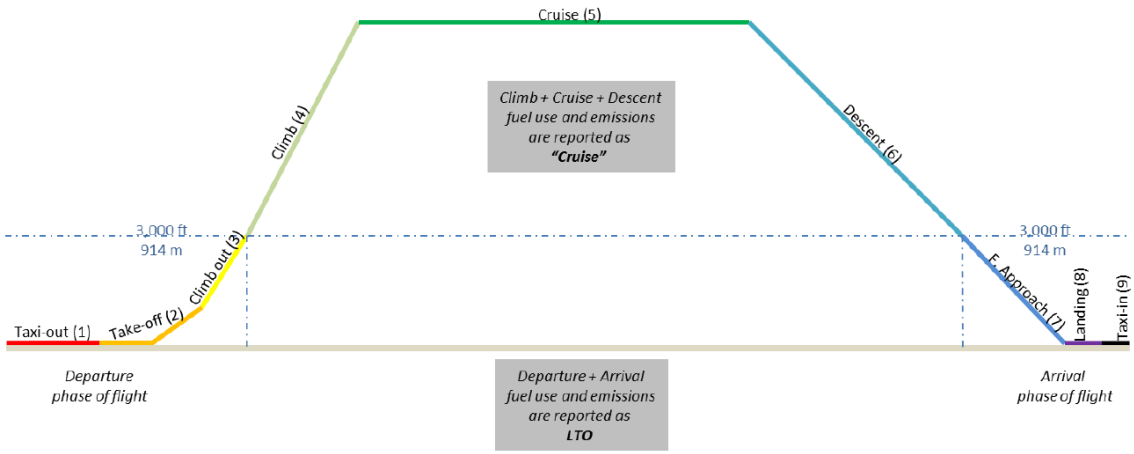


Figure 3.21 Typical LTO cycle. Note the 3,000 ft threshold.

The LTO cycle is defined by taking 4 phases of a prototypal flight profile, namely take-off, climb, approach, and taxi/idle, with corresponding conventional values of thrust setting and duration (see Table 3.10).

Table 3.10 Standard duration and thrust settings for an LTO cycle.

| | Take-off | Climb | Approach | Taxi / Idle |
|---|---|---|---|---|
| Thrust setting [$\%F_{\infty}$] | 100% | 85% | 30% | 7% |
| Time [min] | 0.7 | 2.2 | 4.0 | 26 |

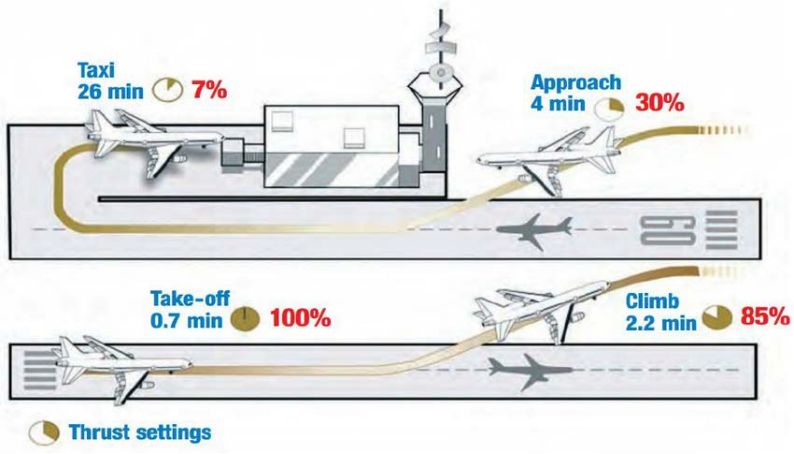


Figure 3.22 Graphical representation of an LTO cycle with standard durations and thrust settings.

With new technologies such as hybrid-electric aircraft, a chance is offered to run some of the mission profile phases (Figure 3.22) on a non-polluting energy and power source. Thereby, the local pollution will be significantly lower compared to the conventional LTO operation of a conventional aircraft.

### 3.2.6 Available emission inventories and design tools

In order to properly bookkeep the chemical emissions due to aviation, several emission inventories have been setup. Generally, these inventories are updated every year with new data. The majority of the emission inventories are based on a bottoms-up modelling approach. Global flight operations are collected in an aircraft movements database. Combinations of routes, aircraft and engines are made, and flight paths and trajectories are assumed. For each single flight, the fuel burned along the corresponding flight path is computed using aircraft and engine performance data. The engine emissions are then determined by making use of an emission model. The result comes in the form of accumulated data from all flights, placed on a 3D world grid. Summarizing, the following elements are required to add to the database:

- Trajectory information
- Detailed performance data of the aircraft and engines
- Detailed data on the emission characteristics for all operating points and flight phases

Clearly, the more detailed the emission models are, the more accurate the final result. Concerning UNIFIER19, the way other inventories deal with the emission characteristics is of particular interest to inspire our own approach.

#### *3.2.6.1 Advanced Emission Model (AEM)*

The *Advanced Emission Model* is developed by EUROCONTROL. It processes flight movements to estimate the amount of fuel burnt, then estimates the emissions that result from the combustion of fuel in engines. A flight movement is defined precisely, as a 4D ground and flight trajectory of an aircraft (i.e. an airframe plus its engine(s)).

Above a 3,000 ft altitude, for climb, cruise and descent phases, this model makes use of the *Base Aircraft Data* (BADA) (see below) database to estimate the fuel burnt. BADA provides altitude- and altitude-dependent performance and fuel burn data for more than 200 aircraft types. Once the fuel burnt is known, the *Boeing Fuel Flow Method 2* (BFFM2) (see above) is used to estimate the $NO_x$, $UHC$ and $CO$ emissions. The emissions of $CO_2$, $H_2O$ and $SO_x$ are assumed to be proportional to the mass of the fuel burnt. The VOCs are assumed to be proportional to the mass of the $UHC$ produced. For altitudes lower than 3,000 ft, the fuel burnt, $NO_x$, $UHC$ and $CO$ are estimated using the ICAO *Aircraft Engine Emissions Databank* (EEDB) (see above) or other databases.

#### *3.2.6.2 Aviation Environmental Design Tool (AEDT)*

The FAA's *AEDT* is a tool capable – among its many functionalities – of modelling fuel burn and emissions for environmental analysis. The emissions modelling is based on the *Boeing Fuel Flow Method 2* and is used to compute $NO_x$, $HC$, and $CO$. Fuel-composition-based factors are used to compute $SO_x$, $CO_2$, and $H_2O$.

#### *3.2.6.3 AERO2k*

The *AERO2k* emission inventories were developed as part of the European Community's 5th Framework Program. Fuel burn and emissions for the LTO cycle are obtained from ICAO's emission database EEDB. For each airport, specific times-in-modes are used. For climb, cruise and descent, look-up tables have been produced by the aircraft performance software PIANO.

#### *3.2.6.4 NASA 1999 inventory*

In the NASA inventories, the flight performance models are based on an in-house developed software called *Boeing Mission Analysis Program* (BMAP). Emission indices synthesized as per ICAO recommendation have been used in combination with estimations from the *Boeing Fuel Flow Method 2*.

#### *3.2.6.5 SAGE inventory*

In the FAA's SAGE inventories, BADA is used as the performance model for in-flight fuel burn calculations. Emission indices synthesized as per ICAO recommendation have been used in combination with estimations from the *Boeing Fuel Flow Method 2*.

#### *3.2.6.6 Base of Aircraft Data (BADA)*

The *Base of Aircraft Data* (BADA) of EUROCONTROL is an aircraft performance model capable of replicating realistic performance of almost any aircraft that flies commercially today. The aircraft model in BADA assumes the aircraft behaves as a point mass moving in 3D space. It balances the rate of work done by forces acting on the aircraft and the rate of increase in potential and kinetic energy. This total energy model is based on the following equation

$$(T - D)V_{TAS} = mg\frac{dh}{dt} + mV_{TAS}\frac{dV_{TAS}}{dt}, \tag{3.33}$$

where $(T - D)$ is excess thrust, $V_{TAS}$ is true airspeed, $m$ is mass and $h$ is altitude.

BADA figures include model specifications which provide the theoretical fundamentals to compute aircraft performance parameters, and the datasets containing aircraft-specific coefficients required to calculate their trajectories.

#### *3.2.6.7 Aircraft Engine Emissions Databank (EEDB)*

The *Aircraft Engine Emissions Databank* (EEDB) is one of the most widespread and complete databases for the calculation of emissions due to aviation activity. It is created by the ICAO, and every engine with a thrust larger than 26.7 kN.

#### *3.2.6.8 Framework for aircraft conceptual design and environmental performance studies*

The purpose of this research by (Antoine & Kroo, 2005) was to explore the feasibility of integrating noise and emissions as optimization objectives at the aircraft conceptual design stage, thereby allowing a quantitative analysis of the trade-offs between environmental performance and operating cost. In the design tool, the researches have incorporated NASA Glenn's *Engine Performance Program* (NEPP) for the engine simulation part. The method to estimate the $NO_x$ emissions is based on an in-house developed *P3T3* relation. Among the variables considered for defining the characteristics of the engines are maximum thrust, turbine inlet temperature, bypass ratio and engine pressure ratio. In Figure 3.23 are reported the typical results of their analysis.

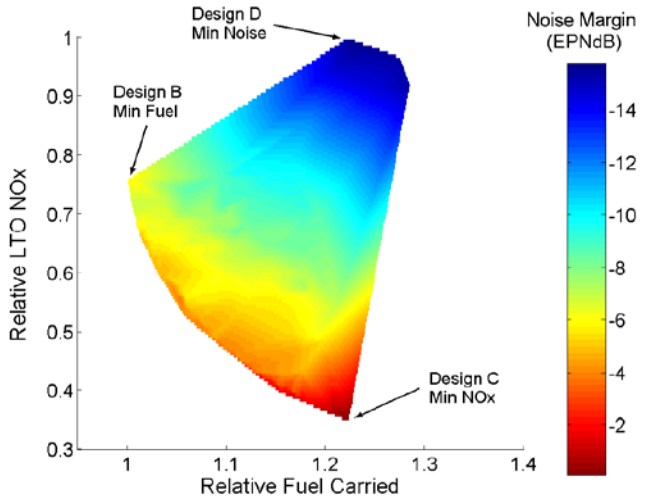


**Figure 3.23 Result of an optimum-seeking analysis in terms of chemical and acoustic emissions vs. fuel carried.**

From this study, it becomes clear that the design space is such that there is not simply one optimal design, but a Pareto front scenario. Depending on what needs to be prioritized, the design and the corresponding outcome in terms of acoustic and chemical emissions may changes dramatically.

#### *3.2.6.9 Multi- objective optimization of aircraft design for emission and cost reductions*

In (Wang, Hailian, Shuai, & Xiongqing, 2014), emissions and direct operating cost are coupled to acquire an insight in the Pareto optimal front introduced above. They proposed an improved method of using the ICAO engine databank EEDB, coupled with polynomial curve fitting methods of representative engines. Also, a new way for accounting for emissions is proposed, in the form of greenhouse gas emission ($CO_2$-equivalent) per seat per kilometre.

#### *3.2.6.10 A commercial aircraft fuel burn and emissions inventory for 2005-2011*

The study (Wasiuk, Khan, Shallcross, & Lowenberg, 2016) is concerned with the emissions of large commercial aircraft that have been already developed, hence they can make use of the existing database of emissions and achieve an accurate estimation of the emissions. For flight performance, BADA has been adopted in this research. The emissions are then corrected for atmospheric conditions encountered in particular flights considered in the scope of the work, by using the *Boeing Fuel Flow Method 2*.

#### *3.2.6.11 Identifying $CO_2$-reducing aircraft technologies and estimating their impact on global emissions*

Reference (Apffelstaedt, 2009) identifies various technological and operational measures to reduce $CO_2$ emissions of individual aircraft and global aviation as well.

Fuel consumption is shown to be a function of mainly aerodynamic efficiency, engine efficiency, empty weight to payload ratio, energy content of the energy carrier per unit weight, specific emission index and the range. The Author adopts the same analysis framework proposed in Greener By Design (2005), yielding the results in Figure 3.24. From this, it can be seen that there is some possible improvement at an engine level.

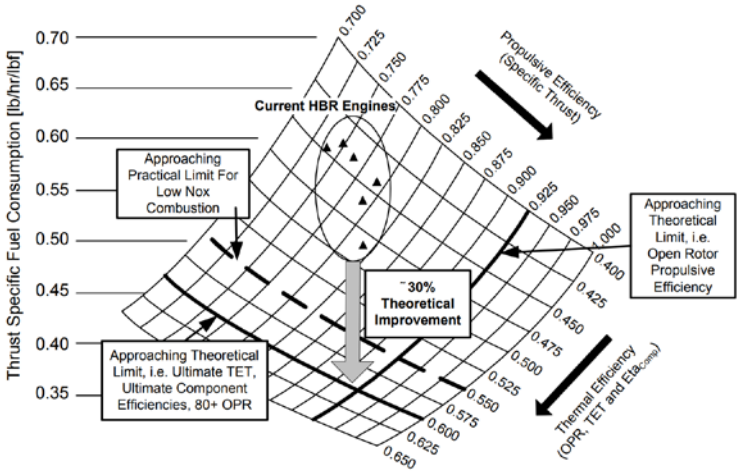


Figure 3.24 Relationship between propulsive efficiency, thermal efficiency and TSFC

### *3.2.6.12 Aircraft APU emissions at Zurich-Kloten airport*

At Zurich airport, a study on the emissions of aircraft APUs has been published in 2005. The importance of taking APUs into account is stressed by the finding that 18.5% of the $NO_x$ emissions during aircraft ground handling are emitted by APUs. The emission factors of various APUs at Zurich airport in 2003 are presented in Table 3.11.

Table 3.11 APU emissions measured at Zurich-Kloten airport in 2003.

| Aircraft group | APU | Representation | FF [kg/h] | $CO$ [g/kg] | $HC$ [g/kg] | $NO_x$ [g/kg] |
|---|---|---|---|---|---|---|
| Large jets | GTCP660-4 | 68% | 435.9 | 8.44 | 0.25 | 5.39 |
| Medium Jets | | 67 | 192.25 | 2.74 | 0.31 | 9.8 |
| Small Jets | GTCP36-150[R] | 28 | 51.95 | 6.12 | 0.84 | 5.59 |
| | GTCP36-300 | 35 | 105.15 | 2.04 | 0.18 | 10.18 |
| | GTCP85-129 | 20 | 86 | 17.86 | 1.13 | 4.63 |
| | Average | 83 | 81.03 | 8.67 | 0.71 | 6.8 |
| Regional Jets | GTCP36-150[R] | 85 | 51.95 | 6.12 | 0.84 | 5.59 |
| Business Jets | GTCP36-150[RR] | 100 | 63.5 | 7.51 | 0.86 | 5.55 |
| Turboprop | GTCP36-150[RR] | 100 | 63.5 | 7.51 | 0.86 | 5.55 |

#### *3.2.6.13 Technical and environmental assessment of all-electric 180-passenger commercial aircraft*

In (Gnadt, Speth, Sabnis, & Barrett, 2018) the potential environmental impact of an all-electric 180-passenger aircraft is assessed.

The size of this aircraft is clearly much larger than a 19-seater of interest for UNIFIER19. However, it is useful to investigate their approach in modelling the environmental impact. The driver for an all-electric aircraft design lies in the opportunity for zero in-flight emissions in the long term, according to the Authors. Biofuels can reduce the lifecycle $CO_2$ emissions, however, the production of these fuels in sufficient quantities would require unprecedented expansions in cultivated land area and rapid investments in biorefinery capacity. On the other hand, the argument of the Authors against hydrogen concerns the danger related to contrails, which can have a significant effect of global climate change.

Reference (Gnadt, Speth, Sabnis, & Barrett, 2018) explains the structure the proposed methodology for the assessment of environmental impact by stating that environmental sustainability depends on the entire energy chain, not just in-flight emissions. They assume two extreme scenarios for evaluating the future environmental performance of aircraft. These are the "business as usual" (BAU) scenario, which assumes limited economic-wide environmental measures, and the "high renewable energy" (HRE) scenario, where substantial economic-wide environmental measures are assumed.

In their methodology, the flight performance module computes the fuel requirements for the conventional aircraft that are needed for the mission. The corresponding equivalent carbon dioxide emissions ($CO_{2,e}$) are then determined using emission indices. The standard emission index for Jet-A fuel is 3,148 $g_{CO2}/kg_{fuel}$. In this research, the current well-to-pump indirect equivalent emissions for Jet-A are assumed to be 826.8 $g_{CO2}/kg_{fuel.}$ Depending on the policy-scenario, this number is assumed to decrease to 616.9 $g_{CO2}/kg_{fuel}$ or 821.3 $g_{CO2}/kg_{fuel}$ respectively by 2050. Another feature of this work is the evaluation of current non-$CO_2$ direct equivalent emissions, namely due to $NO_x$, sulphates, soot, water and contrails. It is estimated between 1,259 and 2,518 $g_{CO2}/kg_{fuel.}$

It is highlighted that the current US average electricity generation shares consist of approximately 17% renewable energy, leading to an emission intensity of around 500 $g_{CO2}$/kWh. That intensity decreases linearly to around 375 $g_{CO2}$/kWh and 150 $g_{CO2}$/kWh in the BAU and HRE scenarios respectively.

In addition, $CO_2$ emissions associated with battery production contribute to the lifecycle emissions for aircraft using batteries. The lifecycle emissions are calculated to be 6 $g_{CO2}/kg_{battery}$ for a Li-ion battery with a specific energy of 114 Wh/kg and a lifetime of around 750-1,200 charge-discharge cycles. Therefore, it can be assumed that for every used kWh, battery production is responsible for the emission of 44-71 $g_{CO2}$/kWh. With some assumptions, the Authors also arrive to a figure of 43-85 $g_{CO2}$/kWh for Li-S batteries. From these results, they conclude that battery manufacturing emissions are around 9% of the total all-electric lifecycle emissions.

### 3.2.7 Prediction of chemical emissions with CHANCES

As mentioned, available methods for the prediction of chemical emissions are classified in three tiers and follow a standard set by the EEA (Winther & Rypdal, 2016). The goal of the existing methods is that of computing chemical emissions at a system level. To this aim, low tier methods apply average data taken from national databases to estimate the number of movements from all airport in a nationwide system and make use of statistical emission data for aircraft. These methods are not sufficiently accurate to resolve the difference between the emission performance of two similar aircraft in a given category and flying an assigned trajectory, as of interest in this study. On the other hand, top-tier methods (class 3B) make use of precise characterization of the aircraft trajectory and flight performance characteristics, and can be profitably applied here.

The same discretization of the flight trajectory adopted for the acoustic analysis (see 3.1.3) and complying with ECAC standard is considered here. The LTO cycle, otherwise associated to a predetermined flight time (lower tier methods), can be computed accurately based on the time actually spent over each leg of the arrival and departure procedures, based on nodal values of speed and geometry data of the discretized trajectory.

A key-factor in the estimation of chemical emissions is the emission index $I_{j,k}$, defined for a chemical component $k$ and a trajectory leg $j$. Databases for estimating this quantity are available from EEA especially for jet engines. Instead, for piston engines such data can be derived from the detailed database by Yakovitch (Yakovitch, et al., 2016), where emission indices for CO, $NO_x$, and UHC (un-combusted hydro-carbons) are provided as a function of the fuel flow. On the other hand, the emission of $CO_2$ is computed based on a pre-determined proportion with respect to the quantity of AVGAS 100LL fuel burned, i.e. 3.067 $g_{CO2}/g_{fuel}$.

A further dependence of the emission index for aspirated engines is from outside air temperature. This has been modelled by FOCA (FOCA, 2007) through a linear law for CO and UHC, whereas no change is expected with temperature for $NO_x$.

According to EEA standard, the mass released in the atmosphere for the $k$-th chemical and due to all contributions from the $N_l$ segments along a trajectory can be computed from Eq.(3.34),

$$m_k = N_e \sum_{j=1}^{N_l} I_{j,k} \dot{m}_{F_j} t_j. \tag{3.34}$$

where $\dot{m}_{F_j}$ is the fuel flow, $t_j$ the time spent by the aircraft in the $j$-th leg. Finally, $N_e$ is the number of engines. As mentioned in the introduction, the LTO cycle is computed below 3,000 ft, hence the mass in Eq.8 corresponds only to the legs of the terminal maneuvers under this altitude. This is not a significant constraint for the case of light-powered aircraft of interest here, which fly terminal maneuvers typically far within this threshold.

The database by Yakovitch provides values for the emission indices and fuel flow, classifying them as related to five flight phases – namely take-off, climb-out, cruise, approach and final approach. In order to compute $\dot{m}_{F_j}$ and $I_{j,k}$ from the database for

each segment in the considered terminal maneuvers (see Figure 3.2), a segment needs to be attributed to one of these categories.

Differently from the noise pollution analysis, no scatter is considered for chemicals, hence the total LTO mass is a primary endpoint of the computation procedure.

To better assess the potential polluting effect of each emitted mass, considering the strong imbalance between mass and harmful effects of some components (like $CO_2$ and $NO_x$), the social cost corresponding to each pollutant has been computed as in Eq.(3.35)

$$C_k = €_k m_k, \tag{3.35}$$

where $C_k$ is the cost per chemical component and $€_k$ is the social cost per unit mass of the $k$-th chemical. Values for the latter can be obtained from the literature (Lu, 2011), and the adopted values are reported in Tab.4 (these refer to currency value in 2008).

**Table 3.12 Social cost per unit mass for the considered chemicals released by internal combustion engines.**

| Chemical | $€_k$ [€/kg] |
|---|---|
| $CO_2$ | 0.035 |
| $CO$ | 0.09 |
| $UHC$ | 4.47 |
| $NO_x$ | 10.05 |

## 3.2.8 Example analysis of chemical emissions with CHANCES

### *3.2.8.1 Effect of power generation system use*

A comparison of the emission of chemicals for different aircraft has been carried out in the same scenario described in section 3.1.7.1.

**Table 3.13 Released masses of chemicals, Milan-Bresso RWY18 right-hand circuit, Cessna T206H Stationair.**

| Circuit leg | $m_{CO2}$ [g] | $m_{CO}$ [g] | $m_{UHC}$ [g] | $m_{NOx}$ [g] |
|---|---|---|---|---|
| Departure | 3,884.7 | 1,320.1 | 35.5 | 6.8 |
| Crosswind | 1,065.0 | 178.5 | 10.3 | 10.4 |
| Downwind | 3,714.4 | 622.5 | 36.0 | 36.3 |
| Base | 783.9 | 212.4 | 9.4 | 3.3 |
| Final | 1,578.2 | 467.6 | 19.3 | 4.3 |

Table 3.14 Released masses of chemicals, Milan-Bresso RWY18 right-hand circuit, Piper PA-31-350 Navajo Chieftain. Computation for one engine only.

| Circuit leg | $m_{CO2}$ [g] | $m_{CO}$ [g] | $m_{UHC}$ [g] | $m_{NOx}$ [g] |
|---|---|---|---|---|
| Departure | 3,330.6 | 1,168.5 | 30.3 | 4.1 |
| Crosswind | 1,134.7 | 398.1 | 10.3 | 1.4 |
| Downwind | 2,566.6 | 445.6 | 24.8 | 24.4 |
| Base | 524.7 | 142.7 | 6.3 | 6.3 |
| Final | 1,196.2 | 354.3 | 14.6 | 3.2 |

Considering a Cessna T206H Stationair and a Piper PA-31-350 Navajo Chieftain, a single engine and twin-engine configuration respectively, the masses released over the five legs of a circuit are reported in Table 3.13 and Table 3.14. Results are proposed for one engine only in the case of the Piper (Table 3.2).

These data show that the Cessna aircraft produces a generally higher mass per engine. As the engines are actually very similar for the two aircraft, this effect is mainly due to the flight trajectory parameters. In particular, as the trajectory is very similar for the two aircraft – only slight discrepancies exist in the access to the crosswind and early downwind legs, as the Cessna climbs faster than the Piper and reaches circuit altitude earlier – the difference is due to airspeed. The higher speed performance of the Piper allows it to fly the circuit faster, hence reducing the time spent over each leg, in turn reducing emissions. For crosswind, the balance is in favour of the Cessna, as part of this leg is flown in cruise mode (lower power setting), as circuit altitude is reached earlier for this aircraft, as just observed.

Table 3.15 Comparison of social cost associated to a single circuit, for different activation strategies of the power generation system.

| ID | Cessna T206H [€] | Piper PA-31-350 [€] |
|---|---|---|
| 1 | 1.990 | 2.901 |
| 2 | 0.781 | 1.217 |
| 3 | 1.593 | 2.325 |
| 4 | 0.811 | 1.108 |
| 5 | 1.208 | 1.684 |
| 6 | 0.397 | 0.576 |
| 7 | 0.0 | 0.0 |

Considering next the same power generation systems activation strategies presented in **Table 3.5**, under the hypothesis of operating an ideal hybrid-electric version of the two aircraft taken as examples (with the same weight and power performance), the results presented in **Table 3.15** are obtained, in terms of social cost for the whole circuit.

It is immediately apparent that the overall cost is generally higher for the twin-engined Piper aircraft, but by a ratio which is clearly less than 2.

This confirms that the number of engines is not the only driver of cost, but the higher airspeed plays a relevant mitigation role.

#### *3.2.8.2 Comparison of different aircraft*

An investigation of the scenario proposed in 3.1.7.2 is proposed also in terms of chemical emissions. Here a Cessna C172R, a Pipistrel Panthera and a Pipistrel Panthera Hybrid fly the same circuit, and the corresponding chemical emissions are predicted. Due to the relevant disproportion between mass and social cost, a comprehensive comparison is more straightforward on the latter performance index. The hybrid version of the Panthera is flown in purely electric mode except above 1,000 ft ground, i.e. basically for the downwind leg.

The results of the analysis are synthetically shown in Figure 3.25.

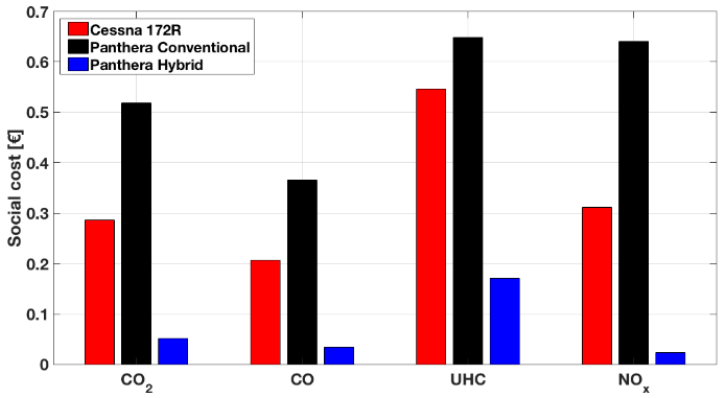


**Figure 3.25 Comparison of social cost corresponding to a Milan-Bresso RWY18 right-hand circuit flown by a Cessna C172R, Pipistrel Panthera and Panthera Hybrid.**

It is noteworthy that from Figure 3.25 it is possible to compute the total mass of each chemical released by each aircraft, using the data in Table 3.12.

The largest contribution to social cost goes generally to the conventional version of the Panthera, which is based on a 260 hp powerplant, whereas the Cessna C172R mounts a less powerful 160 hp engine. The power generation systems of the Panthera Hybrid is also different, besides being activated only for a limited part of the circuit. Looking at the results for the $UHC$, it can be observed that the proportion between the three aircraft, by comparison to the picture for $CO_2$ and $CO$, largely similar to each other, is here in favour of the conventional Panthera. This is specifically due to the better performance of the engine of this aircraft (Lycoming IO-540-V). The opposite happens for $NO_x$, which appears better (lower emissions) for the Cessna C172R. In general terms, the top social cost is due to $UHC$, which despite being associated to a more limited cost per unit mass than $NO_x$, are released in very relevant amounts.

### 3.2.9 Conclusions

The same trajectory segmentation needed to carry out acoustic analyses has been adopted for the assessment of chemical emissions. This has allowed to deploy very accurate methods for the prediction of the social cost of chemicals released by example ideal or existing hybrid-electric aircraft, to the same realistic test case adopted for the acoustic analysis. This analysis too has shown the potential of hybrid-electric powertrains in reducing social cost, thus potentially raising public acceptance and increasing the value of smaller airfields in the air transport infrastructure.

## *3.3 Aircraft costs*

### 3.3.1 Introduction – Life-cycle cost

The costs of development, manufacturing, testing, operation and even disposal are the ultimate drivers in the decision on engaging in a new aircraft programme. A lean and innovative design might look promising from a technical standpoint, but if an advanced performance comes at a high monetary price, e.g. the speed in the Aerospatiale/BAC Concorde, all the technological advantages can be quickly overshadowed by the disadvantageous costs.

Therefore, the cost estimation analysis is a very important – albeit extremely complicated – task, that is essential for the feasibility assessment of the programme.

### 3.3.2 Methodology

In order to estimate the manufacturing and operating costs, several publicly available cost models were analysed to find the most suitable for the case of a 19-seater of interest for UNIFIER19, as none of them is specifically designed for this size of airplane. Also, the adaptation of existing models to cope with new technologies costs has to be feasible without major rework, to allow for a fair and accurate comparison between new and existing technology.

#### *3.3.2.1 Database of existing aircraft and reference aircraft model*

In order to validate the chosen cost models and their adaptation to 19-seater aircraft, a reference airplane was created from a database of the currently existing aircraft in this category. Using existing data, logical values for the different parameters were extracted from average values and trend curves.

The “average” 19-seater aircraft has the characteristics shown in Table 3.16.

Table 3.16: Reference aircraft model parameters.

| | | |
|---|---|---|
| Pax capacity | 19 | seats |
| Pilots | 2 | |
| Maximum Takeoff Weight | 6670 | kg |
| Operating Empty Weight | 3990 | kg |
| Payload Weight | 2140 | kg |
| Average cruise groundspeed | 200 | kt |
| | 370 | km/h |
| Propulsion System | Turboprop | |
| Engines | 2 x | PW PT6A |
| Engine Power (one) | 686 | kW |
| Engine Weight (one) | 192 | kg |
| Engine Weight (with installation) | 259 | kg |
| Fuel consumption (all engines) | 276 | kg/hr |

The typical mission flight and the yearly utilisation of the aircraft was established according to the parameters shown in Table 3.17.

Table 3.17: Typical mission flight and utilization parameters.

| | | |
|---|---|---|
| Flight distance | 160 | nm |
| | 296 | km |
| Flight time | 0.80 | hr/flight |
| Mission time (block time, inc. 2x10 min taxi) | 1.13 | hr/flight |
| Mission fuel | 312 | kg/flight |
| Cycles (flights) per year | 2301 | flight/yr |
| Utilisation (yearly use) | 2600 | hr/yr |

#### *3.3.2.2 High-level analysis*

During the first part of WP2, high level analyses will be carried out to compare the life-cycle costs of the UNIFIER19 competing models with respect to the reference aircraft. The objective is to observe the potential improvement of a future aircraft with all the new technologies from the cost perspective.

In this analysis, general assumptions will be made in terms of material procurement cost, propulsion system costs, hourly salary rates, airport fees, etc. to ensure a fair comparison with respect to other designs.

#### *3.3.2.3 Low-level analysis*

During the last part of Work Package 2, both UNIFIER19 candidate aircraft will be compared against each other, taking into account the technology solutions selected by each partner. At this stage, more accurate assumptions on cost for each compartment will be applied, accounting for the specific features of each aircraft model, to allow for a higher-fidelity cost estimation.

### 3.3.3 Manufacturability and aircraft price

The methodology presented by Raymer (Raymer, 2018) based on the DAPCA IV model was chosen as the most suitable to be adapted to the UNIFIER19 project. The other analysed methods were published by Association of European (AEA, 1989) and by Jan Roskam (Roskam, 1989). Raymer estimates the costs pertaining to each different phase of the aircraft development and production, based on parameters such as the aircraft empty weight ($W_e$), cruise speed ($V$), expected production quantity ($Q$) and number of flight test prototypes ($FTA$), among others.

#### *3.3.3.1 Research, development, testing, engineering and production costs*

Engineering, tooling and manufacturing hours is a measure of the effort required for planning, designing, producing, and ground testing the aircraft through all its life-cycle. As it can be seen in the following equations, the estimated quantity of aircraft to be produced ($Q$) will have an influence on the final price of the aircraft. Designed speed ($V$) will increase the complexity of the aircraft, and the mass ($W_e$) will be directly related to the size and amount of parts to be designed, produced and tested.

$$H_{eng} = 5.18\, W_e^{0.777}\, V^{0.894}\, Q^{0.163}, \tag{3.36}$$

$$H_{eng} = 5.18\, W_e^{0.777}\, V^{0.894}\, Q^{0.163}, \tag{3.37}$$

$$H_{mfg} = 10.5\, W_e^{0.82}\, V^{0.484}\, Q^{0.641}. \tag{3.38}$$

Quality control is estimated to add 10-15% effort to the manufacturing hours:

$$H_{QC} = 0.133\, H_{mfg}. \tag{3.39}$$

All these formulas are calculated for an aluminium aircraft. As more innovative materials are envisioned in this project, the resulting labour hours shall be affected by a "material factor" ($f_{mat}$) to account for a higher design and manufacturing effort of less mature technologies. This will be estimated in the following.

Development support cost includes the manufacture of mock-ups, subsystem simulators, iron-bird, and structural test rigs. They are estimated as a function of the airframe mass and aircraft speed:

$$C_{dev} = 67.4\ W_e^{0.63}\ V^{1.3}. \quad (3.40)$$

Flight test cost will depend on the size and complexity of the aircraft, and clearly on the number of flight test aircraft ($FTA$), yielding

$$C_{FT} = 1947\ W_e^{0.325}\ V^{0.822}\ FTA^{1.21}. \quad (3.41)$$

A typical number for the current of project is 4 airplanes.

Manufacturing material cost is comprised of the cost of raw materials, hardware and equipment from which the aircraft is assembled, including the electrical, hydraulic, and pneumatic systems, the environmental control system, fasteners, clamps, and similar standard parts. A cost estimation relationship for this chapter can be written as

$$C_{mat} = 31.2\ W_e^{0.921}\ V^{0.621}\ Q^{0.799}. \quad (3.42)$$

The propulsion system will be the most important innovation in the UNIFIER19 project with respect to existing commuter aircraft powered by conventional turboprop engines. Not only it is a relevant system in terms of performance and emissions, but also in cost, as the propulsion system usually accounts for around one third of the production cost of the aircraft, and it is responsible for 40% of the Direct Operating Costs.

Turbine engine production cost formula developed in DAPCA IV is designed for turbojet engines, which is inaccurate for this type of aircraft. As currently the engines are procured from external suppliers and their prices are known, real data will be used instead of the formula, which is not well adapted for turboprops. For the reference aircraft, it will be assumed it is powered by two ($N_{eng} = 2$) Pratt & Whitney PT6A engines, which have a list price of around $ 1 million for this power level. Usual discounts for long-term supply of 2000 units can get as high as 50%, therefore a cost per engine of $ 500 000 will be considered as accurate,

$$C_{eng} = 500{,}000\ USD. \quad (3.43)$$

A hydrogen propulsion system cost is comprised by the price of the motors, inverters and controllers, the fuel cell and its accessories, the batteries, and the liquid hydrogen cryogenic tank. It is particularly difficult to estimate the final cost, as the technology is not mature and certified systems are several years away. All the implied costs are expected to decrease as technology progresses.

A very rough estimation sets the specific cost of DAL-C certified electric motors at 250 $/kW, and the inverter at 200 $/kW ($C_{motor}$).

Battery cost ($C_{batt}$) is evolving quickly, but it can be estimated at 300 $/kWh.

Fuel cell technology costs ($C_{fuelcell}$) can be roughly estimated using the presented in Chapter 1. High-volume production of fuel cell systems will result in costs of around 45 $/kW. Adding a margin for certification, we can assume a specific cost by 2025 of 65 $/kW.

$LH_2$ tank costs ($C_{tankLH2}$) are still under research and will be updated as soon as reliable information is obtained.

The calculation of the $LH_2$ system costs is presented here:

$$C_{motor+inv} = FN_{0\,kW}\,(250\ €/kW + 200\ €/kW), \tag{3.44}$$

$$C_{fuelcell} = FN_{0\,kW}\,(65\ \$/kW) \tag{3.45}$$

$$C_{LH2tank} = 1.5\ m_{H2}\ \ (TBD\ \$/kW), \tag{3.46}$$

$$C_{batt} = 1.5\ E_{bloc}\ (300\ \$/kWh) \tag{3.47}$$

where $FN_{0\,kW}$ is the maximum power for one motor, in kW; $m_{H2}$ is the liquid hydrogen mass, in kg, and $E_{bloc}$ the energy, in kWh, needed for a typical mission flight.

These costs are estimated for a low production quantity. It is believed that high volume production will reduce these costs by up to 50%, as defined in (Gudmundsson, 2013, section 2.2.1 Quantity Discount Factor).

A fully electric propulsion system would only consider costs for the motors and the batteries, while a hybrid-electric system would also add the price of a generator ($C_{gen}$).

The general formula for the propulsion system, adaptable to any chosen propulsion system is:

$$C_{prop} = N_{eng}\,C_{eng} + N_{motor}\,(C_{motor} + C_{fuelcell}) + C_{tankLH2} + C_{batt} + C_{gen}\,. \tag{3.48}$$

where $N_{eng}$ is the number of engines and $N_{motor}$ the number of motors.

These costs are estimated for a low production quantity. It is believed that high volume production will reduce these costs by up to 50%, as defined in (Gudmundsson, 2013).

For avionics system (fly-by-wire and instruments), based on research and in-house experience, the avionics system for a modern aircraft featuring fly-by-wire controls and actuators, redundant sensors and digital flight control computers, and advanced cockpit displays, can cost between 500,000 USD and 1,000,000 USD per aircraft, including recurring and non-recurring costs for 1,000 units. This number fits in the estimation given by (Raymer, 2018), which proposes an avionics price between 5% and 25% of the flyaway cost, depending on the sophistication level. It will be assumed that:

$$C_{avionics} = 750{,}000\ USD. \tag{3.49}$$

Finally, hourly rates consist of the salary, benefits, overhead and administrative costs for the personnel involved in the research, design, testing, evaluation, engineering and production. Of these values, slightly less than a half correspond to actual employee wages. As salaries vary considerably between countries, values in (Raymer, 2018) will be used, given in 2012 U.S. dollars, as they do not differ considerably from the current European values, and are sufficiently good for comparison purposes.

Table 3.18 Hourly rates in 2012 U.S. dollars (including administrative and overhead costs).

| Sector | Rate |
|---|---|
| Engineering, *Re* | 115 USD |
| Tooling, *Rt* | 118 USD |
| Quality Control, *Rq* | 108 USD |
| Manufacturing, *Rm* | 98 USD |

Henceforth, total research, development, testing and engineering cost for the whole program is calculated considering all the recurring and non-recurring costs.

$$C_{RDTE} = H_{eng}\,R_e + H_{tool}\,R_t + H_{mfg}\,R_m + H_{QC}\,R_q + C_{dev} + C_{FT} + C_{mat} + (C_{eng}\,N_{eng} + C_{avionics})Q. \quad (3.50)$$

This program cost divided by the production run gives the flyaway cost per aircraft.

### *3.3.3.2 Corrections to the model and Influence of new technologies*

Raymer calculations for RDTE costs are in 2012 U.S. dollars. Inflation rate between 2012 and 2020 was 12%, therefore all costs will be affected by an inflation factor,

$$f_{inf} = 1.12. \quad (3.51)$$

In the present model, U.S. dollars are considered as the reference currency for aircraft costs. Where U.S. dollars (USD) to Euro (EUR) conversion is needed, the average exchange rate in January 2020 is applied,

$$f_{USD\text{-}EUR} = 0.91. \quad (3.52)$$

The choice of materials will have a significant impact on the manufacturing cost, not only due to the cost of the material itself, but also due to the different processes that each material requires during the engineering, tooling, manufacturing and quality control phases.

Raymer (Raymer, 2018) establishes a cost factor for each material, taking aluminium as the reference, as it is the most widespread material throughout the aeronautical industry, and thus its associated costs are easily predictable. Each other material has a different cost factor, as shown in Table 3.19.

Table 3.19 Material cost factor as given by Raymer

| Material | Factor (2012) | Factor (1992) |
|---|---|---|
| Aluminium | 1.0 | 1.0 |
| Carbon-Epoxy | 1.1-1.8 | 1.5-2.0 |
| Fiberglass | 1.1-1.2 | 1.1-1.2 |
| Steel | 1.5-2.0 | 1.5-2.0 |
| Titanium | 1.1-1.8 | 1.7-2.2 |

As seen, these factors are not constant throughout the industry, and may vary with the level of maturity of the technology. For instance, the evolution of materials is reflected in the cost factor reduction between 1992 and 2012 editions of Raymer's book, as seen in Table 3.19. Especially carbon-epoxy and titanium became less expensive over the years.

These cost factors will also depend on the experience of the manufacturer. As an example, Boeing adopted a carbon fibre reinforced polymer (CFRP) fuselage in a commercial aircraft for the first time with the introduction of the Boeing 787. The development, manufacturing and maintenance costs were initially significantly higher than those of a conventional aluminium fuselage, but Boeing decision to invest in this technology will allow them to decrease costs in future developments. In their case, the carbon-epoxy factor shifted to the lower end of the range.

As the airframe consists of different materials, the final material factor ($f_{mat}$) used for the calculations is the summation of the partial cost factors for each material, corresponding to the percentage in weight of each material:

$$f_{mat} = \sum(\%_{mat\,i} * f_{mat\,i}). \tag{3.53}$$

As an example, material cost factors for three similar aircraft will be calculated. The Boeing 787 (first flight in 2009), the Airbus A350 (2011) and the Boeing 777 (1994). As an approximation, mean values of the factor range given in Table 3.19 for each material are assumed. Factors from 2012 edition are considered for the newer aircraft, while 1992 data is used for the Boeing 777.

The same methodology will be applied when calculating the material cost factors for the UNIFIER19 candidate designs, by adapting the factors to the most accurate value deduced from in-house experience.

The resulting factor will be applied to all the development-related hours ($H_{eng}$, $H_{tool}$, $H_{mfg}$ and $H_{QC}$).

Table 3.20 Material factor calculation for three similar aircraft.

| Aircraft | Material | % | $f_{mat}$ ref. | $f_{mat}$ partial | $f_{mat}$ total |
|---|---|---|---|---|---|
| Boeing 787 | Aluminium | 20% | 1.00 | 0.20 | 1.38 |
| | Carbon-Epoxy | 50% | 1.45 | 0.73 | |
| | Fiberglass/Others | 5% | 1.15 | 0.06 | |
| | Steel | 10% | 1.75 | 0.18 | |
| | Titanium | 15% | 1.45 | 0.22 | |

| Aircraft | Material | % | $f_{mat}$ ref. | $f_{mat}$ partial | $f_{mat}$ total |
|---|---|---|---|---|---|
| Airbus A350 | Aluminium | 19% | 1.00 | 0.19 | 1.36 |
| | Carbon-Epoxy | 53% | 1.45 | 0.77 | |
| | Fiberglass/Others | 8% | 1.15 | 0.09 | |
| | Steel | 6% | 1.75 | 0.11 | |
| | Titanium | 14% | 1.45 | 0.20 | |

| Aircraft | Material | % | $f_{mat}$ ref. | $f_{mat}$ partial | $f_{mat}$ total |
|---|---|---|---|---|---|
| Boeing 777 | Aluminium | 70% | 1.00 | 0.70 | 1.23 |
| | Carbon-Epoxy | 11% | 1.75 | 0.19 | |
| | Fiberglass/Others | 1% | 1.15 | 0.01 | |
| | Steel | 11% | 1.75 | 0.19 | |
| | Titanium | 7% | 1.95 | 0.14 | |

The UNIFIER19 reference aircraft model assumes the materials distribution reported in Table 3.21.

Table 3.21 Material factor for UNIFIER19 reference aircraft.

| Aircraft | Material | % | $f_{mat}$ ref. | $f_{mat}$ partial | $f_{mat}$ total |
|---|---|---|---|---|---|
| UNIFIER19 Reference | Aluminium | 65% | 1.00 | 0.65 | 1.17 |
| | Carbon-Epoxy | 20% | 1.45 | 0.29 | |
| | Fiberglass/Others | 5% | 1.15 | 0.06 | |
| | Steel | 8% | 1.75 | 0.14 | |
| | Titanium | 2% | 1.45 | 0.03 | |

The DAPCA IV model is fairly accurate for fighter, transport and cargo jet aircraft, as it is a purely statistical model designed on a pool of aircraft in that category. Smaller

aircraft require less effort, due to lighter certification requirements, lower system complexity, etc. This is reflected in a generally down-scaled cost. Experience and in-house calculations show the DAPCA IV model overestimates general aviation costs by a factor of up to four. A modified version of DAPCA IV for general aviation aircraft is given in (Gudmundsson, 2013).

As 19-seat commuters lie on the higher spectrum of CS-23, but considerably below the big commercial CS-25 aircraft, a cost reduction of 50% of the DAPCA IV method-estimated costs seems coherent with the current market values. Therefore, the following correction factor will be applied to all costs defined in the method,

$$f_{CS23\text{-}commuter} = 0.50. \tag{3.54}$$

#### *3.3.3.3 Purchasing price estimation*

The price paid by the operator to acquire an aircraft includes the manufacturing cost, including the cabin interior fitting, plus a sales or investment margin established by the manufacturer, and negotiated through commercial discounts for quantity and other deal-specific factors. Usually, the final price also comprises a certain amount of spare parts, as well as services such as training and after-sales support, that the manufacturer may offer in the purchase contract.

The passenger cabin equipment (seats, in-flight entertainment system, lavatories, etc.) for this type of aircraft is estimated in 4,000 USD per passenger. Therefore, for a 19-seat airplane, which is relatively simple as it does not include expensive first-class seating or complex in-flight entertainment systems, the interior may cost around 76,000 USD. This cost contributes to the fly-away cost per aircraft,

$$C_{aircraft} = C_{RDTE}/Q + C_{interior}. \tag{3.55}$$

The sales margin is included in the model as an Investment Factor ($f_{invest}$). This value is generally covered by industrial secrecy within the manufacturing companies and may vary from one to another. This methodology assumes a sales margin of 35%, which should be a good approximation for high-level comparison purposes,

$$f_{invest} = 1.35. \tag{3.56}$$

The spare parts and other services included in the aircraft final price usually amount to around 10% of the aircraft sales price (engine spares are not included). Yet again, this value is difficult to predict as it changes with each particular purchase. In order to consider this value within the purchase price, the following Spares Factor ($f_{spares}$) is assumed,

$$f_{spares} = 1.10. \tag{3.57}$$

The final aircraft purchase price is then calculated as

$$P_{aircraft} = C_{aircraft}\, f_{invest}\, f_{spares}. \tag{3.58}$$

### 3.3.4 Marketability: Operating Costs

From the airline's perspective, the most important indicator of profitability and marketability of an aircraft is its operating cost. Operating costs are divided into *Direct Operating Costs* (DOC) and *Indirect Operating Costs* (IOC).

DOC include all aircraft-related and traffic-related costs:

- fuel (or electrical energy),
- crew expenses,
- flight fees: landing and navigation,
- handling fees: passenger check-in and boarding services, cargo loading, ramp services,
- maintenance: airframe and engine personnel and parts, including engine overhaul.

IOC include all costs related to the airline operation, but not directly attributable to a given flight. They are usually computed on an yearly basis, and include:

- aircraft ownership: acquisition, depreciation, insurance and interest,
- amortization of other than flight equipment,
- maintenance and handling operations at base station,
- airline operation related costs: sales & marketing, management, human resources,
- buildings ownership or rental: terminal and maintenance facilities, headquarters, sales offices, etc.

There are several other cost components involved in the operation of an airline, such as catering, advertising, baggage mishandling, cancellation expenses, etc., but they will not be included as they are usually minor, or not relevant in the present study.

DOC are usually defined in terms of cost per flight hour, per flight or per annum. As a result, cost per available seat per mile or km is calculated (CASM or CASK).

Aircraft ownership costs will be considered as DOC components, as they can be easily assigned to each aircraft based on its yearly utilisation.

Other IOC components cannot be estimated uniquely, as they primarily depend on the structure, operational philosophy and business model of the airline.

#### *3.3.4.1 DOC models and adaptation to the 19-seater case*

Several publicly available DOC methods were considered for producing an internal model, as well as advice from industry experts. However, none of the considered methods is specific for this type of aircraft. They are either for big commercial aircraft, or for small general aviation airplanes (for personal/business use). We tried to adapt them in order to see which ones give more reasonable values.

The reviewed methods are listed hereafter. Underlined entries were considered for this project:

- AEA (Association of European Airlines) DOC Method: published in 1989, it is still one of the most accurate. It does not include ground handling fees (probably treated as an indirect cost), and the maintenance model is not accurate for

small aircraft.

- TU Berlin (Thorbeck, Scholz) DOC Method: published in 2013, it is the most up-to-date model. It is easily adaptable to 19-seaters.
- ATA (Air Transport Association) DOC Method: public since 1967, it is comprehensive but outdated.
- NASA cost method: in use from 1976, it is outdated and too specific for airlines.
- Gudmundsson (Embry-Riddle) Business jet DOC Method: despite some very business-jet-specific assumptions, it offers a good approximation to the 19-seater case and is easily adaptable. It is in turn based on the Eastlake method, which is itself based on DAPCA IV.
- Gudmundsson GA DOC Method: similar to previous one, but too simple and very specific for the small personal aircraft case.

The final operating cost model is a combination of the highlighted DOC methods, especially those by TU Berlin and Gudmundsson. Adaptations to the commuter market and UNIFIER19 technological innovations were implemented where needed through factors (materials factor), modifiable constants (personnel salaries, airport taxes) or new technology-specific variables (such as electric consumption). More details are given further in this document.

In order to validate the DOC model by comparing its results with publicly available DOC data of similar aircraft, an "average" 19-seater aircraft was hypothesized, based on the aircraft database, with 2 x PT6A turboprop engines, capable of a 300 km mission flight, with a cruise speed of around 200 kt.

#### *3.3.4.2 DOC models data*

Block time ($T_{bloc}$) is the time from doors closing at departure airport to doors opening at destination. It considers flight time ($T_f$) plus taxi time. In this project, taxi time is assumed to add 10 minutes at each airport, yielding

$$T_{bloc} = T_f + 0.33. \tag{3.59}$$

Flight cycles (FC) per year is the number of typical missions that an aircraft can perform in a year, excluding the time allocated for programmed and non-programmed maintenance, night curfew and other restrictions, as well as turn-around time. According to AEA method, the formula for short range aircraft is

$$FC = 3750 / (T_{bloc} + 0.5). \tag{3.60}$$

Utilisation rate ($U$) is the number of block hours per year,

$$U = FC\ T_{bloc}. \tag{3.61}$$

Cost per available seat mile (CASM) or kilometer (CASK) is the parameter used to evaluate operating cost in the airline industry. It is calculated as

$$CASK = DOC_{total} / (N_{seats}\ D_{f\,km}), \tag{3.62}$$

where $DOC_{total}$ is the sum of all DOC calculated in the following subsections, $N_{seats}$ is the number of available seats (19 here), and $D_r$ are the miles or kilometres flown on a typical mission.

#### *3.3.4.3 Fuel cost*

Fuel cost per flight is simply calculated as the fuel consumption for a typical mission flight ($F_{bloc} = F_{cons}\, T_{bloc}$), where $F_{bloc}$ is the hourly consumption on a typical flight, multiplied by the price of the fuel ($P_{fuel}$), in €/kg.

A more refined $F_{bloc}$ calculation can be made if the duration of each flight phase is known. Taking cruise consumption as a base:

- Take-off and climb consumption is roughly 50% higher than cruise consumption.
- Descent consumption is roughly 50% lower than cruise consumption.

As jet fuel prices fluctuate depending on the country, the airport, the refuelling service provider, and the agreements (hedges) each airline makes with the providers, IATA average fuel price for Europe will be considered. In January 2020, the price of Jet-A1 in Europe averaged 1.90 € per gallon, which translates into 0.753 €/kg, including an estimated 20% fee for the fuel supplier.

In case of adoption of liquid hydrogen ($LH_2$) propulsion, $LH_2$ consumption ($H_{bloc}$) and price ($P_{LH2}$) will have to be defined. According to (Hydrogen Europe, 2018), the current price of liquid hydrogen is 10-15 €/kg, while this cost can descend up to 5 €/kg by 2025. A conservative $P_{LH2}$ of 10 €/kg is used initially, and will be adapted accordingly.

The equivalent quantity of $LH_2$ consumed, to obtain the same energy as with jet fuel, is defined by:

$$m_{H2} = m_{jet\ fuel}\ (ED_{jet\ fuel} / ED_{H2})\ (\eta_{jet} / \eta_{fuel\ cell} / \eta_{electric\ motor}), \tag{3.63}$$

where $m_{jet\ fuel}$ is the mass of jet fuel used as reference (e.g. for a full flight: $F_{bloc}$), $ED_{jet\ fuel}$ is the jet fuel energy density (11.9 kWh/kg), $ED_{H2}$ is the hydrogen energy density (39 kWh/kg), $\eta_{jet}$ is the jet engine efficiency (0.25), $\eta_{fuel\ cell}$ is the fuel cell efficiency (usually 0.5), and $\eta_{electric\ motor}$ is the electric motor efficiency (0.9).

Ideally, hydrogen power should be sufficient during cruise and descent phases, but needs to be complemented by battery-stored electric energy to increase the thrust during take-off and climb. Therefore, battery-based electric energy consumption should be defined for a typical flight, in kWh ($E_{bloc}$). In 2019, Eurostat shows that the average price of plug-in electricity per kWh ($P_{electric}$) for non-household consumers in Europe was: $P_{electric}$ = 0.0855 €/kWh.

Similarly to the equivalent hydrogen consumption formula above, equivalent electric energy can also be computed as:

$$E_{H2} = m_{jet\ fuel}\, ED_{jet\ fuel}\, \frac{\eta_{jet}}{\eta_{electric\ motor}} \tag{3.64}$$

The final fuel (or energy) cost formula is:

$$DOC_{fuel} = F_{bloc}\, P_{fuel} + E_{bloc}\, P_{electric} + H_{bloc}\, P_{LH2} \tag{3.65}$$

The model is also adapted to jet fuel-based hybrid-electric propulsion, or any combination of these propulsion systems, as long as consumption levels can be defined.

#### *3.3.4.4 Crew cost*

Cost of crew depends on the number of crewmembers per flight, as well as the number of full crews, also called crew complement, needed per aircraft ($N_{crews}$) for a normal continuous operation, respecting maximum flight hours limitations, leaves for vacations, trainings and medical checks. It will depend on each operator and is usually between 3 and 5. For this analysis it is assumed to be $N_{crews} = 3.5$. The crew cost equation is:

$$DOC_{crew} = N_{crews}\,(P_{pilots}\, N_{pilots} + P_{fa}\, N_{fa})\, T_{bloc} \tag{3.66}$$

Salaries for cockpit crew ($P_{pilots}$) are calculated at 65 €/hr per pilot on average. Pilot salary is higher than co-pilot's, therefore, if single-pilot operations are adopted ($N_{pilots} = 1$), the pilot salary should be set higher than the average.

Cabin crew salaries ($P_{fa}$) are estimated at 40 €/hr per flight attendant, but CS-23 regulation does not require cabin crew for commuter category aircraft, therefore $N_{fa} = 0$ in the present case.

#### 3.3.4.5 Cost of ownership – Interest, depreciation and insurance

Capitalisation costs are sometimes not included in the DOC, as they must be accounted regardless of the number of flight hours. They can be, however, distributed as a cost per flight hour, especially if the utilisation rate is known.

The model assumes the aircraft is fully purchased through long-term financing with an interest rate ($IR$) of 5%. Depreciation is included in the same equation, considering a depreciation period ($DP$) of 15 years and a residual value factor ($f_{RV}$) at end of life of 10%,

$$DOC_{int} = P_{ac}\, IR\, [1 - f_{RV}/(1+IR)^{DP}] / [1 - 1/(1+IR)^{DP}] / FC. \tag{3.67}$$

Yearly insurance factor ($f_{ins}$) is estimated to be equivalent to 0.5% of aircraft price,

$$DOC_{ins} = P_{ac}\, f_{ins} / FC. \tag{3.68}$$

These yearly costs are divided by the flight cycles per year ($FC$) to give the ownership costs per flight.

### *3.3.4.6 Navigation fees*

EUROCONTROL is the body that manages the navigation fees across all countries of the European Union. Navigation fees include route navigation fees and terminal fees for approach and departure from bigger airports and are explained on their website.

The equation to calculate navigation fees is given by EUROCONTROL as

$$TN = K_{nav}\,(D_{f\,km}/100)\,(MTOW/50)^{0.5}, \tag{3.69}$$

where $K_{nav}$ is a rate that changes for every country, $D_f$ is the great circle distance in km between departure and arrival airports (minus 20 km at each airport), and $MTOW$ is the maximum take-off weight in tons.

Factor $K_{nav}$ is a unit rate of charge, updated and published by EUROCONTROL every month. In January 2020, the average rates for the different European regions were:

- Average for Western Europe = 59 €
- Average for Eastern Europe = 38 €
- Average for Northern Europe = 42 €
- Average for EUROCONTROL countries = 45 €

As it can be seen, there is a considerable difference between different regions. In order to keep on a conservative side in the present computations, Western Europe rates will be adopted in our calculations.

Terminal fees change considerably from country to country and, in some countries, they also depend on the airport. It is important to remark that these charges apply only for bigger airports, with terminal ATC. In UFIER19, only the microfeeder market case can be impacted by these fees.

As a general rule, the equation to compute them may be written as

$$T_{terminal} = K_{tnc}\,(MTOW/50)^{0.7}, \tag{3.70}$$

with $k_{tnc}$ averaging 170 € in January 2020.

### *3.3.4.7 Airport fees*

Airports charge certain fees which differ considerably with the size of the airport, the infrastructure level, etc. Big international hub airports charges can be prohibitive for small operators, while local aerodromes with minimal infrastructure only charge a landing and parking fee. These fees can be based on the MTOW, on the number of passengers or the payload.

Airports of different size and infrastructure level were surveyed to get values of airport fees in different European countries. For example, Barcelona-El Prat airport charges are more than double those of Valencia or Sevilla airports, and more than triple those of smaller airports in Burgos or San Sebastian. However, Barcelona is less expensive than Rotterdam, even if the Dutch airport is smaller.

Usually, airports publish single-use charges, which can be quite costly. However, operators with regular services can sign long-term contracts with a considerable

reduction of the applicable fees, or even get subsidies and benefits from local authorities to operate on certain cities.

Landing fees are dependent on the MTOW of the aircraft, and are either defined as a fixed price, or as a factor of MTOW. It could be observed that for many airports the 6 ton MTOW is a category limit, i.e. the landing fees for aircraft below 6,000 kg can be considerably lower than those for a heavier aircraft. This can be a relevant design driver for the candidate concepts.

As extracted from the airport database, an average landing fee for an aircraft with MTOW = 6,670 kg is around TL = 71.50 € per flight.

This value is very close to the value obtained with the estimation relationships given in AEA and TU Berlin methods (the latter for instance gives TL = 66.70 €).

Ground handling services can be provided either by the airport operator, or by an external provider. As mentioned, airport fees vary considerably with airport size, country, operator, etc., making it difficult to obtain accurate values of these fees.

Usually, ground handling fees encompass one or more of these costs:

- Passenger services, including one or more of these items:
  - boarding or transfer: a fee per passenger that boards an airplane,
  - check-in service: a tax is collected per passenger using the check-in counters,
  - country tax: some countries charge a national tax per boarding passenger,
  - PRM (*Person with Reduced Mobility*): a tax charged to all passengers to pay for hardware and staff dedicated to assisting passengers with special needs.
- Security fees are paid for each screened passenger, or kg of payload.
- Aircraft handling fees, generally depending on the MTOW, but can also be fixed, or payload dependant.
- Infrastructure fees (charged per ton MTOW or number of passenger) are used to pay the cost of ramp and other services such as:
  - passenger handling, either by buses, stairs or air bridges (more expensive),
  - cargo and baggage ramp handling equipment,
  - refuelling services,
  - ground power units,
  - meteorological services (ATIS, weather forecast).
- Parking is usually free of charge for the first hours and will not be considered in the present estimation.
- Hangar costs will not be considered in the present estimation.

In this project, the average ground handling fees of the surveyed airports will be considered. For the reference aircraft mode, TG = 402.19 € per flight.

The MTOW, passengers and payload variations in the candidate aircraft will affect this value.

It is important to note that these high landing and handling fees will only be applicable at bigger airports for the microfeeder case. The smaller airports served by the miniliner case will surely charge much lower fees. Also, long-term contracts with airport operators can decrease these fees substantially.

Therefore, only 50% of the calculated landing and ground handling fees will be considered (TL = 35.74 € per flight, TG = 201.09 € per flight).

#### *3.3.4.8 Maintenance costs*

All the DOC methods include some sort of maintenance costs estimation. Again, it is difficult to obtain accurate values for the type of aircraft of interest here, as the analysed methods refer to bigger aircraft, or fail to capture all the maintenance-related costs.

The most reliable method is described by Gudmundsson (Gudmundsson, 2013), which separates the maintenance into airframe and engine maintenance costs, and engine overhaul (OH) and hot section inspection (HSI) work.

For the personnel and spare parts of airframe and power-plant, Gudmundsson proposes the following formula to give an estimated maintenance cost per flight:

$$DOC_{af\text{-}eng} = F_{mf}\, LR\, T_{bloc} \tag{3.71}$$

where $LR$ is an average qualified maintenance labour rate (around 50 €/hr), and $F_{mf}$ is an "ease of maintenance" factor, in maintenance man-hours per block hour:

$$F_{mf} = 2.00 + F1 + F2 + F3 + F4 + F5 + F6. \tag{3.72}$$

Here the parameters can be specified as follows:

- $F1$ is 0 for easily accessible engines, 0.2 otherwise.
- $F2$ is 0 for fixed landing gear, 0.2 for retractable landing gear.
- $F3$ is 0 for simple avionics, 0.2 for complex.
- $F4$ is 0 if the aircraft has no integral fuel tanks, 0.1 if it has integral fuel tanks.
- $F5$ is 0 for simple flaps, 0.2 for complex flaps.
- $F6$ is 0 for Part 23 certified aircraft, and 0.5 for Part 25.

The reference aircraft model values are highlighted in bold. This gives an $F_{mf}$ = 2.7 MMH/FH (maintenance man-hour per flight hour).

Concerning engine overhaul and related costs, a conventional engine requires an overhaul every certain number of hours, known as *Time Between Overhaul* (TBO). For a turboprop engine of the size of interest here, a typical TBO is 3,600 hours, and the cost of such work ($P_{OH}$) is around 400,000 USD per engine,

$$DOC_{overhaul} = N_{eng}\, (P_{OH} / TBO)\, T_{bloc}, \tag{3.73}$$

where $N_{eng}$ is the number of engines, and the result is the overhaul cost distributed on each typical flight.

Hot-section inspection is performed at mid-life between overhauls, and costs around 50,000 USD per engine. This cost is also split considering all the flights in the period, yielding

$$DOC_{HSI} = N_{eng}\,(P_{HSI} / TBO)\,T_{bloc} \tag{3.74}$$

Use of electric motors in aviation is still in its early stages, and certification and major maintenance procedures have not yet been established. It can be estimated, however, that the useful life of an electric motor before 75% of its components wore-out can be conservatively set at 10,000 hours. Therefore, the overhaul or replacement cost of an electric motor can be calculated with the same overhaul relationship shown above, but with the following parameters:

$$TBO = 10{,}000\ hr \qquad P_{OH} = 0.75\,C_{eng}, \tag{3.75}$$

where $C_{eng}$ is the list price of an electric motor, as previously computed.

There is no hot section, nor any other major maintenance needed for electric motors. Minor maintenance costs can include change of bearings, check of cable connections, etc., but this is included in the basic maintenance costs already computed.

Regular maintenance costs for fuel cells and cryogenic $LH_2$ tanks are unknown for now, as the technology is still under development.

### 3.3.5 Impact of new technologies, procedures, policies and regulations

New technologies can impact the RDTE costs in many ways:

- Use of novel materials will probably increase the manufacturing and maintenance price (changes of $f_{mat}$ factor), but they will help to reduce empty weight ($W_e$) which in turn improves fuel consumption.
- Replacement of turboprop engines by electric motors may reduce considerably the propulsion system price, fuel consumption and maintenance (overhaul) costs. However, addition of a liquid hydrogen system or battery packs will increase overall aircraft cost, as well as the empty weight, and therefore also energy consumption.
- Fly-by-wire controls are more expensive to implement than conventional mechanical controls (increase $C_{avionics}$ value), but there is a potential reduction in weight and maintenance costs (a modification in $F_{mf}$ factor). Moreover, as avionics technology reaches higher maturity, the cost of fly-by-wire systems can be reduced.
- Adoption of single-pilot operations ($N_{pilots}$) will reduce the crew salary costs and slightly reduce aircraft weight.

The current cost model is already adapted to the implementation of the above-mentioned technological innovations. However, it is difficult to predict and adapt the cost model for all the possible innovations that the UNIFIER19 conceptual design candidates may incorporate. These will certainly have an impact on the

manufacturing and operating cost of the aircraft. All these technologies will be individually assessed and this cost model will be adapted accordingly, if needed.

## 3.3.6 Methodology validation results – Global cost figure of merit

### *3.3.6.1 Methodology validation*

The manufacturability cost model for the reference aircraft gives manufacture values and program costs consistent with the publicly available prices of similar-sized aircraft.

The calculated aircraft purchase price is 15 million USD, for an estimated production run of 500 units, including 35% of profit margin and 10% for spare parts and other services. Selling at this price, breakeven point would be reached at 96 sold units.

This value is also consistent with the aircraft price method given by AEA (AEA, 1989), based solely on airframe weight and engine power (6.49 million USD).

As a reference, the list prices of similar aircraft currently in production are:

- Dornier Do-228: $ 8 million,
- Let L410: $ 6.3 million,
- PZL M28: $ 7 million,
- DHC-6 Twin Otter: $ 6.5 million,
- Cessna 408 SkyCourier: $ 5.5 million (in development),
- Indonesia Aerospace N219: $ 6 million (in testing).

The Direct Operating Costs (DOC) methodology gives values that are fairly consistent with the real operating costs of such type of aircraft, on the conservative side, as some costs are dependent on the operator. The total DOC values for the reference aircraft and typical mission flight are

$$DOC_{bloc} = 1737.00\ €/flight\ (or\ 1537.17\ €/hr) \tag{3.76}$$

$$DOC_{per\text{-}pax} = 91.428\ €/pax/flight \tag{3.77}$$

When comparing the three existing methods with the one adapted to the UNIFIER19 project in Figure 3.26, the largest differences are seen on the AEA method – the maintenance cost for airframe personnel is inaccurate for small aircraft, the crew costs are overestimated, and the fees calculation does not include ground handling fees.

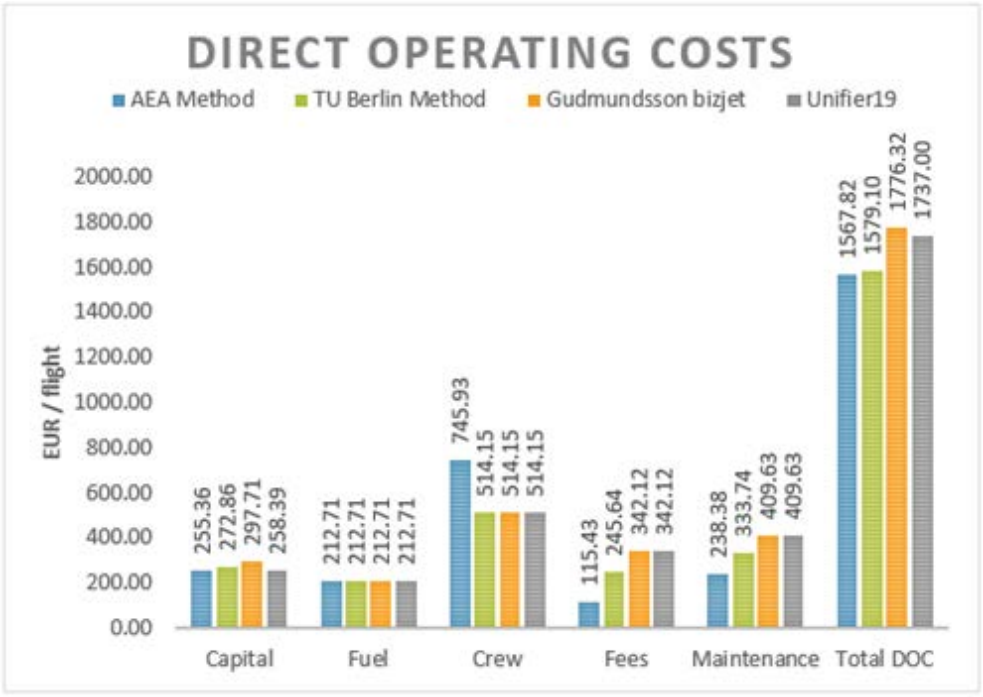


Figure 3.26 Comparison of all considered DOC methods.

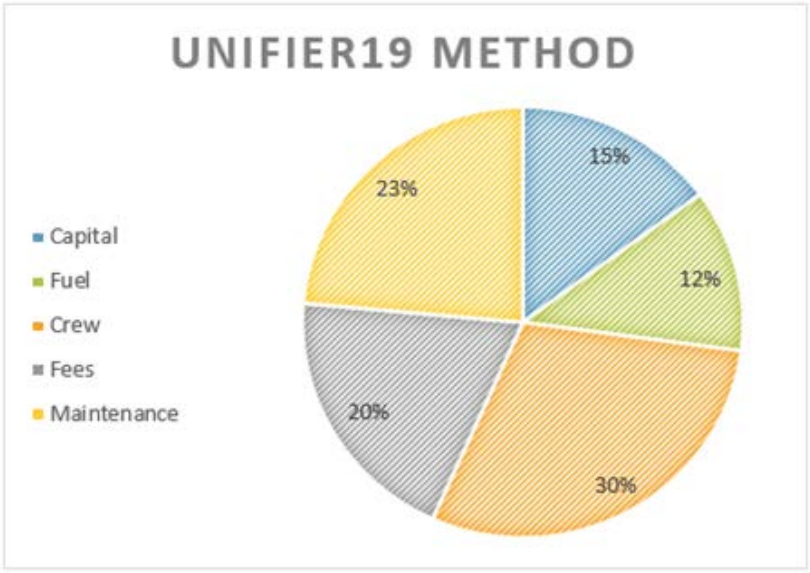


Figure 3.27 Contribution of each cost in the total DOC for the typical mission of the reference aircraft.

As it can be seen in Figure 3.27, the highest costs for this specific mission are the crew, followed by maintenance and fees (navigation and airport). Fuel and capitalisation costs are the lowest contributor, but fuel price fluctuates considerably and can easily increase its share. New technologies should be aimed at mitigating these higher prices first.

### *3.3.6.2 Global cost figure of merit*

The most appropriate cost figure of merit is the CASK. It gives a cost that is easily compared to different aircraft of different configurations and sizes. For the reference aircraft model and the defined mission flight, the CASK is 0.31 €/seat-km (or CASM of 0.57 €/seat-Nm). This value is higher than airline industry standards, but it is also fairly conservative, as some of the operating costs can certainly be reduced by the operator through long-term agreements with suppliers, airports and through other cost-reduction strategies. Nevertheless, for comparison purposes, the methodology is deemed appropriate.

## *3.4 Infrastructural costs*

### 3.4.1 Battery charging infrastructures

#### *3.4.1.1 Introduction*

The introduction of Pure-Electric (PE) or Hybrid-Electric (HE) aircraft fleet in the air transportation system, as envisaged in (Trainelli, Bruglieri, Salucci, & Gabrielli, 2020), requires the definition and deployment of a suitable ground infrastructure. Existing airports will have to take into account an increased electric power supply demand, needed to quickly recharge airplane batteries during turnaround times. Indeed, the price of electricity would come to represent a significant cost driver for the airport operator.

Electricity price usually changes significantly over a daily or weekly period – possibly reaching up to two and four times the minimum, respectively, over these time frames, as in the Italian case (Servizio Elettrico Nazionale (Italian National Electric Service), s.d.). A smart scheduling of the recharging activities should therefore be pursued to reduce the energy supply cost.

Such smart recharge planning is clearly connected to the available ground recharging facilities (Aerospace Standards Committee, 2011), (Sujitha, 2016). Two basic types of chargers were considered (Zheng Y. e., 2014), Battery Plug-in Chargers (BPC) and Battery Swapping Stations (BSS), possibly simultaneously present.

BPCs are conceptually similar to fuel refilling stations. Possible weaknesses of BPCs may arise with large airplanes, whose battery capacity is in the order of several MWh (3.5-7.0 MWh for an aircraft the weight of a B737-800, depending on the mission (Friedrich & Robertson, 2014)), yielding to either very long recharging times, totally unacceptable and incompatible with the usual turnaround time of a liner.

BPCs charging power could be increased to reduce charging time, but, in addition to the procurement cost for the hardware, this would have an impact on the peak power absorbed from the source (typically the grid), which is in turn responsible for a non-negligible fraction of the total cost of energy supply, along with the actual energy acquired. As an example, in the Italian energy supply scenario, the cost of maximum allowed peak power is responsible for 20% of the overall electric energy cost for a typical user (Servizio Elettrico Nazionale (Italian National Electric Service), s.d.).

BSS is an alternative to BPC, allowing batteries to be recharged after having been disembarked from the aircraft. If an appropriate number of spare batteries is available, a smart scheduling of the recharge can be envisaged in order to make it compatible with air operations on one hand, and to minimize the power bill on the other. Clearly, a larger number of batteries represents higher procurement costs and an increased logistic effort (batteries must be transported to and from the aircraft, as well as stored safely after having been recharged and before re-embarking them). Moreover, recharging power for a single BSS, similarly to what happens for BPCs, is limited by technological factors, so a higher number of battery recharges will be needed, resulting in higher acquisition cost.

The energy/power supply required, the number of BPCs and BSSs, and the number of batteries constitute the main output of a sizing problem where the schedule of air operations, i.e. the number of operated flights and their time frames, is given as an input. From the viewpoint of a ground operator, the reconfiguration of an airfield for allowing operations with an PE or HE aircraft fleet should imply defining these outputs, in order to grant minimum procurement and operational costs.

This section will first outline a comprehensive, original method to solve the problem of optimally sizing the ground infrastructure for future electric air transport. Such method was implemented in the Airport Recharging Equipment Sizing (ARES) tool. An application of ARES to the reconfiguration of the Milano Bresso (ICAO code: LIMB) airport will be presented next. This airport is operated by the company Aero Club Milano (Aero Club Milano, 2019), which acts as airport manager, and owns an aircraft fleet, used for instructional as well as sport flights. Finally, an application of ARES to the reconfiguration of the Athens International airport (ICAO code: LGAV) will be analysed. This airport was chosen because it had the largest number of regional aircraft movements in 2018, and electrified versions of current turboprop regional aircraft (such as ATR 72s) are being widely researched on, and their entry in service could reasonably be the first real-world application of PE or HE commercial aviation, as compared to larger liners (de Vries, Hoogreef, & Vos, 2019).

#### *3.4.1.2 Recharging infrastructure sizing and operation: analytic approach*

The airport infrastructure sizing introduced in Section 1 can be analytically modelled as an optimization problem. From an operator standpoint, the optimum represents a balance between the need to grant an assigned operativity level, i.e. a flight schedule, and the necessity of minimizing procurement and operative cost.

In mathematical terms, a suitable cost function J can be built up based on cost chapters as follows:

$$J = C_E + C_P + C_{BSS} + C_{BRS} + C_B \tag{3.78}$$

where the components $C_E$, $C_P$, $C_{BSS}$, $C_{BPC}$ and $C_B$ represent the cost of the electric energy purchased from the grid, the cost of peak power, the procurement cost of the battery swapping stations and of the plug-in chargers and of the batteries, respectively. In seeking for an optimum of the cost function $J$, some constraints need to be considered in order to model inherent technological limitations, as well as to mathematically formulate the physics of recharging operations. With the purpose of correctly evaluating the constraints, the dynamics of the infrastructure is integrated over an appropriate time frame of length $T$. The problem is allocated on a discrete time grid, where the length of each time step is $\tau$.

The cost components and constraint equations will be described in the following subsections, highlighting their respective dependencies.

The cost components and constraint equations will be described in the following subsections, highlighting their respective dependencies.

#### *3.4.1.2.1 Cost components*

The cost components in Eq. (3.78) can be expressed as follows. The cost of energy $C_E$ is bound to the energy amount $E^p\ (t)$ absorbed from the grid over a given period and to the monetary value per energy unit $\lambda(t)$. Due to the very low frequencies in the evolution of both functions of time (compared to a daytime scale), providing definitions in discrete time is more typical to this type of problem. Therefore, it is possible to write

$$C_E = \sum_{t=0}^{T} \lambda_t E_t^p \tag{3.79}$$

where the value of $E_t^p$ represents the energy drained between the current time t and the next one. Clearly, the value calculated in Eq. (3.79) is a function of the time frame $T$ considered for the analysis. That value should be taken consistently with the definitions of the other components of $J$, as described through the next equations.

The cost of power can be expressed as

$$C_P = (N_{BSS}P_{BSS} + N_{BRS}P_{BRS})c_P \frac{N_D}{30} \tag{3.80}$$

where $N_{BSS}, P_{BSS}, N_{BPC}$ and $P_{BPC}$ are the number and nominal power of BSS and BPC, respectively. The sum between braces represents nominal peak power, i.e. the power needed in case all BSS and BPC are operating simultaneously. The term $c_P$ represents the cost per unit peak-power per month, and $N_D$ the number of days in the considered analysis. The value of $N_D$ implicitly defines the limit for the sum in Eq. (3.78).

The component $C_{BSS}$ represents the procurement cost of the BSS, and can be written as

$$C_{BSS} = N_{BSS}c_{BSS}\frac{N_D}{T_{BSS}} \tag{3.81}$$

where $c_{BSS}$ is the acquisition cost per unit of the BSS, and $T_{BSS}$ the expected lifespan of the device. Therefore, $\frac{N_D}{T_{BSS}}$ represents the relative extension of the analysis, measured in days, over the expected lifespan of the device. The cost of the unit BSS can be defined based on a technological regression, as a function of $P_{BSS}$ [9].

In a similar fashion, the cost model for BPC can be written as

$$C_{BPC} = N_B c_{BPC}\frac{N_D}{T_{BRS}} \tag{3.82}$$

Lastly, the cost model for batteries yields

$$C_B = N_B c_B \frac{N_D}{T_B} \tag{3.83}$$

where $c_B$ is the acquisition cost per unit battery and $\frac{N_D}{T_B}$ the usual scaling factor.

### *3.4.1.2.2 Constraints*

The parameters influencing the components of the cost function must satisfy an array of constraints, which reflect both technological limitations and models of the recharging processes.

The state of charge $SoC_{i,t}$ of the $i$-th battery at time index $t$ should be between a minimum $SoC^{min}$ and a maximum $SoC^{max}$, as defined by technological limits. This is expressed by the following equation,

$$SoC^{min} < SoC_{i,t} < SoC^{max} \tag{3.84}$$

Battery charging can be carried out through a BSS or BPC. Battery charging (positive) rate $P_{bat_{i,t}}$ cannot exceed a technological limit expressed by a nominal $P_{bat}^{max}$. This yields

$$\begin{gathered} 0 < P_{bat_{i,t}}^{BSS} < P_{bat}^{BSS,max} \zeta_{i,t} \phi_{i,t} \\ 0 < P_{bat_{i,t}}^{BRS} < P_{bat}^{BRS,max} \xi_{i,t} \psi_{i,t} \\ \phi_{i,t} + \psi_{i,t} \leq 1 \end{gathered} \tag{3.85}$$

At any time, a battery can be recharged only if it is connected to a BSS or BPC, and this is implemented by the use of the binary variables $\zeta_{i,t}$ and $\xi_{i,t}$ in Eq. (3.85) , which will be equal to 1 if the battery is connected to a BSS or BPC device respectively, and 0 otherwise. Two separate constraining equations are written, in case the battery is connected to either a BSS or a BPC. Two further binary variables $\phi_{i,t}$ and $\psi_{i,t}$ are added to exclude simultaneous recharging of the same battery from a BSS and a BPC – the value of their sum is constrained below or at unity.

A further constraining equation is represented by the energy balance for the *i-th* battery, yielding

$$SoC_{i,t} = \left( P_{bat_{i,t}}^{BSS} + P_{bat_{i,t}}^{BRS} \right) \tau \eta_c + SoC_{i,t-1} \tag{3.86}$$

where $\eta_c$ is the efficiency of the recharging process. The initial value of the state of charge $SoC_{i,0}$ needs to be assigned. The energy amount drained from the grid and

corresponding to the recharge power is

$$E_t^p = \tau \sum_i \left( P_{bat_{i,t}}^{BSS} + P_{bat_{i,t}}^{BRS} \right) \tag{3.87}$$

where the sum has to be carried out on the number of active charging devices (BSS and BPC).

Additional binary variables and their corresponding constraints are introduced at an implementation level, to grant global consistency when reducing all constraining equations to a linear form.

#### *3.4.1.2.3 Optimization structure and implementation aspects*

The optimization of the cost function in Eq. (3.78) is carried out with respect to desired operational performance. The flight schedule is assigned over the considered time frame, yielding a number of aircraft that need to be airborne at any collocation point. The number of batteries and recharging devices is then steered by the optimizer to yield the minimum cost as defined by Eq. (3.78).

Retrieving the expression of $J$ from Eq. (3.78), we can see that it can be now computed as a function of the optimization variables $E_t^p$, $N_{BSS}$, $N_{BPC}$, $N_B$ and $N_{AC}$. Other quantities appearing in Eqs. (3.79) through (3.85), namely $\lambda_t$, $P_{BSS}$, $P_{BPC}$, $c_P$, $c_{BSS}$, $T_{BSS}$, $c_{BPC}$, $T_{BPC}$, $c_{BSS}$, $c_B$, $T_B$ can be considered as assigned technological parameters. Further optimization parameters include the binary variables appearing in Eq. (3.87), and those required to express all constraints through linear equations. The resulting optimization problem is based on a mix of discrete and non-discrete variables and can be tackled by means of dedicated MIP (Mixed-Integer Programming) solvers.

An analysis on suitably simplified case studies has been carried out first, in order to check whether the problem was well posed and validate results, and to assess the performance of a number of commercial MIP solvers. The selected solution algorithm is GUROBI, which implements a MILP (Mixed-Integer Linear Programming) approach fully compatible with the proposed linear formulation of the optimal problem.

### *3.4.1.3 Milano Bresso airport study case*

The presented procedure can be applied to the analysis of the reconfiguration of the airport base and fleet of Aero Club Milano (ACM), which operates from Milan Bresso (LIMB).

The Milan Bresso airfield features a single 1,080 x 30 m asphalt runway, which does not pose limits to terminal operations by any aircraft in the single-engine propeller-driven weight category. The current fleet of the ACM is composed of 21 aircraft, of which 20 are single-engine propeller-driven. In the current analysis, it has been hypothesized to switch from the current aircraft models, mainly Cessna C172 and Piper PA-28, to a homogeneous fleet of Pipistrel Panthera Hybrid (20Pi), which is in

an advanced design stage, under the auspices of project MAHEPA (MAHEPA Project, s.d.). The basic features of the battery of this aircraft are reported in Table 3.22.

Table 3.22 Basic data of Pipistrel Panthera Hybrid battery.

| Parameter | Value |
|---|---|
| Nominal capacity | 13.8 kWh |
| Usable capacity | 11-12 kWh |
| Life @ 75% DOD | 800 cycles |
| Charging efficiency | 93% |
| Charging power | 60 kW |

In order to analytically set up the sizing problem, the recharge power values $P_{BSS}$, $P_{BRS}$ of the ground recharging devices have been defined at the nominal recharge power of the aircraft, i.e. 60 kW. Similarly, the maximum $SoC^{max}$, the recharge efficiency $\eta_c$ and the unit cost $w_B$ have been defined based on the data in Table 3.22.

The unit cost of the recharging devices $c_{BSS}$ and $c_{BRS}$ has been fixed at 39.8 k€, based on a technological-statistical regression, for the considered recharge power of 60 kW (A.Schroeder & T.Traber, 2012).

#### *3.4.1.3.1 Simplified sizing problem*

The sizing problem has been carried out at first for a simplified scenario, where only BSS are considered as recharging devices. This yields a simplification in the formulation of the cost function and constraints. The traffic data in input has been taken from the actual operations of the ACM on a given Saturday in October 2017. This month is associated to the most intense flying activity, due to the good weather and shrinking daylight time. It has been selected based on a worst-case, conservative approach for the sizing.

The sizing analysis has been carried out first considering a time frame of a single day, and next on the corresponding week. The considered discretization time $\tau$ is 15 minutes. The top plots of Figure 3.28 display the results in terms of electric energy need over time, compared to the supply cost of energy in Italy, based on historical data (orange line). The results for the one-day and one-week cases are shown on the left and right plots respectively.

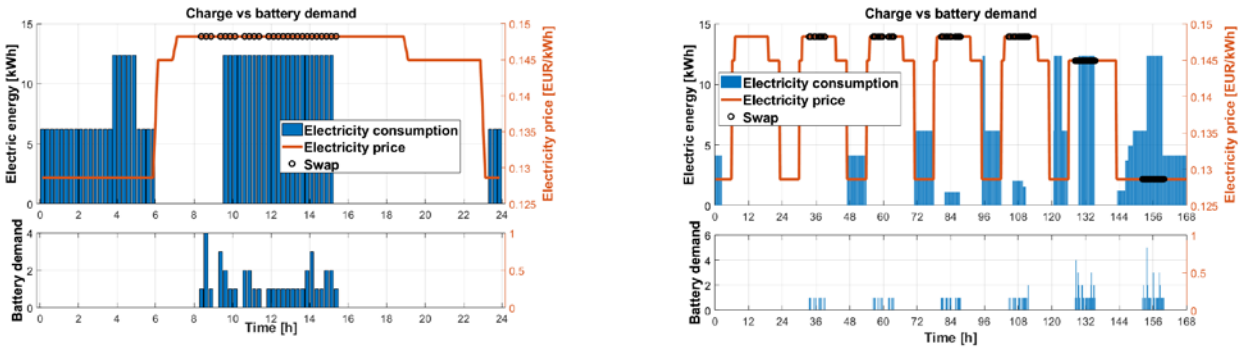


(a) (b)

Figure 3.28: Energy expenditure and recharging schedule at Milan Bresso, BSS only. (a): busiest day; (b) busiest week.

On the bottom plots, the battery requirement bound to the assumed schedule of operations is reported. It is possible to note how the optimal recharge strategy takes advantage of the low energy price during night hours to recharge a first set of batteries. The remaining recharge operations are carried out on condition, soon after the beginning of flight operations during daylight hours. This is more advantageous than having a larger number of batteries, charged ahead of their respective time of use. After use, batteries are not charged until a lower power procurement price is reached, i.e. after daylight hours.Table 3.23 compares the results of the sizing for the one-day and one-week cases. As expected, the number of batteries and BSS is the same, as Saturday corresponds to the most demanding day of the week. The number of aircraft needed to cover the operative requirements is lower than the current fleet of ACM. This is due to the fact that the scenario investigated here does not account for redundancy, which would be required in real-world operations to mitigate the effect of prolonged unavailability of some aircraft resulting from maintenance and faults, nor it considers that some aircraft with specific instrumentation configuration are indeed required for specific missions, like IFR training, but are generally far less used than others in the current ACM fleet.

Table 3.23: Results of sizing, comparison.

| Parameter | One-day sizing | One-week sizing |
|---|---|---|
| Number of batteries ($N_B$) | 16 | 16 |
| Number of chargers ($N_{BSS}$) | 1 | 1 |
| Number of aircraft ($N_{AC}$) | 10 | 10 |
| Recharged batteries | 39 | 136 |
| Overall energy requirement [kWh] | 410 | 1,430 |
| Peak power [kW] | 60 | 60 |
| Power losses [MJ] | 103 | 361 |

### *3.4.1.3.2 Complete sizing problem*

In a more complete scenario, both BSS and BRS are considered. For the case of Milan Bresso, no substantial difference in the output of the design procedure has been highlighted. The recharge time by a BRS is compatible with the 15 minutes average turnaround time for ACM operations, thus the adoption of a BRS or BSS bears a similar impact on operativity. Figure 3.29 highlights the similarity of the sizing solutions in the respective cases, with both BRS and BSS (left) and with BRS only (right). Both compare well with Figure 3.28 (a), where only BSS are considered.

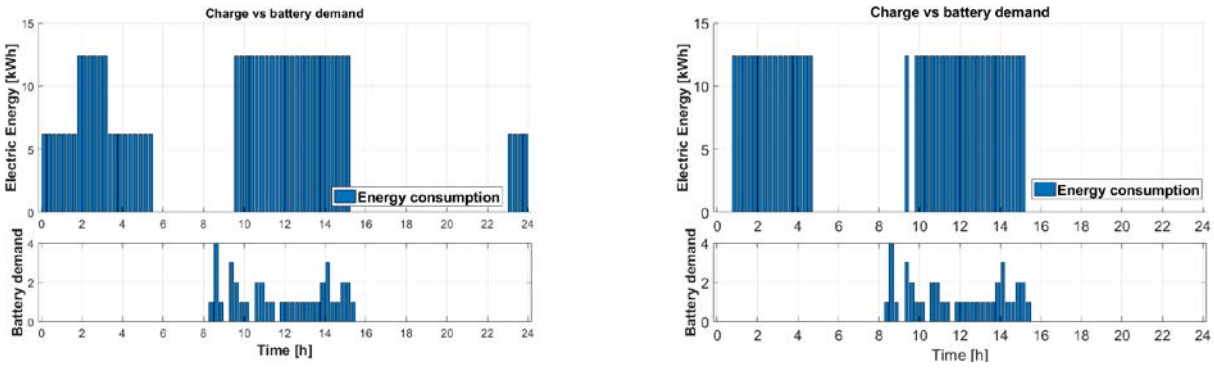


(a) (b)

Figure 3.29: Comparison of sizing solutions. (a) BSS only; (b) BSS and BRS.

The breakdown of optimal cost corresponding to a sizing solution where both BRS and BSS are considered is shown in Figure 3.31. The right plot presents the cost components due to power, as well as procurement of recharging devices and batteries, magnified with respect to the left plot. The latter is dominated by aircraft and energy procurement cost. The columns refer to sizing solutions with different battery unit cost parameter $w_B$.

As previously reported, a change in this quantity has an indirect effect also on the number of charging devices. From the lower plots in Figure 3.30, moving leftwards column by column, it is possible to check that under a certain $w_B$ the solution changes to a higher number of rechargers, which increase greatly the recharging ability of the ground infrastructure, and consequently yield a lower number of required batteries.

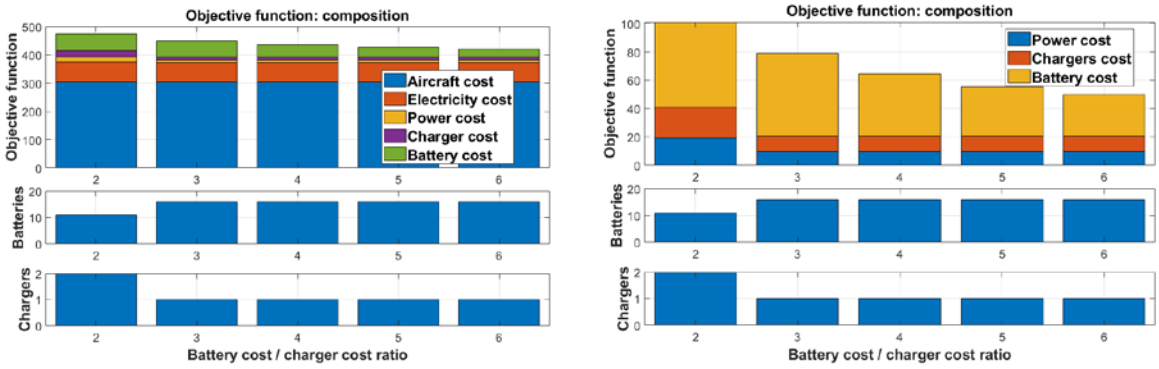


(a) (b)

Figure 3.30: Breakdown of cost for different values of $w_B$.
(a) General view; (b) detail of smaller cost components.

#### *3.4.1.4 Athens international airport study case*

The described procedure can also be applied for the determination of the infrastructure requirements for managing PE and HE aircraft fleets at Athens International Airport *Eleftherios Venizelos* (LGAV). LGAV can be considered a paradigmatic airport for testing the illustrated sizing procedure, since it was the European airport with the largest number of propeller-driven regional aircraft movements in the five years from 2016 to 2018 (Eurostat, s.d.). Regional aircraft are widely used to connect Greek islands to the mainland, thus Athens airport makes a perfect test case to assess the infrastructural needs of regional aircraft operation. Three regional airliners were considered for the case study:

1. Bombardier Dash 8 Q400 (78 passengers),
2. ATR42 (~48 passengers),
3. ATR72 (~70 passengers).

This is the class of aircraft that may be interested, in a relatively short term, in the introduction of versions designed to include an HE powertrain, and will therefore include a battery pack.

We supposed to replace the current conventional fleet of aircraft with vehicles that include a serial HE powertrain, and this will have an impact on their mission profile. In fact, taxiing-out, taking-off and climbing up to a defined 'hybrid transition altitude' (3,000 ft in the present case) will be performed in a zero-emission PE mode. Subsequently, the Power Generation System (PGS, i.e. a thermal engine burning hydrocarbon fuel) will be turned on, both for providing energy during final climb and cruise phases and for recharging batteries, if needed. Finally, when descending below the hybrid transition altitude, the PGS will be shut off, so final descent, approach, landing and taxi-in will again be performed in PE mode. This strategy allows a drastically reduction of gaseous and noise emissions at airport level (Riboldi, Mariani, Trainelli, Rolando, & Salucci, 2020).

The technical specifications of the electrified airplanes were obtained by means of the

Hyperion preliminary sizing tool developed at the Department of Aerospace Science and Technology at Politecnico di Milano (Trainelli, Salucci, Rossi, Riboldi, & Rolando, 2019) (Trainelli L. , Riboldi, Salucci, & & Rolando, 2020) (Rolando A. , Salucci, Trainelli, & Riboldi, 2020). For the sake of clarity, the electrified versions designed by using Hyperion were named as the original model adding an "HE-" prefix, yielding HE-DH8, HE-ATR42 and HE-ATR72 respectively.Table 3.24 shows the estimated battery capacity for each of the aforementioned models. A budgetary price for the batteries (including cells and battery management system) was calculated using 2018 Lithium-ion battery price, i.e. approximately 176 €/kWh (BloombergNEF, s.d.). Even if battery data comes from a fully-fledged aircraft sizing procedure, they should be taken as representative of a reasonable order of magnitude.

Data coming from public flight tracking services was employed for the study (Flightradar24, s.d.). In particular, flights taking off on Friday, December 13, 2019 ("Friday-only case") and the following weekend ("Weekend case") were used to build the flight schedule to be fed to the optimisation algorithm. The bar plots in Figure 3.31 and Table 3.24 depict the relevant departures for the Friday-only case and the Weekend case, respectively. The current fleet of DH8, ATR42 and ATR72 is composed of 10, 9 and 7 airplanes, respectively.

Table 3.24: Aircraft characteristics.

| Name | Pax | Battery Price [k€] | Battery capacity [kWh] |
|---|---|---|---|
| HE-DH8 | 78 | 253.4 | 1,400 |
| HE-ATR42 | 48 | 184.8 | 1,000 |
| HE-ATR72 | 70 | 237.6 | 1,300 |

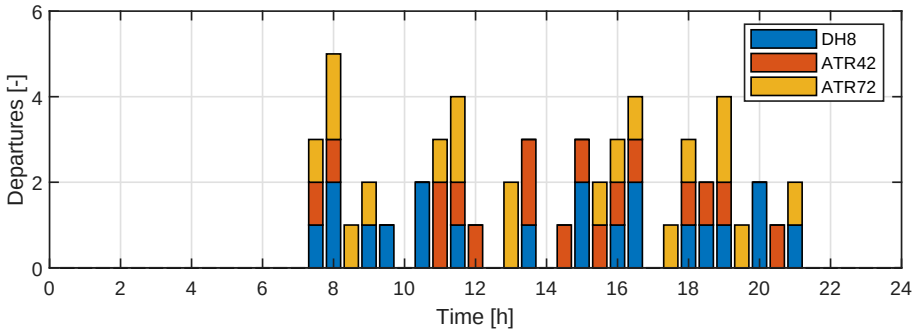


Figure 3.31: Regional airplane departures from LGAV for the Friday-only case.

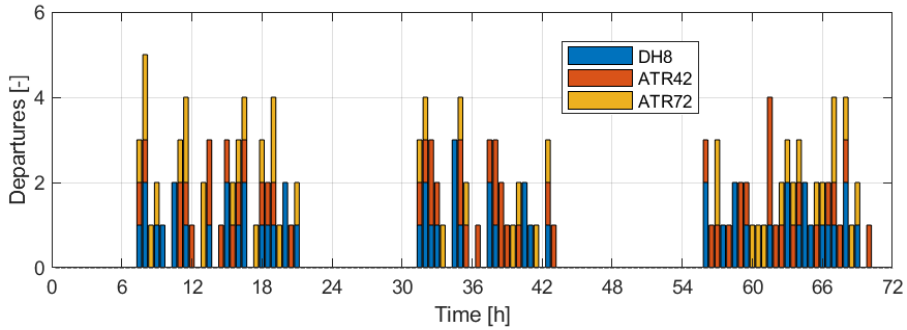


Figure 3.32: Regional airplane departures from LGAV for the weekend case.

Two different values of the recharge power $P_{BSS}, P_{BPC}$ of the ground recharging devices have been considered: 250 kW and 1,000 kW. These two values were selected as representative of current automotive charging infrastructures. 250 kW is already available for Tesla customers who can use Tesla Superchargers (Tesla, s.d.), while 1,000 kW are under development to be employed to recharge fully-electric lorries (Tesla MEGACharger (Electrek , s.d.)).

The cost of the charging devices ($c_{BPC}, c_{BSS}$) was estimated according to (Schroeder & Traber, 2012). An additional 10% was added to account for maintenance costs.

Chargers cost, recharge process efficiency $\eta_c$, charger life and other data can be found in Table 3.25.

Table 3.25: Chargers properties

| Parameter | Value |
|---|---|
| $c_{BPC}, c_{BSS}$ 250 kW chargers | 66.7 k€ |
| $c_{BPC}, c_{BSS}$ 1000 kW chargers | 89.0 k€ |
| Charger life | 10 years |
| Charging efficiency | 93 % |

Electricity prices in Greece for the year 2018 were assumed for the simulation. They are reported in Table 3.26.

Table 3.26: Greek electricity prices for the LGAV study case

| Energy charge | | |
|---|---|---|
| 0.0648 | €/kWh | Daytime |
| 0.0777 | | Nighttime |
| Power charge | | |
| 10.5080 | €/kW/month | Daytime |
| 2.5080 | | Nighttime |

They are composed of a higher Daytime energy charge (from 07:00 to 23:00) and a lower Nighttime energy charge (from 23:00 to 07:00).

#### *3.4.1.4.1 Friday-only case - 250 kW chargers*

The resulting consumed electric energy over time, using 250 kW chargers is displayed in Figure 3.33.

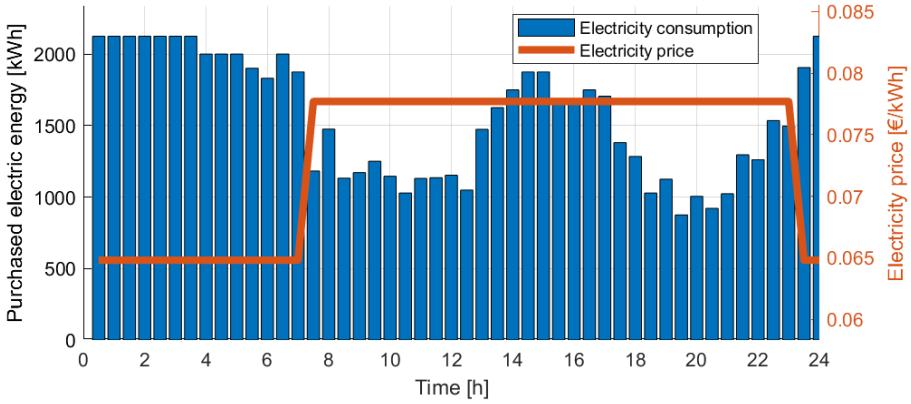


Figure 3.33: Energy consumption at LGAV, with 250 kW chargers. Friday-only case.

Blue bars represent electric energy absorbed every 30 minutes. The orange line delineates the variation of $\lambda_t$ during the day. We can see as a greater amount of electricity is drained from the grid during the night, with a quite uniform energy consumption. On the other hand, energy consumption decreases during the day, but still responds to the increases in battery demand.

Figure 3.34 portrays the power consumption corresponding to energy usage. The bar plot at the bottom shows the number of batteries recharged at each time step. These batteries can either be charged with a BSS or with a BPC. In this case, since the aircraft fleet is fixed, an optimally mixed usage of BSS and BPC comes out from ARES.

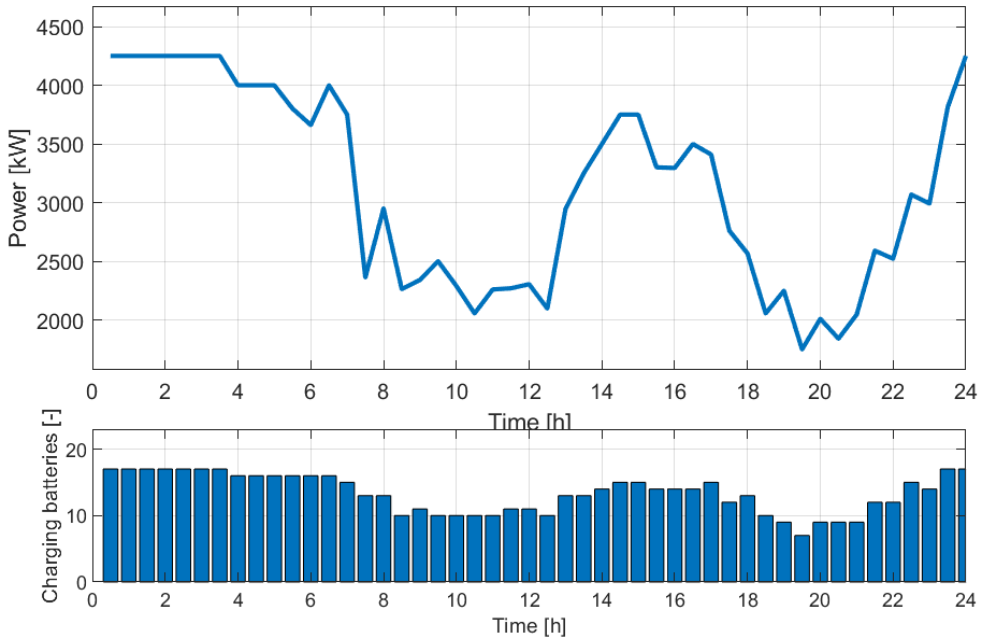


Figure 3.34: Power consumption (upper graph) and charging batteries (lower graph) at LGAV with 200kW chargers. Friday-only case.

Table 3.27: LGAV Sizing results. 250 kW chargers. Friday-only case.

| Item | Value | | |
|---|---|---|---|
| | HE-DH8 | HE-ATR42 | HE-ATR72 |
| No. airplanes | 10 | 9 | 7 |
| No. batteries | 14 | 13 | 13 |
| No. charges | 20 | 17 | 19 |
| No. BSS | 7 | | |
| No. BPC | 10 | | |
| Peak power | 4,250 kW | | |
| Energy consumption | 74,946 kWh | | |

Table 3.27 details the outcome of the optimization in terms of resources. It is interesting to note that charging a battery takes between 4.0 and 5.6 hours (depending on the aircraft model) if operating at full power. This recharge time is not compatible with the available aircraft fleet and could impact on the flight schedule. Therefore, BSS charging is employed to recharge some batteries while these are disembarked from the airplane. As a result, seven BSSs are employed together with ten BPCs. The number of batteries is thus 40, to be contrasted with 26 airplanes (14 for the HE-DH8, 13 for the HE-ATR42 and 13 for the HE-ATR72).

### *3.4.1.4.2 Friday-only case - 1000 kW chargers*

Figure 1.1 depicts the absorbed electric energy in the 1,000 kW charger case. It is immediately clear that the charging process takes place in a shorter amount of time: around 4 times less than the 250 kW case.

No recharges occur between 08:00 and 10:30, avoiding to buy electricity when it is more expensive. On the other hand, Figure 3.36 shows that the peak power required in this case is 6 MW. (42% more than in the 250 kW case).

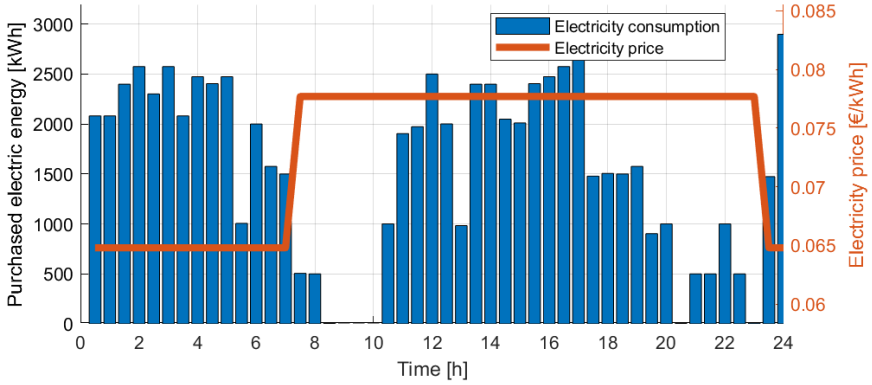


Figure 3.35: Energy consumption at LGAV, with 1,000 kW chargers. Friday-only case.

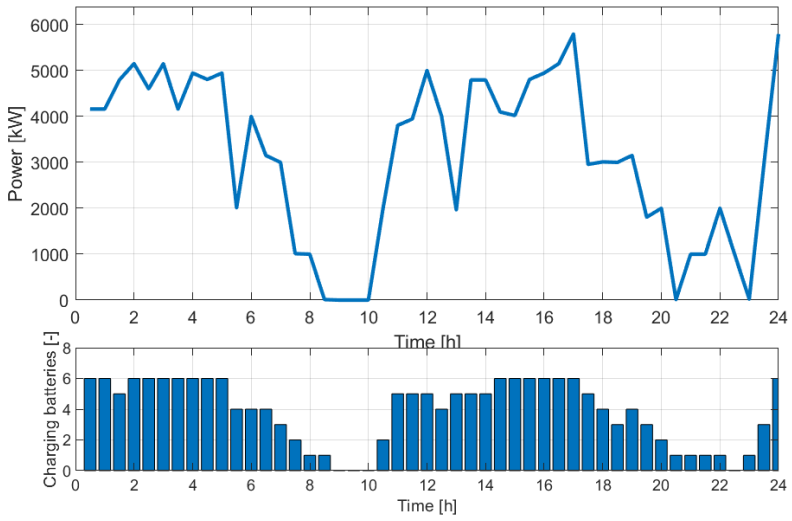


Figure 3.36: Power consumption (upper graph) and charging batteries (lower graph) at LGAV with 1,000 kW chargers. Friday-only case.

Table 3.28: LGAV Sizing results. 1,000 kW chargers. Friday-only case.

| Item | Value | | |
|---|---|---|---|
| | HE-DH8 | HE-ATR42 | HE-ATR72 |
| No. airplanes | 10 | 9 | 7 |
| No. batteries | 11 | 9 | 8 |
| No. BSS | 1 | | |
| No. BPC | 5 | | |
| No. charges | 20 | 17 | 19 |
| Peak power | 5,795 kW | | |
| Energy consumption | 74,946 kWh | | |

As a natural consequence of the higher charging power and the reduced charging time, fewer chargers and batteries are needed, as seen from the results detailed in Table 3.28. In particular, only five BPCs and one BSS are used and a minimum of 28 batteries is required to fulfil the battery demand (11 for the HE-DH8, 9 for the HE-ATR42 and 8 for the HE-ATR72), which means that only one extra battery is required for two out of the three airplane models.

### *3.4.1.4.3 Weekend case - 250 kW chargers*

Weekend case results with 250 kW chargers shown in Table 3.29 imply that more batteries are necessary to satisfy the battery demand with respect to the Friday-only case (44 against 40: 15 for the HE-DH8, 15 for the HE-ATR42 and 14 for HE-ATR72). This is probably caused by the large number of airplanes taking off on Sunday night and the large number of movements in the next morning. Since charging power is limited and charging time is long, a great number of spare batteries is necessary. In this case a total of 19 chargers are required: 8 BPC and 11 BSS slots. On the other hand, the large number of chargers and spare batteries allows lowering the peak power (4.75 MW).

Table 3.29: LGAV Sizing results. 250 kW chargers. Weekend case.

| Item | Value | | |
|---|---|---|---|
| | HE-DH8 | HE-ATR42 | HE-ATR72 |
| No. airplanes | 10 | 9 | 7 |
| No. batteries | 15 | 15 | 14 |
| No. charges | 55 | 55 | 44 |
| No. BSS | 11 | | |
| No. BPC | 8 | | |
| Peak power | 4,750 kW | | |
| Energy consumption | 203,441 kWh | | |

Figure 3.37 and Figure 3.38 depict the energy consumption and power demand

during the three days.

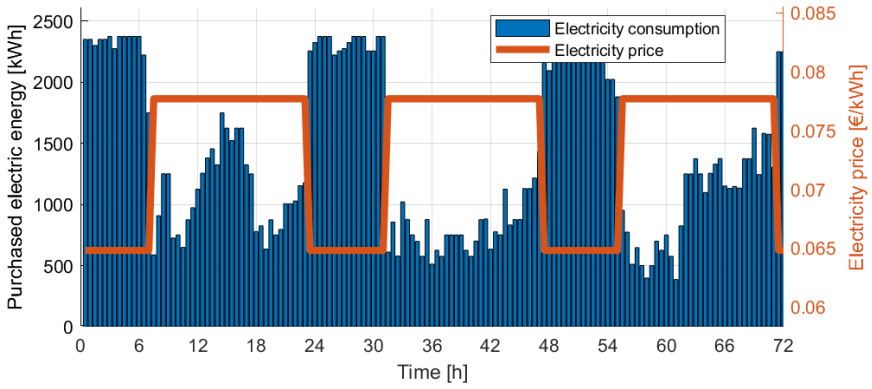


Figure 3.37: Energy consumption at LGAV, with 250 kW chargers. Weekend case.

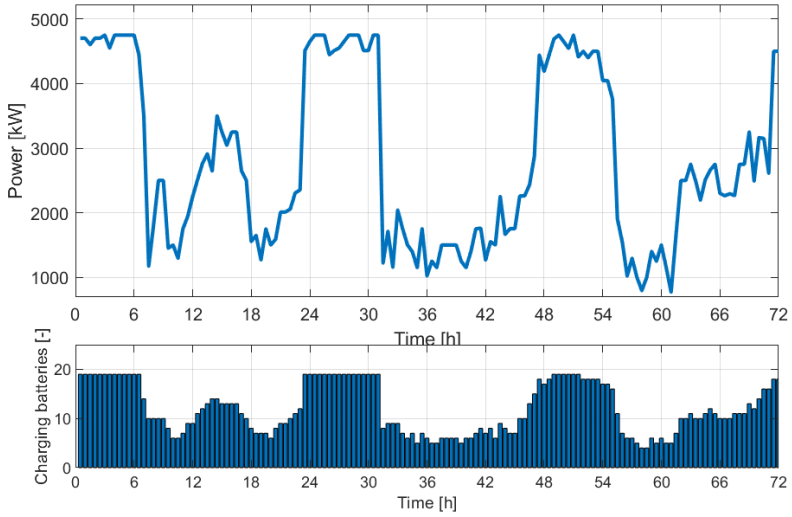


Figure 3.38: Power consumption (upper graph) and charging batteries (lower graph) at LGAV with 250 kW chargers. Weekend case.

### *3.4.1.4.4 Weekend case - 1000 kW chargers*

Table 3.30 shows the main results obtained when the charging power is raised to 1 MW, in the full weekend case: seven BPCs are employed to satisfy the flight schedule presented in Figure 3.32. It is interesting to notice that BSSs are not used. This is a consequence of the fact that charging power is high enough to allow all the 30 batteries to be recharged without being disembarked during the day. However, the minimum number of batteries is higher than the number of flying airplanes. This means that at least three batteries are charged on airplanes that are still on the ground and disembarked afterwards.

Table 3.30: LGAV Sizing results. 1,000 kW chargers. Weekend case.

| Item | Value | | |
|---|---|---|---|
| | HE-DH8 | HE-ATR42 | HE-ATR72 |
| No. airplanes | 10 | 9 | 7 |
| No. batteries | 11 | 11 | 8 |
| No. BSS | 0 | | |
| No. BPC | 7 | | |
| No. charges | 55 | 55 | 44 |
| Peak power | 6,796 kW | | |
| Energy consumption | 203,441 kWh | | |

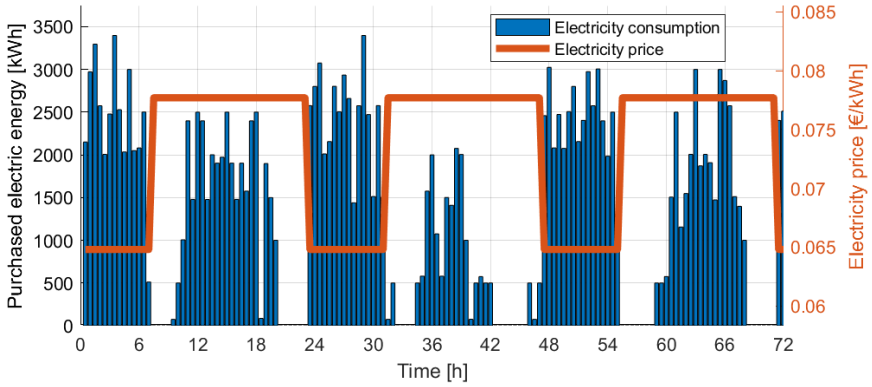


Figure 3.39: Energy consumption at LGAV, with 1,000 kW chargers. Weekend case.

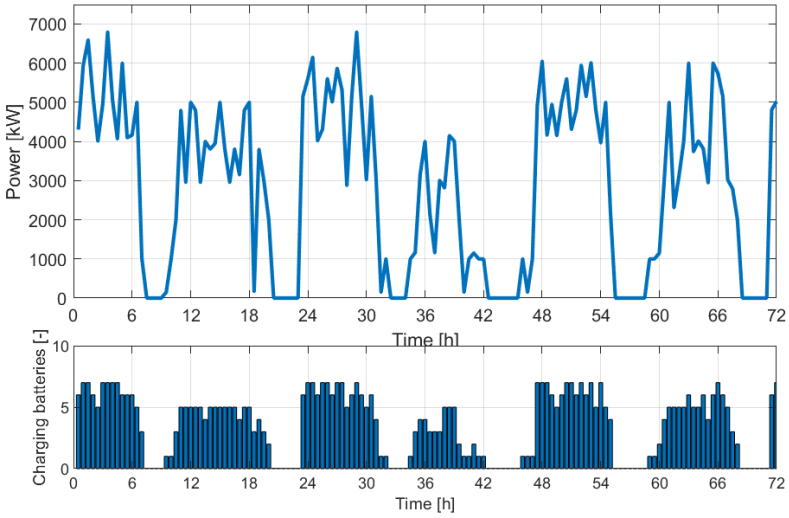


Figure 3.40: Power consumption (upper graph) and charging batteries (lower graph) at LGAV with 1,000 kW chargers. Weekend case.

Figure 3.39 and Figure 3.40 show how the energy consumption and the demanded power evolve in the full weekend case.

By comparing the cost function in the Weekend case, for the two values of charging power, battery cost emerges as the largest part in both the 250 kW and the 1,000 kW case, representing the 61% and 52% of the total respectively. This is shown in Fig. 11, which also shows that the second largest contribution to the cost function is the cost of energy, which is slightly lower in the 1,000 kW case, meaning that it is possible to recharge the batteries in a smarter way, when the electric energy is cheaper. On the other hand, this saving on the energy leads to an increase in the power cost of electricity, which is less is the 250 kW case. The amount related to chargers is of minor relevance, as it accounts for a very small percentage of the cost function: 4.2% and 2.6%, respectively.

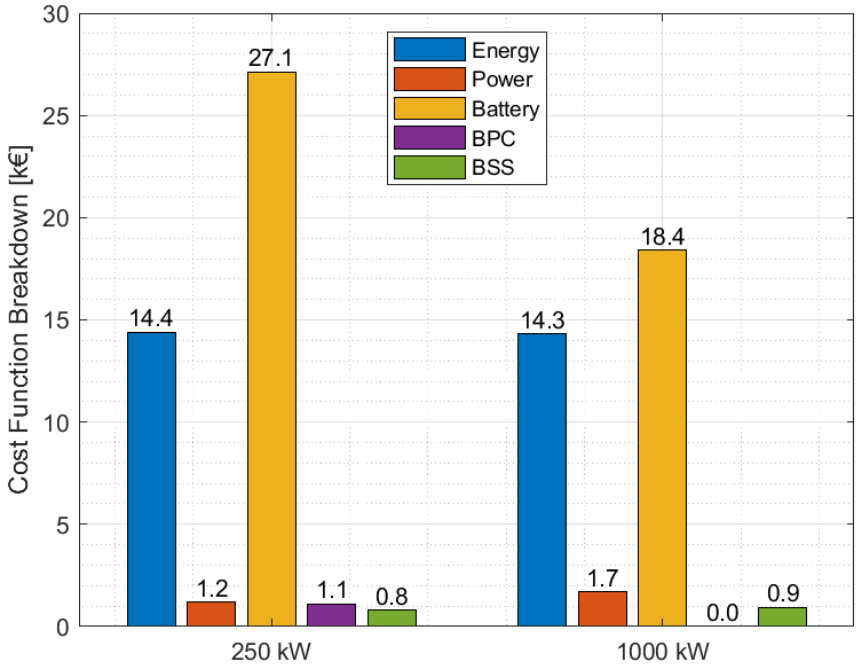


Figure 3.41: Cost function breakdown for the weekend case.

### 3.4.2 Hydrogen infrastructures

This section mainly discusses material taken from Deliverable 10.1 of the MAHEPA project (VV.AA., 2019).

#### *3.4.2.1 General chemical and physical characteristics of hydrogen*

Hydrogen is the lightest and most abundant element in the universe. Nevertheless, in can be rarely found on Earth in a free form as a hydrogen molecule H2. Therefore, it has to be produced from compounds rich with hydrogen, like water or methane. As a gas, hydrogen is odourless, colourless, tasteless, non-corrosive, non-toxic and highly flammable. It changes into liquid at temperatures below 20 K. As a liquid, it is, similar to water, non-corrosive and colourless, with the light blue tint. Due to a small size of its molecule, it has a very low density and a tendency to rise and to defuse quickly, also through solids. Some metals, exposed to hydrogen, can loose on ductility due to penetration of hydrogen atoms into their lattice structure, a phenomenon known as hydrogen embrittlement, or even degradation, if exposed to hydrogen at high pressure and temperatures (hydrogen attack). If released in an atmosphere, hydrogen would rise to the upper atmosphere, where it would oxidize to water, react with pollutants or escape the Earth and not cause any environmental concerns. If released in a closed space, it would rise and accumulate on ceiling.

Table 3.31: Relevant physical and chemical properties of hydrogen

| | |
|---|---|
| Boiling point | 32.938 K |
| Temperature at a critical point | 1.2858 MPa |
| Pressure at a critical point | 0.071 g/cm3 |
| Density of liquid hydrogen at a boiling point | 33 kWh/kg |
| Energy density | 4 % vol. |
| Concentration at lower explosive limit | 77 % vol. |
| Concentration at upper explosive limit | 585°C |
| Auto ignition temperature | 0.02 MJ |
| Minimum ignition energy | 346 cm/s |

Heat capacity of hydrogen is similar to those of other gases, while its thermal conductivity is significantly higher. Hydrogen has also a very low ignition energy and a very broad range between lower and upper explosive limit, meaning that it can burn in broad varieties of concentration mixtures with air. Relevant hydrogen physical and chemical characteristics are presented in the Table 3.31.

Hydrogen is mostly used in chemical industry, but hydrogen as a fuel has great future possibilities. As a fuel, hydrogen can produce heat energy through combustion or electrical energy through fuel cells. Using hydrogen in a fuel cell has several advantages over ICE:

- Better efficiency. Fuel cells reach efficiencies of 40 - 60 % compared to combustion power plants, which reach efficiencies of approx. 30 %.
- Low noise. Fuel cells and electro-motors produce less noise than combustion engines.
- Lesser emissions. Hydrogen combustion cells emit NOx gasses and water, while fuel cells emit only water.
- Power to weight ratio of electric engines is greater than of combustion engines.
- Fuel cells can be easily combined with batteries.

#### *3.4.2.2 Using hydrogen for aircraft fueling*

Due to previously stated reasons and the following recommendations of ISO/PASS 15594, airports would need hydrogen in a liquefied form for fuelling. Based on following recommendations and explanations, stated in ISO 14687-2 and ISO/PASS 15594, hydrogen has to fulfil demands, listed in Table 3.32. Temperature of the liquid hydrogen should be 20 K or lower and pressure should be equal of higher than 700 kPa to achieve acceptable fuelling times (20 min) (ISO/PASS 15594).

Table 3.32: Purity demands for hydrogen at airports.

| Form | Liquid hydrogen, type II, grade D |
|---|---|
| Purity | > 99.9999 % (volume fraction) |
| Para-hydrogen | > 95 % (minimum mole fraction) |
| Total gasses | <100 µmol/mol |
| O2 content | < 0.00002 % (volume fraction) |
| N2 content | < 0.00002 % (volume fraction) |
| H2O content | < 0.00005 % (volume fraction) |
| CnHm | < 0.000001 % (volume fraction) |
| CO content | < 0.000001 % (volume fraction) |
| CO2 content | < 0.000001 % (volume fraction) |
| Total Sulphur compounds | < 0.004 µmol/mol |
| HCHO content | < 0.01 µmol/mol |
| HCOOH content | < 0.2 µmol/mol |
| NH3 | < 0.1 µmol/mol |
| Total halogenated compounds | < 0.05 µmol/mol |
| Particles diameter | < 5µm |
| Maximum particles concentration | 1µg/l in normal conditions |

The transition to hydrogen as an aviation fuel will be influenced by factors, such as the future cost of liquid hydrogen, advances in hydrogen technologies, potential long-

term international restrictions on aircraft emissions and the cost of kerosene. Although sharing the infrastructure with other transport modes could reduce cost for aviation section (Van Zon, s.d.).

#### *3.4.2.3 Hydrogen supply chain*

The standard set of ground infrastructure and operations for hydrogen supply consists of (Figure 3.42):

- Hydrogen production. There are many ways of producing hydrogen, each yielding to a very different cost scheme. The steam methane reforming (SMR) of natural gas (hereinafter NG) prevails as the most widely used in the industry, being currently the cheapest way for producing hydrogen. A technology for bioorganic production of hydrogen (by algae) is still under development.
- Hydrogen transport. Hydrogen can be transported to airports in a liquefied form by road (trailers), rail, and water or by pipelines in gaseous form.
- Hydrogen liquefaction or hydrogen compression. Due to its low density, hydrogen has a large volume as a gas at normal temperature and pressure and is therefore unpractical for storage and transportation purposes. Therefore, hydrogen is usually used in a compressed or liquefied form. Hydrogen liquefies at temperatures lower than 20 K, while different liquefaction methods can be used like Linde's cycle or Claude's cycle.
- Hydrogen storage. Hydrogen can be stored as gas inside underground caverns, as a compressed supercritical fluid, as a liquid in a cryogenic tank, in materials based H2 storage systems, as a slush hydrogen (solid state) in cryogenic tanks as cold-compressed or cryo-compressed hydrogen. The most feasible scenario for supplying hydrogen to airports is with a movable cryogenic storage (cryogenic truck).
- Hydrogen refuelling point. Hydrogen refuelling point is defined in ISO/PASS 15594 and will be described in detail in the following section.

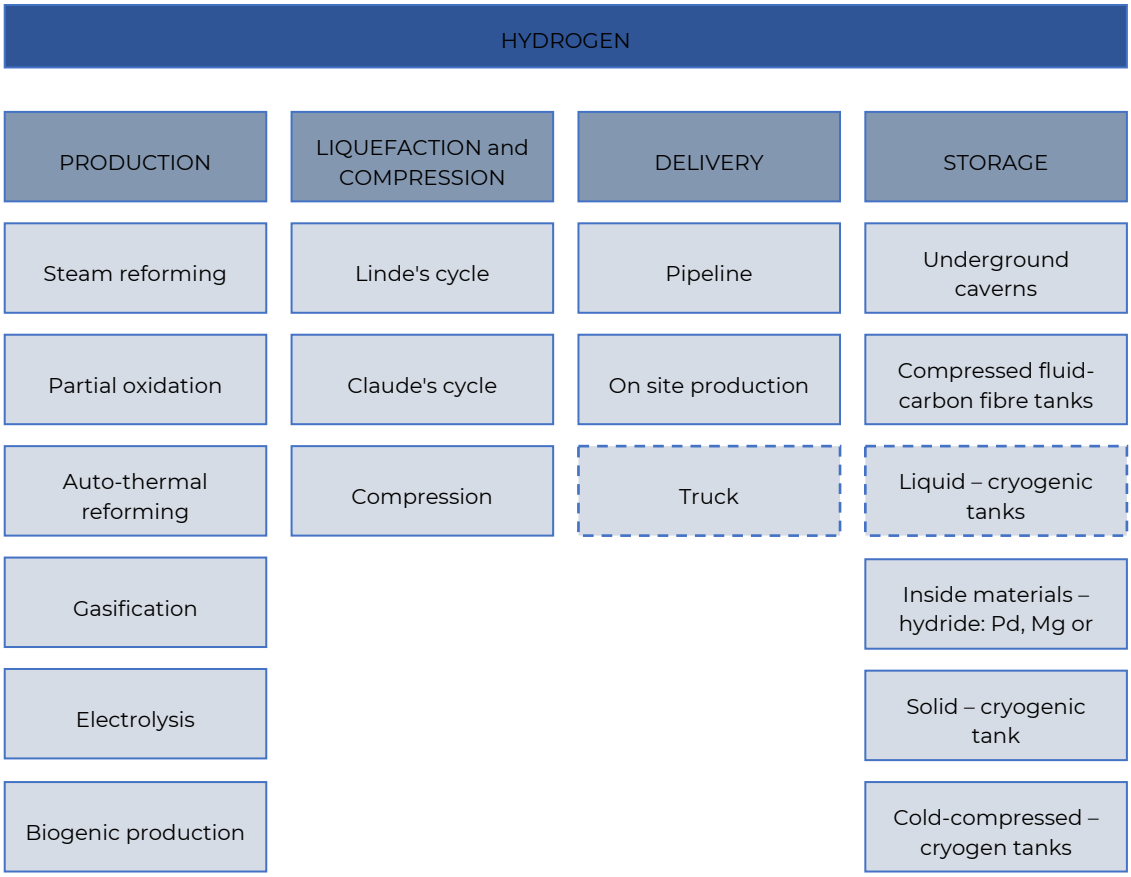


Figure 3.42: A standard set of ground infrastructure and operations for hydrogen supply (VV.AA., 2019).

### *3.4.2.3.1 Hydrogen production*

Hydrogen is mostly produced from methane (68 %), 16 % from oil, 11 % from coal and only 5 % with electrolysis. There are many ways of producing hydrogen, yet only one production method prevails as the most widely used in the industry. This is the steam methane reforming of natural gas. Since this technology is mature, we can conclude that the variations of hydrogen production costs are largely dependent on the price of the NG.

Hydrogen can be produced in the following ways:

- Steam reforming. This is the most common and cheapest way for producing hydrogen. Hydrogen is produced from methane and water vapour through chemical reaction. Instead of methane, other light hydrocarbons like oil can be used. More information on steam reforming and similar processes can be found in ISO 16110: Hydrogen generators using fuel processing technologies.
- Partial oxidation. Process can produce hydrogen from heavy (long-chain) hydrocarbons like coal or heavy fuel oil using oxygen (O2) as an oxidant. This method is more expensive than steam reforming, but it can produce hydrogen from other ingredients.
- Auto-thermal reforming. A combination of steam reforming and partial oxidation. It is more expensive than steam reforming and therefore not commonly used.
- Gasification. A method for producing fuel gases from coal. It uses both water and oxygen as an oxidant.
- Electrolysis. A process, where hydrogen is produced from water and electricity. The method is simple but rarely used due to economic reasons (price of electricity). More information on electrolysis can be found in ISO 16110: Hydrogen generators using fuel processing technologies.
- Biogenic production. Produces hydrogen from biomass, like wood or straw and other bio-fuels (e.g. bio-methane, bioethanol, vegetable oils, biodiesel, etc.). Hydrogen can be produced thermochemical (with a process similar to gasification) or biochemically (using a certain type of bacteria). Biogenic production is a new method and is therefore partly still in an experimental stage.

Figure 3.43: An electrolysis hydrogen production plant (VV.AA., 2019).

### *3.4.2.3.2 The price of hydrogen*

Currently, the hydrogen production in Europe is led by a few large industrial actors, which play a key role in establishing a market price internally. In general, we may describe the commercial transaction as a bilateral hydrogen transaction between two industries, defined by a high price elasticity, and portrayed by different parameters. Firstly, the inexistence of a global price database leading the market to a lack of traceable information. Additionally, prices depend on buyers' location, which defines how hydrogen will be delivered (in a liquid or gaseous form), thereby transport and distribution of hydrogen is especially important, when hydrogen is produced in large scale, to get it from centralized production sites to points of use. Moreover, the purity levels play an important role since higher purity levels imply higher costs of hydrogen. Thus, having a reliable market price is extremely challenging, nevertheless, it is known that prices vary from 10 €/kg to 60 €/kg (34). Finally, encompassing these factors, a more reliable approach to forecast hydrogen price in the industry is by analysing its production cost (Dillich, s.d.).

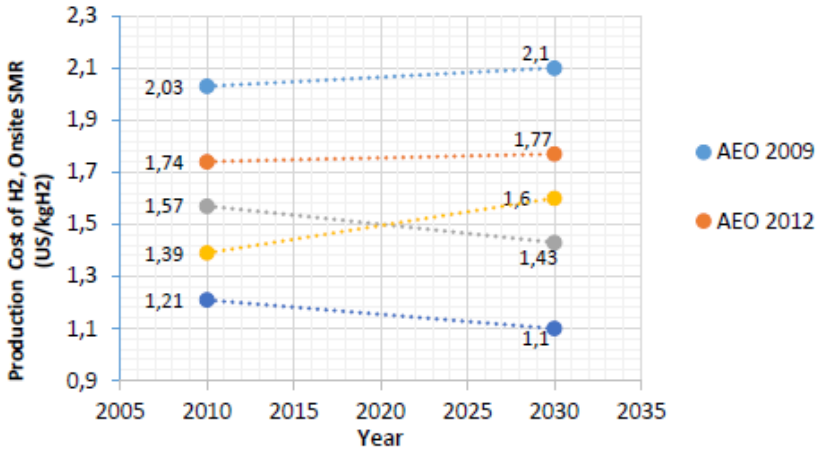


Figure 3.44: Hydrogen from SMR Cost Evolution Sensitivity Analysis (VV.AA., 2019).

Information on different cost ranges for the same technology in several industries was compiled and conducted by the Department of Energy of The United States (Department of Energy of the United States, s.d.). The report proposes 5 different scenarios (considering different NG prices), which were modelled by a tool, called H2A6. The main results of these simulations are shown in Figure 3.44. The first scenario uses Annual Energy Outlook (AEO) 2009 prices for industrial NG as a production feedstock (light blue), while the second scenario uses the same principle but uses AEO 2012 prices instead (orange). Then, the report conveys a sensitivity analysis by setting up three flat prices 2 USD/MMBtu (Million Metric British thermal units) (dark blue), 3 USD/MMBtu (yellow) and 4 USD/MMBtu (grey).

### *3.4.2.3.3 Compression and liquefaction of hydrogen*

Due to its low density, hydrogen has, as a gas at normal temperature and pressure, a large volume and is unpractical for storage and transportation. Therefore, hydrogen is usually compressed or liquefied. Hydrogen liquefies at temperatures lower than 20 K. Most commonly used liquefaction methods are Linde's cycle or Claude's cycle. Namely, two types of H2 molecules are known: para-hydrogen and ortho-hydrogen. Considering ortho- to para-hydrogen conversion, special care has to be taken in the process. At normal temperature and pressure, ¾ of all molecules are in the form of ortho-hydrogen and ¼ in a form of para-hydrogen. In a liquid form, where temperatures drop below 20 K, most of hydrogen (99.8 %) is in a para-hydrogen form. The transition from ortho-hydrogen to para-hydrogen occurs very slow (can last several days) and releases energy. Therefore, if hydrogen is liquefied too quickly, after liquefaction, transition from ortho- to para-hydrogen will cause considerable release of energy and consequential boil-off. Therefore, special catalysers are used to fasten the ortho- to para-hydrogen conversion and liquefaction.

Compressor can be either reciprocating or centrifugal. Reciprocating compressors are most commonly used for hydrogen applications, but centrifugal compressors are also an option. Reciprocating compressors cost about 50 % more than a comparable centrifugal compressor but have higher efficiencies (Timmerhaus & Mendelssohn, 2017). Compressor costs are based on the amount of work done by the compressor, which depend on the inlet pressure, outlet pressure, and flow rate. Larger compressors are quite cheaper on a unit basis compared to smaller ones. The capital cost (CX) of compressors and liquefiers depend on compressor/liquefier size and can be estimated with the following equation

$$C_x = C_0 \left(\frac{S_x}{S_0}\right)^y \tag{3.88}$$

where parameters C0, S0 and y are defined in the Table 3.33, while SX denotes the size of compressor (in kW) and liquefier (in kg of liquefied hydrogen per day). To compress 1 kg of hydrogen or 2 – 3 % of hydrogen energy content 0.7 - 1.9 kWh of energy is used, while liquefaction requires 11 kWh/kg or 33 % on base energy content.

Table 3.33: Estimated costs and energy inputs of compression and liquefaction (VV.AA., 2019).

| | Compressor | Liquefier |
|---|---|---|
| Base size (S0) | 10 kW | 30 000 kg/day |
| Base capital cost (C0) | 13 500 EUR | 36 000 000 EUR |
| Scaling factor (y) | 0.579 | |
| Operation and maintenance cost (fraction of capital cost) | 4 % | 4 % |
| Energy use | 0.7 - 1.0 kWh/kg | 11 kWh/kg |

Figure 3.45: Hydrogen compressor (left) and hydrogen liquefier (right) (VV.AA., 2019).

### *3.4.2.3.4 Hydrogen transport*

Hydrogen is most commonly transported by trucks or via a pipeline system. Other possibilities of delivery are by train or ship, but they are not analysed in detail in this study (due to a similar approach).

#### 3.4.2.3.4.1 Transport by truck

Hydrogen can be transported either in a gaseous form with tube trailer or in a liquid form with cryogenic truck (Figure 3.47). If there is no direct delivery from truck to aircraft, storage and dispenser are also needed for fuelling (Figure 3.46). Compared to pressure gas vessels, a higher amount of hydrogen can be carried out with a LH2 trailer, as the density of liquid hydrogen is higher than that of gaseous hydrogen. At a density of 70.8 kg/m3, around 3 500 kg of liquid hydrogen or almost 40 000 Nm3 can be carried at a loading volume of 50 m3. Over longer distances it is usually more cost-effective to transport hydrogen in a liquid form, since a liquid hydrogen tank can substantially hold more hydrogen than a pressurized gas tank. Hydrogen is loaded into insulated cryogenic tanks for transportation of liquid hydrogen. LH2 trailers have a range of approximately 4 000 km. While transporting the hydrogen to its final destination, the cryogenic hydrogen heats up, causing the pressure in the container to rise. Similar to lorry transport, LH2 can also be transported by ship or by rail, given that suitable waterways, railway lines and loading terminals are available (Hydrogen Europe, s.d.).

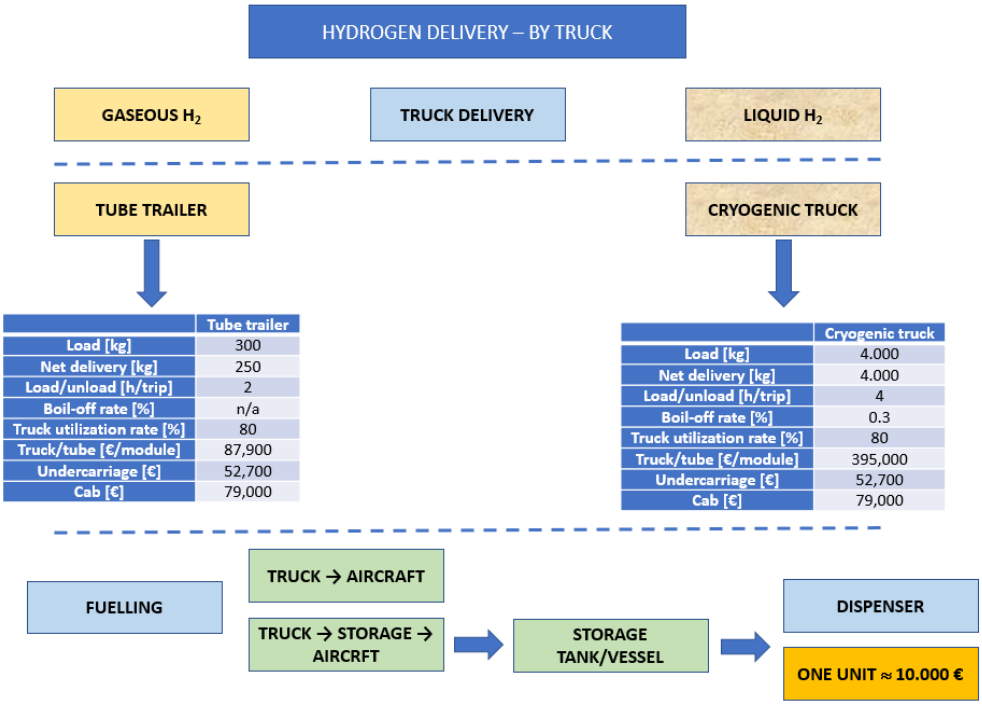


Figure 3.46: Hydrogen delivery by truck (VV.AA., 2019).

The cost of liquid tank truck delivery is about 10 % of tube trailer delivery (0.16 €/kg vs. 1.82 €/kg). Tube trailer investment costs and energy efficiencies are more sensitive to the delivery distance than those of road tankers. An example of needed equipment for tube trailer delivery is shown in Figure 3.46.

Figure 3.47: Gaseous hydrogen delivery by tube trailer (left) and liquid hydrogen delivery by cryogenic truck (left) (VV.AA., 2019).

#### 3.4.2.3.4.2 Transport by pipeline

If hydrogen is being delivered continuously by pipeline (Figure 3.48), little, if any hydrogen storage may be required, and it would not make sense to liquefy the hydrogen and then deliver it to a pipeline as a gas. In pipelines with large variations in

flow, hydrogen may need to be stored to meet the peak demand. The method of storage in that case would depend on the stored quantity and the storage time. Piping systems are usually several km long, in some cases even hundreds. Due to a great length of these piping systems, and therefore a great volume, even a slight change in the pipeline system operating pressure can result in a large change of amount of gas, contained within the piping network. By making small changes in operating pressure, the pipeline can be used to handle fluctuations in supply and demand, avoiding the cost of onsite storage. Typical specifications for hydrogen pipeline systems are:

- pipe size: 10 cm – 30 cm,
- minimum depth of a pipeline: 90 – 120 cm,
- operating pressure: between 24 – 130 bar,
- most current system is constructed using steel and carbon steel pipes with corrosion protective coatings (mild strength steel – API 5L X42 or X52 and ISO 13847),
- extensive use of automated excess flow valves.

The cost of a H2 pipeline installation is very dependent on the location (state, rural, street, etc.). As seen from Figure 3.49, the initial capital investment into pipelines vary from 270 000 € to 810 000 € per km (Amos, 1998). The cost of compression, storage and dispensing is to be between 1.72 €/kg and 2.41 €/kg, with a likely cost of 2.06 €/kg of hydrogen for a pipeline station.

Figure 3.48: Hydrogen pipelines (VV.AA., 2019).

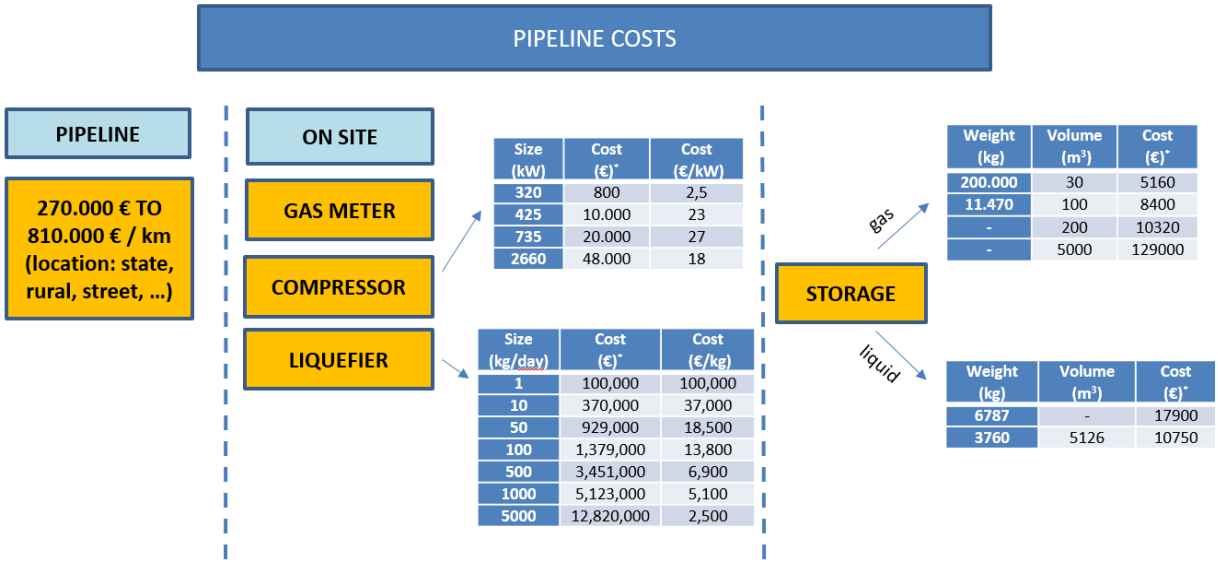


Figure 3.49: The cost of a pipeline for hydrogen (VV.AA., 2019).

Although hydrogen pipeline transport is technologically mature and the transport costs are similar to those of natural gas, most of the hydrogen is produced in the place of demand, with an industrial production facility every 80 to 160 km. In EU, the most developed pipeline supply is in Belgium (613 km), followed by Germany (376 km), France (303 km) and Netherlands (237 km). A similar pipeline supply and infrastructure could be set in place for transportation of hydrogen to airports. Innovative solutions are emerging, which could allow faster transport of larger capacities of hydrogen. The new technology allows hydrogen to be stored in a solid state inside a chemical, called sodium borohydride, which is much denser than liquid hydrogen. The great sustainable aspect shows that when extracting the hydrogen to refuel an aircraft, the chemical returns back to borax, and the compound, from which it is originally produced. As a result, it is fully recyclable and can therefore be reused for further transport of hydrogen (McLanagen, 1992).

### *3.4.2.3.5 On-site production*

One of the options, beside truck or pipeline delivery, is also on-site production of hydrogen at airport site, whereas as mentioned before, most likely the steam reforming method for producing hydrogen from natural gas would prevail, as it is widely used in chemical industry (as seen on Figure 3.50). The prices vary from 10 €/kg to 60 €/kg and the variations of hydrogen production cost are largely dependent on the price of NG.

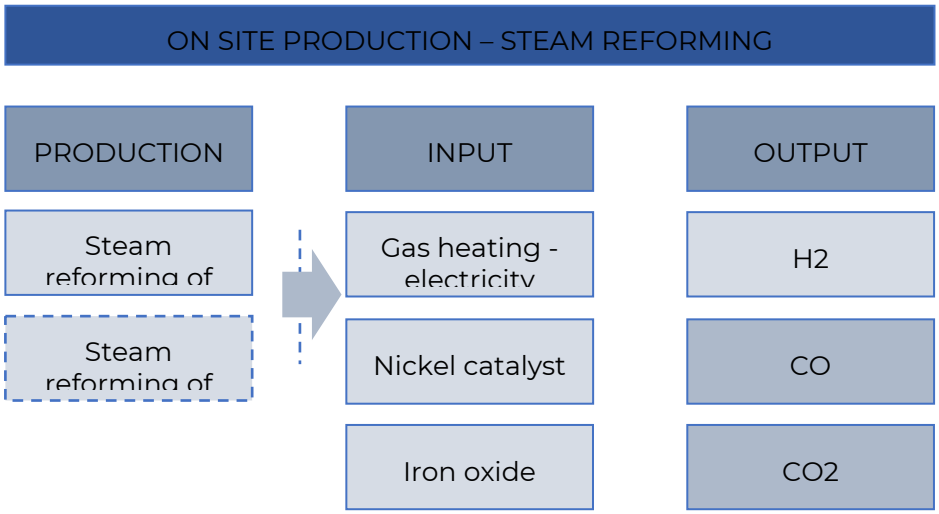


Figure 3.50: On site production of hydrogen (VV.AA., 2019).

### *3.4.2.3.6 Hydrogen storage*

Hydrogen can be stored in one of the following ways:

- As a gas inside underground caverns.
- As a compressed supercritical fluid at room temperature and pressure up to 70 MPa in a tank, made of carbon fiber or other composite materials. Hydrogen has a volumetric energy density of 4.8 MJ/l (1.33 kWh/l) at pressure 70 MPa, while it has a volumetric energy density of 2.9 MJ/l (0.81 kWh/l) at pressure 35 MPa. Requirements for physical storage of hydrogen can be found in ISO 19881.
- As a liquid at normal pressure in a cryogenic tank. Liquid hydrogen has a volumetric energy density of 8.5 MJ/l (2.36 kWh/l). Cryogenic tanks are made of multiple layers with vacuum or special isolation materials in between the layers and a small vent that releases hydrogen in the atmosphere, when the pressure in a tank increases over the limit due to a boil off. If hydrogen is stored in a liquid form, losses due to a boil-off have to be taken into consideration.
- Inside materials in materials based H2 storage systems. The most common method is a hydride storage, where hydrogen is absorbed inside metallic lattice of metals like palladium, magnesium or aluminium, but also other possibilities are known or tested. This kind of storage is still in an experimental phase and is nowadays commercially not competitive with physical storage.
- As a slush hydrogen (solid state) in a cryogenic tank. Due to economic reasons, slush hydrogen is rarely used.

- As cold-compressed or cryo-compressed hydrogen, where hydrogen is both compressed and cooled. This method is still in an experimental stage but can reach relatively high volumetric energy densities (similar to slush hydrogen).

Above-ground storage of gaseous hydrogen typically employs high-pressure spherical or cylindrical tanks with pressure ratings as high as 30 MPa, but low-pressure spherical tanks with large diameters are also used. Capital costs for such storage vary between 26 and 172 €/kg of hydrogen. In many cases, small tanks are rented by the gas supplier for a couple thousand dollars a month.

Liquid hydrogen storage vessels are low pressure but have high capital costs because of the insulation required to prevent boil-off. Small vessels can be quite expensive, and the economy of scale savings are not significant except with large volumes. There is also a reduction in hydrogen losses with larger vessels because of the lower surface area per unit volume at the larger sizes. Perlite insulated tanks cost less than Mylar wrapped tanks, but still provide good insulating properties. The costs for liquid hydrogen storage vary between 27 and 610 €/kg (7.13 - 280 €/lb).

Because not all aircraft are going to change to LH2 overnight it must be kept in mind that during the transition period an airport must be able to handle both LH2 as well as kerosene aircraft. Most large airports have onsite kerosene fuel storage tanks. Similar tanks will need to be built to store LH2 below 25 K. The easiest solution would be to subsequently deliver the fuel to the aircraft via a well-insulated refuelling truck. Special care must also be taken for airport vehicles servicing LH2 powered aircraft (Van Zon, s.d.).

Figure 3.51: Hydrogen liquid storage (VV.AA., 2019).

### *3.4.2.4 Hydrogen manufacturers in Europe*

According to preliminary market analysis of existing hydrogen manufacturers in Europe, we noticed actual feasible possibilities to provide hydrogen for aviation sector,

when necessary. We can compare geographical position of hydrogen manufacturers and airports that operate flights with 9-19-seater aircraft (Figure 3.52).

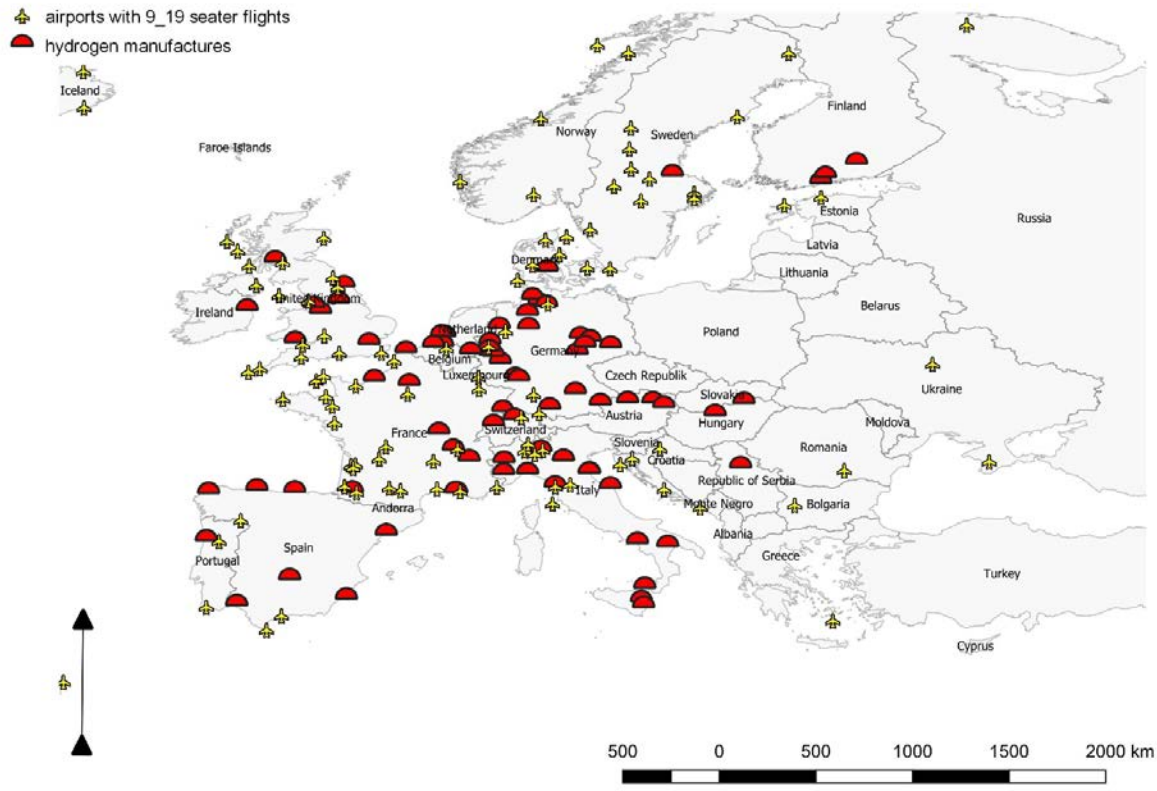


Figure 3.52: Hydrogen producers in Europe vs. airports operating with 9-19-seater aircraft (VV.AA., 2019).

We identified several nearby manufacturers, who could supply airports with necessary hydrogen supply in the central Europe (such as western part of Germany, Belgium, Luxemburg, Switzerland, Netherlands, northern part of Italy, etc.). However, in northern parts of Norway, Sweden and United Kingdom we noticed several airports operating above mentioned flights, but they have no nearby hydrogen suppliers. Several EU countries, such as Austria, Czech Republic, Hungary, Slovakia, southern part of Italy, western part of Germany, and Spain have several hydrogen producers, but no nearby airport that would operate flights with 9-19-seater aircraft. Countries such as Slovenia, Croatia, Montenegro, Bulgaria, Romania, and Ukraine have few daily flights operating with 9-19 aircraft, but no hydrogen manufacturer nearby.

Considering the airports in EU, operating flights with 20-70-seater aircraft, the geographical dispersion is very similar (Figure 3.53). Central Europe has a large amount of hydrogen suppliers, which cannot be said for Eastern Europe (Belarus, Bulgaria, Czech Republic, Hungary, Poland, Moldova, Romania, Russia, Slovakia, Ukraine. The biggest producers of hydrogen in Europe are: Air Liquide, Air products, Linde, Messer and Praxair.

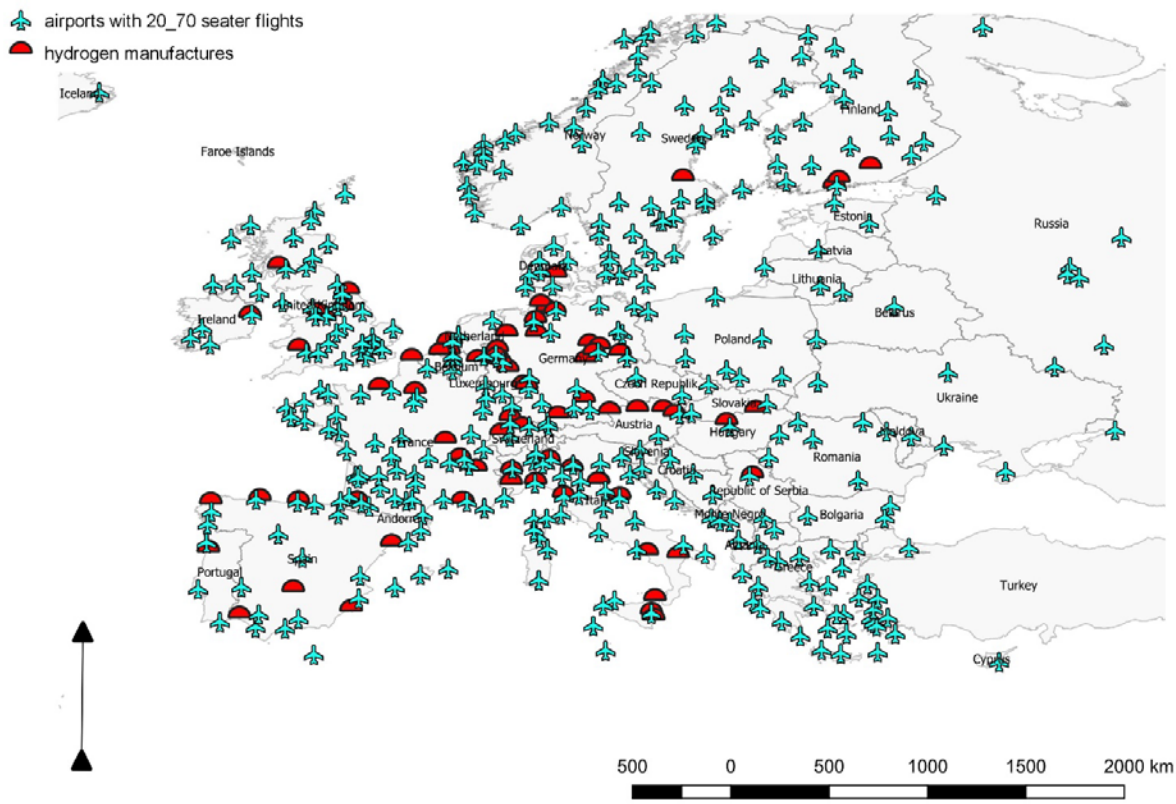


Figure 3.53: Hydrogen producers in Europe vs. airports operating with 20-70-seater aircraft (VV.AA., 2019).

### *3.4.2.5 Requirements for hydrogen refueling*

Airports should be able to provide following services for the hydrogen fuelled aircraft:

- Normal refuelling during aircrafts' turnaround between two flights (a cold system fuelling).
- De-fuelling due to planned maintenance activities and troubleshooting.
- First refuelling of new aircraft or refuelling an aircraft after maintenance and troubleshooting (warm system refuelling).
- Boil-off management due to overnight parking, long-time overhauls or failure cases.

Due to safety reasons, all above stated procedures have to be performed in open space, free from flammable and combustible objects (e.g. trees) and restricted only to personnel preforming the fuelling or de-fuelling operations. Aircraft, storage and connecting pipeline have to be properly grounded and bounded before an operation of fuelling or de-fuelling starts. During warm system de-fuelling or refuelling, a fuel tank has to be purged with inert gas (helium or nitrogen) to prevent mixing hydrogen with air. More details on how to preform stated procedures can be found in ISO/PASS 15594: 2004 Airport hydrogen fuelling facility operations.

For minimal requirements, hydrogen can be pursued from hydrogen production facilities and transported to the airport. In this case, no stationary storage of the fuel at airport is needed or recommended – fuelling should take place directly from movable storage, in which hydrogen was transported to the airport (e.g. truck), as shown on Figure 3.54. At the aircraft interface refuelling point, the temperature of the liquid hydrogen should be 20 K or lower. The pressure should be higher than 700 kPa to achieve acceptable fuelling times (20 min).

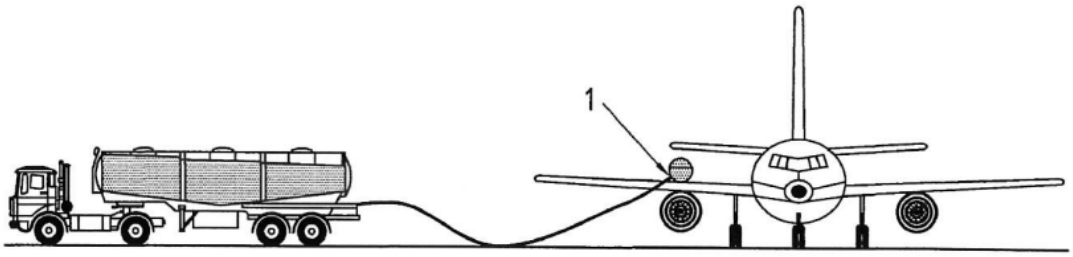


Figure 3.54: An example of aircraft fuel system layout (VV.AA., 2019).

A refuelling coupling unit for a small aircraft, defined as Type I in ISO/PASS 15594, can be manual and has to include a refuelling hose, a refuelling connector, and safety monitoring equipment. A refuelling connector, together with the attached part of refuelling hose, cannot exceed 10 kg (or preferably 7 kg). Connector should have a diameter of 30 mm (Yang & Ogden, 2007) to meet the requirements of the connectors used for road vehicles. A system should include a filter for filtering particles larger than 5 micrometres. Filter should be detachable and cleanable. The safety equipment should include a monitoring equipment, powered by batteries that would measure pressure, temperature, flow rate, filling level of the tank, hydrogen leak and valve position and a transportable detector of hydrogen concentration and heat.

For minimal requirements, boil-off hydrogen can be directly released safely (open environment). Nevertheless, an equipment for re-catching of hydrogen should be preferred for economical and safety reasons.

### *3.4.2.6 Relevant standardization*

Main standards concerning hydrogen storage, transport, operation and handling are reported in Table 3.34.

Table 3.34: Relevant hydrogen standards.

| | |
|---|---|
| ISO 16110 | Hydrogen generators using fuel processing technologies |
| ISO/PASS 15594: 2004 | Airport hydrogen fuelling facility operations |
| ISO 14687-2:2012 | Hydrogen fuel - Product specification - Part 2: Proton exchange membrane (PEM) fuel cell applications for road vehicles |
| ISO 19881: 2018 | Gaseous hydrogen - Land vehicle fuel containers |
| ISO 13847:2013 | Petroleum and natural gas industries - Pipeline transportation systems - Welding of pipelines |
| ISO/TR 15916:2015 | Basic considerations for the safety of hydrogen systems |
| ISO 13984:1999 | Liquid hydrogen - Land vehicle fuelling system interface |

### *3.4.2.7 An assessment of ground infrastructure for hydrogen supply*

A study from C. Young and J. Ogden (Yang & Ogden, 2007) considers different hydrogen delivery scenarios for USA. Although the analysis is considering equipment and transport costs characteristically adjusted for USA market in 2007, the obtained conclusions can be generalized to todays' EU market as well. A study considers three different delivery scenarios: delivery by gas truck, delivery by cryogenic truck and delivery by pipeline.

In the first scenario (delivery by gas truck), hydrogen is compressed at a production site and transported to the local consumer by tube trailer trucks. It is assumed that the full trailer is dropped at the delivery site and that the empty trailer is picked up afterwards. The largest cost component in the gas truck delivery scenario are the operating and maintenance costs of the truck, including drivers' labour. Therefore, transport distance has the greatest effect on delivery costs and scales linearly with distance, while on the other hand, costs are relatively independent on hydrogen flow rate (amount of hydrogen delivered to the consumer per day).

In the second scenario (delivery by cryogenic truck), hydrogen is liquefied at the production site and transported to the consumer by cryogenic truck. A study assumes that trailers are not left at consumers' site and that in each trip the truck empties its entire load, and that the minimal capacity of the liquefier, used at the production site, is 30 tons of H2 per day. The largest cost component, if using cryogenic truck delivery scenario, is liquefaction (80 % - 95 % of all costs), therefore the overall costs of liquid hydrogen delivery strongly depends on hydrogen flow and is almost independent on distance.

In the third scenario (delivery by pipeline), hydrogen is first pre-compressed at the production site and then delivered to the consumer by pipeline. With regards to the use, hydrogen can be further compressed at consumer's site as well. In this scenario, the most important cost component is the pipeline capital cost. Therefore, the overall costs depend both on hydrogen flow rates and distance.

Figure 3.55 presents an optimal hydrogen transmissions scenarios and minimal transmission costs for different hydrogen flow rates and transport distances. It can be concluded that delivery of a compressed gas by truck is an optimal solution for short distances and low hydrogen quantities. Delivery by a cryogenic truck is optimal for large distances and low hydrogen flow rates, while the delivery by a pipeline is optimal for high hydrogen flow rates and large distances.

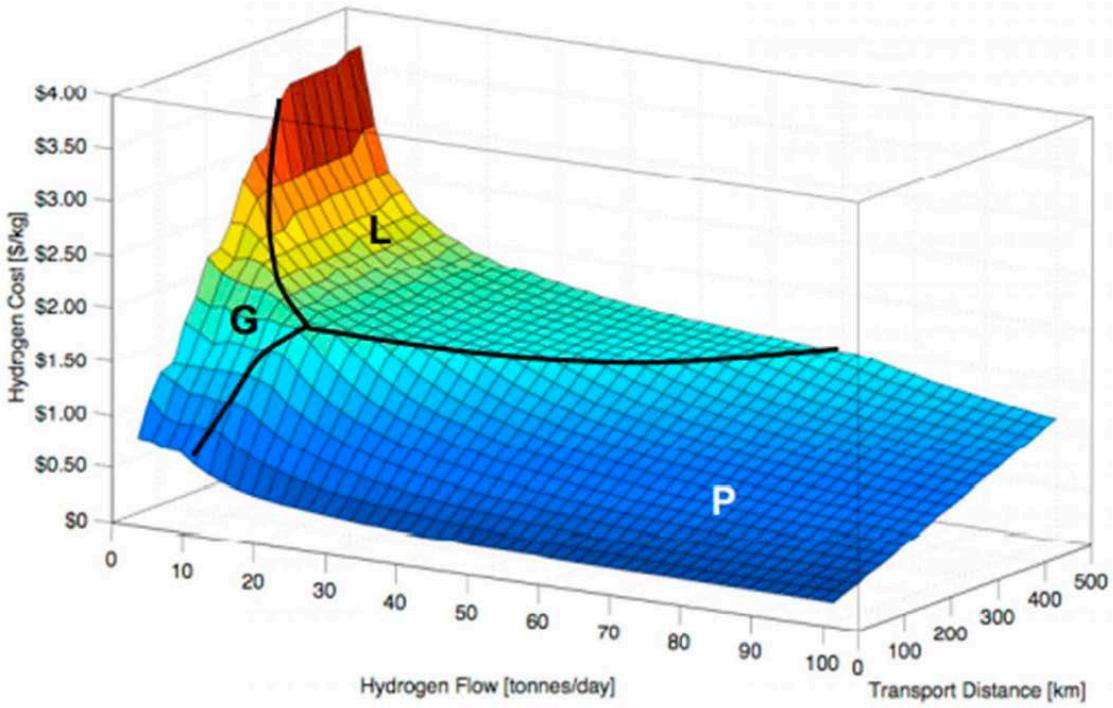


Figure 3.55: Optimal hydrogen transmission scenarios and minimal hydrogen transmission costs depending of hydrogen flow rates and transport distances (VV.AA., 2019).

Nevertheless, above mentioned study assumes that the end user does not differentiate between gaseous and liquid hydrogen. However, aircraft should be fuelled by hydrogen in liquefied form for two reasons. First, an effective specific energy of hydrogen and tank system is higher for liquid hydrogen compared to gaseous hydrogen. Therefore, an aircraft flying on liquid hydrogen is lighter than the aircraft using compressed hydrogen. As aircraft consumption is proportional with aircraft

mass, aircraft flying on liquid hydrogen consumes less hydrogen. Moreover, cryogenic hydrogen tanks are smaller than compressed hydrogen tanks, leading to better aerodynamic properties and therefore even lower consumption. To assess the hydrogen transmission economy, aircraft efficiency consumption has to be considered in the analysis as well. Unfortunately, an exact energy efficiency of a hybrid fuel-cell aircraft is still unknown as it largely depends on the design of an aircraft.

Under the present conditions, where the energy efficiency of a hybrid fuel-cell aircraft is similar to the conventional aircraft (this can be considered a reasonable assumption for 19 and 70 seater aircraft), we can conclude that a 19-seater aircraft would need approximately 200 kg of hydrogen for 500 km range flight, while a 70-seater aircraft would need approximately 700 kg of hydrogen for the same range.

If all regional aircraft in EU would be swapped for hybrid fuel-cell aircraft, 90 % of airports would need less than 10 tons of hydrogen daily to fuel them. Evermore, 80 % of airports operating with 19-seater aircraft and 50 % of airports operating with 70-seater aircraft would need less than 1 ton of hydrogen per day. On the other hand, an airport with the most regional daily flights in Europe (i.e. Tromsø airport, Norwegian) would need around 40 tons of hydrogen per day. Nevertheless, it should be taken into account that hydrogen is even more appealing fuel for large aircraft and therefore, one should not limit on assumption that only regional aircraft would fly on hydrogen. In that case, the daily consumption at large airport hubs could be even much larger.

References(n.d.). (Pipistrel d.o.o.) Retrieved 03 01, 2020, from http://www.pipistrel-aircraft.com

A.Schroeder, & T.Traber. (2012). The economics of fast charging infrastructure for electric vehicles. *Energy Policy, 43*, 136-144.

AEA. (1989). *DOC Method for short and medium range aircraft.* Association of European Airlines.

Aero Club Milano. (2019). *Aero Club Milano*. Retrieved 2019, from https://www.aeroclubmilano.it

Aerospace Standards Committee. (2011). *Aircraft Connectors for ground electrical supplies Part 2: Dimensions.*

Amos, W. (1998). *Costs of Storing and Transporting Hydrogen.* ( National renewable energy laboratory) Retrieved 03 30, 2019, from https://www.nrel.gov/docs/fy99osti/25106.pdf

Antoine, N., & Kroo, I. (2005). Framework for Aircraft Conceptual Design and Environmental Performance Studies. *AIAA Journal, 43*(10), 2100-2109.

Apffelstaedt, A. (2009). *Identifying CO2 Reducing Aircraft Technologies and Estimating Their Impact on Global Emissions.* Hamburg, Germany: Hochschule fur Angewandte Wissenschaften Hamburg - Studiendepartment Fahrzeugtechnik und Flugzeugbau.

Bertsch, L., Dobrzynski, W., & Guerin, S. (2010). Tool development for low-noise aircraft design. *Journal of Aircraft, 47*(2), 694-699.

BloombergNEF. (n.d.). *A Behind the Scenes Take on Lithium-ion Battery Prices*. Retrieved 01 13, 2020, from https://about.bnef.com/blog/behind-scenes-take-lithium-ion-battery-prices/

Bruce, R. D., Moritz, C. T., & Bommer, A. S. (2007). Sound power level predictions for industrial machinery. In *Handbook of noise and vibration control* (pp. 1001-1009). Hoboken, NJ: John Wiley & Sons, Inc.

Bruglieri, M., Marchionni, A., & Trainelli, L. (2019). Optimization of the demand satisfied by a micro-feeder hybrid-electric air transport service. *25th AIDAA International Conference.* Rome, Italy.

CHARM. (n.d.). Continuum Dynamics, Inc. Retrieved from https://www.continuum-dynamics.com/pr-charm.html

Chase, D. M. (1972). Sound radiated by turbulent flow off a rigid half-plane as obtained from a wave vector spectrum of hydrodynamic pressure. *The Journal of the Acoustical Society of America, 52*(3B), 1011-1023.

de Vries, R., Hoogreef, M., & Vos, R. (2019). Preliminary Sizing of a Hybrid-Electric Passenger Aircraft Featuring Over-the-Wing Distributed-Propulsion. *Proceedings AIAA Scitech 2019 Forum.* San Diego, CA, USA.

Department of Energy of the United States. (n.d.). *Prices and trends*. Retrieved 02 13, 1019, from https://www.energy.gov/

Deutsche Umweltbundesamt. (2007). *Anleitung zur Berechnung von Larmschutzbereichen (AzB).*

Dillich, S. e. (n.d.). *Hydrogen Production Cost Using Low-Cost Natural Gas*. Retrieved 02 12, 2019, from https://www.hydrogen.energy.gov/pdfs/12024_h2_production_cost_natural_gas.pdf

Drela, M., & Youngren, H. (n.d.). XRotor.

DuBois, D., & Paynter, G. C. (2006). *Fuel Flow Method 2 for Estimating Aircraft Emissions.* Everett, WA: The Boeing Company.

ECAC. (2016). *Report on standard method for computing noise contours around civil airports - Volume 2: Technical guide.* Neuilly-sur-Seine, France.

Electrek . (n.d.). *Tesla is in talks with electric truck customers to install 'Megacharger' stations, report says*. Retrieved 01 13, 2020, from https://electrek.co/guides/tesla-megacharger/

EUROCONTROL. (2006). The Aircraft Noise and Performance (ANP) database: an international data resource for noise modellers.

EUROCONTROL. (2016). *IMPACT: EUROCONTROL's ingegrated aircraft noise and fuel burn & emission modelling platform.*

Eurostat. (n.d.). *Aircraft traffic data by main airpor*. Retrieved 01 13, 2020, from https://ec.europa.eu/eurostat/web/transport/data/database

Eyers, C., Norman, P., Middel, J., Plohr, M., Michot, S., & Atkinson, K. (2004). *AERO2k Global Aviation Emissions Inventories for 2002 and 2025.* Hampshire, UK: European Commission; QinetiQ Ltd.

Farassat, F., & Succi, G. P. (1980). A review of propeller discrete frequency noise prediction technology with emphasis on two current methods for time domain calculations. *Journal of Sound and Vibration, 71*(3), 399-419.

Filippone, A. (2014). Aircraft noise prediction. *Progress in Aerospace Sciences, 68*, 27-63.

Fink, M. R. (1979). Noise component method for airframe noise. *Journal of Aircraft, 16*(10), 659-665.

Flightradar24. (n.d.). *ATH/LGAV Athens Eleftherios Venizelos Greece Departures*. Retrieved 01 13, 2020, from https://www.flightradar24.com/data/airports/ath

FOCA. (2007). Appendix 5: Calculation of emission factors. In *Aircraft piston engine emissions.* Bern, Switzerland: Federal Office of Civil Aviation.

Friedrich, C., & Robertson, P. (2014). Hybrid-electric propulsion for aircraft. *Journal of Aircraft*, 176–189.

Gasco, L., Asensio, C., & de Arcas, G. (2017). Communicating airport noise emission data to the general public. *Science of The Total Environment, 586*, 836-848.

Ginsberg, J. (2018). *Acoustics - A Textbook for Engineers and Physicists, Volume I: Fundamentals.* Springer.

Gnadt, A. R., Speth, R. L., Sabnis, J. S., & Barrett, S. R. (2018). Technical and Environmental Assessment of All-Electric 180-Passenger Commercial Aircraft. *Progress in Aerospace Sciences, 105*, 1-30.

Goldman, B. (2012). Modifications to Psu-wopwop For Enhanced Noise Prediction Capabilities (Master Thesis). Penn State University.

Gudmundsson, S. (2013). *General Aviation Aircraft Design: Applied Methods and Procedures (1st Ed.).* Butterworth-Heinemann.

Guo, Y. P. (2005). A statistical model for landing gear noise prediction. *Journal of Sound and Vibration, 282*(1-2), 61-87.

Guo, Y. P. (2013). Flap side edge noise modeling and prediction. *Journal of Sound and Vibration, 332*(5), 3856-3868.

H. Hubbard, H. (1991). *NASA Reference Publication 1258, Vol. 1 WRDC Technical Report 90-3052. Aeroacoustics of Flight Vehicles.* Hampton, Virginia: NASA Langley Research Center.

Hanson, D. B. (1984). Shielding of prop-fan cabin noise by the fuselage boundary layer. *Journal of Sound and Vibration, 92*(4), 591-598.

Hendricks, E. S., & Gray, J. S. (2019). PyCycle: A Tool for Efficient Optimization of Gas Turbine Engine Cycles. *Aerospace, 6*(8), 1-36.

Howe, M. S. (1978). A review of the trailing edge noise. *Journal of Sound and Vibration, 61*(3), 437-465.

*Hydrogen Europe*. (n.d.). Retrieved 04 30, 2019, from https://www.hydrogeneurope.eu/

Ibrahim, R. (2018). *Market and cost analysis for hybrid-electric aircraft.* Milan, Italy: Politecnico di Milano.

International Civil Aircraft Organization. (2014). *Annex 16 - Environmental Protection, Vol. 1, Aircraft Noise.* International Civil Aircraft Organization.

Isermann, U., Matschat, K., & Müller, E. A. (21-23 July 1986). Prediction of aircraft noise around airports by a simulation procedure. *Proceedings of Inter-Noise 86.* Cambridge, MA.

Kyprianidis, K. G., Nalianda, D., & Dahlquist, E. (2015). A NOx Emissions Correlation for Modern RQL Combustors. *Energy Procedia*.

Lim, T. C., & Singh, R. (1991). Statistical energy analysis of a gearbox with emphasis on bearing path. *Noise Control Engineering Journal, 37*(2), 63-39.

Lopes, L. V., & Burkley, C. L. (5-8 June 2011). Design of the next generation noise prediction program: ANOPP2. *Proceedings of the 17th AIAA/CEAS Aeroacoustic Conference.* Portland, OR.

Lu, C. (2011). The economic benefits and environmental costs of airport operations: Taiwan Taoyuan International Airport. *Journal of Air Transport Management, 17*(6), 360-363.

*MAHEPA Project*. (n.d.). Retrieved 03 01, 2020, from http://www.mahepa.eu

McLanagen, S. R. (1992). Toward a hydrogen economy: The storage and transmission of hydrogen: Technical note. *International Journal of Ambient Energy , 13:* , 49-52.

Miller, L. N., Wood, E. W., Hoover, R. M., Thompson, A. R., & Patterson, S. L. (1984). *Electric power plant environmental noise guide.* Washington, DC: Edison Electric Institute.

Moshkov, P. A. (2018). Integral model of noise of an engine-propeller power-plant. *Journal of Engineering Physics and Thermophysics, 91*(2), 332-338.

Ollerhead, J. B., Rhodes, D. P., Viinikainen, M. S., Monkman, D. J., & Woodley, A. C. (1999). *The UK civil aircraft noise contour model ANCON: Improvements in Version 2.* NATS.

P. Succi, G. (1979). Design of Quiet Efficient Propellers, SAE Paper 790584.

P. Succi, G., Munro, D., & Zimmer, J. (1982). Experimental Verification of Propeller Noise Prediction. *AIAA Journal, 20*.

Papacostas, C., & Prevedouros, P. (2001). *Transportation engineering and planning, 3rd Ed.* Upper Saddle River, NJ: Prentice Hall.

Pegg, R. (1979). *A summary and evaluation of semi-empirical methods for the prediction of helicopter rotor noise (NASA-TM-80200 Technical Report).* Hampton, VA, United States: NASA Langley Research Center .

Pietrzko, S., & Bütikofer, R. (13-15 November 2002). FLULA - Swiss aircraft noise prediction program. *Proceedings of Acoustics 2002 Innovation in Acoustic and Vibration.* Adelaide, Australia.

Pipistrel Vertical Solutions d.o.o. (2012). *Panthera*. Retrieved 2019, from https://www.panthera-aircraft.com

Raymer, D. P. (2018). *Aircraft Design: A Conceptual Approach (6th Ed.).* Washington, D.C.: AIAA, Inc.

Riboldi, C. E., Mariani, L., Trainelli, L., Rolando, A., & Salucci, F. (2020). Assessing the effect of hybrid-electric power-trains on acoustic and chemical pollution. *Aerospace Europe Conference (AEC2020).* Bordeaux, France.

Rolando, A., Salucci, F., Trainelli, L., & Riboldi, C. E. (2020). On the Design of an Electric-Powered Micro-Feeder Aircraft. *Proceedings of the Aerospace Europe Conference (AEC).* Bordeaux, France.

Rolando, A., Salucci, F., Trainelli, L., Riboldi, C. E., & Khan, Y. M. (2020). On the Design of an Electric-Powered Micro-Feeder Aircraft. *Aerospace Europe Conference 2020 (AEC2020).* Bordeaux, France.

Roskam, J. (1989). *Airplane Design (Vol. I-VIII).* Wichita, KS: DAR Corporation.

S. Brentner, K., & Farrasat, F. (2003). Modeling aerodynamically generated sound of helicoptor rotors. *Progress in Aerospace Sciences, 39*, 83-120.

SAE Aerospace. (1977). *Prediction procedure for near-field and far-field propeller noise - AIR 1407.*

SAE Aerospace. (1986). *Procedure for the calculation of airplane noise in the vicinity of airports - AIR 1845.*

Salucci, F., Riboldi, C. E., Trainelli, L., & Rolando, A. (2020). Optimal Sizing and Operations of a Battery Recharging Infrastructure for a Regional Airport. *Aerospace Europe Conference (AEC 2020).* Bordeaux, France.

Schaefer, M. (2006). *Methodologies for Aviation Emission Calculation-A Comparison of Alternative Approaches towards 4D Global Inventories.* Berlin, Germany: DLR;TUB.

Schroeder, A., & Traber, T. (2012). The economics of fast charging infrastructure for electric vehicles. *Energy Policy, 43*, 136–144.

*Servizio Elettrico Nazionale (Italian National Electric Service)*. (n.d.). Retrieved 01 13, 2020, from https://www.servizioelettriconazionale.it

Sujitha, S. (2016). RES based EV battery charging system: A review. *Renewable and Sustainable Energy Reviews*(75), 978-988.

Synodinos, A. P., Self, R. H., & Torija, A. J. (2018). Framework for Predicting Noise-Power-Distance Curves for Novel Aircraft Designs. *Journal of Aircraft, 55*, 781-791.

Tacina, K. M., & Wey, C. (2008). *NASA Glenn High Pressure Low NOx Emissions Research.* Cleveland, OH: NASA Glenn Research Center.

Tada, H. (1999). *An intermittent-combustion general aviation aircraft engine exhaust noise prediction algorithm.* Daytona Beach, FL: Embry-Riddle Aeronautical University.

Tesla. (n.d.). *Charge on the road – Tesla*. Retrieved 01 13, 2020, from https://www.tesla.com/supercharger?redirect=no

Timmerhaus, K., & Mendelssohn, C. (2017). In *Advances in Cryogenic Engineering.* New York, NY, USA: Springer.

Trainelli, L., Bruglieri, M., Salucci, F., & Gabrielli, D. (2020). Optimal Definition of a Short-Haul Air Transportation Network for Door-to-Door Mobility. *Proceedings of Aerospace Europe Conference AEC.* Bordeaux, France.

Trainelli, L., Riboldi, C. E., Salucci, F., & & Rolando, A. (2020). A General Preliminary Sizing Procedure for Pure-Electric and Hybrid-Electric Airplanes. *Proceedings of the Aerospace Europe Conference (AEC 2020).* Bordeaux, France.

Trainelli, L., Riboldi, C. E., Salucci, F., & Rolando, A. (2020). A General Preliminary Sizing Procedure for Pure-Electric and Hybrid-Electric Airplanes. *Aerospace Europe Conference (AEC 2020).* Bordeaux, France.

Trainelli, L., Salucci, F., Rossi, N., Riboldi, C., & Rolando, A. (2019). Preliminary Sizing and Energy Management of Serial Hybrid-Electric Airplanes. *Proceedings AIDAA 2019 XXV International Congress.* Roma, Italy.

United States Department of Transportation. (2017). *Aviation Environmental Design Tool (AEDT) - Version 2d - User guide.*

Van Zon, N. (n.d.). *Liquid Hydrogen Powered Commercial Aircraft: Analysis of the technical feasibility of sustainable liquid hydrogen powered commercial aircraft in 2040*. Retrieved 02 12, 2019, from https://hydrogeneurope.eu/sites/default/files/2

Villafana, W. (2016). Rotorcraft noise abatement procedures development. *A Thesis in Aerospace Engineering*. The Pennsylvania State University.

VV.AA. (2019). *MAHEPA D10.1 Ground infrastructure investment plan.*

Wang, Y., Hailian, Y., Shuai, Z., & Xiongqing, Y. (2014). Multi-Objective Optimization of Aircraft Design for Emission and Cost Reductions. *Chinese Journal of Aeronautics., 17*(1), 52-58.

Wasiuk, D. K., Khan, A. H., Shallcross, D. E., & Lowenberg, M. H. (2016). A Commercial Aircraft Fuel Burn and Emissions Inventory for 2005–2011. *Atmosphere, 7*(78), 1-14.

Winther, M., & Rypdal, K. (2016). 1.A.3.a Aviation. In *European Environment Agency - EMEP/EEA Air Pollutant Emission Inventory Guidebook 2016 - Part B.* Luxembourg: Publications Office of the European Union.

Worley, O., & Klabjan, D. (2011). Optimization of battery charging and purchasing at electric vehicle battery swap stations. *IEEE Vehicle Power and Propulsion Conference (VPPC).*

Yakovitch, T. I., Yu, Z., Herndon, S. C., Miake-Lye, R., Liscinsky, D., Knighton, W. B., . . . Pringle, P. (2016). *Exhaust emissions from in-use general aviation aircraft - Research report 164.* ACRP.

Yang, C., & Ogden, J. (2007). Determining the lowest-cost hydrogen delivery mode. *International Journal of Hydrogen Energy, 32*(2), 268-286.

Zheng, Y. e. (2014). Electric vehicle battery charging/swap stations in distribution systems: comparison study and optimal planning. *IEEE Transactions on power Systems*(29), 221–229.

Zheng, Y., Dong, Y., Xu, Y., Meng, K., Zhao, J. H., & Qiu, J. (2014). Electric vehicle battery charging/swap stations in distribution systems: comparison study and optimal planning. *IEEE Transactions on Power Systems, 29*, 221-229.

# 4 Data exchange format

## *4.1 Motivation*

When multiple organizations/expertises are involved in a common project and several tools and software are used in a possible integrated framework, the share and exchange of knowledge and sensible data can represent a critical step, often causing mistakes and delays.

In order to overcome possible risk connected to possible inconsistencies in the shared data, it is agreed among the consortium to identify not only a common data structure but also a common data format.

As reported in Figure 4.1, this approach allows for a paradigm shift from a “expertise based” data exchange (that usually depends specifically on the involved experts/modules case by case) to a “data-centred” exchange where a common structure and format is shared.

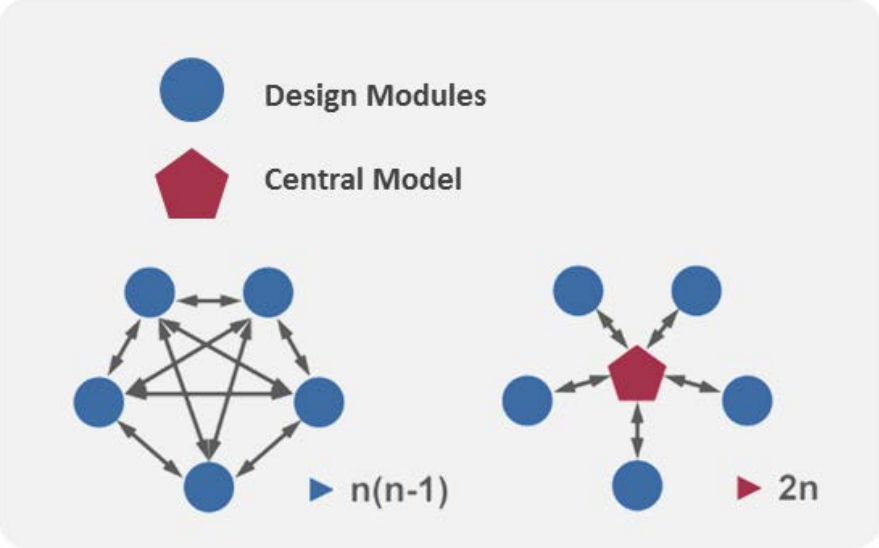


Figure 4.1: Comparison of module depending and centralized model data sharing paradigms.

The following consequences can be appreciated when passing to a centralized data schema:

- All the involved modules (in the present project case the modules are the software and design tools that will be used by the consortium) must be input/output compatible with the proposed centralized data format; this aspect usually requests an initial effort at once by each partner in adapting his own tool(s).
- The number of different interfaces reduces drastically at increasing the number of active modules.

- A centralized structure allows to store multi-fidelity data simply adding different levels. As an example, if the aerodynamic forces of a wing are calculated through a lifting line theory during a first conceptual sizing, the possible results can be stored in 'Analysis/Aerodynamics/Lift/WingspanDistribution'. If consequently, a CFD analysis allows to retrieve a more detailed pressure distribution, it could be stored under "Analysis/Aerodynamics/Lift/PressureDistribution', without interfering with the initial lifting line results.
- When all the tools are proven to be compatible, it is possible to automate part of the design process without importing/exporting manually the data limiting the manual intervention. This characteristic is a valuable advantage especially when several design iterations are needed to converge a design configuration.

## *4.2 Proposed data schema and format*

The present task deals with two complementary aspects: the choice of a common data structure and the choice of a specific exchange format.

The firs one consists in the determination of a data structure capable to store in a unique and efficient way (without any conflicts and repetitions) all the input/output produced during the conceptual and preliminary design analyses to be faced in WP2 and WP3. The second aspect deals with the determination of a specific file format compatible with both the data structure and the tools developed for the analysis.

Without the aim to reinventing the wheel, the UNIFIER19 consortium uses an existing open source structure and format named "Common Parametric Aircraft Configuration Schema" or CPACS developed by DLR [1].

The CPACS formats allows to store geometrical data, structure arrangements as well as subsystem and analysis data in a hierarchal tree format for a wide variety of air vehicles also with non-conventional configuration (eg. BWB or PrandtlPlane).


Figure 4.2: CPACS Hierarchical tree relative to the definition of the wing geometry.

As an example, a part of the hierarchical tree reported in Figure 4.2 shows the geometrical definition of the wing, done by means of sections, each one of them located at a precise span position. The Child-Parent relations of all the objects presented in the schema is well explained in [2].

An important feature present in the CPACS schema is that, in addition to the predefined data for conventional “objects” of the aircraft, it is also possible to define a “Tool-Specific” Data Set in such a way possible novel solutions and configuration can be included.

Hence, the definition of the novel propulsion architecture together with its performance, will be included in the CPACS schema according this metric.

This task will be tackled at the beginning of the WP2 when the qualitative trade off will highlight the list of possible powertrain option that will undergo in the conceptual concurrent analysis.

The CPACS data are stored in a XML file with pre-defined formatting rules so that the parent/child relations structure is guaranteed. The XML file format is compatible with most of the software environments used as design tools. As an example, Matlab®, which the current conceptual design tools of both POLIMI and TUDELFT are

developed in, allows to read/write data from/to an external XML source. In addition, a range of open source geometric kernels, as for instance SALOME, allows to generate a parametrized CAD model directly from the geometric information contained in the data structure. As an example, the open source software TIGL is expressly conceived y DLR to generate (and modify) an aircraft geometric model simply loading A CPACS source as shown in Figure 4.3.

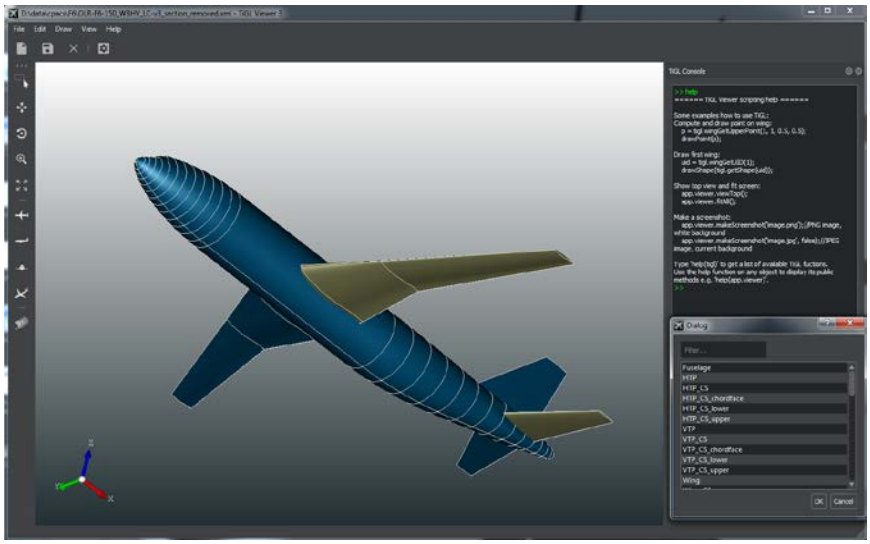

Figure 4.3: Geometric model of an aircraft in TIGL from a CPAC data [2].

Finally, open source tools are available, as RCE by DLR, that allow to control in an automated way a complex workflow when different tools are involved. For instance, it is assumed to perform a conceptual design of an aircraft involving only a simple aerodynamic Vortex Lattice Method based tool, a mission analysis tools and a weight estimation procedure; the three tools are somehow linked together with known input-output relations. Therefore, under the assumption that all the three tools are CPACS compatible, it is possible by using RCE to establish an automatic workflow that automates the different analyses. In the contest of WP3, where high fidelity tools are involved, this design strategy might be beneficial and efficient in order to ensure in a due computational time, the correct number of iteration loops and to achieve a converged consistent design.

## *4.3 References*

[1] B. Nagel, D. Böhnke, V. Gollnick, P. Schmollgruber, A. Rizzi, G. La Rocca, J.J. Alonso, (2012) Communication in Aircraft Design: Can we establish a Common Language?, 28th International Congress of the Aeronautical Sciences, Brisbane, Australia, 2012.

[2] VVAA. (2020) CPACS version 3.20; CPACS Documentation. https://www.cpacs.de/documentation/CPACS_3_2_0_Docs/html/89b6a288-0944-bd56-a1ef-8d3c8e48ad95.htm

## Concept: Commuting by Mini-Plane

For millions who drive to work every day, travelling along highways and encountering heavy traffic is typically something to be endured and rarely something to enjoy. The EU is funding UNIFIER19, a **new airliner concept** that will offer a new, sustainable and **cost-efficient air mobility solution**. The 19-passenger **near-zero-emission aircraft** is designed to provide a diffused service **connecting smaller airports** to each other and **with hubs**, accommodating both scheduled and on-demand shuttle flights. Exploiting the sparse, underused **European small airport network**, UNIFIER19 will offer commuters a **radically new, comfortable mobility experience** that will be as simple to use as a bus.

## Setting Design Requirements for a New Mobility Experience

Our design requirements start with **providing** to our citizens **a new, near-zero emission travel experience**. The design requirements include:

- **Embarking/disembarking experience as easy as a bus**: access provisions integrated in the airframe featuring facial recognition to authenticate pre-registered and security-approved travelers.
- **Operations from unpaved runways**: low infrastructure investments from municipalities exponentially increase the number of communities served by this miniliner.
- **Propellers/impellers** configured and actively controlled to provide an acoustically acceptable footprint.
- **Flexible cabin layout**: passengers, cargo, mixed use or medevac to increase versatility.
- **Fly-by-wire control system**: smooth ride by propulsion response integration in the control laws, cruise performance optimization by reducing trim drag, pilot workload reduction in the envisioned single-pilot operations, paving the way to future upgrades to autonomous/remotely-piloted flight.

## Design Approach – A Systematic Analysis of Potential Solutions

**Hybrid-electric propulsion** is one of the enabling technologies for quieter, more efficient and environmentally sustainable aircraft. It can be effectively coupled with:

- **Lightweight electric motors** can be structurally installed on the airframe, where beneficial airframe-to-propulsion interactions may be created. Their wide operating range permits to **design propellers** and **ducted fans** which are **quieter** and **more efficient** than conventional designs.
- In a **distributed propulsion** configuration, the wing surface area can be minimized without sacrificing fundamental performance, such as take-off distance. Additionally, the effect of distributed propellers can be integrated in the fly-by-wire flight control architecture to supplement aircraft control surfaces and augment their authority, resulting in **overall system mass reduction**.

These and other features translate into a very **wide solution space**. In this proposal, **one of the project's strengths is the systematic approach devised to analyze such solution space and extract the optimal configurations**, which not only cater for near-zero emission travel, but **that can actually be built**, **certified and sustain commercially successful operations** in the near future.

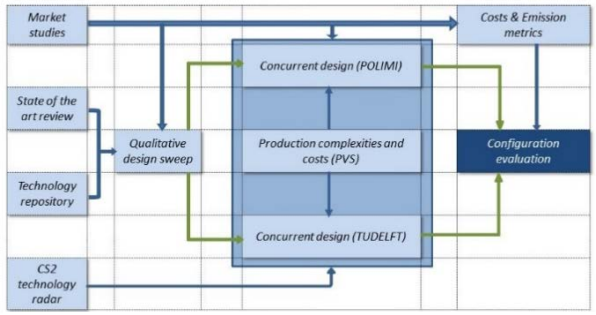


*The concurrent design loop workflow producing an optimal configuration*

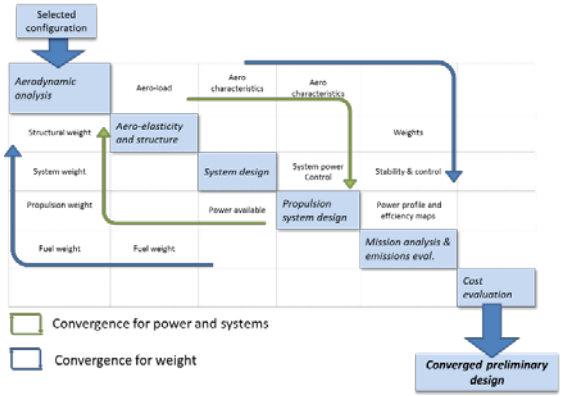


*Detailed evaluation of the selected configuration*

## Detailed Evaluation of the Winning Design Configuration

The winning configuration will undergo a **high-fidelity synthesis.**

The sub-tasks that will be carried out in this phase include

- **Propulsion architecture and propeller design**
- FHA/FMEA and a more detailed estimate of certification complexity, **certification, production and maintenance costs**.
- Weight and balance, performance, stability and control analysis
- Structural sizing and basic aeroelasticity
- Sizing of **ground infrastructures**.
- An extensive **CFD simulation** campaign, in order to assess the aerodynamics characteristics under different operating conditions

By adopting a common design framework where each partner manages its own discipline enables the chance to improve the design loops and iteration effectiveness during the synthesis of the configuration when using **high-fidelity tools**.

## CONTACTS

### *Coordinator*


➔ **Pipistrel Vertical Solutions**

Vipavska Cesta 2 – 5270 Ajdovscina – Slovenia
Contact person: Dr. David Erzen
e-mail: david.erzen@pipistrel.si
Tel.: +386 (0)5 366 38 73


### *Partners*


➔ **Politecnico di Milano**

**Department of Aerospace Science and Technology**

Via La Masa 34 – 20156 Milano – Italy
Contact person: Prof. Lorenzo Trainelli, PhD
e-mail: lorenzo.trainelli@polimi.it
Tel.: +39 02 2399 8347

➔ **Technische Universiteit Delft**

Kluyverweg 1 – 2629HS Delft – The Netherlands
Contact person: Prof. Fabrizio Oliviero, PhD
e-mail: F.Oliviero@tudelft.nl
Tel.: +31 (0)15 278 9045


UNIFIER19
COMMUNITY FRIENDLY MINILINER


The project has received funding from the CleanSky2 Joint Undertaking (JU) under grant agreement NO 864901. The JU receives support from the European Union's Horizon 2020 research and innovation programme and the Clean Sky 2 JU members other than the Union.